LITHIUM NIOBIUM OXIDE MULTIFUNCTIONAL MATERIALS AND APPLICATIONS IN NEUROMORPHIC COMPUTING

A Dissertation
Presented to
The Academic Faculty

by

Marshall Brooks Tellekamp Jr.

In Partial Fulfillment
of the Requirements for the Degree
Doctor of Philosophy in the
School of Electrical and Computer Engineering

Georgia Institute of Technology
December 2017

COPYRIGHT © 2017 BY MARSHALL BROOKS TELLEKAMP JR.

LITHIUM NIOBIUM OXIDE MULTIFUNCTIONAL MATERIALS AND APPLICATIONS IN NEUROMORPHIC COMPUTING

Approved by:

Dr. W. Alan Doolittle, Advisor
School of Electrical and Computer Engineering
Georgia Institute of Technology

Dr. Faisal Alamgir
School of Materials Science and Engineering
Georgia Institute of Technology

Dr. P. Doug Yoder
School of Electrical and Computer Engineering
Georgia Institute of Technology

Dr. Arijit Raychowdhury
School of Electrical and Computer Engineering
Georgia Institute of Technology

Dr. William Hunt
School of Electrical and Computer Engineering
Georgia Institute of Technology

Date Approved: [Nov 09, 2017]

Even the simplest brains of the simplest animals are awesome computational instruments. They do computations we do not know how to do, in ways we do not understand.

-Carver Mead

ACKNOWLEDGEMENTS

I wish to acknowledge the contributions of the many people who have supported me, encouraged me, and given me the confidence and skills for which I am very thankful. First, I would like to thank my friends and family who are the most important people in my life, especially my wife Page who has provided me with a truly unreasonable amount of support. I would like to thank those educators who have worked many thankless hours to provide younger generations with the toolsets to succeed in their lives and careers, with special respect for Dr. Doug Yoder and Dr. Bill Hunt who, in addition to aiding me both in and out of the classroom, have agreed to serve on my Ph.D. committee. This work was greatly aided by my fellow researchers in the Advanced Semiconductor Technology Facility with whom countless hours of discussion have occurred, namely Jordan Greenlee, Brendan Gunning, Joshua Shank, Chloe Fabien, Evan Clinton, Ehsan Vadiee, and Joe Merola. Finally, I want to thank my advisor Dr. Alan Doolittle for his unwavering support and instruction, without which I would not have pursued this degree.

TABLE OF CONTENTS

LIST OF TABLES

LIST OF FIGURES

LIST OF SYMBOLS AND ABBREVIATIONS

a	Lattice constant
α	Inverse transfer length
c	Lattice constant
C	CTLM geometric correction factor – Section 4.1
C	Charge rate = Full capacity in 1 hour – Section 4.2
C_{sat}	Saturated battery capacity
ΔR	Optically induced resistance change – Chapter 5
$\Delta R/R$	Memristor Figure of Merit
d_0	Characteristic length for scaling annular ring-dot memristors
DI	De-ionized
E×N(E)	Energy specific Auger intensity N(E) multiplied by energy E
E_g	Band Gap Energy
FOM_0	Memristive figure of merit for an infinitely small inner contact
FOM_∞	Memristive figure of merit for an infinitely large inner contact
I_0	Final Auger peak height – Chapter 3
I_0	Modified Bessel function of the first kind – Chapter 4
K_0	Modified Bessel function of the second kind
L_T	Transfer length
m/q	Mass to charge ratio
n	Electron concentration
N_A	Donor concentration
p	Hole concentration
ϕ	Lithium to metal-chloride flux ratio

ϕ	Rotational angle for XRD scans
q	Elementary electric charge
R_T	Total resistance
R_{SH}	Sheet resistance
R_{SC}	Sheet resistance underneath a contact
R_1	Annular ring-dot: dot contact resistance
R_2	Annular ring-dot: ring contact resistance
R_{semi}	Annular ring-dot: semiconductor field resistance
r	Annular ring-dot: ring contact inner radius
r’	Annular ring-dot: ring contact outer radius
r_0	Annular ring-dot: dot contact radius
ρ	Resistivity
ρ_c	Specific contact resistivity
σ	Conductivity
τ	Time constant, various usages
T_c	Superconducting Critical Temperature (K)
Q_f	Quality Factor
μ_n	Electron mobility
μ_p	Hole mobility
V_{charge}	Upper limit for calculating battery capacity
$V_{discharge}$	Lower limit for calculating battery capacity
V_{OC}	Open-circuit voltage
ω	XRD stage rocking angle
2θ-ω	XRD diffraction angle for symmetric scans
2θ	Characteristic XRD diffraction angle

AES	Auger Electron Spectroscopy
AFM	Atomic Force Microscopy
BCC	Body-Centered Cubic
BCT	Body-Centered Tetragonal
BEP	Beam Equivalent Pressure
CTE	Coefficient of Thermal Expansion
CTLM	Circular Transfer Length Mesurement
CVD	Chemical Vapor Deposition
EIS	Electrochemical Impedance Spectroscopy
FCC	Face-Centered Cubic
FIB	Focused Ion Beam
FWHM	Full Width at Half Maximum
GSG	Ground-Signal-Ground
GST	$Ge_2Sb_2Te_5$
ICP	Inductively Coupled Plasma
IEN	Institute for Electronics and Nanotechnology
LCO	$LiCoO_2$
LPE	Liquid Phase Epitaxy
LPEE	Liquid Phase Electro-Epitaxy
LTCC	Low Temperature Co-fired Ceramic
LMIG	Liquid Metal Ion Gun
MBE	Molecular Beam Epitaxy
MEIC	Mixed Electronic-Ionic Conductor
MFC	Mass Flow Controller
MIT	Metal-Insulator Transition

n-BuLi	n-butyllithium
NDR	Negative Differential Resistance
NMDA	N-methyl-D-aspartate
PBN	Pyrolytic Boron Nitride
PLD	Pulsed Laser Deposition
PPF	Paired Pulse Facilitation
RHEED	Reflection High Energy Electron Diffraction
RIE	Reactive Ion Etching
RMS	Root Mean Squared
SCCM	Standard Cubic Centimeter per Minute
SIMS	Secondary Ion Mass Spectrometry
STDP	Spike-Timing Dependent Plasticity
STP	Short Term Potentiation
TEM	Transmission Electron Microscopy
TLM	Transfer Length Measurement
TOF	Time of Flight
UHV	Ultra-High Vaccuum
XPS	X-ray Photoelectron Spectroscopy
XRD	X-Ray Diffraction
XRR	X-Ray Reflectometry

SUMMARY

This work explores the growth fundamentals and multifunctional applications of materials in the Li-Nb-O family with specific focus on the memristive applications of $LiNbO_2$ as a synaptic analogue in neuromorphic computing architectures. Among other important studies, the use of Li-alloying contacts is explored as a method to induce non-volatile behavior in natively volatile $LiNbO_2$ memristors, a feature critical for neuromorphic behavior.

Chapter 1 provides a brief introduction to the topics presented, including an overview of neuromorphic computing, spike-timing dependent plasticity (STDP), and the materials which make up the Li-Nb-O system. Chapter 2 provides a more detailed investigation of background material including a history of the molecular beam epitaxy (MBE) growth of Li-Nb-O materials, a discussion of state-of-the-art memristor technology, and a thorough overview of the multifunctional material $LiNbO_2$ which is the primary focus of this work.

Chapters 3 – 5 deal with lithium-niobium-oxide epitaxial growth, material characterization, and devices based on these materials. Contained is an exploration of the MBE growth of lithium niobium oxides including equipment, experiment design, an exploration of the temperature vs. flux phase space, and material characterization. Structures and devices based on MBE grown lithium niobite are investigated. This includes studying the effects of alloying and non-alloying contacts on $LiNbO_2$ memristor volatility. The effects of chemical insertion and removal of lithium into/from lithium niobite are also investigated.

Finally, Chapter 8 provides a concise conclusion along with an outlook on the future of the technology presented in this dissertation.

CHAPTER 1. INTRODUCTION

1.1 Neuromorphic Computing and Memristors

Neuromorphic computing is a field that aims to mimic the computational function of the brain through circuitry and materials engineering. With the impending end of Moore scaling of transistors due to geometric and tunneling limitations[1] there are many "more-than-Moore" research efforts to efficiently handle complex computing problems[2]. One of these solutions is the adaptive learning and noisy data processing capabilities found in the human brain. These same tasks which are computationally expensive for a Von Neumann based CMOS computer are easily performed by a neural computer with incredibly low power consumption, approximately 20 Watts for the human brain[3].

Neuromorphic computing, in its most basic sense, can be broken down into three primary functional components demonstrated pictorially in Figure 1-1. First is signal generation, performed by the soma. In the biological context, the signal is called an action potential which is a specifically shaped voltage spike in time, consisting of polarization often followed by brief hyperpolarization. Next is signal propagation and conditioning, performed by axons and dendrites. Finally there is signal weighting and adaptation, performed by the synapses which connect each neuron to thousands of other neurons by neurotransmitters across the synaptic cleft between the pre-synaptic axon and the post-synaptic dendrite. Of all the neural components required to build a neuromorphic

computer, synapses have received the most attention recently due to their understood role in learning and memory[4], and their functional similarity to memristors[5].

Memristors are a passive circuit element showing resistance modification as a function of

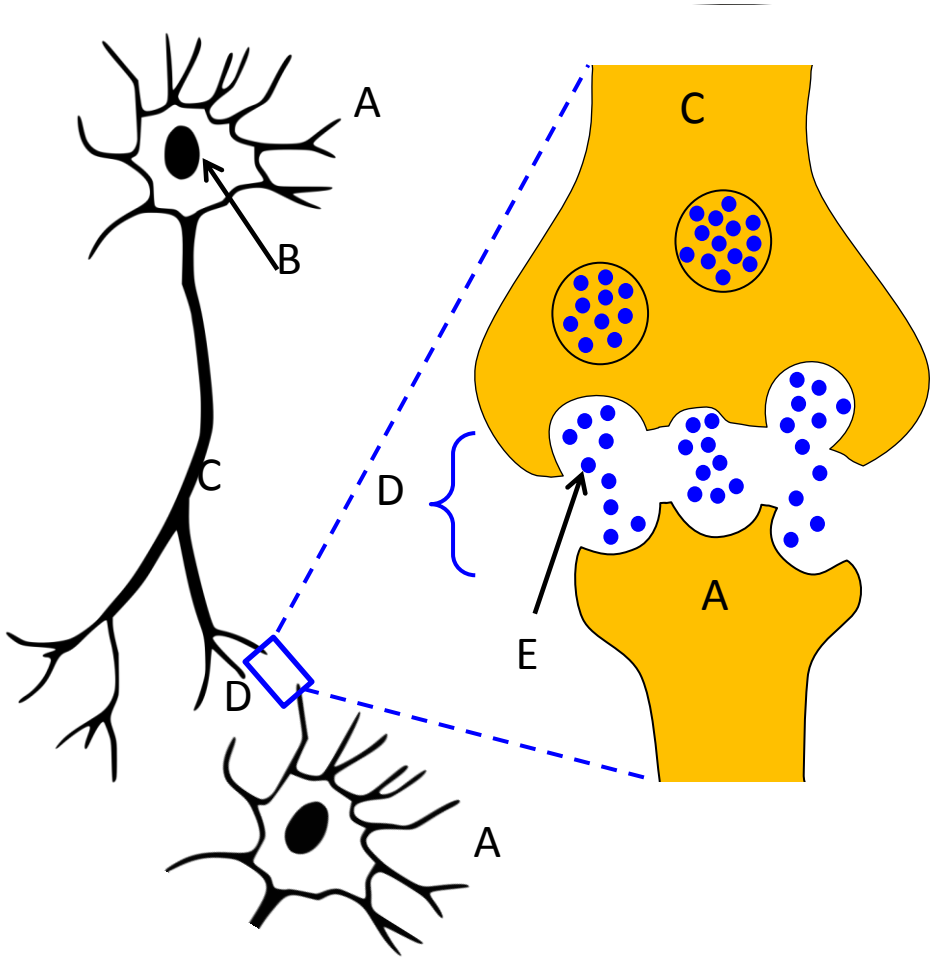

Figure 1-1. Schematic of a neuron. (A) Dendrites which propagate signals to the soma. (B) The soma which integrates charge from the dendrites and produces an action potential. (C) The axon which propagates the signal from the neuron cell body to the synapses. (D) The synapse which weights the transport of signals from one neuron to the next acting as a charge gate. (E) Neurotransmitters which facilitate the synaptic function. © Looxix/ Wikimedia Commons / CC-BY-SA-3.0 / GFDL

prior input current or voltage. The current memristor technology primarily focuses on binary state resistive switches which succeed in basic synaptic weighting processes[6–10], but often provide no inherent pathway for more intricate biological mechanisms such as short term potentiation (STP), paired pulse facilitation (PPF), and spike-timing dependent plasticity (STDP) which are analog processes linked to basic brain functions such as learning and memory. Recent technologies are however beginning to take these processes into account[11–18] via external control through more complex circuitry. An important feature of these mechanisms which is often overlooked is the timescale on which they occur. These processes occur on biological timescales from milliseconds to minutes in the case of STP and multiple minutes or longer for long term potentiation (LTP).

A memristor, in order to emulate synaptic behavior, should show LTP and STP[19] in an analog manner[5]. Embedded in these functions are deep forms of data processing and memory. To the best of our understanding at this point, LTP is an important part of long term memory functions[4] and STP is partially responsible for learning and adaptation through STDP. STDP is the rule embedded in synapses which allows correlations to occur based on action potential timing and was theorized by Hebb's postulate[20], which can be summarized by the adage "neurons wire together if they fire together."[21]

When a neuron fires, or creates an action potential, this action potential propagates down the axon to the synaptic cleft, where the charge causes neurotransmitters to be released. These neurotransmitters accumulate on the other side of the synaptic cleft at the dendrite, propagating charge to the soma of the post-synaptic neuron. The efficacy with which the synaptic cleft releases and transports neurotransmitters is the state variable defined by STDP, and can be thought of as a weighting function. When the pre-synaptic neuron fires just before the post-synaptic neuron this positive feedback is encoded into the synapse as a positive correlation by the STDP function. When the post-synaptic neuron fires prior to

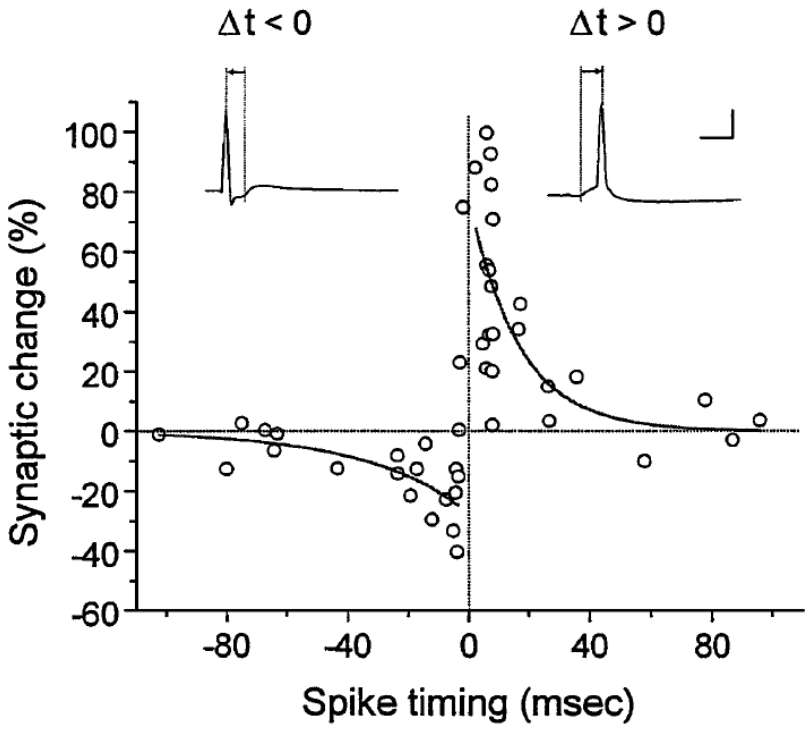

Figure 1-2. Spike-timing dependent plasticity (STDP) measured in cultured rat hippocampal neurons by *Bi and Poo* [30]. Positive arrival offset (pre-synaptic spike arrives first) results in positive weight change (positive correlation), while negative arrival offset results in negative correlation.

the pre-synaptic neuron it is encoded as a negative correlation by the STDP function. The degree of weight change is partially determined by the decay rate of the synapse and the timing between the two action potentials. Finally, if two action potentials meet at the synaptic cleft separated by a time larger than the synapses decay constant, termed the critical window for the induction of synaptic potentiation, there is no weight change by the STDP function. These two action potentials are not correlated! The STDP function is shown in Figure 1-2 as a plot of % synaptic weight change versus action potential arrival offset in ms measured in rat hippocampal neurons in 1998[22]. It should be noted that in the memristor community STDP is often erroneously attributed to a purely potential driven process where the polarization of a pre- (post-) synaptic action potential sums with the hyperpolarization of the post- (pre-) synaptic action potential to produce the STDP curve[14,19,23]. This convenient interpretation is however incorrect, as the mechanisms for STDP and more complicated functions such as PPF[24], where pulse trains induce larger changes which scale by pulse number, are volatile in nature[24–26]. The behavior originates from the ion diffusive dynamics[11,27,28], and while voltage-dependent learning rules exist the correlation between voltage summing of action potentials and STDP is purely coincidental.

While STDP is the primary focus of learning rules in the current neuromorphic community, additional intricacies of neuro-synaptic function must be addressed in order to understand the scope of neural function in comparison to neuromorphic computing. Hebbian theory, as previously introduced, refers to synaptic weight changes affected by

both pre- and post-synaptic neuron firing events[29]. STDP is a Hebbian learning rule observed in biological synapses, but it is not the only observed rule. There are various other learning rules, both Hebbian and non-Hebbian. These rules can be (but are not limited to) spike-timing dependent (Hebb and non-Hebb)[30], spike-rate dependent[31], voltage dependent[32], and transmitter induced (both dependent on and independent of pre- and/or post- synaptic potential) at both pre- and post-synaptic receptors by neurotransmitters such as N-methyl-D-aspartate (NMDA)[33]. Additionally, some sources consider STDP and STP as separate long- and short-term effects which play both concurrent and separate roles in neural function[26,34]. The roles of these adaptation rules are also convoluted by many different types of neurons which exist in the brain, some placing limits on the types of synapses (and therefore learning rules) connecting these neurons[29]. Finally, there are additional complications from non-learning synaptic activity such as conditioning and redistribution which provide long term stability over a network of neurons[29,35,36]. The above learning rules behave at different timescales from a few seconds to tens of seconds (induction) all the way to 10 minutes or greater (homeostatic), and it has been theorized and shown by modelling that rather than serving separate functions these rules act in concert to prevent system runaway and provide stable memory formation and recall in excitatory synapses[34]. This result illustrates the importance of a variety of synaptic timescales, an important feature found in $LiNbO_2$ based memristive devices explored in this thesis.

The vast set of neuron types, interconnection types, and learning rules both discovered and undiscovered presents the neuromorphic community with a difficult question to be answered. Namely, to what degree is biomimicry necessary to achieve the functionality desired from a neuromorphic computer? A complete understanding of the interactions of neural units is likely many decades away, and the result of studies such as *Zenke et. al.* 2015[34] have shown that these various processes may work together to facilitate useful, long-term learning and memory in ways beyond our current understanding. It is possible that by using ion-diffusive dynamics, such as those found in mixed electronic-ionic conductors (MIEC) like $LiNbO_2$, many synaptic functions may be replicated due to the ion driven dynamics found in neural systems. It is also possible that a minimalist replication of neural architecture is sufficient to achieve the desired function in a cost-effective way and that biologically realistic ion-diffusive dynamics are not necessary. Only through the continued concerted effort of the neuromorphic scientific community can we begin to answer these questions, and it is the goal of this thesis to be, in some way, a small part of that work.

1.2 The Li-Nb-O Material Family

The lithium niobium oxide family consists of conducting, semiconducting, and insulating materials across a wide resistivity and bandgap range. Figure 1-3 lists the resistivity of a few materials in the system as a function of niobium valence, ranging from conducting niobium to insulating lithium niobite ($LiNbO_3$). These materials span 22 orders of magnitude in resistivity with bandgaps from IR to UV[37–43]. Oxides in general have many desirable multifunctional properties, for example; piezoelectric, pyroelectric, and ferroelectric effects which can exist in a single material such as lithium niobate[44,45].

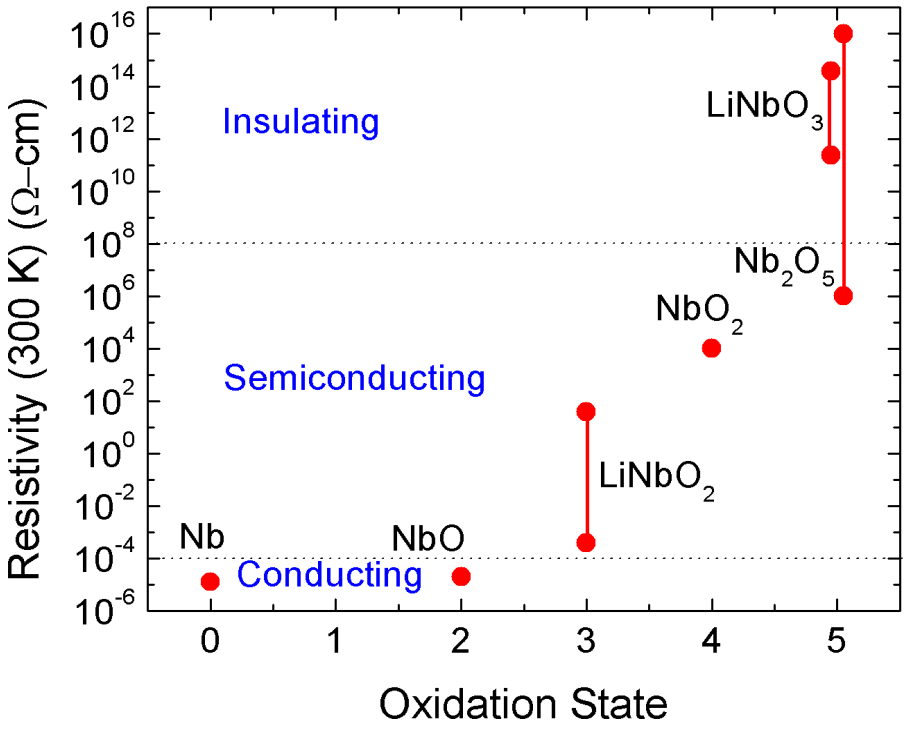

Figure 1-3. (Lithium) Niobium oxides plotted by their resistivity versus niobium valence, spanning 22 orders of magnitude resistivity. Materials can be conducting, semiconducting, or insulating depending on the oxidation state.

Lithium niobite ($LiNbO_2$), a suboxide of the same family, is currently the focus of multiple research areas. $LiNbO_2$ is used as a memristor for neuromorphic applications, a battery cathode material showing potential for high rate capability and long term cycle stability, and is also studied for unique optical properties[46–48]. NbO_2 acts as a digital volatile memristor, a device with discrete on and off resistance states. NbO_2 is currently used in memory, neuristor circuitry, and relaxation oscillator circuitry[8,49,50]. The Li-Nb-O material family also includes other ceramics of various dielectric constants used in a variety of applications including battery electrodes, microwave frequency dielectrics, phosphors, photocatalysts for water reduction, and hysteretic MIM tunnel diodes or "memdiodes" (Li_3NbO_4, $LiNb_3O_8$, and Nb_2O_{5-x})[40,51–56].

The growth optimization of these materials in a single deposition system is desirable due to the variety of properties that can be achieved and the potential heterostructure devices that can be imagined. Among these possibilities are strain enhanced sensors and MEMS, high K dielectrics, superlattices, thin film batteries, memtransistors, multi-layer neuromorphic heterostructures, and ferroelectric switching transistors with switchable enhanced channel conductance[57,58].

Despite the potential for new and enhanced functional devices and materials, this Li-Nb-O multifunctional material family remains relatively unexplored. A many-phased oxide system inherently contains significant complexity. The phase diagram of the Li_2O-Nb_2O_5 system is complicated by multiple phases existing in a very small range of temperature

and stoichiometry[59]. Due to these tight tolerances, precise control and understanding of all parameters is necessary for controllable growth of heterostructures and single phase materials. Molecular Beam Epitaxy (MBE) is an excellent platform for high stoichiometry control and crystalline quality, and therefore a good candidate for controlled growth of these materials[57].

1.3 Thesis Topic

Since 2008, memristors have been heavily studied for impact in non-volatile memory applications and to a lesser degree as functional synapses for neuromorphic computing[60,61]. The primary materials studied, filamentary memristors, do not provide analog resistance modulation; they show binary switching and through external engineering can exhibit multi-resistance state behavior through extremely precise pulse timing and shape control[62]. It is therefore desirable to identify a material system which can host neuromorphic functions in a biologically realistic way in order to more accurately implement the complex learning and adaptation algorithms native to the mammalian brain. Lithium niobite ($LiNbO_2$) has been proposed as a host material for biologically realistic synaptic function based on a continuum of resistance states across a theoretically large range[46,63]. The use of lithium niobite as a non-volatile memristor, or a device with "permanent" states useful for LTP, has not yet been explored. Additionally, the thin film growth of lithium niobite opens up significant potential for integration with other materials in the Li-Nb-O family which show multifunctional behavior such as

$LiNbO_3$ and NbO_2. The objective of the proposed research is to explore the growth fundamentals and multifunctional applications of materials in the Li-Nb-O family with specific focus on the memristive applications of $LiNbO_2$ as a synaptic analogue in neuromorphic computing architecture.

CHAPTER 2. BACKGROUND

2.1 MBE of Li-Nb-O Materials

$LiNbO_3$ was the first Li-Nb-O material grown by MBE. The first report in 1985 employed $LiNbO_3$ and Al_2O_3 substrates, showing polycrystalline material of unreported but "poor crystalline quality" for the homoepitaxial case and cubic Li_3NbO_4 for the Al_2O_3 substrate[64]. Another report in 1996 attempted homoepitaxial growth on $LiNbO_3$ substrates at 750 ℃ – 900 ℃ with 60° rotational domains (twin planes) and other no report of crystalline quality, as well as a $LiNbO_3/LiTaO_3$ superlattice [65]. NbO was first grown by *Petrucci et. al.*[66] in 1988 single crystalline and mixed phase with NbO_2 on $LiNbO_3$ substrates. *Posadas et. al.*[37] demonstrated the first growth of single crystalline NbO_2 by MBE on (111) $(La,Sr)_2(Al,Ta)_2O_6$ and $SrTiO_3$ substrates at 750 ℃. These films had a best XRD symmetric rocking curve FWHM of 252" and showed 60° rotational domains. NbO_2 has also been grown by other methods on c-plane sapphire. *Wang et. al.*[67] reports epitaxial growth by ion beam deposition giving an epitaxial relation of $<100>(110)\ NbO_2 \parallel <10\bar{1}0>(0001)\ Al_2O_3$, a rocking curve FWHM of 151°, and 60° rotational domains.

The remaining reports of Li-Nb-O growth by MBE have come from the Doolittle laboratory, my present Ph.D. advisor, who reported $LiNbO_3$ growths on SiC and Al_2O_3 at 900 ℃ with no report of rotational domains and a best crystalline uniformity, measured

by XRD rocking curve FWHM, of 150"[57,68–70]. The growth of NbO, $LiNbO_2$, and Li_3NbO_4 was also reported[69,70]. These materials are all grown by a lithium-assisted metal chloride growth chemistry at 900 ℃. In this method, the precursor $NbCl_5$ can be reduced to elemental niobium in the presence of lithium and a hot substrate where lithium getters the chlorine. LiCl desorbs due to its high vapor pressure leaving elemental niobium to react with oxygen and excess lithium. The method of single parameter phase control in the Li-Nb-O system described limits the lithium supply while niobium and oxygen are supplied in excess. The lithium flux directly controls the amount of adsorbed niobium so that adjusting the Li flux modifies niobium to oxygen ratio, and therefore the oxidation state, with respect to the constant O_2. This growth chemistry is also used in the present work, building on the previous single-parameter phase control method to include substrate temperature in a flux-temperature phase diagram.

2.2 $LiNbO_2$

Lithium niobite ($LiNbO_2$) is a lithium intercalated suboxide in the Li-Nb-O family. The $LiNbO_2$ unit cell belongs to the trigonal crystal system, space group $P6_3/mmc$ (no. 194)[71]. The crystal structure is depicted in Figure 2-1, with the unit cell highlighted by yellow lines. $LiNbO_2$ belongs to a family of layered ABX_2 structures, where A: Li, Na, Mg, Ca, Sc, Mn, Fe, Cu, Ag, Nb, Mo, Ta, W; B:Nb, Mo, Ta, W; X: O, N[72]. These structures all form layers of either (or both) octahedral or trigonal-prismatic symmetry. In $LiNbO_2$ the Li atoms form octahedral layers while the Nb atoms sit on the trigonal-prismatic site.

Each Nb atom aligns with two O atoms in the next layer, causing the trigonal prisms to be offset and 180° rotated from layer to layer.

$LiCoO_2$ is a widely studied battery cathode material and is structurally similar, forming in the $R\bar{3}m$ (no. 166) space group[73]. The only structural difference from $LiNbO_2$ is that

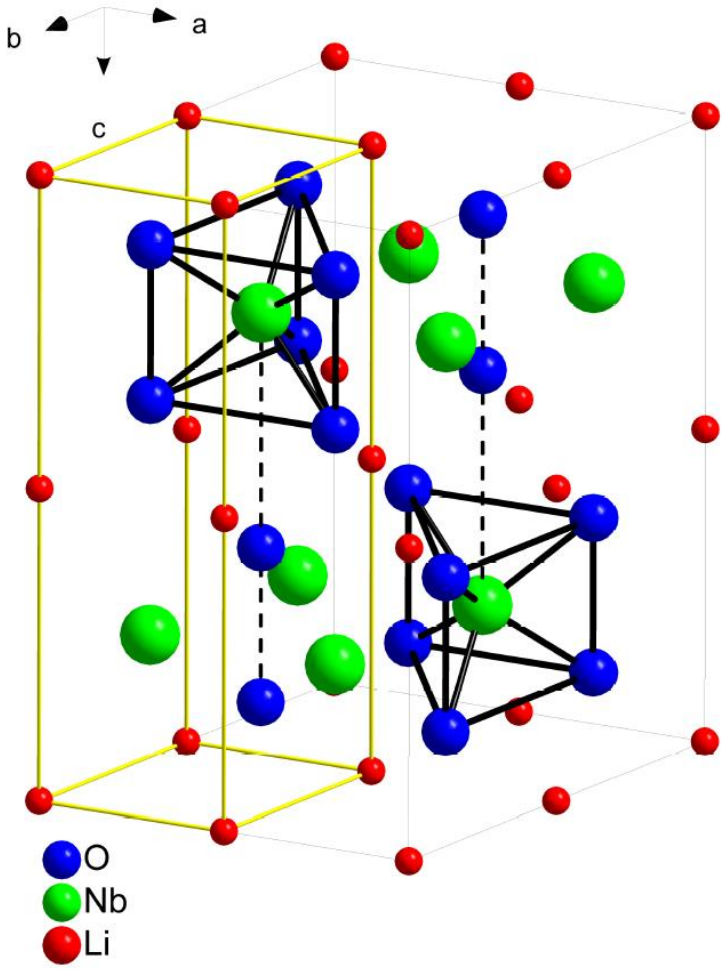

Figure 2-1. $LiNbO_2$ trigonal crystal structure. Sheets of Li separate NbO_6 trigonal prismatic layers, denoted by bolded black lines. The rhombohedral unit cell is shown in yellow. Dashed lines indicate the offset trigonal-prismatic alignment, screened by the Li layer, which are offset and rotated 180° between layers.

the $LiCoO_2$ crystal structure does not contain a 180° rotation or offset, resulting in both Li and Nb octahedral layers. Electronically, trigonal layers exhibit a higher degree of metal-metal orbital overlaps than octahedral layers and thus metallic type conductivity[72], which is shown experimentally by high conductivity in $LiNbO_2$[69] and insulating behavior in $LiCoO_2$[74].

$LiNbO_2$ was first synthesized by Meyer and Hoppe in 1976[71] by the heated reaction of powdered precursors forming a polycrystalline powder from which to obtain the crystal structure data. $LiNbO_2$ was not studied again experimentally until 1988 when many transition-metal dichalcogenides were explored for Li-ion battery applications. *Kumada et al.*[75] showed that $LiNbO_2$ may be chemically deintercalated, forming $Li_{1-x}NbO_2$, and that by removing Li from the crystal the lattice parameters and conductivity change. The material was also successfully incorporated into a battery cell with an open circuit voltage of 2.5 – 2.95 V for x = 0.96 – 0.5, respectively[75]. Beginning in 1990 $Li_{0.5}NbO_2$ was investigated for superconducting properties due to a crystalline similarity to high temperature cuprate superconductors, and was found to be superconducting below T_c = 5.5K[76]. *Geselbracht et. al.*[77] performed NMR measurements to determine the hopping time of mobile Li atoms, determined to be in the 10^{-4} s range, as well as optical absorption spectroscopy observing an absorption onset at ~2eV, agreeing with the hypothesis of *Kumada et. al.*[75] that $LiNbO_2$ is a semiconductor.

Electronic structure calculations were performed by *Novikov et. al.*[78] in 1994 showing that the band structure should theoretically transition from a direct bandgap material (E_g=1.4 eV) to an indirect bandgap material upon deintercalation to x = 0.5, noting that for nonstoichiometric material the Fermi level lies within the valence band. Li was shown to be completely ionized, donating an electron to fill the valence band. Additionally, experimental hall coefficient measurements determined that $Li_{1-x}NbO_2$ is degenerately doped with ~4.3×10^{21} holes/cm^3, or approximately 0.2 holes per molecule. Another first principles density functional theory study confirmed the findings in *Novikov et. al.* Specifically, the band structure is modified upon deintercalation transitioning from direct to indirect bandgap while simultaneously reducing the Fermi level into the valence band[79]. This feature was later observed experimentally by photoluminescence spectroscopy[80].

Single crystal $LiNbO_2$ was first produced as a bulk crystal in 1999[81] and an epitaxial thin film in 2011 by lithium-assisted metal-chloride MBE[69]. Thin film $LiNbO_2$ demonstrated extremely high p-type conductivity of 2500 S/cm at a hole concentration of 1×10^{21} cm^{-3} and a bandgap of 2.04 eV[69].

$LiNbO_2$ was first recognized as a memristor by *Greenlee et. al*[70] in 2012 by electrically stimulated resistance modification in simple metal-$LiNbO_2$-metal devices. This was later attributed to electrical coupling into loosely bound Li ions by *in situ* near edge x-ray absorption fine structure spectroscopy (NEXAFS), where the application of a bias causes

Li-ion drift across the device modifying the effective Li-vacancy hole doping profile[82]. Subsequent simulations and experimental electrochemical impedance spectroscopy (EIS) models show that the primary resistance modification occurs at the $LiNbO_2$-metal interface[83] and that the resistance change figure of merit, $\Delta R/R$, is maximized through a constrictive flow geometry where the benefit saturates at a cathode-to-anode contact periphery ratio is ~10:1[63].

Most recently, $LiNbO_2$ has been grown in high quality bulk crystal form by liquid phase electro-epitaxy (LPEE)[46] and in thin film form by reactive sputtering[84]. Current LPEE technology produces crystallites unsuitable for microelectronics due to their small size and nonuniformity. Sputtering produces preferentially oriented material of inferior crystalline quality compared to MBE films and these sputtered films are (101) oriented in contrast to (001) oriented MBE grown films.

2.3 $LiNbO_3$ Thin Films

Lithium niobate is a mature technology when considering bulk Czochralski grown material, but epitaxial thin films have yet to make commercial impact as research was largely abandoned in the late 1990s and early 2000s in favor of ion sliced or “smart cut” lithium niobate[85]. Ion slicing is a method of cleaving a bulk wafer along a plane weakened by H^+ or He^+ ion implantation. After the implantation step the thin film is removed from the bulk wafer by wafer bonding and shearing. While ion sliced lithium niobate has been successful in providing “thin film” materials, it has significant

limitations. Ion sliced material is limited to thicknesses greater than ≈ 500 nm, it must be polished to improve the surface roughness, it cannot be centrally incorporated into heterostructures, and it must be annealed at high temperatures to regain the electro- and nonlinear optical properties[85].

Epitaxial lithium niobate will only be commercially viable if the crystal quality can be improved to minimize optical and acoustic losses to acceptable values, especially if it can be grown on a low index material such as sapphire which can be beneficial for optical waveguiding. Previous techniques used to grow thin film lithium niobate include sputtering[86–90], sol-gel methods[91], pulsed laser deposition (PLD)[92–95], liquid phase epitaxy (LPE)[96,97], chemical vapor deposition (CVD)[98–101], and molecular beam epitaxy (MBE)[57,64,65,68,70] on substrates including $LiNbO_3$, $LiTaO_3$, Al_2O_3, and SiC. Most of these methods produce material with 60° rotational domains and large symmetric rocking curves. Rotational domains are undesirable in optical devices due to scattering at domain boundaries. LPE produces material of nearly bulk quality with symmetric rocking curves of 11", but in-plane structural characterization was not reported[96,97]. PLD grown material has also shown near-bulk rocking curves of 13" but reported rotational domains[95]. Other PLD grown material is single domain, but with a larger symmetric rocking curve of 612"[92]. Sputtered material shows higher overall rocking curve values and rotational domains; only one example shows minimal but still present twin planes[102]. Feigelson and Lee have produced the best overall material by CVD with rocking curves of 158" on sapphire substrates and 36" on lithium tantalate. These sapphire based films showed

minimal twin planes which are removed by a 750 ℃ 24 h anneal and the lithium tantalate based films did not show twin planes[98,99].

Previous MBE grown material is poorly reported in general with only one reference analyzing rotational domains[65] which were present, and two quoting symmetric rocking curves of 936" and 150", both grown on SiC[57,70]. There is no discussion of surface morphology for MBE grown material in current literature.

2.4 Memristors and Synaptic Application

Memristors are a class of fundamental two-terminal passive devices first suggested by Leon Chua in 1971[103]. Memristors were theorized out of completeness from an analysis of coupling between the four fundamental properties voltage (V), current (I), charge (Q), and magnetic flux-linkage (ϕ). Resistors couple voltage and current, capacitors couple voltage and charge, inductors couple current and flux-linkage, and the theorized memristor couples charge and flux-linkage in order to mathematically satisfy a relationship between the fundamental electromagnetic properties. A mathematical exploration of this completeness theorem described a device whose resistance changed as a function of input, and it was termed a memory-resistor[103]. While no memristor is known to fully satisfy the conditions first derived by Chua[104], an extension of this device class termed memristive systems enables a broad definition based on possible physical properties, devices which are recognized by a pinched hysteretic *I-V* characteristic[105,106]. In 2008 the formal connection between device properties and the term memristor was

realized and published in the form of TiO_2 resistive switching crosspoint devices[9], although resistive switching devices can be found in the literature as early as 1962[107]. After the connection between theory and device was recognized many devices have been researched and published as memristors. Among these memristors are various proposed mechanisms for operation including anion migration based filamentary conduction through an insulating layer[9,108], cation migration[12,70,109] , metal-insulator transitions and phase change materials[17,110,111], and spin or ferroelectric effects[112,113].

2.4.1 Filamentary Memristors

A foremost class of memristors being studied is the filamentary memristor, with filamentary switching observed in at least 24 binary oxides including TaO_x, TiO_x, AlO_x, NiO_x, WO_x and HfO_x[61]. The *I-V* characteristics of an HfO_x filamentary memristor are shown in Figure 2-2a. Filamentary memristors operate by the electric field induced growth of conductive filaments in amorphous transition-metal oxides. The generally agreed upon process is the initial formation of a current path through vacancies, defects, or grain boundaries, progressing via Joule heating to form a conducting filament[60,114]. The physical mechanism behind this filament growth is an active research area despite reports of cation[115], anion[116], and vacancy migration[114] as the mechanism. For all these devices the application of an initial electroforming pulse, a higher voltage than normal operation current-limited step which purposefully induces dielectric breakdown, is required for the onset of resistive switching unless the devices are made sufficiently thin

(<3 nm)[117]. The electroforming pulse is theorized to modify the composition of a laterally confined portion of the active material as the filament pathway.

Filamentary memristors were initially two state devices unsuitable for neuromorphics[9]. However, through clever device and input engineering filamentary memristors can show multi-state behavior and therefore some synaptic weighting[5,19]. Ag_2S filamentary devices can show multi-state behavior through the focused ion beam (FIB) milling of a nanometer sized gap between the active material and the electrode[118]. WO_{3-x} can show analog resistance modification by purposeful sub-stoichiometric oxygen content, allowing oxygen vacancy migration which can form a multi-state bridge between the electrode and the conducting filament[28,119].

Forming a 5 nm switching HfO_x switching layer on a TiN bottom electrode allows multi-state behavior theorized as an areal affect by modification of the effective reaction cross

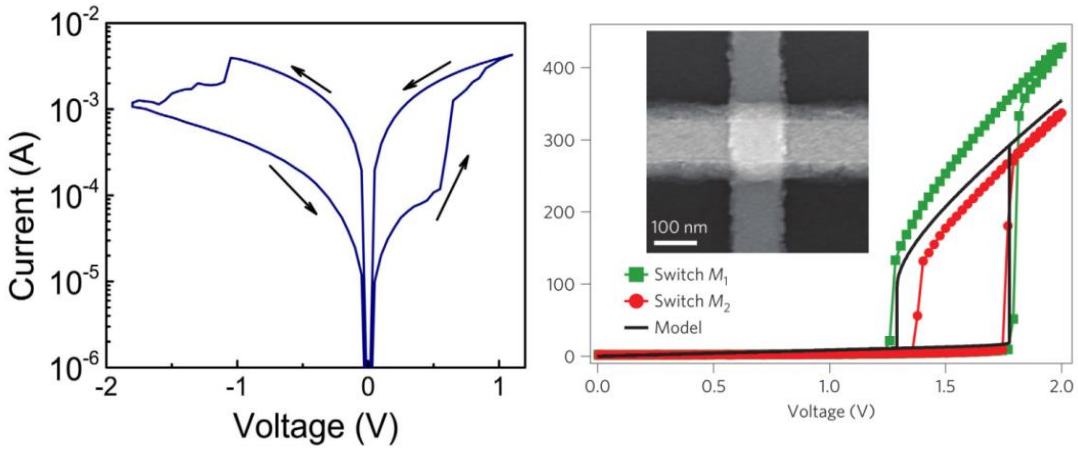

Figure 2-2. (a) *I-V* characteristics of a non-volatile Pt/HfO_2/Ta filamentary memristor (*Yang et. al.* 2013)[60]. (b) *I-V* characteristics of a volatile Pt/NbO_2/Pt (*Pickett et. al.* 2013)[49].

section of a filament through the removal of individual atoms[120]. TiN is theorized to aid in the memristive effect through reaction with oxygen[121]. Filamentary behavior may be entirely removed from HfO_2 by co-sputtering with a Mn dopant, enabling analog resistance modification[23]. $Ag/Ag_2S/Pt$ filamentary devices can modify conductance through the changing width of a Ag filament within the Ag_2S matrix due to the infinite Ag source from the contact. Although these devices are geometrically filamentary, the cation drift is analogous to a mobile ion wavefront memristor[11]. It was also shown that through careful input pulse control the tunnel barrier at the tip of a Ta_2O_{5-x}/TaO_y device synaptic plasticity can be obtained, where the TaO_y layer is theorized to act as an oxygen vacancy reservoir[14]. Recently a diffusion based mobile ion memristor has been shown using Ag co-sputtered with SiO_xN_y, HfO_x, and MgO_x, showing electromigration of Ag ions through the matrix which diffuse away after bias removal due to interfacial energy at the electrode, providing STP-like behavior[27]. This device, like the $Ag/Ag_2S/Pt$ device, is filamentary due to lateral confinement of conduction but evolves like a mobile ion wavefront memristor.

2.4.2 Mobile Ion Wavefront Memristors

Mobile ion wavefront memristors operate in a similar manner to filamentary memristors in that they are drifting ions to modify conductance, however mobile ion wavefront memristors are not laterally confined, producing a scalable conductance change with analog behavior[12]. Ag-Si mixtures show analog resistance change without lateral

confinement and can emulate potentiation, depression, and STDP although at a low ΔR/R compared to filamentary devices[12]. Various other mixed ionic-electronic conductors show the same trend of biologically realistic conductance modulation at lower magnitude ΔR/R[109]. The $LiNbO_2$ memristors described in this dissertation are also mobile ion wavefront memristors, with both drift and diffusion modifying local hole doping concentrations through the migration of Li ions and vacancies[63,82]. $LiNbO_2$ shows a large theoretical ΔR/R[63] and native analog memristance[70], although such resistance change is yet to be experimentally determined.

2.4.3 NbO_x Based Memristors

NbO_x is a volatile memristive material typically formed by depositing a thin layer of Nb_2O_5 between electrodes and applying an electroforming pulse to form a filament of reduced NbO_2. NbO_x memristors are often formed from sputtered Nb_2O_5 which is locally reduced, as shown by EELS, and in some cases TEM diffraction patterns show the crystallization of NbO_2[121]. The *I-V* characteristics of an NbO_x memristor are shown in Figure 2-2b. Initially the memristive switching observed in these devices was attributed to a Mott metal-insulator transition of NbO_2 which occurs at 1081K[111]. Modelling has since shown that device temperatures do not reach this transition point, and the low resistance state of these devices is due to thermal runaway in the Poole-Frenkel conduction mechanism[121,122]. This feature was experimentally proven by showing both the lower temperature non-linear Poole-Frenkel-transport-driven NDR and the metal-

insulator transition based NDR through current-controlled operation of a 7nm thick NbO_2 device with TiN electrodes[123,124]. NbO_2 memristors, originally but erroneously called "Mott memristors", are volatile devices, meaning that they do not retain the resistance state once the bias is removed. Current technology uses NbO_x as an oxide memory selector to increase on/off resistance ratio[8], relaxation oscillator element[50,123], and in a neuristor circuit[49].

For neuromorphic computing architectures NbO_x memristors form the core element of the neuristor circuit[49]. Originally theorized in 1961[125], a neuristor is a signal propagation device inspired by the Hodgkin-Huxley circuit model for a giant squid axon[126]. Along with charging capacitors and a coupling resistor, NbO_x memristors form a pull down/pull up element that can propagate an action potential through the hysteretic switching behavior seen in Figure 2-2b. This function is useful for axonic and dendritic behavior, but does not incorporate any adaptive learning or memory behavior[49]. Additionally, the requirement for electroforming means each device must be individually initialized, a significant issue considering the scalability demands of neuromorphic computing where each biological neuron is connected to approximately 10^3 - 10^4 other neurons at a density of ~ 10^6 neurons/cm^2 or higher[5].

2.4.4 Phase Change Memristors

Phase change devices operate using materials which exhibit a reversible transition between crystalline and amorphous phases, corresponding to low and high resistance

states respectively. Materials which undergo this process reversibly do so through a glass transition from a molten state to an amorphous state through quenching[127]. $Ge_2Sb_2Te_5$ (GST) is the foremost example of a phase change material for neuromorphic applications. GST is already a commercially viable nanoscale technology, used in rewritable CDs and DVDs[128] and later as RAM[129]. These devices use GST in a binary two-state configuration, on and off, however GST exhibits a continuous resistance change between these two limits. The resistance state scales with the thickness of the amorphous region. This amorphous (crystalline) thickness can be increased (decreased) by pulses above the melting threshold (T_{melt} = 877 K) or decreased by lower energy thermal annealing pulses above the minimum temperature for crystallization (540 K) but below the melting threshold[130,131]. The crystal growth velocity is temperature dependent with a maximum observed at 750 K[131]. These reversible resistance modulation dynamics make GST suitable for neuromorphic applications. Due to its resistance change dynamics, GST has been largely researched and implemented as an electronic and optical synapse[17,132]. These devices show STDP and LTP with a cycleability of up to 10^{12} cycles achievable[127] and different time constants for different configurations of the pre- and post-spike amplitudes and spacings. These devices are unipolar; a positive pulse is used for both SET and RESET. Multiple crystallization pulses induce gradual analog increases to the device resistance whereas a single melting pulse returns the device to the low resistive state. Due to this unipolar feature a two device circuit, one positive and one negative, are required to implement both LTP and LTD simultaneously for STDP[18,133].

GST phase change devices have also recently been used to implement an integrate-and-fire type neuron device which is stochastic and therefore computationally robust in nature[130]. By utilizing the positive feedback dynamics inherit to the GST phase change crystallization process a train of pulses can cause the device to gradually crystallize, eventually exceeding a threshold where a large amount of current flows through the device, subsequently resetting the device a high resistance state. Using this formulization a single phase change neuron is able to train itself to pick out small pulses from a noisy signal[130]. Most recently these two configurations, phase-change neurons and synapses, have been successfully used in concert for correlated input detection[133].

CHAPTER 3. MOLECULAR BEAM EPITAXY OF LITHIUM NIOBIUM OXIDES

3.1 Growth Chemistry and Custom Source Cell Design for Oxide MBE

Historically, refractory metals have been evaporated by electron beam to achieve growth level fluxes in MBE; however, the hot filament used to create the electron beam oxidizes and breaks easily in an oxide growth environment. For this reason, niobium oxides have been previously deposited using a lithium assisted metal-halide growth chemistry[68–70]. In this method the niobium source is $NbCl_5$, present as the dimer Nb_2Cl_{10}, which has an equilibrium vapor pressure of ~1×10^{-4} torr at 20 ℃. Lithium getters the chlorine from $NbCl_5$ forming LiCl that desorbs from the substrate surface at high temperatures (vapor pressure = 3.61 torr at 900 ℃). This growth method is described in depth by *Doolittle et. al*[68], *Greenlee et. al*[70] and *Henderson et. al*[69]. In this previous work, the material was evaporated from a Createc NATC-40-40-290 oil/water heated cell, which provided

Figure 3-1. (left) Custom NbCl5 cell with (center) tip filament, bulk water, tip and bulk thermocouple feedthroughs, and (right) a 5x5 hole pattern aperture plate.

temperature stability of ~0.1%. Despite this stability, radiation from the hot substrate (~900 ℃) caused the $NbCl_5$ cell temperature to rise, increasing the sublimation rate gradually over the course of the growth.

To overcome this problem, a custom effusion cell was designed featuring two-zone heating and an aperture plate. The cell, shown in Figure 3-1, was manufactured by VESCO-NM. The bulk material zone of the cell is, like the former case, temperature controlled by an oil or water bath to maintain stable temperatures in the near-ambient range. A second heating zone was added at the tip of the cell, heated by a traditional

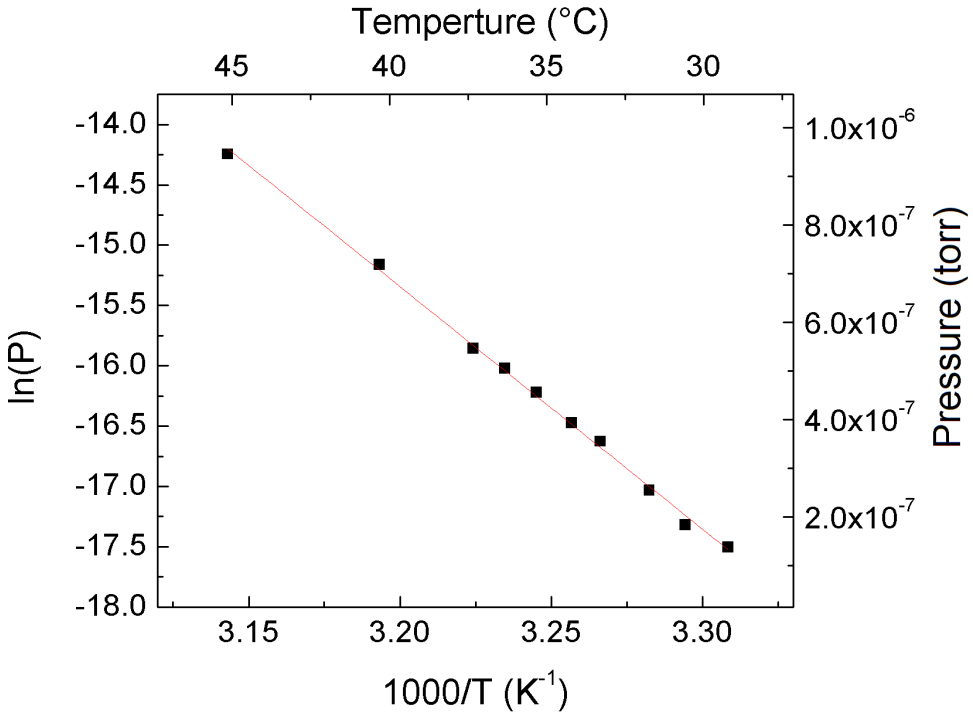

Figure 3-2 The measured $NbCl_5$ flux (BEP) versus temperature on an Arrhenius plot follows an expected linear trend. Growth level fluxes occur above ~30 ℃. The included fit gives an equation $\ln(P) = 49.0 - 20.1 \frac{1000}{T(K)}$

filament that along with a PBN aperture plate provides thermal isolation from the substrate radiation. The hot zone also prevents condensation on the aperture plate and allows a back pressure of $NbCl_5$ for more stable flux control. The crucible is an 82 cc elongated quartz tube, which is filled half full of material to avoid evaporation from the hot zone. A custom substrate heater was also installed, manufactured by VESCO-NM, which provides oxygen corrosion resistance at high temperatures. The cell is rated for 1000 ℃ in up to 5×10^{-5} torr oxygen, and experimentally can survive for at least 6 months of regular use.

The vapor flux from the new cell design, measured in beam equivalent pressure (BEP), follows a linear trend with temperature on an Arrhenius plot, shown in Figure 3-2, as is expected for Knudson flow. Growth level $NbCl_5$ fluxes can be achieved at 30 ℃ - 60 ℃ compared to previous work at 25 ℃ - 35 ℃, indicating flow retardation by the aperture plate. After 6 months of use, the aperture plate shows no corrosion or clogging, indicating the hot zone operating temperature of 100 ℃ -150 ℃ is sufficient to prevent any condensation.

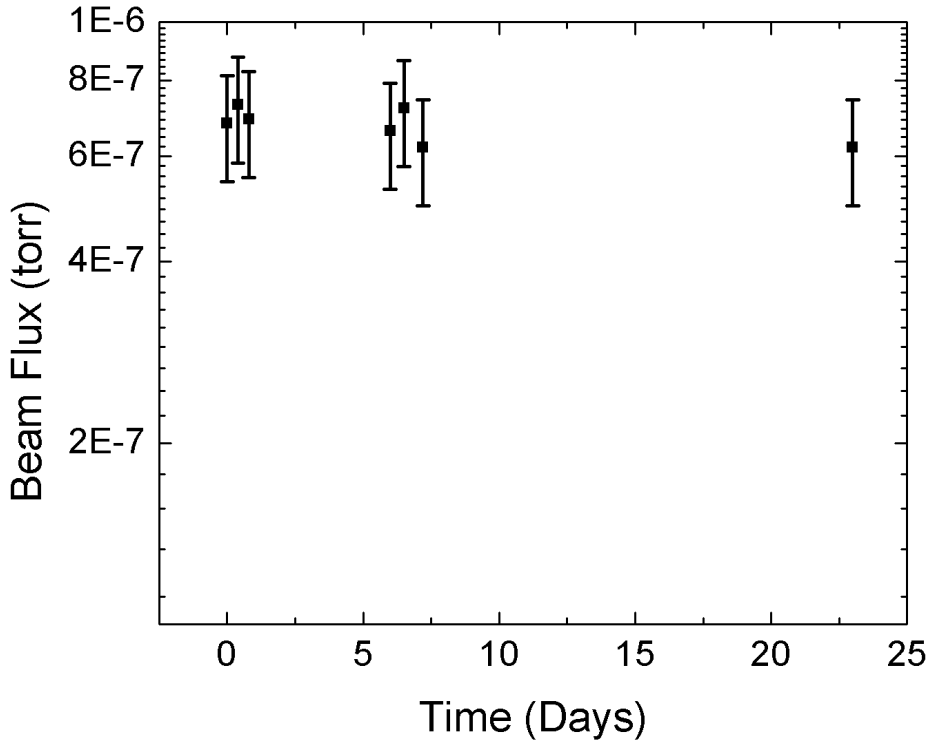

Figure 3-3 Measured $NbCl_5$ flux at a single setpoint over a period of 24 days. The cell remains stable within the error range (20 %) of a standard ion flux gauge, depicted by error bars ($\sigma = 4.39 \times 10^{-8}$ torr).

The cell was measured for long term flux stability over a period of 24 days, shown in Figure 3-3, and shows stability within the quoted error range of a standard ion flux gauge (20 % within a pressure decade), indicating that flux drift is reasonably controlled with this design. Figure 3-4 shows the effusion cell and crucible in cross section. Hollow walls comprise the lower bulk section to allow heating and cooling by liquid.

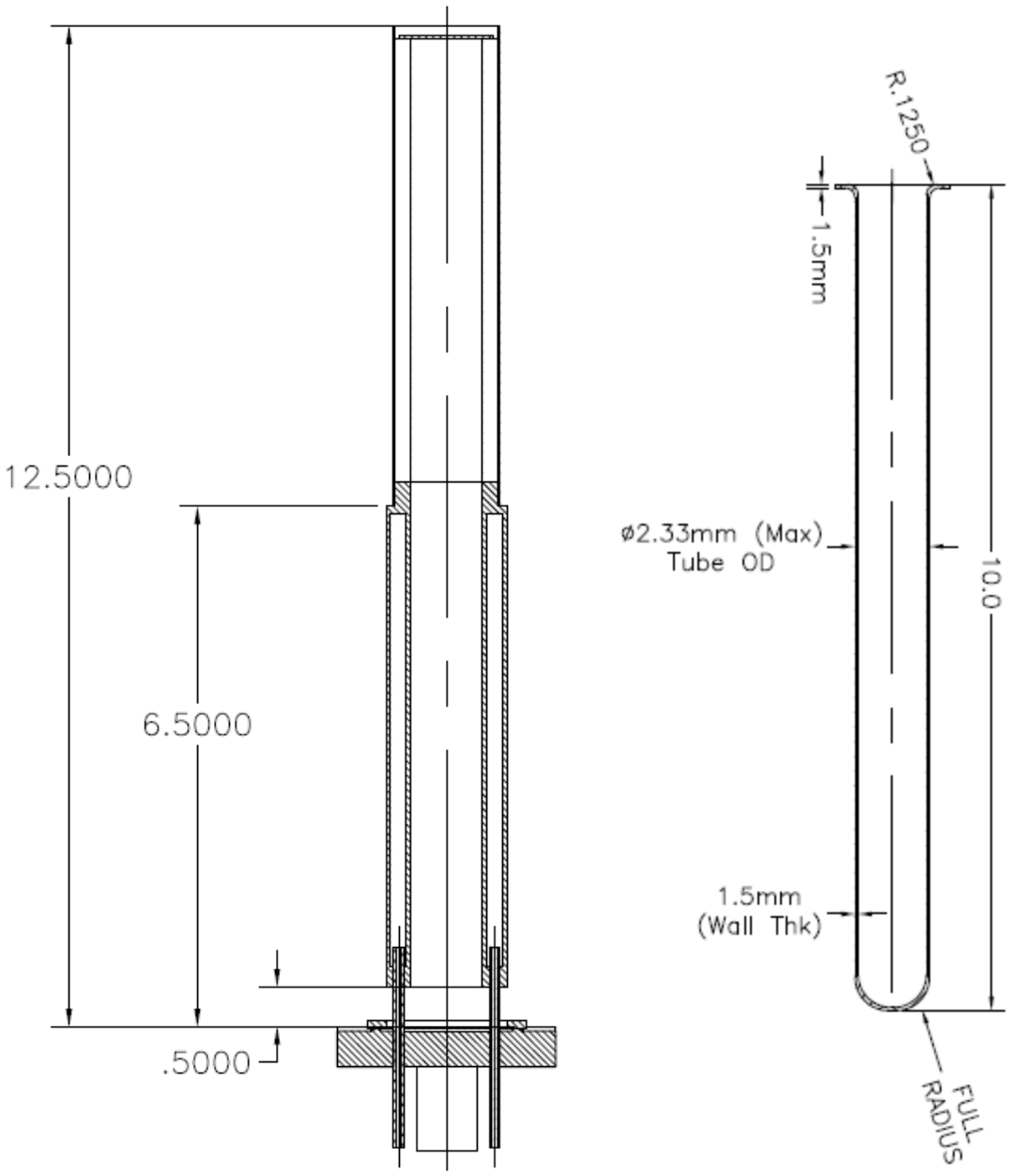

Figure 3-4. Dimensioned drawings of the custom near-ambient effusion cell (left) and quartz crucible (right). All dimensions are in inches unless otherwise specified. Provided with permission by Vesco-NM.

3.2 Lithium Perchlorate ($LiClO_4$) as a Solid/Liquid State Oxygen Source

The growth of stoichiometric refractory metal oxides by MBE is traditionally difficult because of inadequate oxygen and low vapor pressure metal sources leading to extremely low growth rates[134]. Transition metals are difficult to evaporate controllably due to high temperature requirements and the poor compatibility of a hot electron beam filament with an oxygen environment. $LiNbO_3$ is very difficult to grow stoichiometric in oxygen, and it is often annealed post-growth to incorporate more oxygen in the film[68]. It is difficult for any niobium film to reach full oxidation in an MBE environment at the high growth temperatures required for quality single crystalline material, and therefore a more reactive oxidizer is desirable to reach these fully oxidized states. Previous work has explored oxidizers such as oxygen plasmas and dangerous ozone sources to achieve highly reactive species O and O_3[135]. This work investigates lithium perchlorate, $LiClO_4$, as a solid/liquid state oxygen source alternative to these gas based methods, as well as a new style of MBE effusion cell for the evaporation of metal-halide sources which offer much lower evaporation temperatures and therefore greater flux stability[69].

3.2.1 Lithium Perchlorate

Previous work has indicated that oxygen incorporation into a niobium oxide films at high temperatures (> 650 ℃) is difficult, with the fully oxidized state of niobium (chemical valence +5) difficult to achieve. $LiNbO_3$ films have been grown by MBE in the past, as well as the ceramics Li_3NbO_4 and $LiNb_3O_8$, but the repeatability of these growths is poor

due in part to low and variable oxygen incorporation[68]. This oxygen incorporation issue has led to the exploration of a stronger oxidizer than molecular oxygen, lithium perchlorate ($LiClO_4$), as an alternative to a higher reactivity sources such as ozone and oxygen plasmas which require a very specific flow control and in the case of the former extensive safety regulation due to reactivity. Lithium perchlorate has the highest volumetric density of oxygen of any material, including liquid oxygen. The volumetric density of oxygen for several chemical oxygen generators is shown in Table 3-1. Lithium perchlorate is also the only member of the perchlorate family that is stable above its melting point[136], meaning that it will form a liquid before decomposing while all others sublime.

Table 3-1. Density, mass percentage, and oxygen volumetric density of various materials used to evolve oxygen gas including lithium perchlorate and liquid oxygen, sorted by oxygen volumetric density. Adapted from Peters et al. [136]

Material	Density (g/cm^3)	Mass % O_2	Grams O_2 gas per cm^3
$LiClO_4$	2.43	60.1	1.45
$NaClO_4$	2.53	52	1.31
$KClO_4$	2.52	46.2	1.16
$LiClO_3$	1.12	53	0.59
$NaClO_3$	2.49	45.1	1.13
$KClO_3$	2.32	39.2	0.91
98 % H_2O_2	1.43	46.1	0.66
Liquid Oxygen	1.14	1.14	1.14

Lithium perchlorate is traditionally used as a chemical oxygen generator for emergency oxygen candles as well as a method of chemical oxygen storage[136,137]. In this form, lithium perchlorate exists in the solid form with a binder and a small mole fraction of fuel such as magnesium which provides the heat for the decomposition of oxygen. Lithium perchlorate is also highly soluble in a number of solvents and is used in this form as a soluble electrolyte for lithium ion batteries.

Lithium perchlorate exists in the solid state as salt granules at room temperature. The substance melts at 236 ℃ in its anhydrous form, although it is highly hygroscopic and should be handled in a dry environment. Once hydrated (lithium perchlorate forms both a mono- and trihydrate) the anhydrate can be reclaimed by heating the system to above 145 ℃ [40]. Lithium perchlorate begins to decompose near 400 ℃, with the reaction becoming exothermic around 420 ℃[136,138,139]. The material decomposes according to equations (1)-(3).

$$LiClO_4(l) \rightarrow LiCl(sol.) + 2O_2(g) \quad (1)$$

$$LiClO_4\,(sol.) + LiCl(sol.) \rightarrow LiClO_3\,(sol.) + LiCl(sol.) + O(g) \quad (2)$$

$$LiClO_3(sol.) \rightarrow LiCl(sol.\ or\ s) + {}^3/_2\ O_2(g) \quad (3)$$

The decomposition of $LiClO_4$ is autocatalytic, catalyzed by the product LiCl[138], where the formation of LiCl is thought to assist in rupturing the Cl-O bond. This rupture theory is consistent with an observed activation energy of 222 kJ[139]. The decomposition is shown

to simplify to a standard first order reaction at a LiCl composition of ~40 %, at which point the solution is saturated. Equations (2) and (3) indicate both molecular and atomic oxygen species are evolved during the decomposition process. The presence of atomic oxygen provides the potential for higher reactivity and stronger oxidation. The LiCl autocatalysis necessitates preconditioning the material by prolonged heating or pre-mixing of LiCl to reach the 40 % LiCl saturation point. In addition, the 400 ℃ decomposition temperature places an upper limit on the operational temperature of the cell as well as the temperature ramp rate to prevent local heating exceeding the full decomposition temperature.

3.2.2 Design Constraints

Lithium compounds have been proven incompatible with quartz and PBN, and in a previous attempt $LiClO_4$ catastrophically reacted with a niobium crucible. Thus, the $LiClO_4$ bulk material was heated in a beryllia crucible, shown in Figure 3-5, in a standard Knudsen effusion cell. To date there has been no observable degradation of the crucible,

Figure 3-5. Custom beryllia crucible made to hold $LiClO_4$ in a Knudsen effusion cell. Previous work has indicated that $LiClO_4$ will corrode anything that can oxidize, and Li will intercalate into and swell PBN.

indicating that BeO is resistant to lithium perchlorate corrosion on this timescale.

3.2.3 Material Characterization

Oxygen evolution begins shortly after the material melts with growth level fluxes of oxygen obtained at cell temperatures between 250 and 350 ℃. The measured flux is shown on an Arrhenius plot in Figure 3-6 for the range 250 to 325 ℃, showing the expected linear trend with a measured flux of approximately 1.5×10^{-5} torr at 325 ℃.

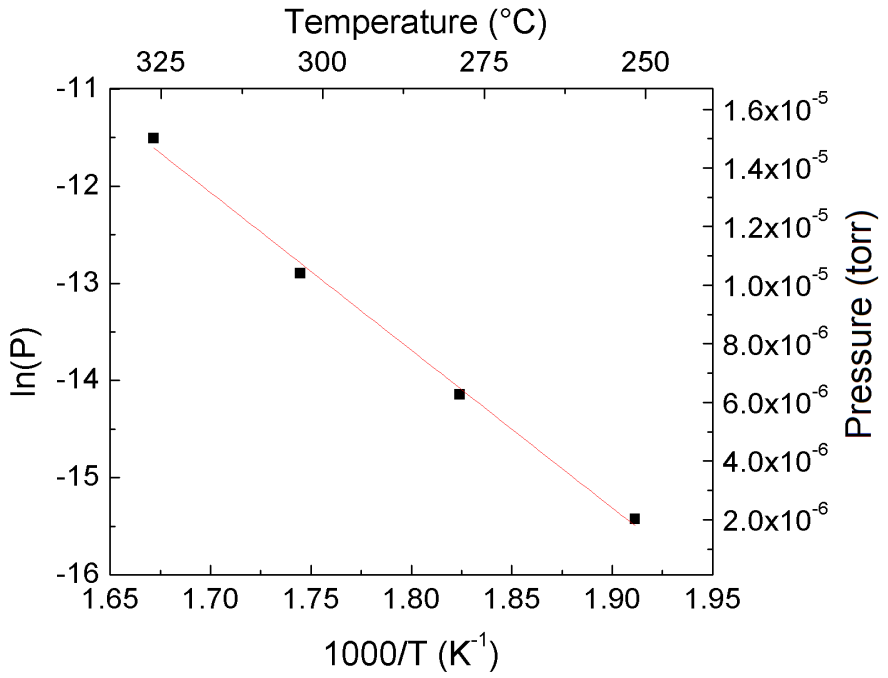

Figure 3-6 The measured $LiClO_4$ flux (BEP) versus temperature on an Arrhenius plot follows an expected linear trend. Growth level fluxes occur above ~250 ℃, the approximate temperature at which oxygen evolution begins. The included fit gives an equation $\ln(P) = 15.5 - 16.2 \frac{1000}{T(K)}$

3.2.3.1 Pressure Instabilities

During the operation of the $LiClO_4$ cell, pressure variations become an issue significantly affecting the overall chamber pressure. Once oxygen evolution begins at approximately 250 ℃ the pressure in the growth chamber, as measured by cold cathode gauge, rises sharply with the decomposition of the $LiClO_4$ bulk material. The oxygen RGA signal also becomes noisy, varying around its mean by $\sim \pm 5 \times 10^{-8}$ torr. Monitoring residual gas analysis (RGA) signals at mass to charge ratio 32 for oxygen and 16 for doubly ionized oxygen and molecular oxygen, as shown in Figure 3-7, the same noise is observed indicating that oxygen is the source of the pressure variations. These pressure variations are not present for gas source molecular oxygen indicating that the RGA signal from $LiClO_4$ is relevant. Other monitored signals such as water, carbon dioxide, and hydrogen do not show these noise trends.

While the source of the pressure instabilities is unknown, some hypotheses can be made about the origin and solutions to the problem. Pressure instabilities could be caused by bubbling from the crucible sidewall as the oxygen evolution occurs, causing droplets of liquid $LiClO_4$ to spit from the cell. If true, then a valved or aperture sealed cell such as the $NbCl_5$ cell described in this work could resolve these instabilities, allowing a back pressure of oxygen to develop for more uniform flow. Previous reports of chemical additives used to stabilize the decomposition of $LiClO_4$ such as $AgNO_3$ and $AgClO_4$

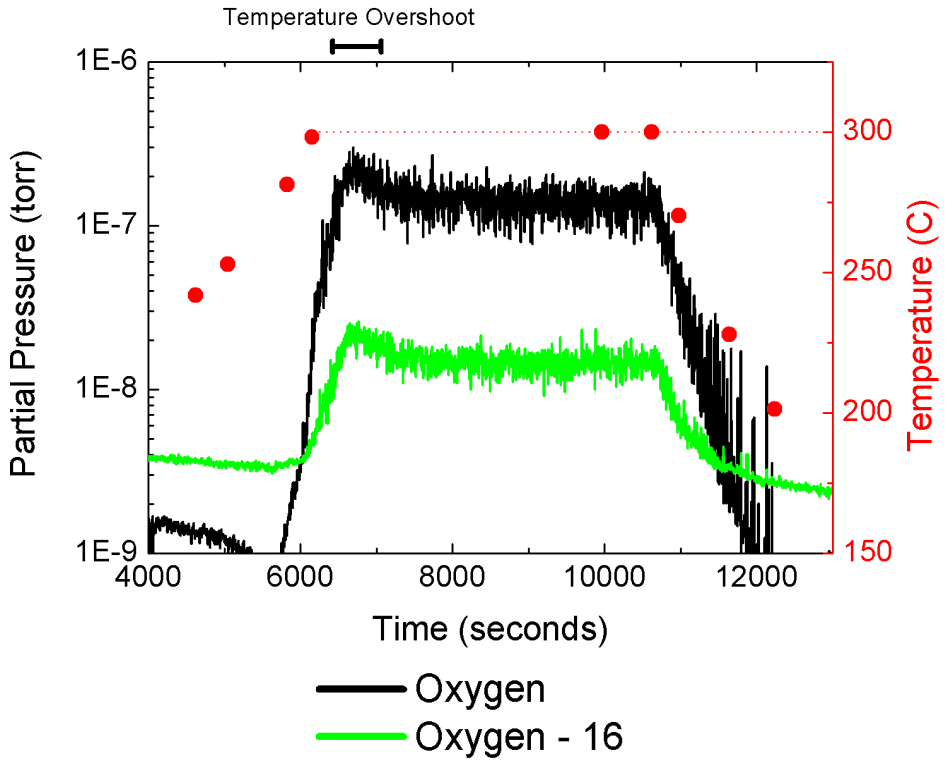

Figure 3-7. RGA partial pressures measured at mass to charge ratio (m/q) 32 (black) and 16 (green) as the $LiClO_4$ cell is heated to 300 ℃ (temperature shown in red), held constant for 1 hour, and then subsequently cooled.

could also be used to reduce the pressure fluctuations[140].

3.2.3.2 Comparison with Molecular Oxygen

RGA signals exhibit specific cracking patterns for various materials relating to the probability of double ionization as well as the probability of cracking a dimer such as O_2. For molecular oxygen, the measured ratio of the RGA signals at mass to charge ratio 16 to 32 is 5.67 %, while that ratio is 8.42 % for $LiClO_4$. This corresponds to a 48.5 % increase in signal at mass to charge ratio 16. This increase supports the mixed oxygen species theory, suggesting that the $LiClO_4$ is evolving both molecular and atomic oxygen. It is hypothesized that this is the mechanism behind the faster oxidation rate per flux beam equivalent pressure revealed by the *in situ* Auger transient experiment.

3.3 *In situ* Auger Electron Spectroscopy

To quantify the oxidation rate of niobium using the $LiClO_4$ oxygen source, the oxygen KLL Auger peak is monitored for changes in overall intensity. An *in situ* Auger probe (Staib Instruments) is used to examine reactions on the surface of growing films by Auger Electron Spectroscopy (AES). In this configuration shown in Figure 3-8, an electron probe is used to analyze Auger electrons excited by the RHEED gun and the probe is mounted in the pyrometer port of a Varian Gen II MBE system normal to the

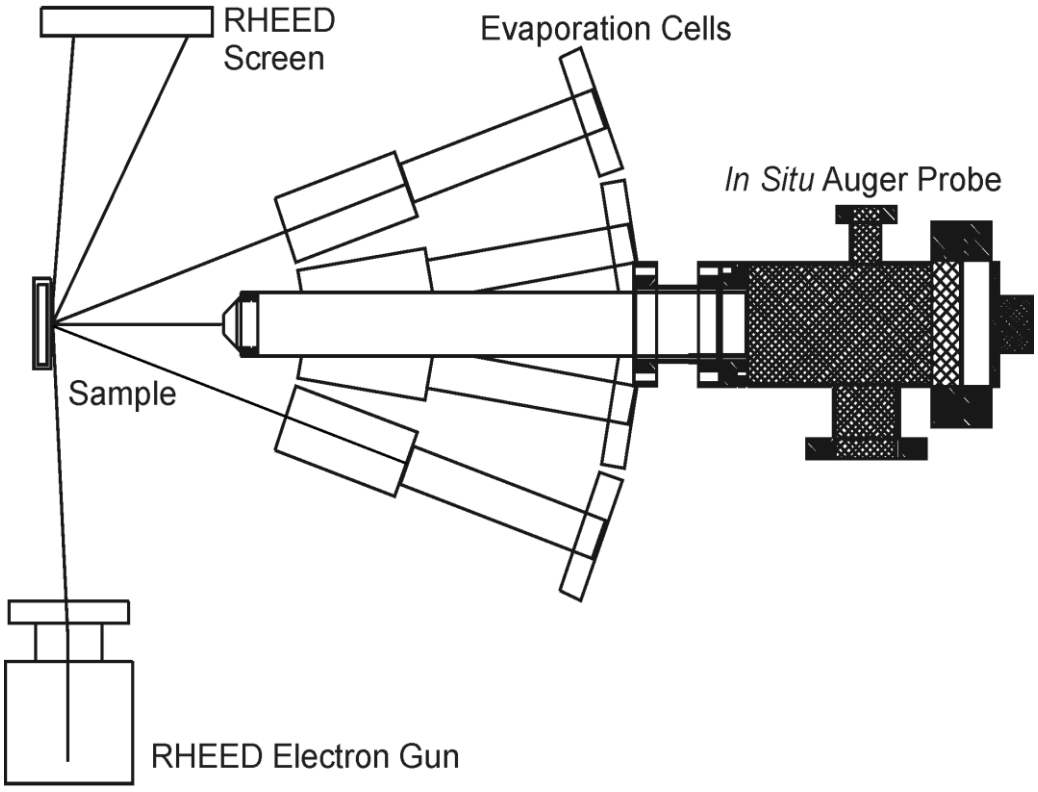

Figure 3-8. *In Situ* Auger Probe setup in the MBE system showing the geometric relations of the electron gun, sample, evaporation cells, and probe body. Adapted with permission from *Calley et. al.* [193]

substrate. Focusing optics provide energy selectivity, and counts are collected from a scintillator fed photomultiplier.

AES is a surface sensitive technique, and the *in situ* Auger Probe uses glancing angle electrons from the RHEED gun making the technique highly surface sensitive and therefore sensitive to the oxidation reaction at the surface of the thin film[141]. This particular system has shown sub-monolayer surface sensitivity to changing elemental compositions[141,142]. Unlike traditional Auger systems, the Staib Auger probe supplies the direct, non-differentiated signal representing the $E \times N(E)$ spectra.

3.3.1 Niobium Oxidation Rate Studies

To quantify the oxidation rate of niobium the oxygen KLL Auger peak can be monitored for changes in overall intensity during exposure to oxygen. In a particular experiment crystalline BCC Nb is deposited on sapphire, growth is halted, and the surface is exposed to oxygen while monitoring the Auger signal, both in a step-wise manner and in real time. Successive oxygen KLL and niobium MNN peaks are shown as a function of exposure time in Figure 3-9. These spectra were obtained in a step-wise manner, alternating exposure and measurement, to ensure sampling of a constant oxidation state over the approximately minute long measurement time. Because of the step-wise data point collection it is likely that oxidation times are slightly overestimated due to excess oxygen in the chamber after the valves and shutters are closed. The oxygen KLL peak increases as a function of exposure time to diffuse (indirect) O_2 as expected.

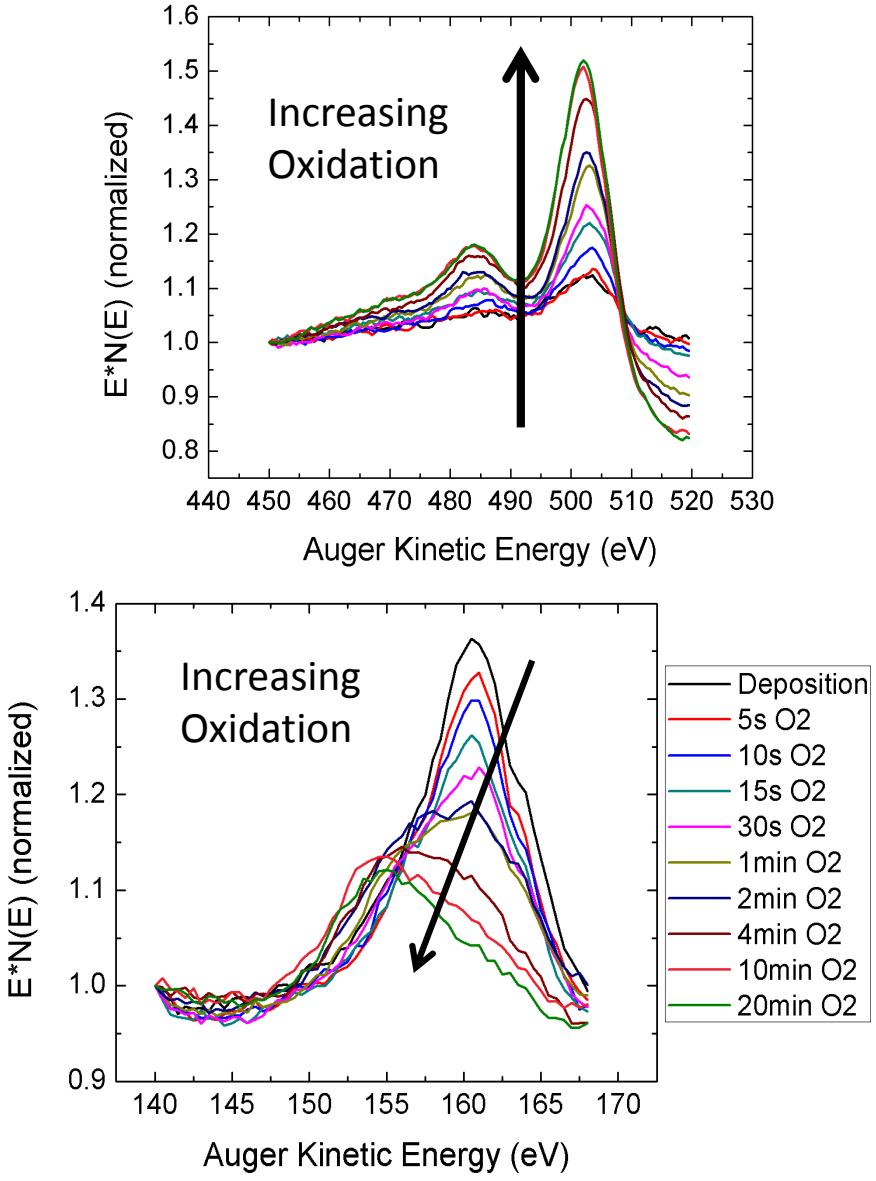

Figure 3-9. (top) Successive Auger oxygen KLL peak scans showing increasing surface oxidation. The peak doublet shows the split lower and higher energy auger recombination-emission processes, O-KL_1L_{23} and O-KL_1L_1 respectively. A low level of surface oxide is present after deposition, before oxidation, due to residual oxygen in the chamber. (bottom) Successive Auger niobium MNN peaks show a decrease in intensity as well as a shift to lower energy corresponding to shifts in the oxidation state.

The post-deposition scan (before oxygen is first introduced to the chamber) shows that residual background oxygen in the MBE growth chamber is present and binding to the surface of the grown Nb film. Subsequent scans show that uptake of oxygen saturates around 10 minutes of indirect exposure to ~2×10^{-5} torr partial pressure of O_2. The lower intensity feature of the oxygen KLL spectra at 483 eV represents the oxygen KL_1L_{23} Auger transition, while the most intense peak at (initially) 503.5 eV represents the oxygen KL_1L_1 Auger transition. As the oxygen content of the surface increases charging begins to occur on the surface of the now partially insulating film, resulting in a slight (1.5 eV) spectral shift to lower Auger kinetic energy.

The niobium MNN spectra show a few more interesting features. Oxidation causes the Nb MNN peak height to decrease partially due to a decrease in niobium concentration. There is also a 6 eV peak shift from 160.5 eV to 154.5 eV, much larger than the 1.5 eV charging shift observed in the corresponding oxygen spectra. This shift is analogous to binding energy shifts observed in x-ray photoelectron spectroscopy (XPS), where chemical bonding slightly alters the core electron energy levels of both elements involved due to a change in electron density and electrostatic screening. For the oxidation of a metal the electron density decreases as oxygen binds with the metal valence electrons to fill the outer electron shell. This decrease in electron density results in an increased binding energy because the electron orbitals participating in bonding (valence electrons) “relax” slightly further from the nucleus. The outward shift of the valence electrons decreases the overall electron screening which in turn pulls the core level electrons closer

to the nucleus resulting in a higher binding energy. An increase in binding energy equals a decrease in measured kinetic energy, corresponding to the shift observed in Figure 3-9. Auger kinetic energy shifts should however be much smaller than photoelectron binding energy shifts because the Auger recombination process occurs between two core levels, both of which unidirectionally shift during the oxidation reaction. This results in an observable shift at only a fraction of the overall core electron level shift. The shift observed in Figure 3-9 is likely a combination of chemical shifts and charging. Considering the charge shift observed in the oxygen peak of 1.5 eV, the estimated total chemical shift due to oxidation in the niobium spectra is 4.5 eV.

Peak fitting of the scans in the bottom of Figure 3-9 can result in the determination of chemically shifted peaks. Assuming that after 20 minutes a fully oxidized state is reached in some portion of the sampled area, four peak locations can be empirically determined from the scans. These peak locations, determined by fitting, are approximately 165.5eV, 161.5eV, 158.5eV, and 154.5eV, possibly corresponding to Nb^{+0}, Nb^{+2}, Nb^{+4}, and Nb^{+5}, respectively. These peaks likely cannot be used for identification alone, and should be tested against a reference sample to confirm. Additionally the effects of charging have not been accounted for in these fitted peaks. The peak fitting process, however, leads to the idea that oxidation state information could be obtained by *in situ* AES through careful experimental confirmation.

3.3.2 $LiClO_4$ Oxidation Quantified by AES

AES studies were performed to quantify the oxidation rate of niobium in the presence of evaporated $LiClO_4$. Upon opening the $LiClO_4$ shutter, the oxygen KLL peak immediately begins to intensify. When plotted against time the Auger peak height follows a first order exponential relation, saturating as the surface reaction comes to completion as shown in Figure 3-10. The Auger peak height is proportional to the overall number of oxygen KLL auger electrons which is directly related to the number of oxygen atoms present in the energized volume, which increases exponentially toward a saturated value representing the final (but not necessarily full) oxidation state. In a similar work Sanz et. al[143] exposed niobium and tantalum films to controlled oxygen fluxes *at room temperature* and monitored the oxygen KLL auger signal to determine reaction trends, coming to the conclusion that at room temperature oxidation proceeds in multiple regimes, forming

Table 3-2 Summary of Sanz et. al[143] study of the oxidation of niobium at room temperature.

Oxygen dose (Langmuir)	Result
0-2 L	Rapid uptake of oxygen below the metal surface
2-7 L	Formation of 2 – 3 monolayers of the suboxides NbO and NbO_2 on the surface of the film.
>7 L	Formation of Nb_2O_5 covering the suboxide layer.

both suboxides and fully oxidized films. The findings of this work are summarized in Table 3-2.

Multiple data points are taken from 40 eV wide scans of the oxygen KLL peak with a resolution of 0.5 meV, examples of which are shown in succession in Figure 3-9. The measurement time is 30 s. Scatter plots are fit to a first order exponential following the form of Equation 4, where measured peak intensity is taken from the E × N(E) spectra.

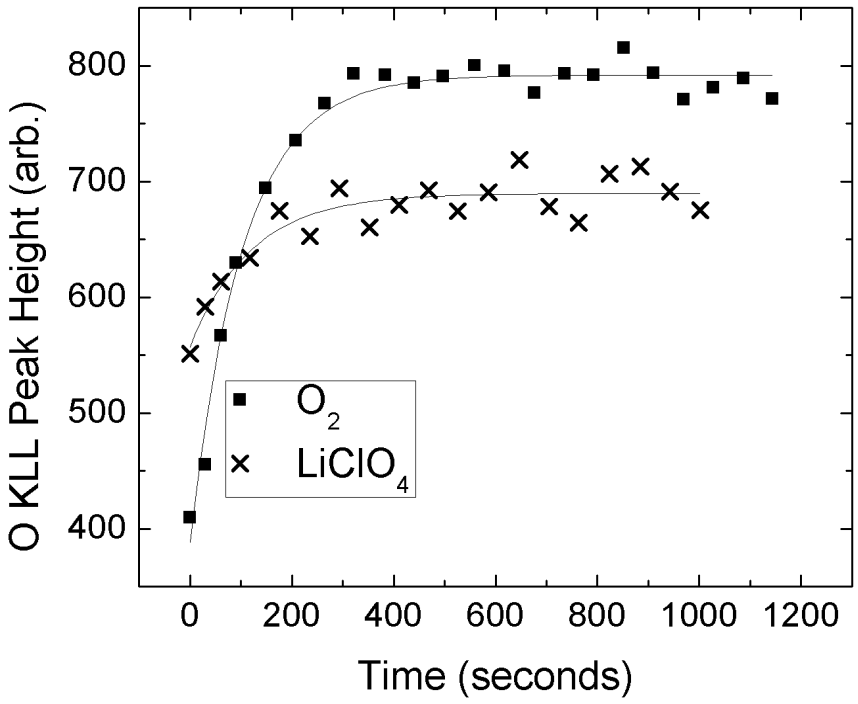

Figure 3-10 Auger oxygen KLL peak height as a function of time. The included fit is a first order exponential, characteristic of the oxidation time constant for the given system for a) $LiClO_4$ at 300 ℃, beam flux 8×10^{-7} torr, $\tau = 120$ s, and b) 1 SCCM diffuse O_2, beam flux 3×10^{-6} torr, $\tau = 110$ s.

$$I = I_0 - Ae^{-\frac{t}{\tau}} \quad (4)$$

I_0 is the final peak height, t is time, τ is the time constant characteristic of the oxidation, and A is a fitting constant not equal to I_0, indicating a non-zero initial concentration of surface oxide due to background level oxygen in the MBE system.

Characteristic oxidation peak height transients are shown in Figure 3-10 for 1 SCCM diffuse O_2 and $LiClO_4$ at 300 ℃. While these two transients have similar time constants, the measured beam flux for $LiClO_4$ is about 4 times lower than that of diffuse O_2. It is theorized that the mixture of molecular and atomic species present in the $LiClO_4$ oxygen evolution allows faster oxidation, providing the possibility of faster growth rates for oxide films than previously possible.

3.4 MBE Growth Methods by Lithium-Assisted Metal Chloride Growth Chemistry

3.4.1 Growth Parameters

Previous work in Li–$NbCl_5$–O_2 growth chemistry indicated that phase control was best mediated by a lithium controlled niobium incorporation rate approach. Because the niobium supply is controlled by reaction with lithium, the niobium to oxygen ratio can be adjusted by varying a single parameter, the Li flux. It was shown that through this

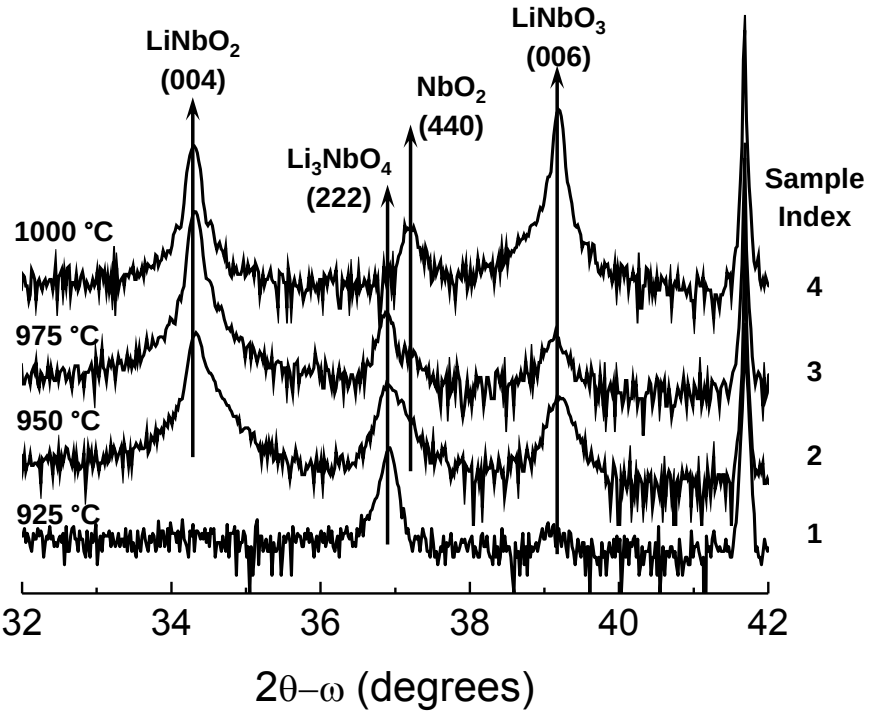

Figure 3-11. X-ray diffractograms of films grown at increasing substrate temperature while holding all fluxes constant (ϕ = 0.6). From bottom to top in 25 degree increments, 925 ℃ primarily produces Li_3NbO_4, 950 and 975 ℃ primarily produces $LiNbO_2$, and 1000 ℃ primarily produces $LiNbO_3$. All films are multi-phase. The temperature dependence is attributed to increased Li desorption.

method increasing the Li flux produced films of reduced oxidation state, resulting in a progression from Li_3NbO_4 → $LiNbO_3$ → $LiNbO_2$ →NbO as the Li flux is increased holding all other fluxes constant at constant substrate temperature[69].

Motivated by the prevalence of multi-phase films using this prior approach, the effect of substrate temperature on the nucleation of various phases was studied. Figure 3-11 shows the x-ray diffractograms of films grown at constant flux while substrate temperature is increased from 925 – 1000 ℃ in steps of 25 degrees. For these growths the beam equivalent pressures as measured by Bayard-Alpert ion flux gauge were approximately 6×10^{-7} torr for Li and 1×10^{-6} torr for $NbCl_5$. For the sake of clarity, data will be presented as Li:$NbCl_5$ flux ratio, with all data presented for growths at the same O_2 flow. We define $\phi = \phi_{Li}/\phi_{NbCl5}$ where ϕ_m is the flux of source *m* measured in beam equivalent pressure (BEP), in units of torr. The O_2 flow was set at 4 SCCM by mass flow controller (MFC) resulting in a background oxygen pressure of approximately 4.5×10^{-5} torr. The 925 ℃ substrate temperature condition resulted in (222) oriented Li_3NbO_4 with a small fraction of c-oriented $LiNbO_3$. Increasing the substrate temperature to 950 ℃ resulted in c-oriented $LiNbO_2$ along with Li_3NbO_4, (440) NbO_2, and $LiNbO_3$. Further increasing the substrate temperature to 975 ℃ produced higher quality $LiNbO_2$ as evidenced by Pendellösung fringes and a decrease in (002) XRD rocking curve from 410" to 307". Li_3NbO_4, NbO_2, and $LiNbO_3$ are also present in the film. Finally, increasing the substrate temperature to 1000 ℃ significantly increased the $LiNbO_3$ diffraction signal with respect to all others, and the Li_3NbO_4 phase was eliminated.

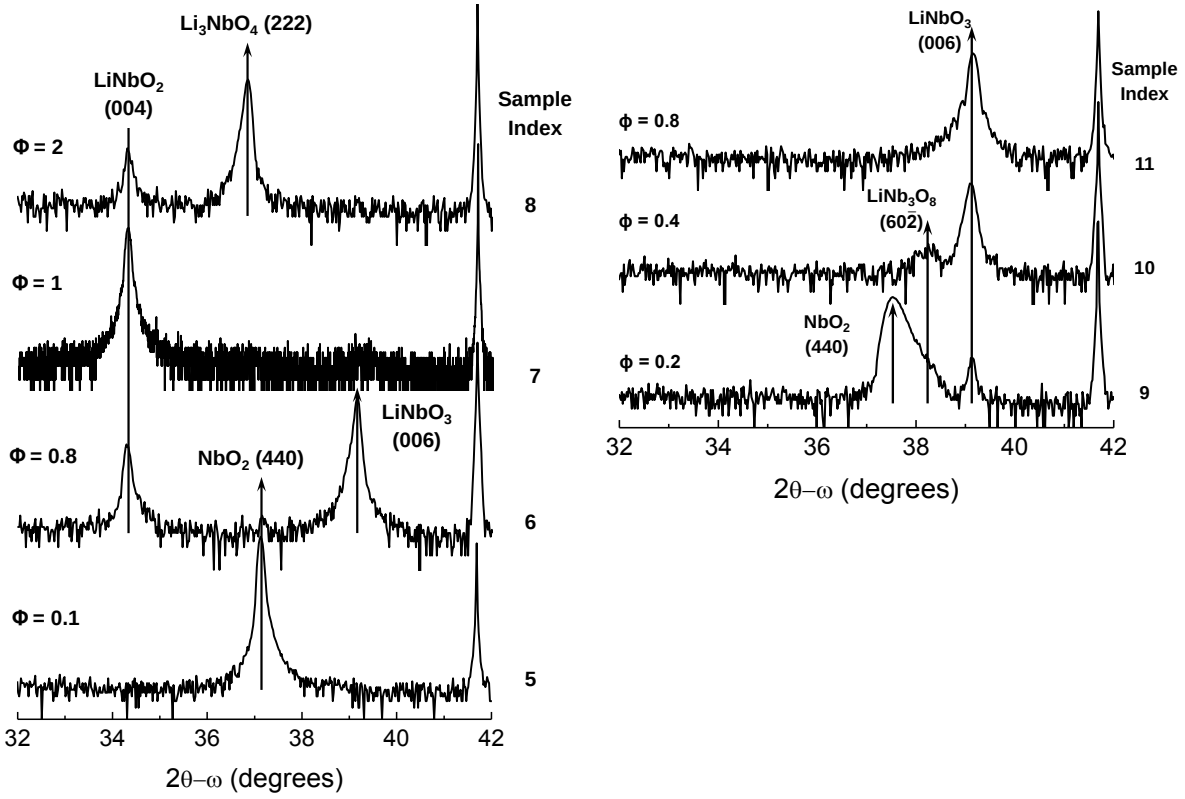

Figure 3-12. (a-left) X-ray diffractograms of films grown at 975 ℃ and increasing ϕ from bottom to top. As ϕ increases the films transition from NbO_2, through $LiNbO_3$ and $LiNbO_2$, to Li_3NbO_4. (b-right) X-ray diffractograms of films grown at 1000 ℃ and increasing ϕ from bottom to top. As ϕ increases the phase progresses from NbO_2, through $LiNb_3O_8$, to $LiNbO_3$.

It was also determined that the optimal growth temperature and ϕ are coupled parameters for obtaining single phase material. Figure 3-12a shows the effect of ϕ on phase nucleation at 975 ℃. At a Li-poor flux of ϕ = 0.1 there is not enough Li to incorporate into the growing film, and at 975 ℃ pure phase NbO_2 nucleates. Increasing ϕ to 0.8 results in the appearance of $LiNbO_2$ and $LiNbO_3$ and the reduction of NbO_2 to a small fraction of the film indicating the presence of a multi-phase region in ϕ. Further increase to unity ϕ results in pure phase $LiNbO_2$, while additional Li at ϕ = 2 introduces the Li-

Table 3-3. Optimal substrate temperatures for MBE growth of Li-Nb-O phases at 4 SCCM O_2 flow.

Material	Optimal Temperature (℃)
Nb	> 850
NbO	800 - 900
NbO_2	950 – 1000[†]
$LiNbO_2$	950 - 975
$LiNbO_3$	1000 – 1050[*]
Li_3NbO_4	850 - 925
$LiNb_3O_8$	975 – 1050[*,†]

[*]1050 ℃ is the upper operational limit of the substrate heater. The optimal range may extend beyond this limit.
[†]Further optimization not pursued.

rich phase Li_3NbO_4. Figure 3-12b explores the same trend at 1000 ℃. A Li-poor flux ratio of 0.2 still results in NbO_2, but the higher substrate temperature allows small fractions of $LiNbO_3$ and its Li-poor counterpart $LiNb_3O_8$ to form. Increasing the flux ratio to 0.4 prevents NbO_2 from forming; however there is still not enough Li for pure $LiNbO_3$ and the Li-poor phase ($LiNb_3O_8$) is still present. Finally, increasing ϕ to 0.8 results in pure $LiNbO_3$ in contrast with the 975 ℃ case where the same flux ratio produces both $LiNbO_3$ and $LiNbO_2$. With this in mind, optimal temperature ranges can be approximately constructed based on experimental data at various flux ratios. Table 3-3 presents the temperature ranges appropriate for the growth of various material phases at 4 SCCM O_2 flow.

Using optimized substrate temperatures allows more control when employing the lithium controlled niobium incorporation rate method. When growing at optimal temperatures, flux conditions can be slightly altered to promote single phase growth. Temperature

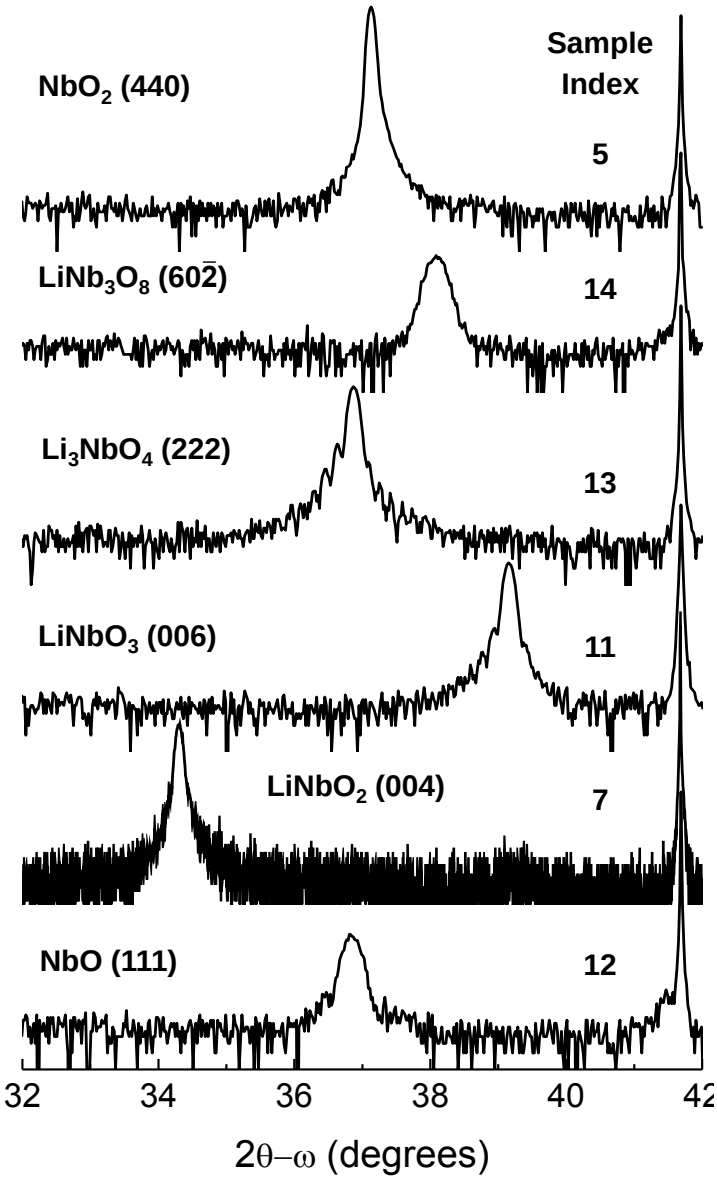

Figure 3-13. From bottom to top, c-oriented $LiNbO_2$, (111) oriented NbO, (222) oriented Li_3NbO_4, c-oriented $LiNbO_3$, (60$\bar{2}$) oriented $LiNb_3O_8$, and (440) oriented NbO_2, all grown single phase on c-oriented Al_2O_3.

conditions from Table 3-3 were applied to the Li-limited growth technique, increasing ϕ for materials of lower oxidation state and decreasing it for higher oxidation state, to achieve single phase films of different phases.

Figure 3-13 shows symmetric x-ray diffractograms of phases grown using this combined method. $LiNbO_2$, NbO, Li_3NbO_4, $LiNbO_3$, $LiNb_3O_8$ and NbO_2 are all grown single phase as evidenced by XRD. All of the films shown in Figure 3-13 are grown on c-plane sapphire by adjusting the Li:$NbCl_5$ flux ratio while growing in the optimal temperature regime defined in Table 3-3.

3.4.2 Phase Diagram Analysis

Using the understanding outlined above and empirical results which followed this understanding a phenomenological phase diagram has been developed to represent the coupled effect of substrate temperature and flux ratio on the nucleation of niobium oxides and lithium niobium oxides. This diagram is shown in Figure 3-14a as a function of Li:$NbCl_5$ flux ratio, ϕ, and temperature, T. The boundaries and areas are phenomenologically and empirically derived based on growth parameters, XRD phase analysis, and optical transmission analysis. Figure 3-14a is not a true phase diagram in the classical sense but is intended as a visual guide to understanding the complex phase nucleation of niobium oxides and lithium niobium oxides on c-plane sapphire at high temperatures in high vacuum conditions. Figure 3-14a represents a number of key points, namely:

(1) Films grown below ~ 925 ℃ will be Li_3NbO_4 or NbO, depending on ϕ,

(2) There exists a negative slope in the ϕ-T space between region I and V due to the increase in Nb:O_2 ratio as ϕ is increased,

(3) There exists a positive slope in the ϕ-T space at the II-III and III-IV boundary due to increased Li desorption at higher temperatures,

(4) There exists a mixed phase region from T ≈ 925 ℃ – 1000 ℃ and ϕ ≈ 0.3 – 0.8 represented in Figure 3-14a as a hashed oval, and

(5) Narrow growth windows exist for the desired phases III, IV, and V both in T and ϕ.

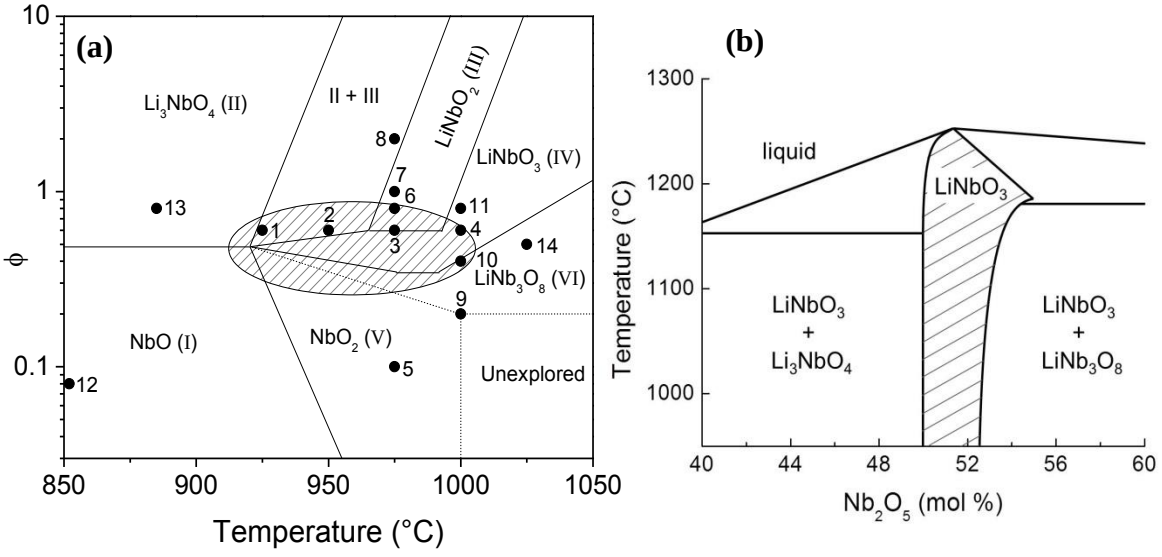

Figure 3-14. (a) Phenomenologically and empirically derived phase diagram for the nucleation of niobium oxides and lithium niobium oxides on c-plane sapphire at high temperature and vacuum conditions. Data point indices correspond to the diffractograms labeled in Figure 3-11 - Figure 3-13. (b) High temperature portion of the Li_2O – Nb_2O_5 phase diagram from 40 – 60 mol % Nb_2O_5. $LiNbO_2$ is not present because sub-oxides are not possible in this system. Analogous to Figure 3-14a, Li_3NbO_4 appears to the Li-rich side of $LiNbO_3$ and $LiNb_3O_8$ appears to the Li-poor side and at higher temperatures. Redrawn from *Kitamura et. al.*[144] and *Reisman et. al.*[59].

As stated above, there is a mixed phase region in the middle of the diagram marked by a hashed oval. Growths in this region of ϕ-T space result in multi-phase films which contain at least 2 but more often 3 phases. A detailed understanding of this region is not necessary because it is an undesired result, and is therefore not pursued. Additionally, multi-phase mixing is expected at the boundaries between phases though this mixed-phase result is not depicted. Finally, Figure 3-14a is presented in terms of flux ratio rather than an absolute value. This allows the adoption of different O_2 flow rates by adjusting the overall cation flux values while maintaining the same ratio to oxygen anions. For the data given $\phi = 1$ represents $\phi_{NbCl5} = 7$ torr BEP $\pm 1.4 \times 10^{-7}$ torr BEP at 4 SCCM O_2 which results in a partial pressure $p_{O2} \approx 4.5 \times 10^{-5}$ torr oxygen. Adjustment of either the

Table 3-4. Thicknesses and symmetric rocking curves determined by XRD of selecte films along with RMS roughness determined by AFM. Lower rocking curve values i uniformity with respect to tilt in the c-axis.

Material	Growth Rate (nm/h)	Symmetric Rocking Curve (arcseconds)	RMS Roughness (nm) 1 μm^2 area
Nb	30[f]	180	1.55
NbO	100[p]	1192	3.23
NbO_2	430[p]	220	1.24
$LiNbO_2$	85[f]	107	2.37
$LiNbO_3$	60[f]	8.6	*
Li_3NbO_4	55[f]	14	1.03
$LiNb_3O_8$	45[p]	860	19

* $LiNbO_3$ films are highly columnar with misleading RMS roughness values. Detailed structural and morphological characterization is given in Section 3.6.
[p] Growth rate determined by profilometer
[f] Growth rate determined by Pendellösung fringes

O_2 flow rate or the absolute flux values individually will result in a modification of the growth windows, and can be visualized as a third orthogonal dimension to the diagram into and out of the page which represents the Nb:O_2 ratio.

The oxygen deficient vacuum conditions in MBE, far from equilibrium, enable meta-stable sub-oxide phases like $LiNbO_2$ not possible at higher oxygen partial pressures. In the traditional phase diagram of the Li_2O-Nb_2O_5 system, recreated in Figure 3-14b from Kitamura et. al.[144] and Reisman et. al[59], $LiNbO_2$ is not present because sub-oxides are not possible in this fully oxidized system. Similarities may however be noted between the two diagrams. Li_3NbO_4 lies to the Li-rich side of $LiNbO_3$ in both diagrams while $LiNb_3O_8$ lies to the Li-poor side of $LiNbO_3$ in both diagrams existing at higher temperatures than Li_3NbO_4. NbO and NbO_2 are not present in Figure 3-14b because they do not contain Li, but can be grown by MBE due to the Li-poor conditions under which they are grown where all Li is desorbed as LiCl. Table 3-4 shows the currently achievable structural and morphological quality of films grown by the above method in terms of symmetric rocking curve as determined by XRD and RMS roughness as determined by AFM.

3.5 MBE Grown Thin Film Analysis

3.5.1 $LiNbO_2$

The primary challenge when growing $LiNbO_2$ is the limited phase space in which growth is possible, limited both above and below by temperature and flux. The growth space is defined by the parameters Li flux, $NbCl_5$ flux, O_2 flow, and substrate temperature, and the effect of each parameter is coupled to the other parameters. No single parameter acts alone, therefore strict control is necessary for repeatable growth. This also indicates that there may be multiple equivalent growth conditions not explored in this dissertation. For instance, the relationship of the parameters may not be linearly correlated between a high growth rate and low growth rate condition. Likewise the Li:Nb flux ratio required for $LiNbO_2$ growth may not scale linearly with substrate temperature. Both the substrate temperature and the Li/Nb flux ratio also may scale by a different relationship with oxygen flux. In other words, the growth of $LiNbO_2$ by the methods shown here is one single, basic understanding of a highly complex system of at least four interdependent variables which requires in-depth coupled thermal, chemical, and kinetic modelling to be understood and used to full potential.

Due to the small growth window, lithium niobite films are often multi-phase and non-coalesced. $LiNbO_2$ often co-nucleates with NbO_2 due to the similar temperature range for growth, 950 – 1000 ℃, depending on the flux. The appearance of lithium niobate with lithium niobite generally indicates the substrate temperature was too hot for the given

flux condition. Likewise the appearance of Li_3NbO_4 generally indicates a cold substrate. Oxygen poor growth, in practice, does not result in single phase $LiNbO_2$. Experimentally, for growths with measured fluxes in the 10^{-7} torr BEP range, single phase results were only achieved when increasing the O_2 flux to 4 SCCM. It is possible that the use of oxygen plasma could increase the growth rate, allowing higher Li and $NbCl_5$ flux for a faster growth rate; however this has not been investigated within the current growth scheme.

Two separate $LiNbO_2$ conditions have been developed, one falling on the phase diagram shown in Figure 3-14a and another at a separate $Nb:O_2$ ratio (visualized as another parallel flux ratio versus temperature slice translated in a third orthogonal dimension representing the $Nb:O_2$ ratio).

Condition 1

The first condition for lithium niobite growth is represented by point 7 on the phase diagram in Figure 3-14a where $\phi_{Li} = \phi_{NbCl5} = 7 \times 10^{-7}$ torr BEP, 4 SCCM O_2, and T_{sub}= 975 ℃. A characteristic diffractogram of a film grown using condition 1 is shown in Figure 3-15 exhibiting Pendellösung fringes indicating a smooth surface and interface with a narrowest measured rocking curve FWHM of 78". The growth rate of condition 1 is approximately 85 nm/hr. Films grown in this manner range in color from red to green-blue in reflected light, likely dependent upon the lithium content of the film.

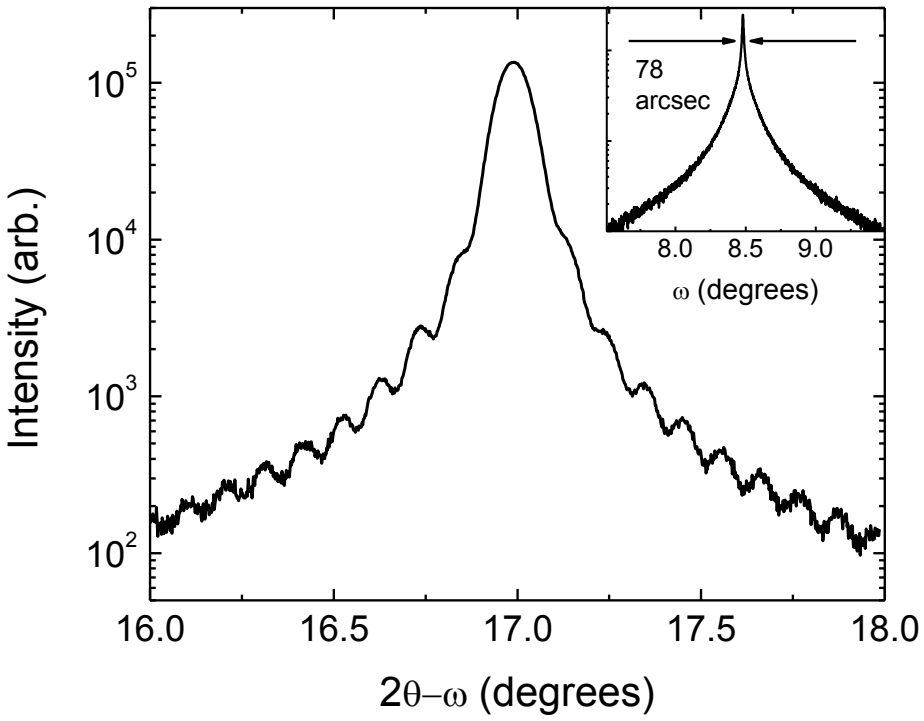

Figure 3-15. X-ray diffractogram and rocking curve (inset) at the $LiNbO_2$ (002) peak from a film grown using condition 1. Pendellösung fringes indicate a smooth surface and interface with a thickness of 85 nm.

Condition 2

The second condition developed for growth of $LiNbO_2$ does not lie on the phase diagram presented in Figure 3-14a. The parameters chosen for this condition occur on an assumed orthogonal slice of the phase space at a lower Nb:O ratio with $\phi_{Li} = 1.7 \times 10^{-7}$ torr BEP, $\phi_{NbCl5} = 3.4 \times 10^{-7}$ torr BEP, 4 SCCM O_2, and $T_{sub} = 1000$ ℃. A characteristic diffractogram of a film grown using condition 2 is shown in Figure 3-16 exhibiting Pendellösung fringes indicating a smooth surface and interface with a narrowest

measured rocking curve FWHM of 107". The growth rate of condition 2 is approximately 60 nm/hr. Films grown in this manner range in color from blue to silver in reflected light, likely dependent upon the lithium content of the film.

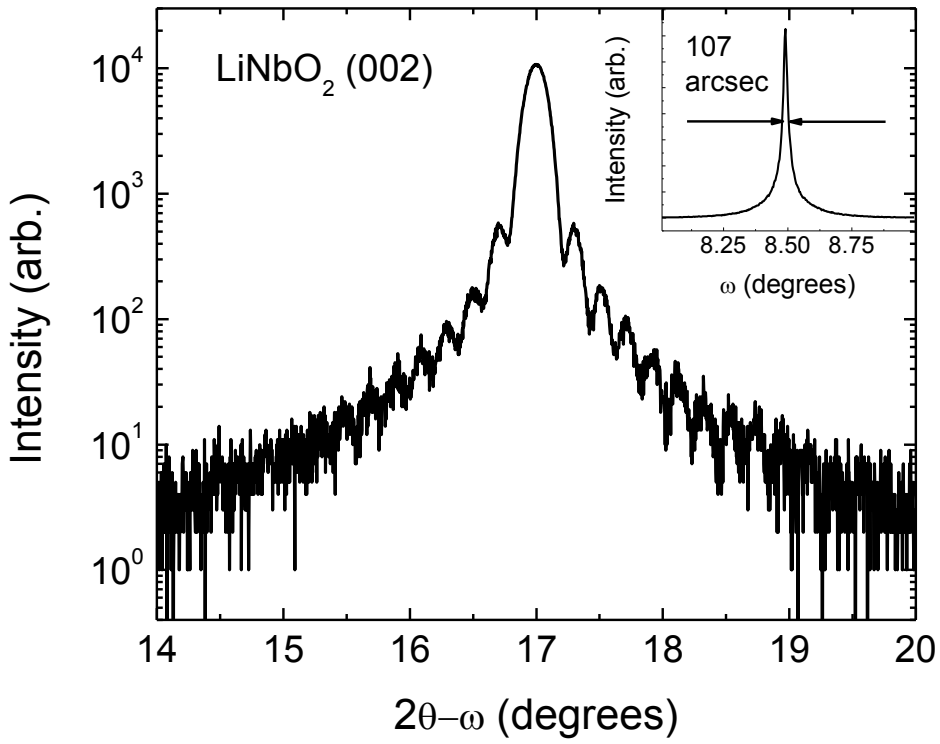

Figure 3-16. X-ray diffractogram and rocking curve (inset) at the $LiNbO_2$ (002) peak from a film grown using condition 2. Pendellösung fringes indicate a smooth surface and interface with a thickness of 44 nm.

3.5.2 Niobium

Niobium is a type-II superconductor and one of a few elemental superconductors such as tin, lead, vanadium, and technetium, where most superconductors are alloys. It undergoes the superconducting transition at T_c = 9.25 K[145]. Niobium and niobium alloys are of particular importance because they are the primary materials used in Josephson tunnel junctions[146]. Epitaxial niobium thin films have previously been grown on sapphire substrates by MBE using electron beam heated sources[147].

Niobium films may now be grown, using the new near ambient two-zone cell described in section 3.1, on sapphire substrates by lithium assisted growth chemistry. The $NbCl_5$ cell is operated at a tip temperature of 130 ℃, while the bulk is maintained at 50 ℃ by a heated recirculating water bath, with a measured flux by ion gauge of ~ 7×10^{-7} torr beam equivalent pressure (BEP). The $NbCl_5$ is reduced to Nb with a coincident Li flux, which is maintained in the range of 5×10^{-7} torr and varied to adjust the growth rate. Films are deposited slowly, at approximately 20 - 50 nm/hr at a substrate temperature of 850 – 950 ℃. The Nb thin films are analyzed for crystalline quality using a Panalytical MRD XRD system (Cu-K_α). The Nb primarily nucleates (110) oriented BCC on c-plane sapphire, indicated by the diffraction scan shown in the inset of Figure 3-17. The presence of Pendellösung fringes indicates a smooth surface and interface with a thickness of 160 nm. The film also exhibits an omega rocking curve FWHM of ~130", shown in Figure 3-17, indicating excellent crystal quality. Secondary Ion Mass Spectroscopy (SIMS) profiling

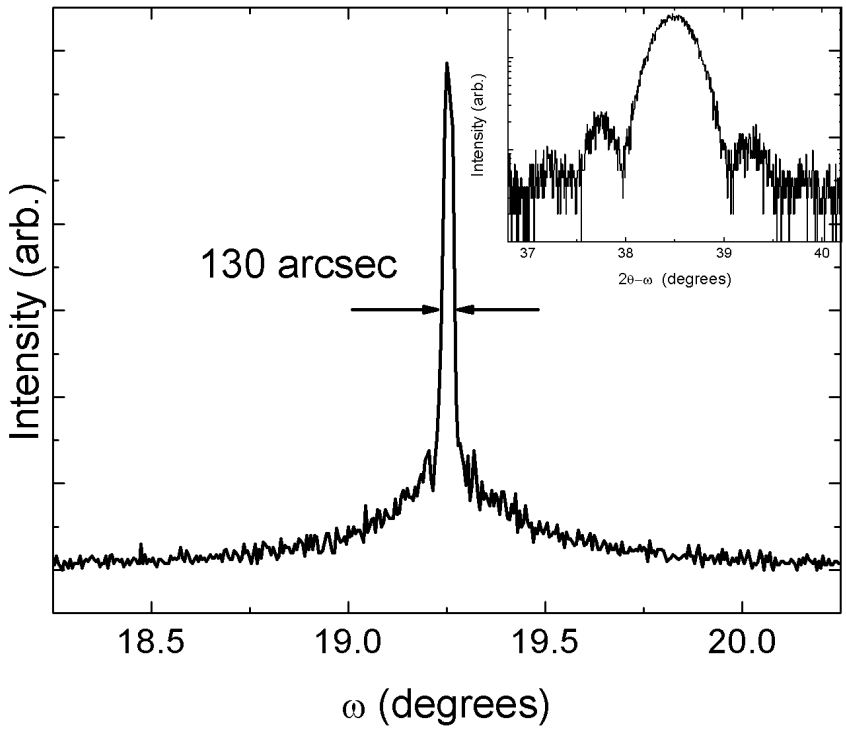

Figure 3-17. XRD rocking curve of the BCC Nb film with a FWHM of 130" indicating excellent crystalline uniformity. Inset X-ray Diffraction scan showing (110) oriented BCC Nb with Pendellösung fringes indicating a smooth surface and interface and a thickness of 16 nm.

of the films show no chlorine or lithium contamination with the signals for both elements below the detection limit of the spectrometer.

Thicker films of epitaxial niobium on sapphire reveal a lower intensity secondary peak in XRD representative of another crystalline phase. This secondary phase is likely strained FCC (111) niobium, whose bulk peak is at $2\theta = 36.77°$, however NbO cannot be completely ruled out due to low levels of background oxygen in the chamber. This secondary peak in a 33nm film is shown by XRD in Figure 3-18.

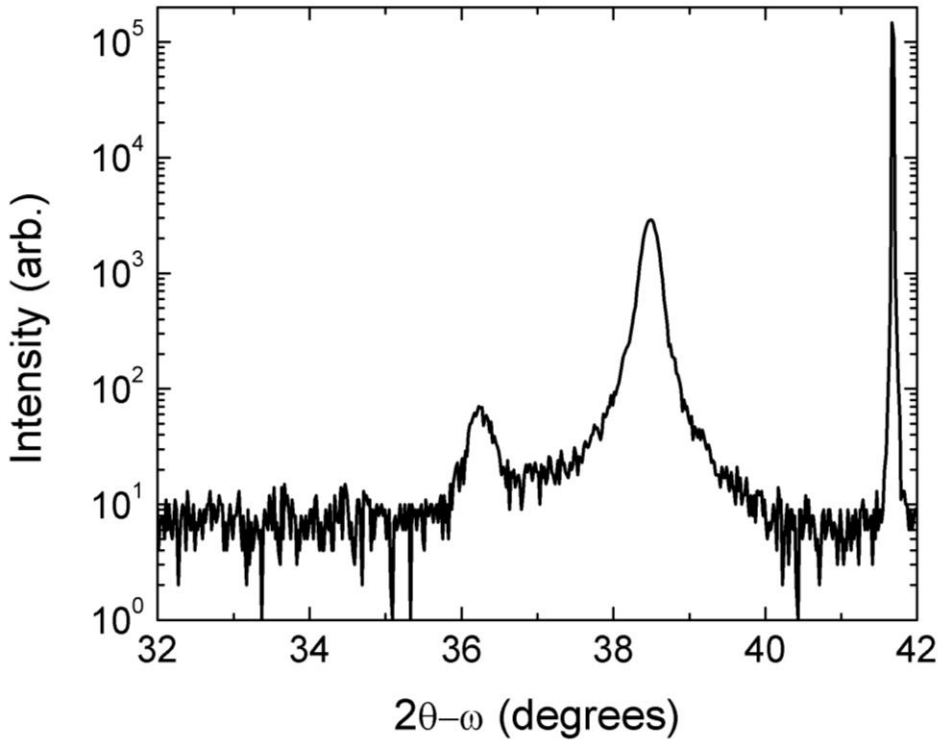

Figure 3-18. A secondary phase is observed in XRD for the growth of crystalline niobium thin films. The phase is attributed to FCC (111) niobium which is strained from its ideal value (2θ = 36.77°), however NbO cannot yet be ruled out.

3.5.3 NbO

Nb oxidized in the +2 valence state forms NbO, which is normally an unstable compound. NbO typically exists as an intermediate oxide layer in the formation of Nb_2O_5 on Nb in the presence of oxygen[143,146]. NbO is a semi-metal with a resistivity on the order of 10^{-5} Ω-cm as noted in Figure 1-3[148], and is cubic in the *Pm3m* space group with a

lattice parameter a = 4.21 Å. The unit cell is a derivative of rocksalt structure with 25 % ordered vacancies of both cations and anions[148,149].

NbO has been grown by limiting the Li cell to fluxes where all of the lithium is consumed by cracking $NbCl_5$ and forming desorbing LiCl rather than incorporating in the film. Lower oxygen pressures are used to promote the metastable phase and films are grown around 850 ℃. Figure 3-19 shows a characteristic NbO film grown by this

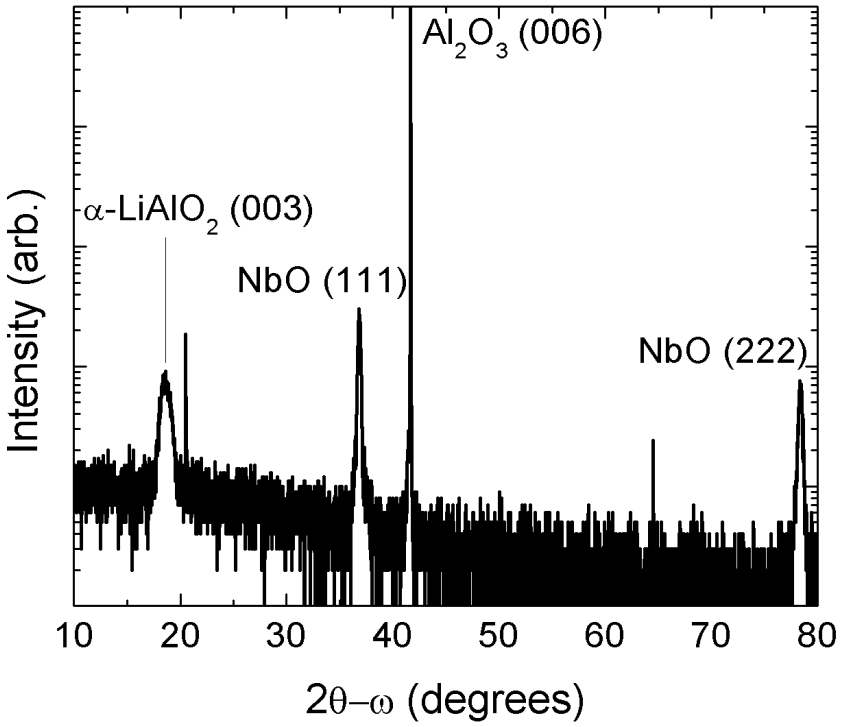

Figure 3-19. XRD 2θ-ω scan of (111) oriented NbO with an interface layer of α-$LiAlO_2$.

method. The film in Figure 3-19 is approximately 100 nm thick and is grown slowly to encourage growth of the suboxide, and shows a γ-$LiAlO_2$ (003) oriented interface layer related to Li reaction with the Al_2O_3 substrate. The symmetric rocking curve of the NbO film is ~1200", a large value indicating crystalline degradation. The defective material is likely due to a large lattice mismatch with the substrate which has a pseudo-hexagonal a-spacing of 2.75 Å compared to the film's 2.977 Å pseudo-hexagonal lattice constant.

3.5.4 NbO_2

NbO_2 is a +4 valence suboxide in the niobium-oxygen system which has received significant interest in recent years due to its threshold switching behavior which occurs with hysteresis as shown in *Pickett et. al.*[49]. As shown in the phase diagram in Figure 3-14a, NbO_2 is grown in the Li-$NbCl_5$ system at slightly lithium poor conditions and moderately high temperatures ranging from approximately 925 ℃ – 1000 ℃, depending on the flux condition. NbO_2 undergoes a metal-insulator transition as discussed in Section 2.4.3 which physically manifests as a dimerization of Nb-Nb bonds destabilizing the high temperature rutile structure into a low temperature distorted rutile body-centered tetragonal (BCT) phase[37,150]. This dimerization is present in many transition metal oxides which undergo a MIT, however the 3d materials like VO_2 are often dominated by an electronic correlation making them more Mott-like[151], where NbO_2 is purely due to a lattice dimerization of the Peierls type[150,152–154].

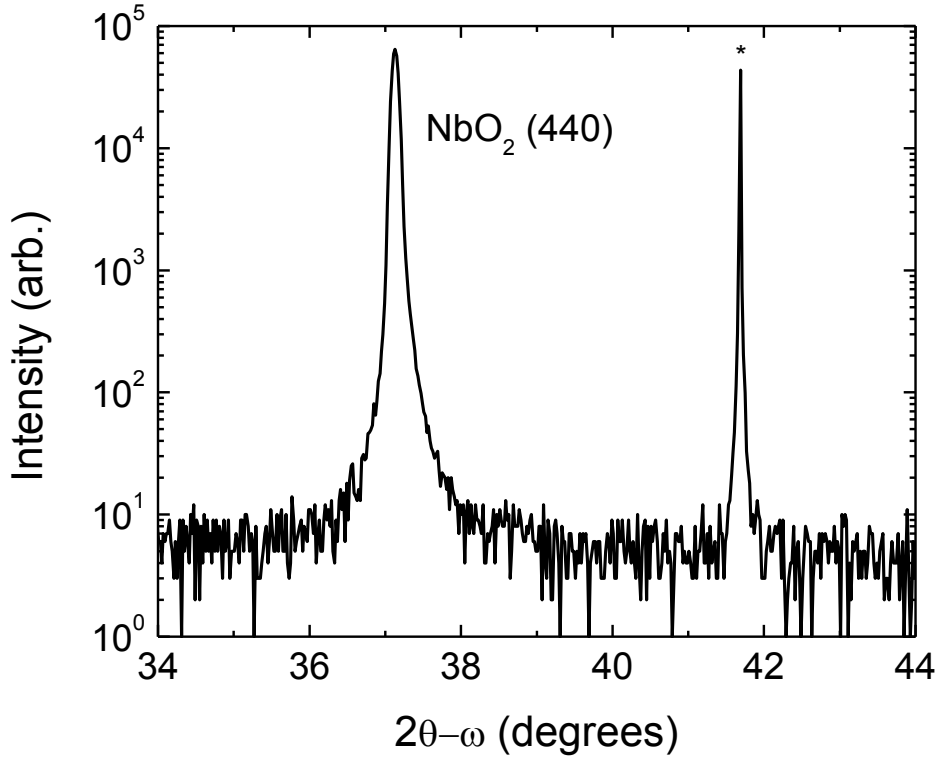

Figure 3-20. X-ray diffractogram of (440) oriented NbO_2 grown on (006) Al_2O_3 (*).

The high temperature rutile structure crystallizes in the $P4_2/mnm$ space group and the low-temperature distorted rutile structure crystallizes in the BCT $I4_1/a$ space group with lattice parameters a = 4.8463 Å, c = 3.0315 Å, a_{BCT} = 13.7020 Å, and c_{BCT} = 5.985 Å, the pseudo-rutile relationship between them being $a \approx 2\sqrt{2a_{BCT}}$ and $c \approx 2c_{BCT}$ [150,152,155]. On c-plane sapphire the distorted rutile NbO_2 crystallizes in the (110) direction, which is parallel to the pseudo-rutile (100), along the hexagonal oxygen sublattice with a pseudo-hexagonal a spacing of 2.895 Å (5.6 % mismatch). A diffraction scan characteristic of NbO_2 grown by the lithium-assisted metal halide MBE method is shown in Figure 3-20

with an epitaxial relationship (110)[100] NbO_2 || (0001)<1$\bar{1}$00> Al_2O_3[155]. NbO_2 crystallizes in the current growth conditions with 60° rotational domains as measured by a ϕ scan of the (400) reflection as shown in Figure 3-21 arising from rotationally defective nucleation on the hexagonal substrate lattice.

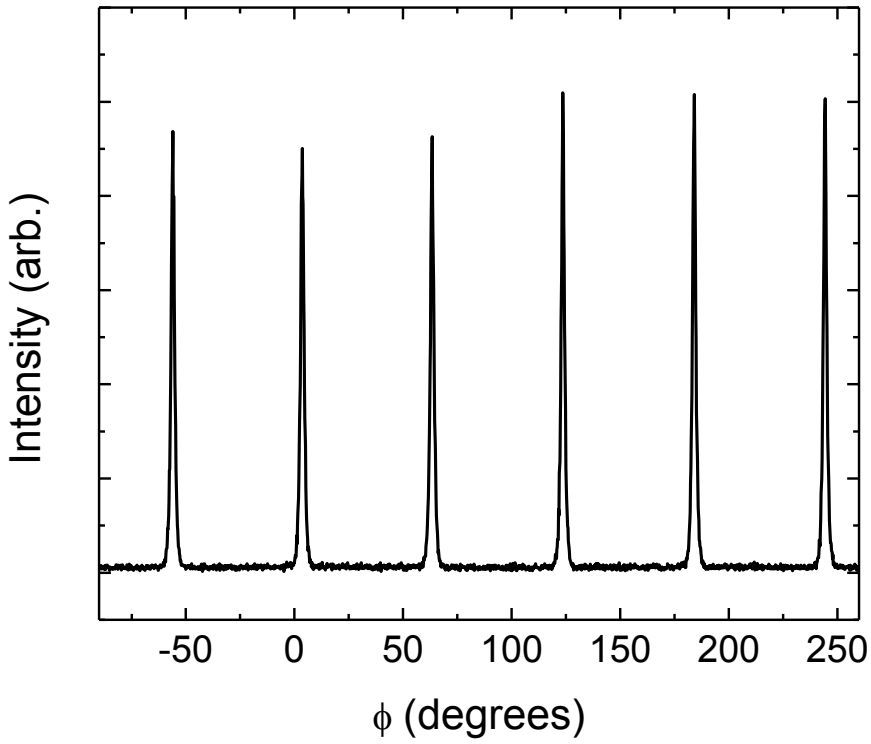

Figure 3-21. ϕ scan of the NbO_2 (400) reflection showing 60° rotational domains when grown on (006) Al_2O_3.

3.5.5 Nb_2O_5

It is theorized that in the phase space there exists another phase below NbO_2, where extremely lithium limited conditions slow the growth rate enough for niobium to fully oxidize to form Nb_2O_5. This has been observed experimentally with lithium limited flux conditions $\phi < 0.1$ resulting in a diffraction peak at $2\theta \approx 37.6°$. Nb_2O_5 is monoclinic and therefore has many diffraction peaks making identification difficult. If the observed diffraction peak is from Nb_2O_5 then it corresponds to the $(\bar{6}10)$ reflection at $2\theta = 37.602°$.

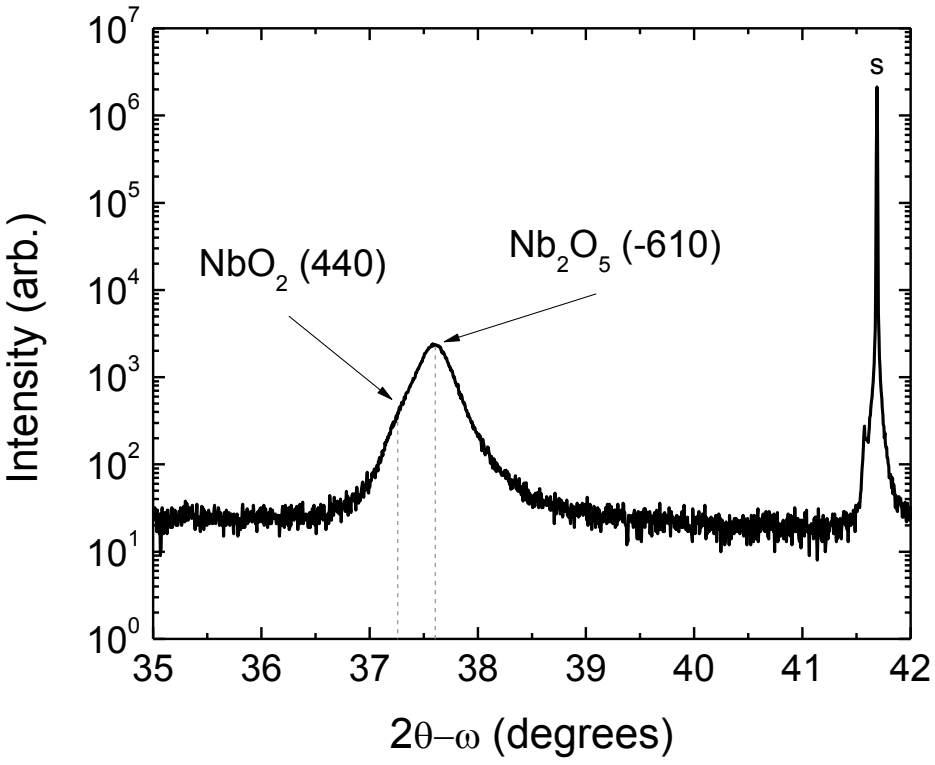

Figure 3-22. X-ray diffraction scan of a thin film grown at flux ratio $\phi = 0.07$ with a reflection at $2\theta = 37.6°$ possibly identified as Nb_2O_5 $(\bar{6}10)$ with a shoulder at $2\theta = 37.24$ corresponding to (440) NbO_2. The substrate (s) is (006) Al_2O_3.

It is possible that it is highly strained (440) NbO_2 (bulk $2\theta = 37.069°$) or $(60\bar{2})$ $LiNb_3O_8$ (bulk $2\theta = 38.104°$). Due to the range of stoichiometries observed in other transition-metal oxides it is also possible the compound is more correctly NbO_x where $2 < x < 2.5$, making XRD identification more difficult without corroborating characterization.

A film grown at $\phi = 0.07$ ($\phi_{Li} = 5 \times 10^{-8}$ torr BEP) and 4 SCCM O_2 was characterized by both XRD and XPS to help identify the phase. The symmetric diffraction scan of this film is shown in Figure 3-22 with a clear peak at $2\theta = 37.6°$ and a shoulder at $2\theta = 37.24°$, most likely corresponding to $(\bar{6}10)$ Nb_2O_5 and (440) NbO_2. A rocking curve taken at the main reflection had a FWHM of 508" indicating a well oriented film, and a ϕ scan around the NbO_2 (400) off axis peak revealed 6-fold rotational symmetry confirming the presence of NbO_2. XPS measurements of the same film, shown in Figure 3-23 and carbon corrected to C1s = 284.5 eV, confirm a mix of oxidation states after sputtering away the surface oxide which shows primarily Nb^{+5} and a small fraction of Nb^{+4}. It is clear that multiple oxidation states are present from Nb^{+5} at $3d_{5/2}$ = 207.4 eV, Nb^{+4} at $3d_{5/2}$ = 206 eV[156], and Nb^{+3} interpolated between the +2 and +4 states at $3d_{5/2}$ = 205 eV as shown in *Shank et. al.*[84]. Further experiments are clearly needed to understand this section of the phase space and to characterize the films discussed here.

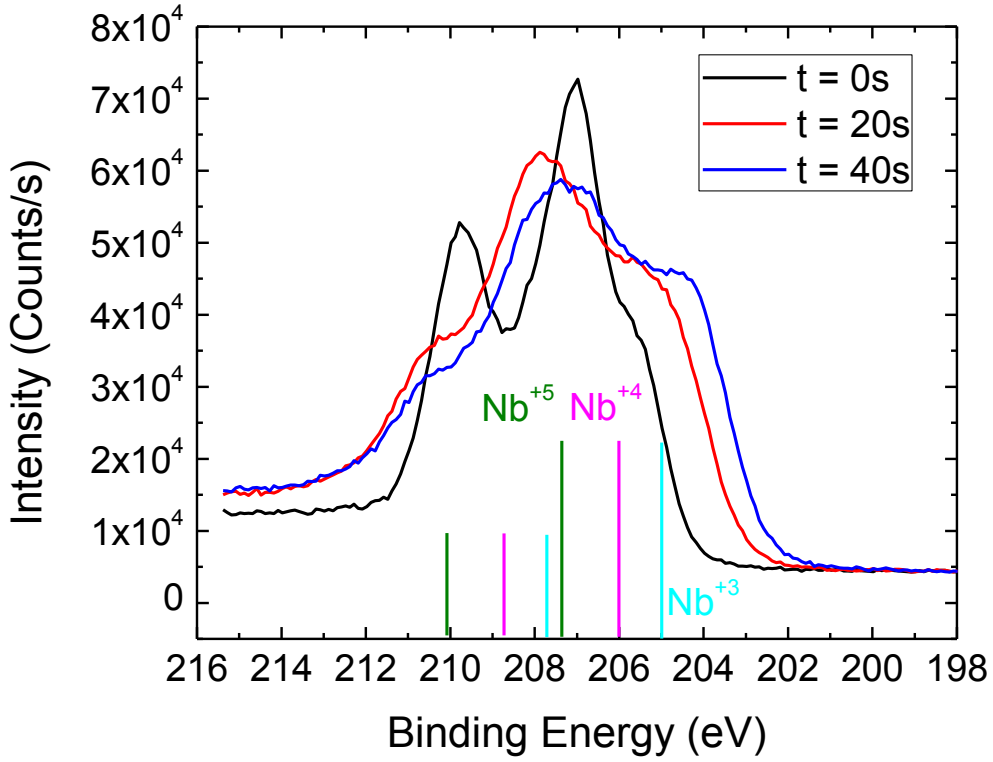

Figure 3-23. XPS as a function of sputter time for a film grown at flux ratio ϕ = 0.07 showing a surface oxide and a mix of oxidation states from +3 to +5 after surface removal. Preferential sputtering shifts the spectra to lower binding energy as sputter time increases.

3.5.6 Li_3NbO_4

The lithium rich state of fully oxidized niobium, tri-lithium niobate (Li_3NbO_4), has been grown using the same methods. Tri-lithium niobate is a lithium rich niobate existing towards Li_2O compositions greater than ~50 % as shown on the Li_2O-Nb_2O_5 phase diagram[59,157]. Tri-lithium niobite has been investigated as a Low Temperature Co-fired Ceramic (LTCC) for microwave frequency dielectrics with a permittivity of 15.8 and a

quality factor ($Q \times f_0$) of 55,009 GHz[51]. LTCC's are important for microwave frequency dielectric circuits to avoid migration of metal electrode atoms into the dielectric during firing, however the ceramic sintering temperature is often very high for materials with desirable dielectric figures of merit. Ag is the most common electrode material for this technology, and therefore dielectrics that can be sintered at T < 960 ℃ are a topic of research[51,158]. It is also reported that Li_3NbO_4 exhibits luminescence at 376 nm from the niobate octahedra group[55].

Using the methods described herein, high quality single crystal tri-lithium niobate has

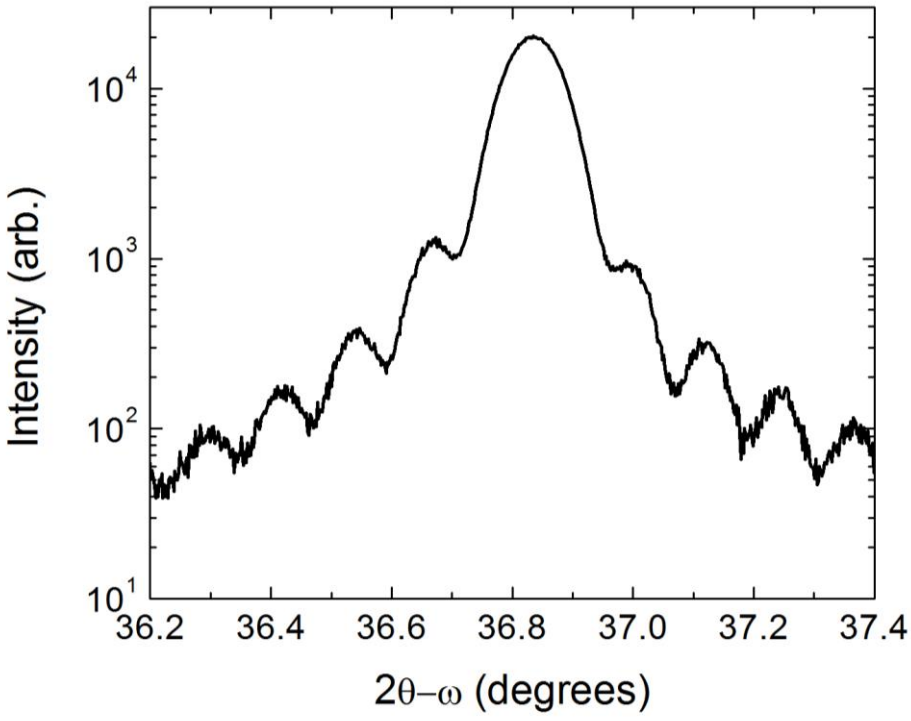

Figure 3-24. XRD symmetric scan around the Li_3NbO_4 (222) reflection showing Pendellösung fringes indicating a smooth 75nm thick film.

been grown using slightly lower growth temperatures than used for lithium niobite. At approximately 850 ℃ – 950 ℃ the lithium rich environment preferentially nucleates to cubic tri-lithium niobite, which nucleates in the (222) direction along the hexagonal sapphire c-face with cubic lattice parameter a = 8.45 Å (bulk value 8.41 Å). The diffractogram of a characteristic Li_3NbO_4 film is shown in Figure 3-24, exhibiting Pendellösung fringes indicating a smooth surface and interface, and giving a film thickness of 75 nm for a 60 minute growth. The rocking curve for this reflection is shown in Figure 3-25 with a FWHM of 14" indicating extremely high crystalline quality with respect to tilt in the c-axis.

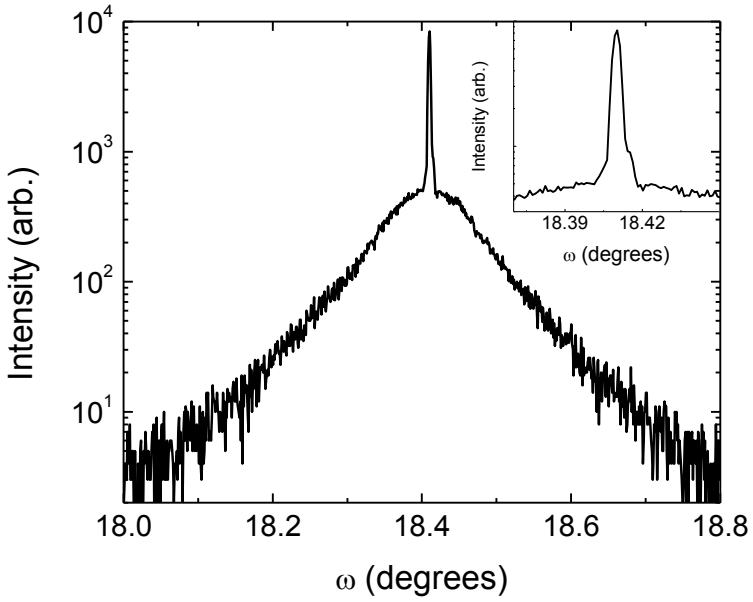

Figure 3-25. Rocking curve about the Li3NbO4 (222) reflection indicating a high degree of crystalline uniformity with a FWHM of 14". The inset shows the narrow peak is well resolved. The lower intensity wider portion indicates epitaxial matching to tilted grains in the substrate as investigated for LiNbO3 in Section 3.6.3.

Despite the lack of functional properties (aside from dielectric) in Li_3NbO_4, the high crystalline quality observed in MBE grown material suggests use as a nucleation layer for more desirable materials like $LiNbO_3$, $LiNbO_2$, and NbO_2. $LiNbO_2$ and $LiNbO_3$ both have coalescence issues when grown on Al_2O_3, and NbO_2 shows 3-fold rotational domains. It is likely that these nucleation issues could be resolved through a high quality buffer layer which reduces the encountered strain of the target film. Table 3-5 shows the hexagonal a-spacing for various desired functional materials and their mismatch to either sapphire or Li_3NbO_4 which has an oxygen sublattice with hexagonal spacing a = 2.88 Å as shown in Figure 3-26.

Table 3-5. Hexagonal a-spacing and mismatch for selected films with and without a Li_3NbO_4 buffer layer.

Material	pseudo-hexagonal a-spacing (Å)	Mismatch to Al_2O_3	Mismatch to Li_3NbO_4
$LiNbO_3$	2.98	8.05%	3.35%
$LiNbO_2$	2.92	6.16%	1.36%
NbO_2	2.89	5.19%	0.35%
Al_2O_3	2.75	N/A	4.73%

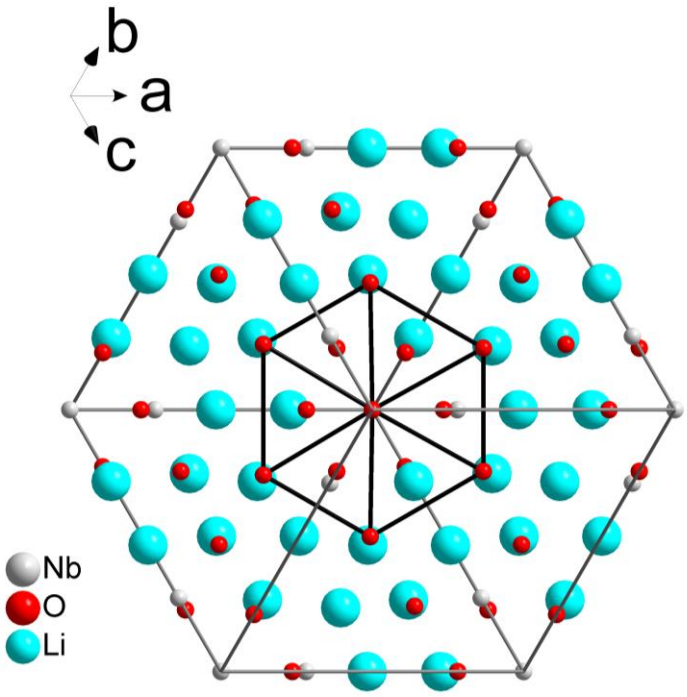

Figure 3-26. Hexagonal oxygen lattice (a = 2.88 Å) of Li_3NbO_4 as viewed from the unit cell {111} direction.

If grown at similar substrate temperatures in severely oxygen depleted environments, Li_3NbO_4 can be grown (100) oriented. Figure 3-27 shows a two-phase diffractogram of a film grown at low $LiClO_4$ fluxes in a severely lithium rich environment showing the (200), (400), and (600) reflections. Niobium (II) oxide, a suboxide with niobium in the +2 valence, is also present due to the oxygen starved atmosphere. While the results of this growth are interesting, further work to optimize the (100) oriented Li_3NbO_4 was not pursued.

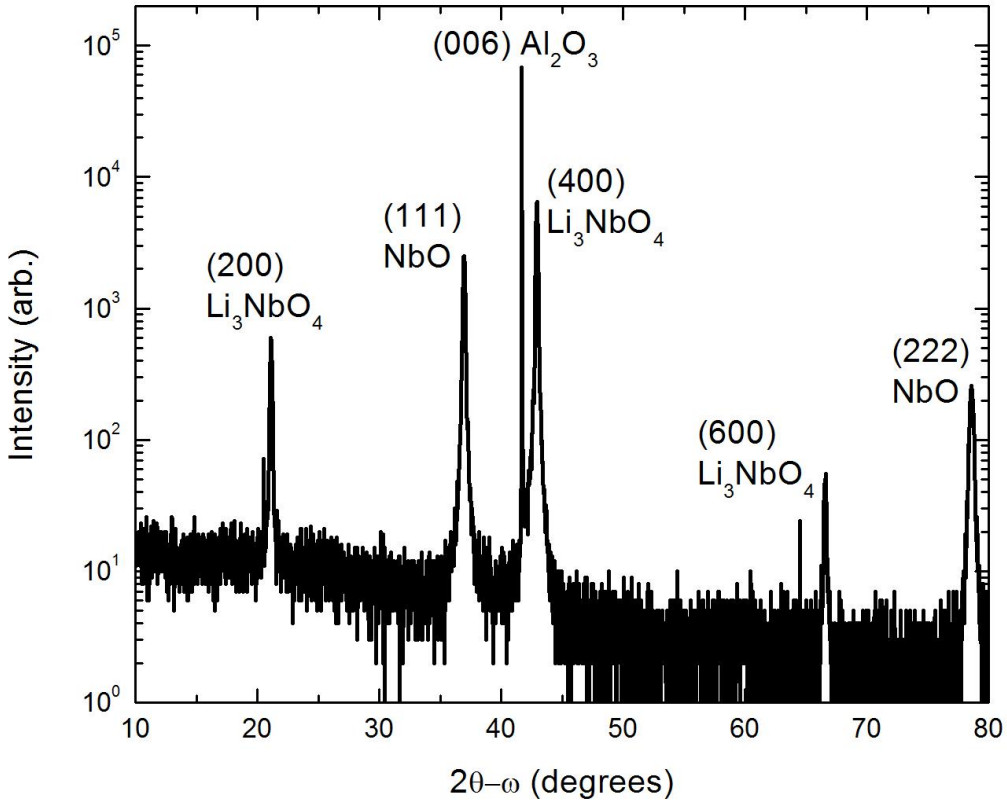

Figure 3-27. X-ray diffractogram showing a two phase film composed of (100) oriented Li_3NbO_4 and NbO. This result was obtained by oxygen deficient growth conditions in the Li_3NbO_4 growth window on an Al_2O_3 substrate.

3.5.7 $LiNb_3O_8$

Lithium tri-niobate ($LiNb_3O_8$) is a lithium poor phase grown at similar conditions to $LiNbO_3$ and readily forms from $LiNbO_3$ that is vacuum annealed preferentially losing Li_2O from the surface[159]. $LiNb_3O_8$ is also a LTCC material with quality factor ($Q \times f_0$) 58,000 GHz and dielectric constant $\epsilon_r = 34$, and solid solution with 35 % TiO_2 enhances these microwave dielectric properties to a maximum $\epsilon_r = 46.2$[158]. $LiNb_3O_8$, like Li_3NbO_4,

also has a negative temperature coefficient of resonance frequency τ_f, meaning it can be mixed with a ceramic of positive τ_f to form a dielectric with a resonant frequency unaffected by temperature. Lithium tri-niobate has also shown use as a photocatalytic material for water reduction to hydrogen. $LiNb_3O_8$, $LiNbO_3$, and their mixtures are highly active for photocatalytic water reduction under UV irradiation[160]. $LiNb_3O_8$ is a direct band material with a gap of 3.9 eV, but substituting Cu for Li in solid solution with $CuNb_3O_8$ results in additional indirect and direct visible light transitions. This indirect transition is tuneable by Cu mole fraction from 1.5 eV – 1.27 eV and the secondary direct transition is tuneable from 1.91 eV - 1.44 eV. The material exhibits photocatalytic water reduction to hydrogen across the entire range with maximum activity at $Li_{0.5}Cu_{0.5}Nb_3O_8$[40]. Aside from the photocatalytic effect $LiNb_3O_8$ is primarily considered an unwanted phase in the synthesis of $LiNbO_3$ and is generally characterized in order to increase the purity of $LiNbO_3$ samples for optical applications.

In the Li-$NbCl_5$-O_2 system $LiNb_3O_8$ can be grown at the same temperatures as $LiNbO_3$, $T_{sub} \geq 1000$ ℃, at slightly lithium poor conditions as shown in Figure 3-14. A diffractogram of lithium tri-niobate is shown in Figure 3-28 which has a corresponding rocking curve FWHM of 860". Due to the low quality of this film, difficult growth conditions, and lack of potential heterostructures uses, the optimization of $LiNb_3O_8$ growths was not pursued.

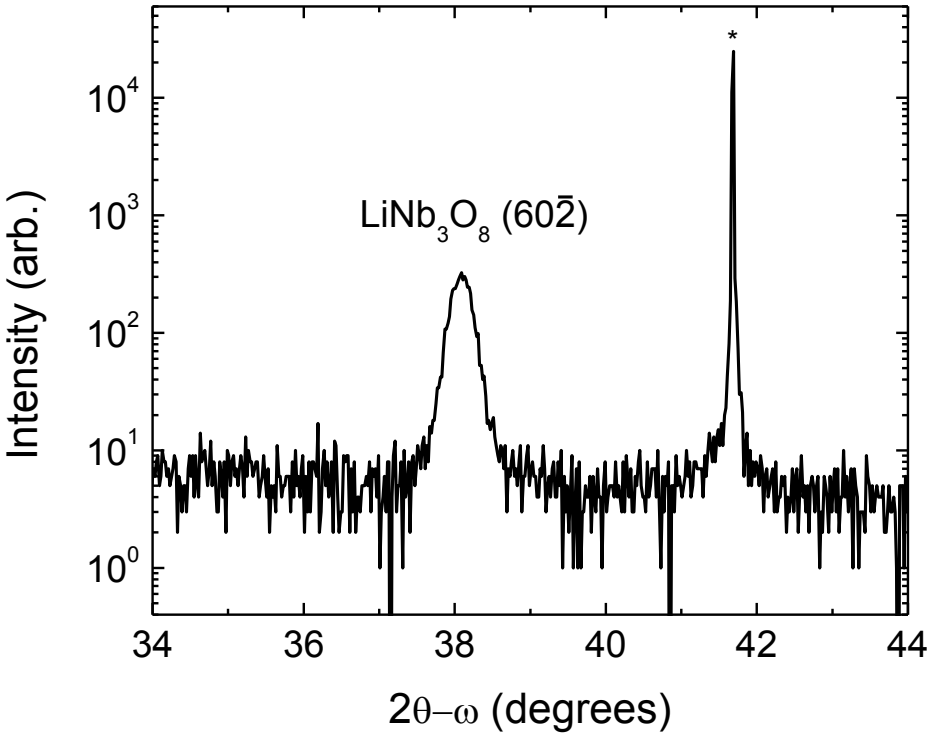

Figure 3-28. Diffractogram of single phase lithium tri-niobate grown on sapphire (*) at a substrate temperature of 1025 ℃ with a rocking curve FWHM of 860".

3.6 Epitaxial Lithium Niobate Thin Films on Lattice Matched and Mismatched Substrates

3.6.1 Substrates

Lithium niobate is a trigonal crystal in the R3c space group with a unit cell comprised of oxygen octahedra with interstices that are one third lithium, one third niobium, and one third vacant[44]. The hexagonal oxygen sublattice forms layers in the basal plane, and in the ferroelectric phase the lithium atoms are positioned 0.37 Å above or below these layers, with both sites equally energetically favorable[44]. This offset produces the polar and ferroelectric nature of lithium niobate. A sufficient applied field shifts the lithium atoms across the oxygen layer switching the polarity[44].

The hexagonal relationship in the crystal structure that is exploited for epitaxy on sapphire is not the supercell based hexagon a = 5.148 Å but the pseudo-hexagonal average oxygen sublattice a = 2.986 Å which is 30 degrees rotated from the supercell. The three distinct atomic distances are a_1 = 2.718 Å, a_2 = 2.878 Å, and a_3 = 3.363 Å. This distinction is illustrated in Figure 3-29.

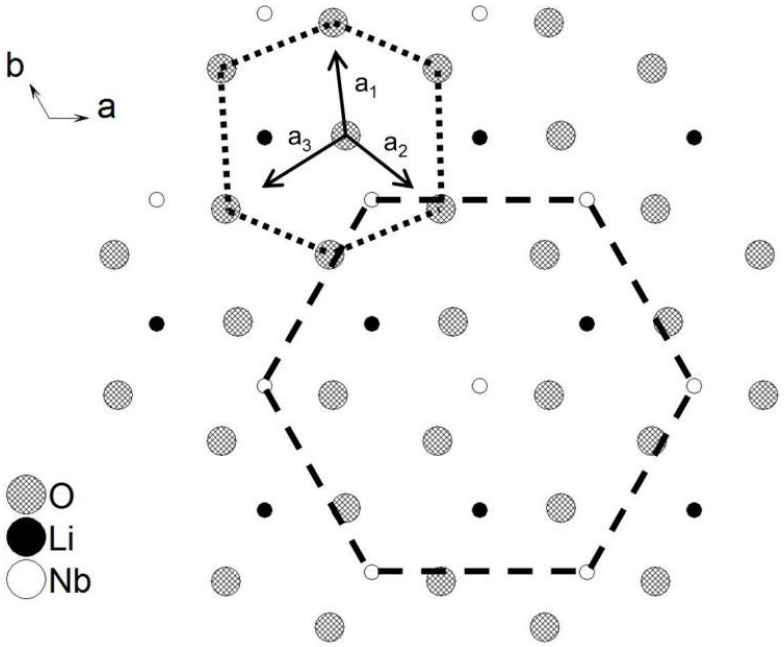

Figure 3-29. The c-plane of lithium niobate (c-axis out of plane) showing the hexagonal supercell as a dashed line (a = 5.148 Å) and the 30° rotated pseudo-hexagon in the oxygen sublattice as a dotted line (a = 2.986 Å). The three weighted pseudo-hexagonal parameters are notated a_1, a_2, and a_3.

In order to understand the role of the substrate on film quality and nucleation, films in this work were grown on both lattice matched and mismatched substrates. The lattice parameters and coefficient of thermal expansion (CTE) of selected substrates and nucleation layers are given in Table 3-6. For lattice mismatched growth, c-plane (006) sapphire was used, and for lattice matched growth c-plane $LiTaO_3$ was used which has been shown to be more vacuum stable than $LiNbO_3$[159,161].

The 1 cm square substrates are backside metallized with ~2 μm chrome followed by ~2 μm chrome oxide in a Denton Discovery reactive sputtering system. The substrates are

then cleaned by solvents followed by H_2SO_4:H_2O_2 in a 4:1 ratio at 120 ℃ before loading into an introductory vacuum chamber and degassed at 200 ℃ for 1 h.

3.6.2 Characterization

The films in this work were structurally characterized by x-ray diffraction (XRD) using a Phillips X'pert Pro MRD with a hybrid parabolic mirror/Ge 4-bounce crystal monochromator delivering Cu-Kα_1 radiation (λ = 1.54056 Å) in both double- and triple-axis geometries. For double axis measurements, a 0.0625° slit was used on the incident optics and a 0.25° slit was used on the detector optics. For triple-axis measurements no slits were used on the incident optics. Symmetric scans were used to determine c-spacing strain and uniformity, single phase nature, tilt angle, and thickness when applicable. Asymmetric scans were used to analyze films for rotational domains and twist.

Table 3-6. Selected substrates and their properties for $LiNbO_3$ epitaxy.

Material	pseudo-hexagonal a-spacing (Å)	CTE ($\times 10^{-6}$ /℃)
$LiNbO_3$	2.98	16.2 [194]
$LiNbO_2$	2.92 (2.2%)	Unknown
$LiTaO_3$	2.99 (0.1%)	15.4 [194]
Al_2O_3	2.74 (8.7%)	5.2 [195]
SiC (6H)	3.08 (3%)	3.27 [196]
Nb (BCC)	2.86 (4.4%)	7.3 [197]

The surface morphology of the lithium niobate films was analyzed by a Veeco atomic force microscopy (AFM) system in tapping mode using silicon probes with a tip radius of 7 nm and theoretical horizontal resolution of 5 nm.

3.6.3 Lattice Mismatched Substrate

$LiNbO_3$ thin films were grown on c-plane Al_2O_3 substrates to analyze the effects of lattice mismatch on nucleation, structure, and morphology. Al_2O_3 has a pseudo-hexagonal structure with a weighted lattice constant shown in Table 3-6 giving a mismatch of 8.7 % with $LiNbO_3$. Additionally, the CTE of $LiNbO_3$ is nearly 3 times larger than that of sapphire. Because of this large lattice mismatch, films are expected to relax quickly during growth and undergo tensile strain during cool down due to the CTE mismatch.

Figure 3-30 shows an x-ray diffractogram of single phase c-oriented $LiNbO_3$ grown on c-oriented sapphire at a substrate temperature of 1000 ℃. The film shows Pendellösung fringes which give a thickness of 57 nm and indicate a smooth surface and interface. It was observed that the rocking curve of the (006) reflection could only be resolved in the triple-axis configuration. Figure 3-31a shows the triple-axis measured symmetric rocking curve with a wider low intensity portion and a higher intensity peak in the center. The low intensity peak was fit to a FWHM of 121", and the higher intensity central peak has a narrow FWHM of 8.6" (0.0024°). This value approaches the theoretical minimum resolvable peak for the XRD system in the triple-axis configuration; however, the peak

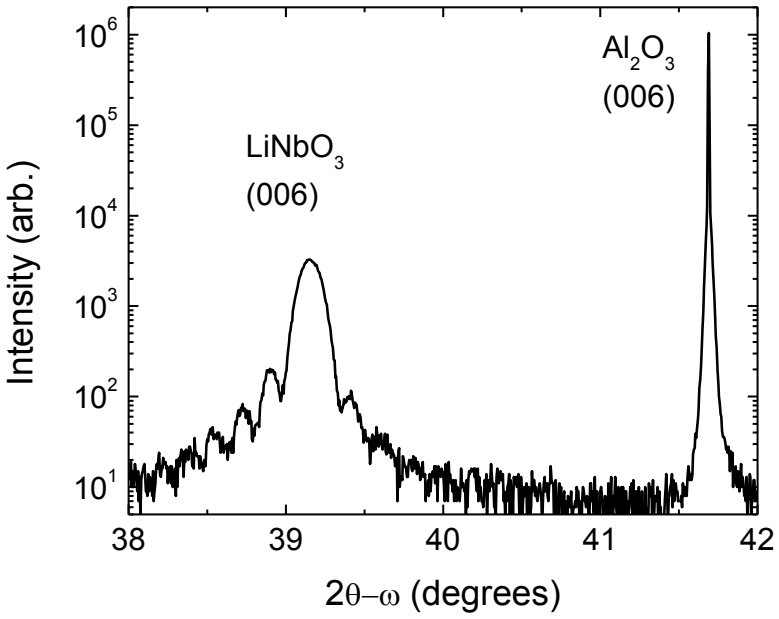

Figure 3-30. XRD 2θ-ω scan of c-oriented $LiNbO_3$ grown on c-oriented sapphire (*) at a peak 2θ-ω value 0.43% strained tensile to the bulk value. Pendellösung fringes indicate a thickness of 57 nm.

shows ~30 data points, which can be seen in the inset of Figure 3-31a, showing that the value is well resolved. Figure 3-31b shows the symmetric (006) rocking curve of the Al_2O_3 substrate which contains the same features observed in the film rocking curve. The narrow peak is 5.8" FWHM with a wider low intensity portion fit to 67" FWHM. The coincidence of these features implies the $LiNbO_3$ tilt uniformity is matched to that of the Al_2O_3 substrate with slightly titled grains appearing in both substrate and film.

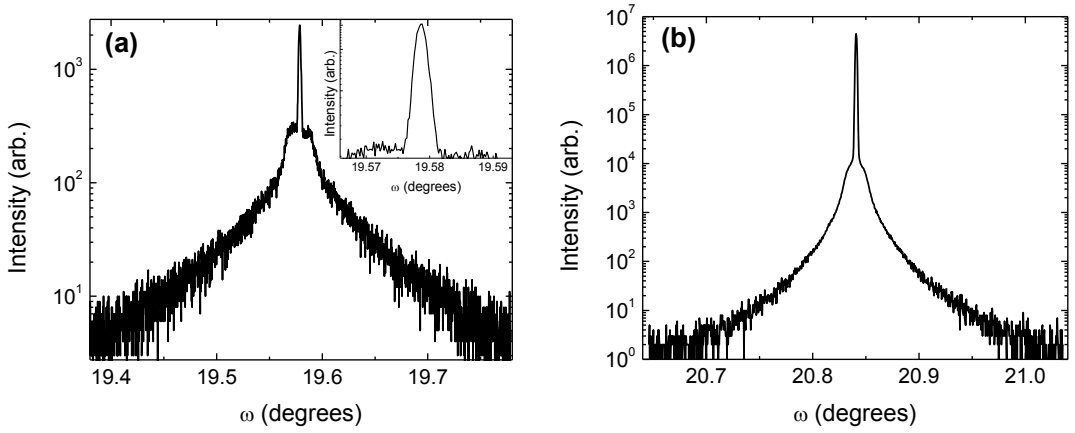

Figure 3-31. (a) Symmetric rocking curve of $LiNbO_3$ (006) on sapphire measured in triple-axis mode with a FWHM of 8.6" (0.0024°). The low intensity secondary peak was fit to a FWHM of 121". Inset Enlarged view of the symmetric rocking curve maxima with ~30 data points indicating the measured value is well resolved. (b) Symmetric rocking curve of the substrate Al_2O_3 (006) peak showing coincident features for the film in (a). The FWHM of the narrow higher intensity section is 5.8", while the lower intensity portion was fit to a FWHM of 67".

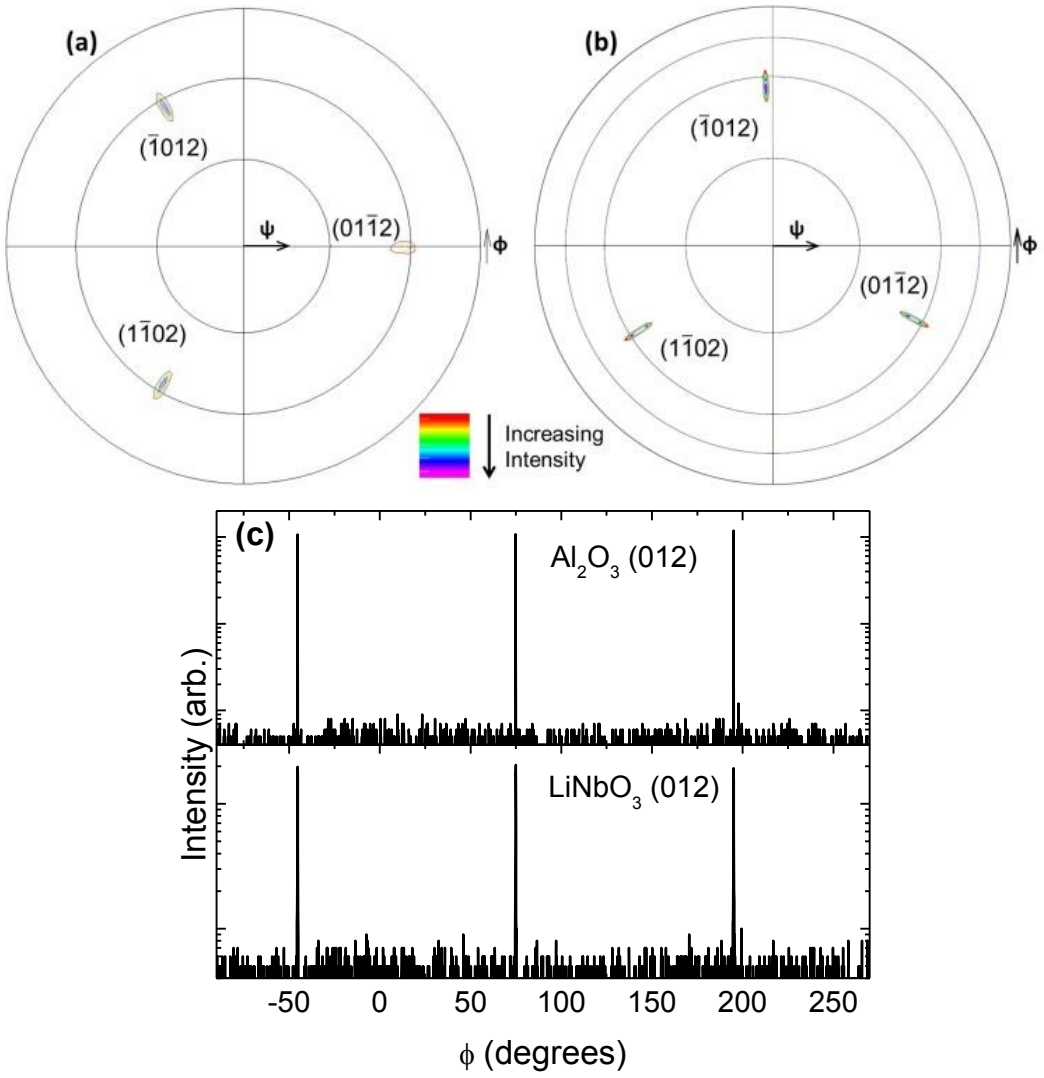

Figure 3-32. Pole figures around the $LiNbO_3$ (012) reflection on (a) sapphire and (b) $LiTaO_3$ substrates showing threefold symmetry. The absence of 60° rotational domains indicates the lack of twin planes. (c) XRD phi scans of the Al_2O_3 and $LiNbO_3$ (01$\bar{1}$2) reflections, respectively, showing the in-plane epitaxial relationship.

An asymmetric rocking curve of the $LiNbO_3$ (012) reflection was also obtained in a skew geometry. The FWHM of this asymmetric peak is 510". The asymmetric rocking curve FWHM is indicative of crystalline twist angle, and using the rocking curve value from the symmetric case the twist angle was calculated to be 601" (0.1669°)[162]. In order to observe any possible rotational domains (twin planes) a pole figure was performed around the $LiNbO_3$ (012) reflection. Figure 3-32a shows threefold rotational symmetry and the absence of 60° rotational domains, indicating that any twin planes are minimized below the detection limit of the diffractometer, which is estimated at approximately 1 % rotational domains by volume. The epitaxial relationship of the $LiNbO_3$ film (subscript f) on sapphire substrates (subscript s) is $<0001>_f \parallel <0001>_s$ and $<10\bar{1}0>_f \parallel <10\bar{1}0>_s$, which was determined by XRD phi scans shown in Figure 3-32c. While both crystals belong to 3m symmetry groups, rotated grains may also nucleate with the relationship $<0001>_f \parallel <0001>_s$ and $<10\bar{1}0>_f \parallel <11\bar{2}0>_s$.

Twin plane suppression of lithium niobate on sapphire has been previously theorized from the standpoint of energetics[98,99]. A slightly energetically unfavorable cation alignment between Al, Li, and Nb exists at the interface, but it was shown that below 700 ℃ there is not enough thermally driven surface diffusion for all nucleation sites to form in the lowest energy configuration resulting in the growth of rotational domains. In MOCVD growth, which has produced some of the higher quality films, this lower limit for substrate temperature is a significant issue due to undesirable gas phase reactions which occur above 650 ℃ – 700 ℃ and can degrade the quality of the films as measured

by symmetric XRD rocking curve[98]. By growing these MBE films at 1000 ℃, twin planes are eliminated.

The surface morphology of thin lithium niobate on sapphire was studied by AFM and is

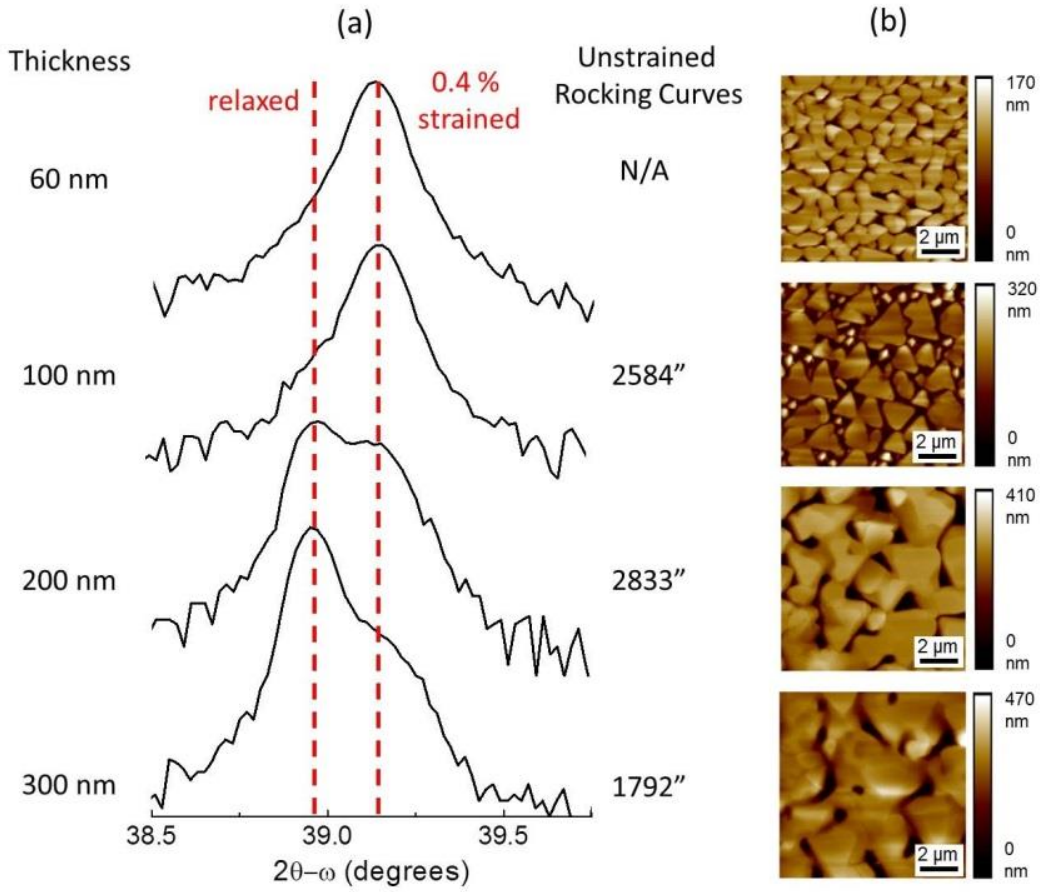

Figure 3-33. The evolution of relaxation and grain size/coalescence as a function of thickness is investigated by (a) XRD and (b) AFM. Relaxation, as shown by XRD 2θ-ω scans in (a), increases as the film thickness increases. Grain size also increases as a function of thickness, shown by AFM in (b), with incomplete coalescence at 300 nm. The unstrained rocking curve values (2θ = 38.98°), shown on the right of (a), indicate the onset of relaxation between 60 and 100 nm with the creation of defects and the subsequent annihilation of those defects as thickness increases.

shown Figure 3-33. Non-coalesced columnar grains are sparsely nucleated with voids extending to the substrate. The plateau-like tops of the columnar grains are atomically flat with a measured surface roughness 0.1 nm – 0.2 nm RMS. Sparse grains like those observed in the present films have also been observed in materials grown by PLD and CVD[94,98]. Grain growth and coalescence was, therefore, studied as a function of film thickness and is depicted in Figure 3-33.

Two phenomena are observed as the film thickness increases. Morphologically, the grain size increases and cracks appear as the films thicken, observed by AFM and shown in Figure 3-34. Structurally, film relaxation through defect formation is observed. The

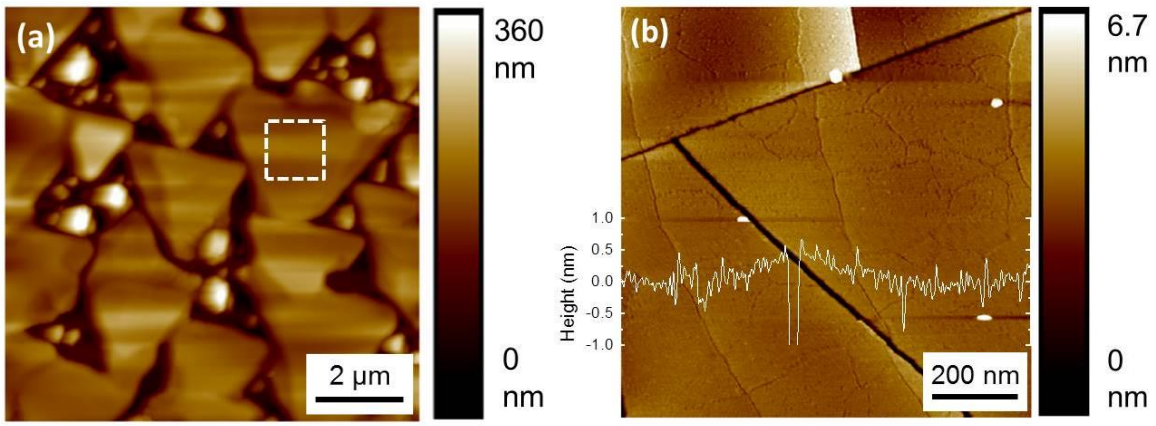

Figure 3-34. (a) AFM determined surface morphology of a 160 nm thick $LiNbO_3$ film grown on sapphire at 1025 ℃ showing increased grain size and decreased nuclei density. The dotted box shows the scan location of (b) 1 µm square AFM image of the same film in (a) showing an atomically smooth surface with cracks. A line scan is overlaid to show the surface height in nanometers, confirming the atomically smooth surface of the plateau. The plateau surface roughness is 0.676 nm RMS.

diffractograms in Figure 3-33a show a shift from 2θ = 39.15°, corresponding to 0.43 % tensile strain as expected from the CTE mismatch, to relaxed lithium niobate at 2θ = 38.98° as the film thickness increases. Figure 3-33b shows the observed grain size and coalescence as measured by AFM. It was also observed that the symmetric rocking curve FWHM of the unstrained (006) reflection was initially very wide and subsequently narrows as the film thickness increases. This trend, shown in the right of Figure 3-33a, likely corresponds to the creation of defects upon film relaxation and subsequent partial annihilation of those defects. As shown in Figure 3-34a, it was observed that increasing the substrate temperature from 1000 ℃ to 1025 ℃ lead to a ~60 % decrease in nuclei density and ~35 % increase in grain size. These two general features, the inverse relationship between nuclei density and substrate temperature and the direct relationship between grain size and temperature, are common in epitaxy and has been observed before in the CVD growth of lithium niobate on sapphire[98,99].

3.6.4 Lattice Matched Substrate

Lithium niobate films were also grown on c-plane lithium tantalate which is lattice matched (0.12 % mismatch) and isostructural. Films were grown under similar conditions to the films grown on sapphire at 1000 ℃. In order to avoid cracking due to thermal expansion, samples must be mounted in housings with significant expansion room (≫200 μm for a 1 cm square sample) and loose mechanical retaining clips to decrease the force

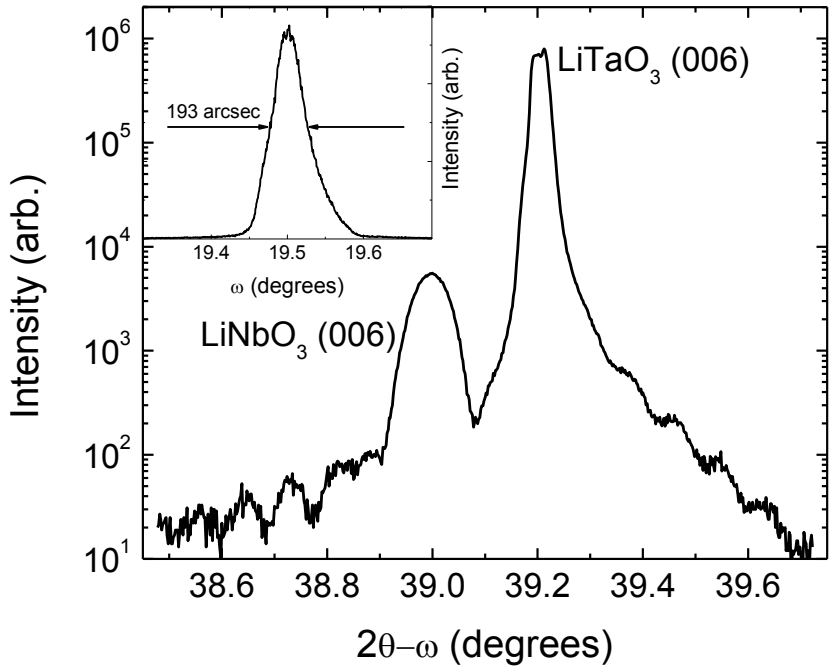

Figure 3-35. X-ray diffractogram of c-oriented $LiNbO_3$ grown on c-oriented $LiTaO_3$ with a peak location identical to the bulk value. Pendellösung fringes indicate a thickness of 112 nm. Inset Symmetric rocking curve at the $LiNbO_3$ (006) reflection with a FWHM of 193", similar to the measured rocking curve of the underlying substrate which was 194".

on the sample surface[163] and transitioned at slow temperature ramp rates ≤20 ℃/min. Figure 3-35 shows the x-ray diffractogram of the lithium niobate on lithium tantalate with a peak value of 2θ = 38.999°, nearly identical to bulk $LiNbO_3$ (2θ = 38.98°). The diffractogram shows Pendellösung fringes which indicate a thickness of 112 nm and a smooth interface and surface. The inset of Figure 3-35 shows the symmetric rocking curve of the (006) lithium niobate reflection which has a FWHM of 193". This value is nearly identical to the rocking curve value measured for the lithium tantalate substrate, 194". Additionally, a pole figure shown in Figure 3-32b around the (012) lithium niobate reflection shows no twin planes as is the case for the films grown on sapphire. In contrast to the lithium niobate on sapphire samples, lithium niobate grown on lithium tantalate has

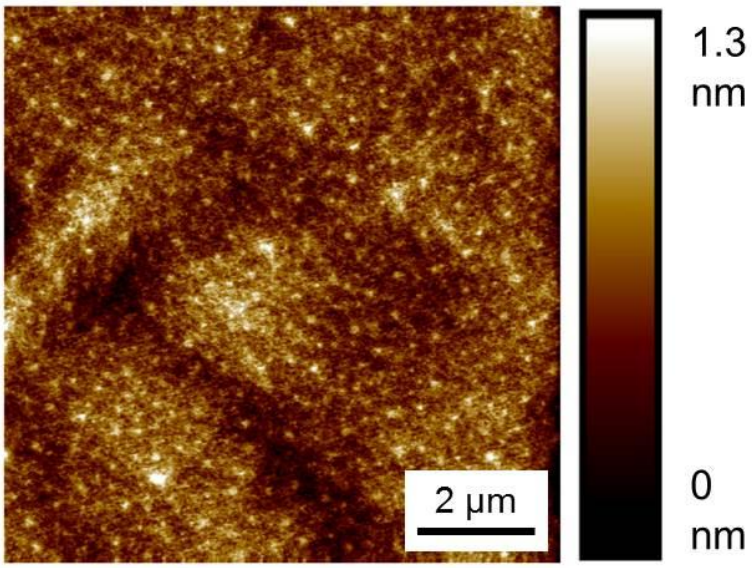

Figure 3-36. Surface morphology of 112 nm thick lithium niobate grown on lithium tantalate with a roughness of 0.175 nm RMS.

a fully coalesced atomically smooth surface, shown in Figure 3-36 with a surface roughness of 0.175 nm RMS.

3.7 $Li(Nb,Co)O_2$

For battery cathode materials of the form ABO_2, where A = Li and M is a transition metal, it is common practice to mix and press powders of various transition metals to incorporate properties such as improved conductivity, capacity, open-circuit voltage, cycle endurance, and reactivity. Examples include mixtures of nickel, manganese, cobalt, niobium, vanadium, and iron on the metal site such as the high voltage compound $LiMn_{3/2}Ni_{1/2}O_4$[72,164–167]. $LiNbO_2$ has shown use as a high discharge rate, high conductivity battery cathode material[47,56,75], but is relatively unstudied compared to the lithium manganates, nickelates, and cobalt oxides. $LiCoO_2$ is one of the primary battery cathode materials in Li- ion batteries for superior capacity, voltage, and cycleability, however suffers from resistive losses due to the low resistivity on the order of $10^3 – 10^{12}$ Ω-cm depending on method of synthesis and purity where single crystals have the highest resistivity[168,169]. It has been shown that the addition of 5 molar percent Mg ($LiMg_{0.05}Co_{0.95}O_2$) can decrease the resistivity of the material to 10^0 Ω-cm[168]. $LiNbO_2$ is one of the most conductive p-type oxides ever measured at 10^{-4} Ω-cm[69], therefore it is reasonable to hypothesize that alloying with low concentrations of Nb in $LiCoO_2$ will reduce the resistivity. It is also possible that a low concentration alloy of Co in $LiNbO_2$

will induce a magnetic moment which may be tunable by Li concentration as is seen for Li_xCoO_2[170].

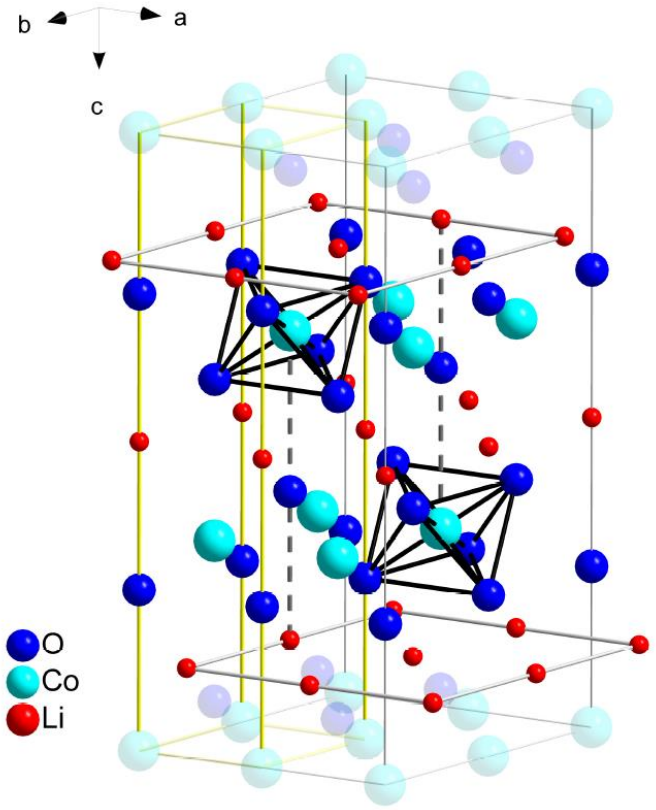

Figure 3-37. $LiCoO_2$ crystal structure, space group $R\bar{3}m$, highlighted to show similarities with $LiNbO_2$ (Figure 2-1). The unit cell is highlighted in yellow, hexagonal lithium planes are shown by grey solid lines, and the octahedral oxygen groups are shown in black with Co on the octahedral site.

3.7.1 Comparisons with $LiNbO_2$

Stoichiometric $LiCoO_2$ is a p-type band semiconductor crystallizing in the $R\bar{3}m$ space group. The crystal structure of $LiCoO_2$ is shown in Figure 3-37, using transparency to

identify similarities between $LiCoO_2$ and $LiNbO_2$ shown in Figure 2-1. The unit cell is outlined in yellow, the equatorials are shown by dashed lines, and the oxygen octahedral units are shown in black with Co sitting on the octahedral site. A comparison of relevant parameters for a $LiNbO_2/LiCoO_2$ epitaxial alloy is shown in Table 3-1. The relatively small mismatch between hexagonal lattice constants and ionic radii (3 %) indicate that substitution of Co on a Nb site (or vice versa) may be possible without extensive straining of the lattice.

Table 3-7. Comparison of relevant parameters for a $Li(Nb,Co)O_2$ alloy.

	$LiNbO_2$	$LiCoO_2$	Mismatch
space Group	$P6_3/mmc$	$R\bar{3}m$	
M-O coordination	trigonal prismatic	octahedral	
Conductivity (Ω-cm)	$10^{-4} – 10^{2}$	10^{3} - 10^{12}	
Li-Li plane spacing	10.44 Å	9.26 Å	12 %
hexagonal a-spacing	2.900 Å	2.815 Å	3 %
B-site metal atomic radius	145 pm	135 pm	7 %
B-site metal ionic radius	72 pm	74.5 pm	3 %

3.7.2 $LiCoO_2$

A well characterized $LiCoO_2$ growth condition is a useful endpoint for alloy quantification and the first step towards a $Li(Nb,Co)O_2$ alloy. To grow $LiCoO_2$ in the same MBE chamber as the films discussed in previous sections cobalt (II) chloride ($CoCl_2$) was loaded in a standard Knudson effusion cell as a cobalt source taking advantage of the same lithium-assisted metal-halide growth chemistry discussed in

Sections 2.1 and 3.1. The equilibrium vapor pressure of $CoCl_2$ is shown in Figure 3-38 as calculated by HSC© chemical modelling software. Based on the vapor pressure curve the $CoCl_2$ cell should be operated in the range 300 ℃ – 500 ℃ to obtain growth level fluxes.

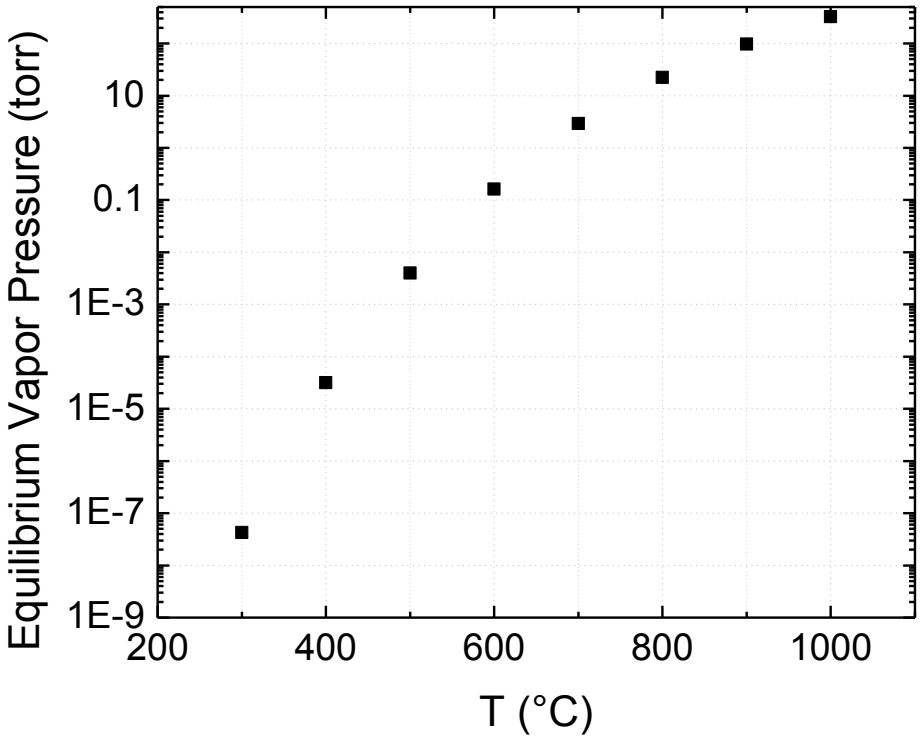

Figure 3-38. Calculated equilibrium vapor pressure, in torr, for $CoCl_2$. Growth level fluxes are expected in the range 300 ℃ – 500 ℃.

In practice, growth level fluxes were achieved in the range of 800 ℃ – 1000 ℃, indicating some severe departure from ideality. An offset of 1 to 2 orders of magnitude between equilibrium vapor pressure and measured beam equivalent pressure is expected, however this offset is much larger at about 8 orders of magnitude. This discrepency in flux possibly indicates contamination, conversion, or depletion of the source material.

Initial growths of $LiCoO_2$ were attemtped despite the obvious flux discrepency due to time constraints. Growths were attmepted at high temperature, 950 ℃, for compatibility with the already established $LiNbO_2$ growth condition and at flux setpoints $\phi_{Li} \approx 3 \times 10^{-7}$ torr BEP – 9×10^{-7} torr BEP and $\phi_{CoCl2} \approx 3 \times 10^{-7}$ torr BEP – 1.4×10^{-6} torr BEP for a flux ratio range ϕ = 0.35 – 1.8. The oxygen flow was held constant at 4 SCCM for all growths. An x-ray diffractogram of the ϕ = 0.35 film is shown in Figure 3-39. The main peak observed is at 2θ = 18.7° with a relatively wide rocking curve FWHM of 3.8 degrees.

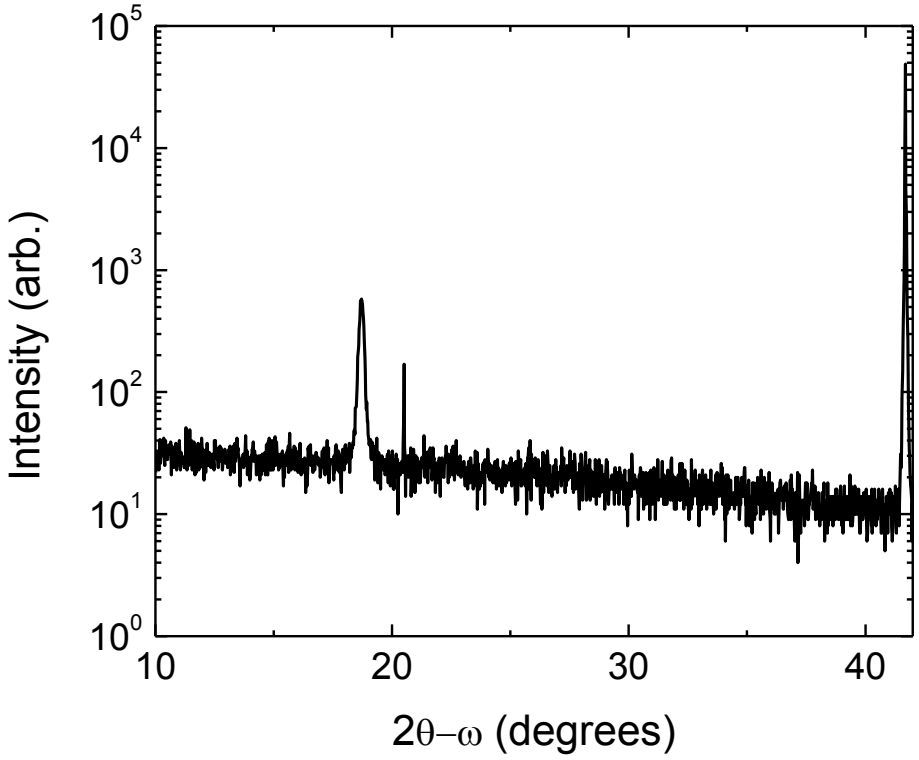

Figure 3-39. X-ray diffractogram of an attempted $LiCoO_2$ growth where flux ratio ϕ = 0.35 at T_{sub} = 950 ℃ and 4 SCCM O_2. The reflection shown is 2θ = 18.7°.

The high-temperature (HT) rhombohedral $LiCoO_2$ phase primary (003) reflection bulk value is $2\theta = 19.153$. If the grown film is indeed $LiCoO_2$ then the strain level is ~2.4%, however the corresponding (006) reflection at $2\theta = 36.89$ is not observed. The theoretical intensity relation of (003) to (006) for HT-$LiCoO_2$ is $I_{006}/I_{003} = 0.06$ indicating the reflection, if observed, would barely rise above the noise floor. Another option, if growth was severely lithium limited, is cubic Co_3O_4 with a (111) reflection at $2\theta = 19.00°$ (~1.6% strain). Once again the half-reflection (222) is not present and the intensity relation $I_{222}/I_{111} = 0.47$ suggests this phase is unlikely. XRD peaks at this d-spacing are occasionally observed in other growths that do not contain $CoCl_2$ and are typically associated with a partial surface conversion of Al_2O_3 to α-$LiAlO_2$ (003) which has a reflection at $2\theta = 18.68°$. When observed in other growths this peak often has a wide rocking curve, similar to that observed here. Therefore to isolate the effects of lithium based surface conversion, another film was grown with only Li flux. This Li-only growth did not result in any observable XRD signature, indicating the $CoCl_2$ or O_2 flux is playing a role in the growing film.

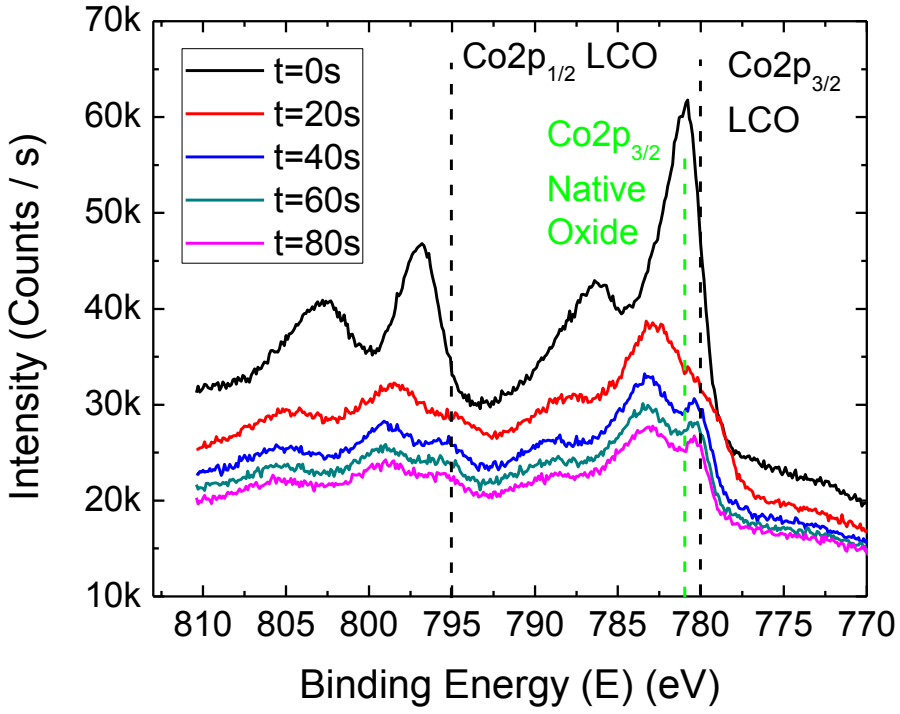

Figure 3-40. XPS spectra of the Co 2p transition showing that Co is present in the film. The surface scan shows a Co 2p binding energy consistent with the native surface oxide, and the satellite peak at 786 eV is consistent with Co^{2+}. Depth profiling with Ar reveals a mix of Co^{2+} and Co^{3+} which has a satellite peak at 790 eV. The overall intensity of the cobalt is qualitatively low, suggesting the film primarily consists of other elemental constituents. LCO – $LiCoO_2$.

XPS was performed to gain further chemical information on the $\phi = 0.35$ film, mainly to determine if Co is present, and if so to determine bond information and concentration. The XPS spectra of the Co 2p transitions are shown in Figure 3-40. Cobalt in $LiCoO_2$ exists in the +3 valence with a primary $2p_{1/2}$ peak at 780 eV[171]. Co^{2+} has a primary $2p_{1/2}$ peak at 780.3 eV which is difficult to separate from Co^{3+}, but the two oxidation states

show easily separable satellite peaks at 790 eV (9% relative intensity) for the Co^{2+} state and 786 eV (33% relative intensity) for the Co^{3+} state[171]. Based on these peak identifications, the spectra in Figure 3-40 show a surface of oxidized cobalt consistent with a Co^{2+} native oxide. Depth profiling reveals what is most likely a mix of Co^{2+} and Co^{3+}, although the preferential sputtering of oxygen makes the analysis inconclusive. Finally, the count rate reveals a low overall concentration of cobalt which reduces upon depth profiling. This trend is shown by normalized peak area of the observed primary constituents versus sputter time in Figure 3-41. Cobalt is present in single percent concentrations and the film primarily consists of aluminum and oxygen. The sputter rate can be approximated at 1 nm/s ± 0.5 nm/s for the 3 keV Ar sputter beam, giving a maximum sputtered depth of ≈ 90 nm. Profilometer measurements indicate that the film is 268 nm ± 66 nm thick, indicating the etch pit has not yet reached the Al_2O_3 substrate. This result indicates that the film may be α-$LiAlO_2$. The XPS, XRD, and profilometer results do not give a complete understanding of the grown film complicating the completion of this experiment. Clearly more experiments outside the scope of the proposed work are required, in both growth and characterization, to develop an MBE based $LiCoO_2$ growth condition. This condition is a necessary step for the full characterization of the proposed $Li(Nb,Co)O_2$ alloy.

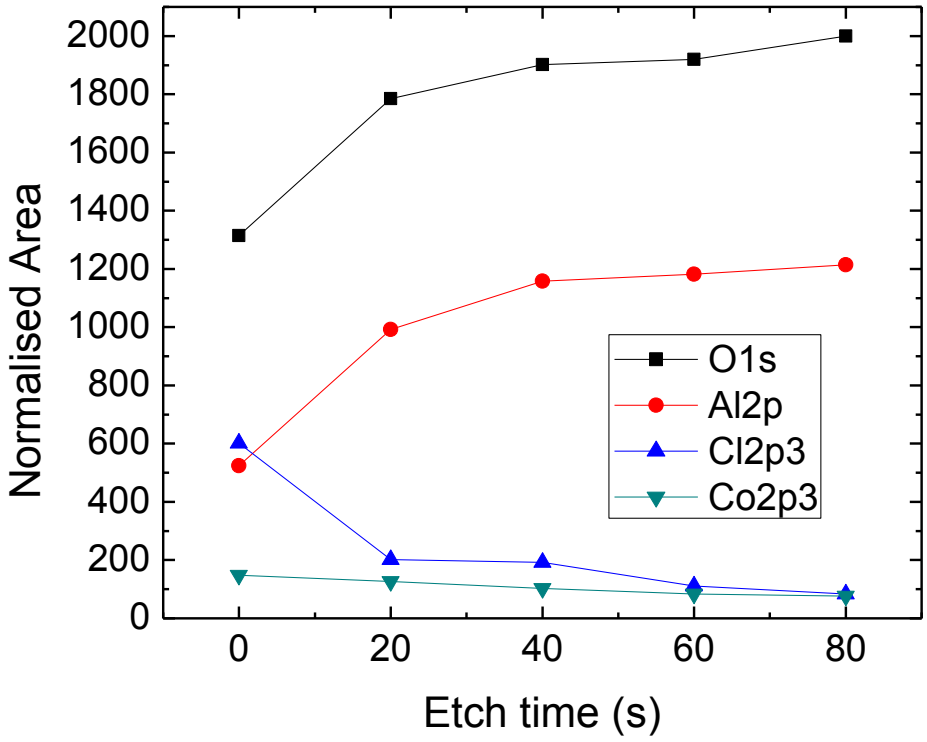

Figure 3-41. XPS determined elemental composition plotted as normalized peak area versus etch time. Cobalt is a small fraction of the total film which primarily consists of aluminum and oxygen.

CHAPTER 4. LITHIUM NIOBITE STRUCTURES AND DEVICES

4.1 Non-Volatile $LiNbO_2$ Memristors

Memristors are considered a key enabling technology for neuromorphic computing due to their applications as synaptic analogues and signal propagation elements. Current memristor technology focuses on binary state resistive switches which succeed in basic synaptic weighting processes[6–10], but often provide no pathway for more intricate biological mechanisms such as short and long term potentiation (STP and LTP) effects and spike-timing dependent plasticity (STDP) which are analog processes linked to basic brain functions such as learning and memory, although some technologies are beginning to take these processes into account[11–14]. These processes occur on biological timescales from milliseconds to minutes in the case of STP and multiple minutes or longer for LTP[34].

$LiNbO_2$ is a natively volatile analog memristor. It can take on a continuum of resistance states based on input voltage, but will relax to its original state upon bias removal. This volatile behavior, seen in devices with Li-blocking electrodes, is useful for STP and STDP but is not able to implement LTP. It has been theorized and experimentally confirmed that using a lithium-alloying contact will induce non-volatile behavior in $LiNbO_2$ memristors[56], however the effect was not well studied and no physical

mechanism was shown. These devices were also fabricated from sputtered (101) oriented material, meaning the 2-dimensional plane of Li is not parallel to the current path in the device potentially limiting the number of li atoms available for reaction with the contact. While an Al contact was used in previous experiments on sputtered material, there are many candidate metals for a Li alloying contact based on electrochemical potential, solubility limits, and alloy phases. These materials include but not are not limited to Al, Mg, Sn, Pb, Ag, Au, Pt, Cd, Cr, and Zn[172]. This chapter focuses on testing the effects of both alloying and non-alloying metals on $LiNbO_2$ memristors in multiple geometric configurations. The goal of this study is to characterize a range of device response time scales for the implementation of synaptic learning rules such as STP, LTP, and STDP.

4.1.1 Fabrication and Testing

Following growth and characterization MBE grown $LiNbO_2$ thin films were fabricated

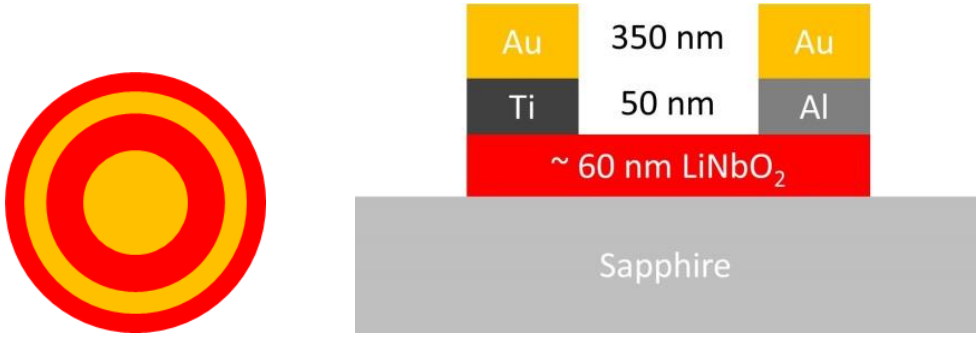

Figure 4-1. Non-volatile $LiNbO_2$ memristor device structure seen from above (left) and in cross-section (right). The outer ring and inner dot correspond to the Ti/Au and Al/Au contacts, respectively. Volatile memristors use Ti/Au for both contacts. The current convention is a positive bias on the outer ring electrode.

into isolated annular ring-dot structures shown in Figure 4-1 by etching, photolithography, and liftoff. A mesa etch was first performed using dual-layer photoresist S-1813 and LOR-5B as a positive etch mask. After a hard bake at 155 ℃ the sample was dipped in 1:1:1 HF:HNO_3:H_2O to etch the field and isolate the devices, preventing the in-diffusion of lithium. This allows devices to operate with a finite supply of lithium enabling resistance modification of the $LiNbO_2$ bulk as discussed further in CHAPTER 5. After stripping the photoresist mask, the ring and dot contacts are formed by negative profile photolithography, metallization, and liftoff. To create a volatile memristor, a single liftoff step may be used with a lithium blocking electrode using image reversal photoresist and electron beam evaporation. To create a non-volatile memristor the ring and dot contacts are formed in two separate steps by the same liftoff process. The inner contact uses an interface metal which is known to be lithium alloying, while the outer contact interface metal is non-alloying titanium[172]. Both contacts have 50 nm of interface metal topped with 350 nm of gold as a probing layer. Devices were then probed and electrical characterization was performed with a Keithley 2410 source meter and 34401A digital multimeter.

4.1.2 Results

Non-volatile memristors were probed by a series of pulses at multiple bias points, durations, and duty cycles following characterization by 100 mV *I-V* sweeps according to the current convention in Figure 4-2. 100 mV signals were used as “sense” or “read”

signals between pulses, and to set up a baseline before pulse application. Figure 4-2 shows the application of a 1 V, 10 ms long pulse at a duty cycle of 10% for a pulse frequency of 1 Hz. Following continuous sense signals the resistance of the device changes upon application of the first pulse and continues to change incrementally following each subsequent pulse until saturating around 30 pulses with a resistance change $\Delta R/R$ of ~300%.

It was also observed that the application of negative pulses results in a decrease in resistance as shown in Figure 4-3. Subsequently larger bias pulses are applied to the device to achieve increasing resistances, which are followed by negative pulses resulting

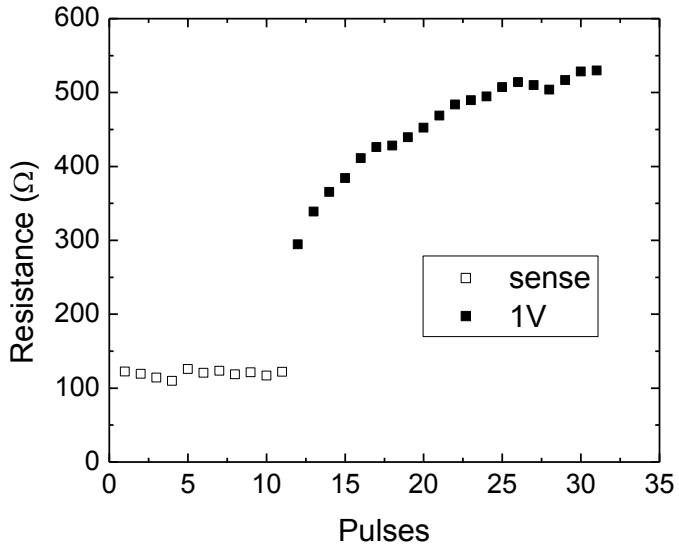

Figure 4-2. Non-volatile $LiNbO_2$ memristor with dot diameter of 45 µm and gap spacing of 35 µm showing incremental pulse response and state retention as a function of 10 ms long pulses at 1 V and a duty cycle of 10 %, saturating after ~30 pulses at $\Delta R/R \simeq 300$ %.

in decreasing resistances. These trends correspond to both potentiation and depression in the biological synapse.

It was observed that the magnitude of the resistance change was dependent on a variety of factors including pulse frequency, duration, and potential, as well as geometric factors, primarily inner dot radius. Table 4-1 lists the maximum and stable figures of merit for devices of varying inner dot radius. The maximum ΔR/R figure of merit is achieved by biasing a device beyond a stable state as an irreversible process, while stable ΔR/R is defined as the largest value for which stable operation was observed. As will be outlined

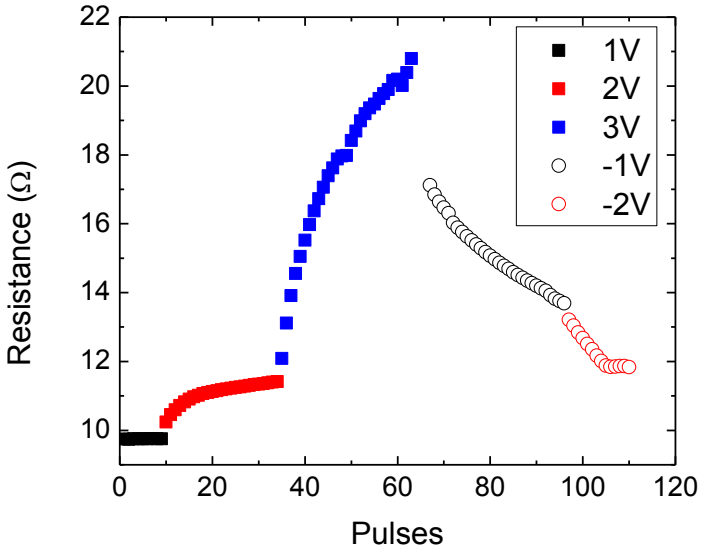

Figure 4-3. Measured resistance of a large dot device (dot diameter = 300 µm, gap spacing = 35 µm) as a function of 10 ms long pulses of various potential at a duty cycle of 10 %. Consecutive positive pulses increase resistance, and increasing the potential increases the rate of resistance change. Negative pulses show the opposite effect by decreasing the resistance as a function of pulse number and potential.

in the next section, device variation as a function of gap spacing was very small and therefore not tabulated.

The measured non-volatile devices appear to have a threshold for steady-state non-volatile behavior. Figure 4-4 shows a device with a 90 μm inner dot diameter and 60 μm electrode spacing that exhibits steady-state LTP. After 20 1 V pulses with 1 s duration and a 10 % duty cycle the device is measured for approximately 40 minutes showing no relaxation in resistance state. Following this steady state "read" cycle, -0.9 V and -1.5 V pulses were applied in the same timing scheme, bringing the device resistance back to a low state ($R \approx 175\ \Omega$) similar to the starting value. A similar device (90 μm dot, 200 μm gap) was tested with a sub-threshold number of pulses in the same scheme, ten 1.5 V pulses. Contrary to the 20 pulse case, a slow decay is observed when monitoring the device resistance with a small signal. Biologically, LTP occurs on a timescale of minutes to hours exhibiting a slow decay sometimes referred to as an Ebbinghaus forgetting curve[29,34,173]. This sub-threshold pulsing scheme appears to behave in precisely the same manner, as shown in Figure 4-5 with a decay time of ~ 10 minutes.

Table 4-1. Maximum achieved and stable figures of merit (ΔR/R) for increasing inner contact radius at a constant gap spacing of 35 μm.

L (μm)	Max ΔR/R	Stable ΔR/R
45	1898 %	500 %
75	1587 %	485 %
150	400 %	113 %
250	175 %	50 %

$LiNbO_2$ memristors show a variety of decay times which span from hundreds of milliseconds to steady state, as shown in Figure 4-4 and Figure 4-5. Non-volatile memristor responses are shown as a function of pulse number (10 ms duration at 10 % duty cycle) and show either long term decay or steady state based on an inferred pulse/bias threshold. Figure 4-5 (bottom) shows a volatile memristor with non-alloying Ti/Au contacts exhibiting volatile decay with a time constant of approximately 300 ms. These three decay times span the full gamut of relaxation shown by biological synapses from STP relaxations which range from tens of milliseconds to multiple seconds[25] to LTP which decays on the timescales of minutes to hours or longer[26] and steady-state behavior.

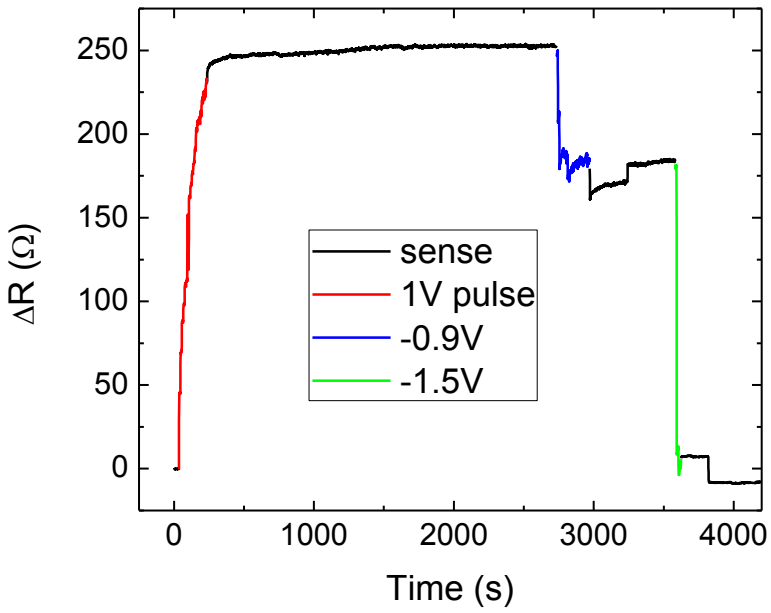

Figure 4-4. Resistance change versus time as a function of opposite polarity biasing. This device (90 µm dot diameter, 60 µm gap) shows quasi-steady state LTP following 20 1 V pulses (red). After ~2500 seconds at a stable resistance state, negative bias pulses of -0.9 V and -1.5 V are used to return the device to a low resistance state comparable to the original state.

This result illustrates that $LiNbO_2$ memristors can form a basis for biologically realistic synapses performing multiple synaptic learning rules at various time scales, and is enabled through specific design of device geometry and electrode composition.

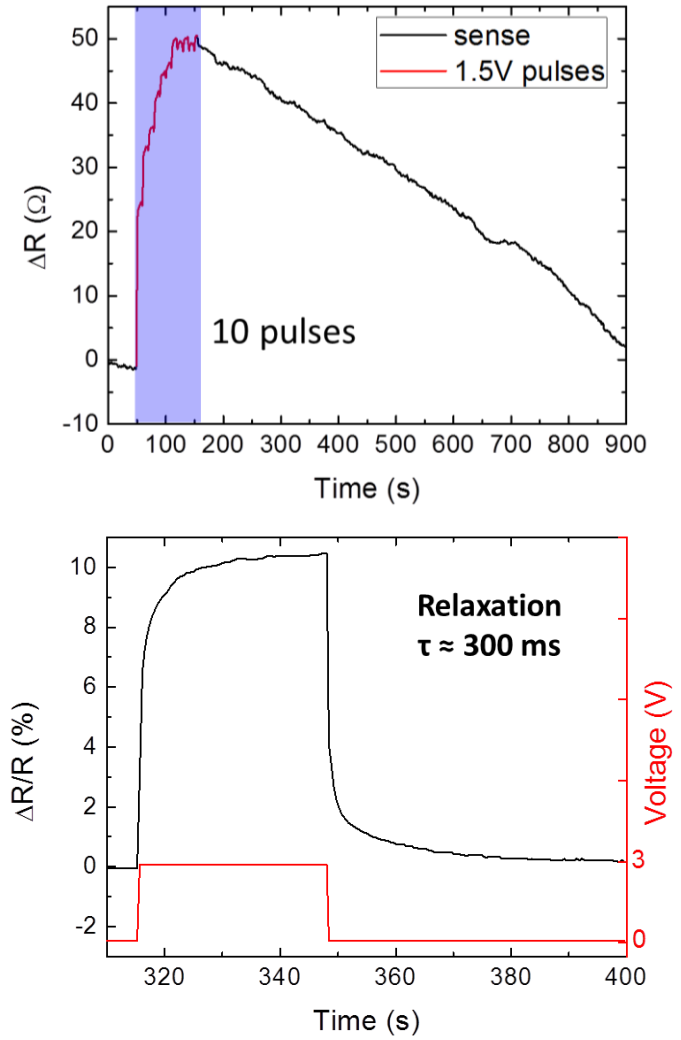

Figure 4-5. Top - LTP decay observed in $LiNbO_2$ non-volatile memristors. Non-volatile devices show pseudo-stable states with decay on the order of 0.06 percent/second (90 µm dot diameter, 200 µm gap). Bottom - Memristive behavior in a volatile $LiNbO_2$ device with Ti/Au contacts. The resistance increases in a saturating manner as a DC bias is applied, and relaxes back once the bias is removed. The relaxation occurs at a time constant of ~300ms, similar to the STP time constants observed in biological systems.

4.1.3 Device Cycleability

The first generation of non-volatile $LiNbO_2$ memristors based on MBE grown material, while promising in their ability to emulate LTP across a wide range of time scales, show poor response after multiple cycles. This behavior is similar to the cycleability issues observed in early Li-ion batteries. The effect of multiple cycles is shown in Figure 4-6, showing an initially large resistance change for a 3 V pulse, a return to the original value for a -2 V pulse, followed by a decreased capacity to change resistance for ± 2 V and no

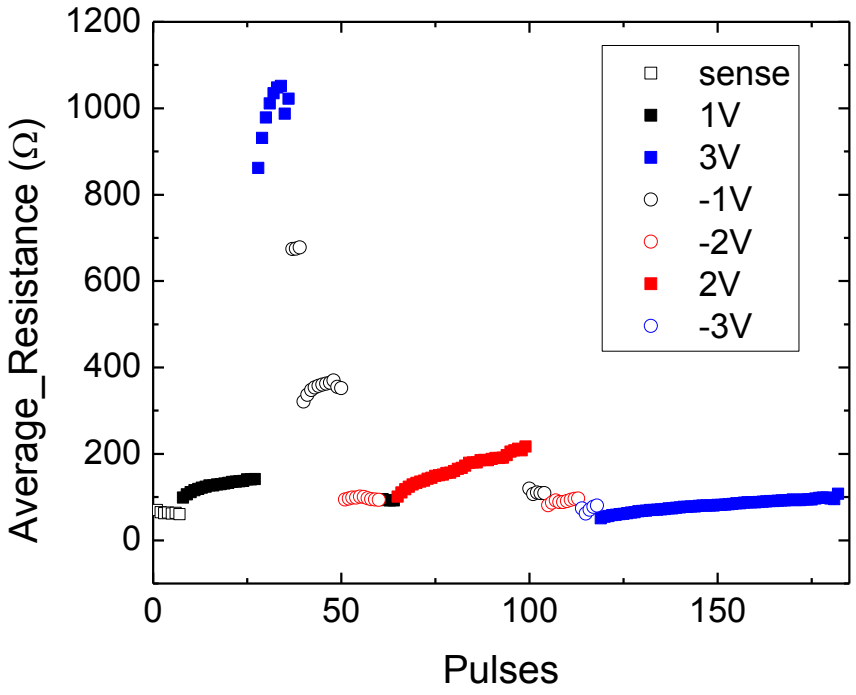

Figure 4-6. Device failure after cycling. At the first +3 V cycle, the device (dot radius 150 µm, electrode gap 35 µm) resistance jumps by approximately 900%, and is returned to the original resistance state with -2 V pulses. Subsequent 2 V pulses change the device at a lower magnitude, and the following set of 3 V pulses shows little resistance change.

appreciable resistance change following that cycle.

To evaluate the role of aluminum versus other metals a second generation of devices was fabricated with multiple inner dot interface metals, all on the same sample, with a Ti blocking and adhesion between the interface metal and the Au probing layer. The metals tested were Sn, Ag, Al, and Cr, with Ti as the non-alloying outer ring interface metal. The adhesion of Sn to $LiNbO_2$ was poor, and no devices were testable. The adhesion of

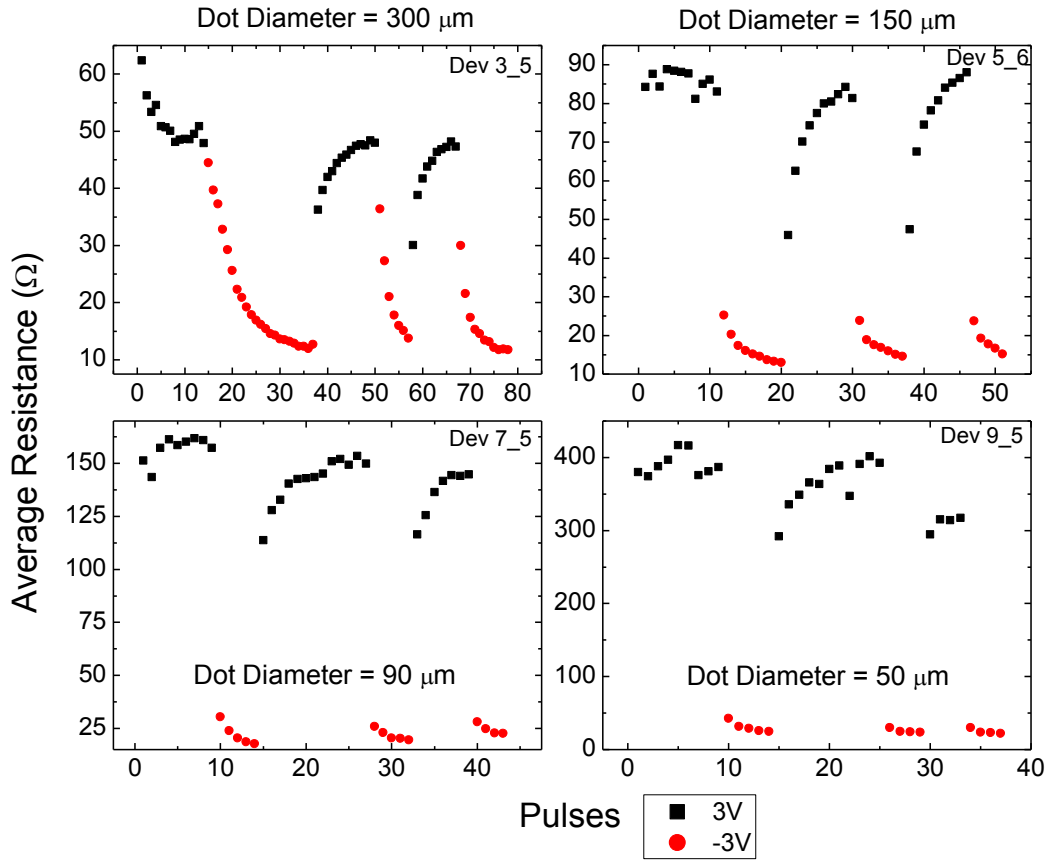

Figure 4-7. Resistance response of devices with Ag/Ti/Au center contacts. All devices have the same electrode gap spacing (35 μm) and different inner dot diameters (300, 150, 90, and 50 μm). For ± 3V signals devices show repeatable switching and an increased ΔR for decreasing dot diameter.

Cr was sufficient; however resistance cycling below ± 5 V was insignificant in magnitude, non-repeatable, and inconsistent. At ± 5 V the resistance change was minimal although the response was repeatable and non-volatile.

Devices with Ag also had poor adhesion, but a few devices were testable. Figure 4-7 shows the switching profile at ± 3 V for devices with a 35 μm gap and inner dot diameters of 300, 150, 90, and 50 μm. The cycleability of the Ag electrode devices is improved in comparison to the first generation Al based devices, showing multiple iterations of cycling to high and low resistance states through incremental intermediate

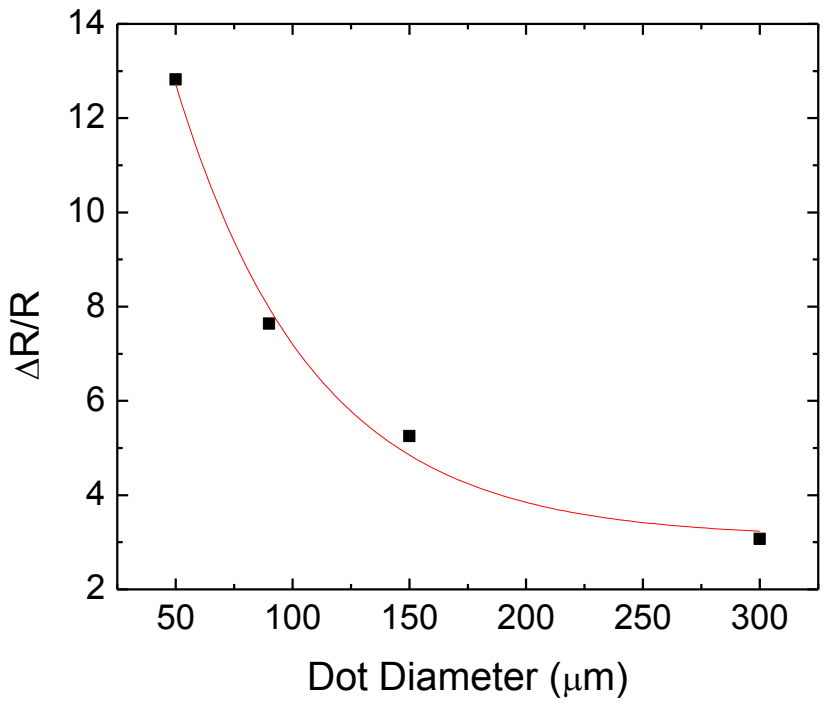

Figure 4-8. Figure of merit ΔR/R versus inner dot diameter for the Ag based devices in Figure 4-7. The included fit, to guide the eye, shows that ΔR/R increases exponentially as the inner dot diameter decreases for constant electrode spacing.

states. Repeated cycling for these devices was not observed for pulses at ± 0.5 V, ± 1 V, and ± 2 V, suggesting an energy barrier corresponding to the physical phenomenon responsible for state modification. The energy barrier could be electrochemical, electromechanical, or purely electrical and is elaborated in the discussion section.

The resistance change in Figure 4-7 is plotted vs. device dot diameter in Figure 4-8, with an included fit to an exponential decay following the form in Equation 5.

$$\frac{\Delta R}{R} = FOM_0 e^{-\frac{d}{d_0}} + FOM_\infty \quad (5)$$

FOM_∞ is the value of ΔR/R at d = infinity, d is the dot diameter, and $FOM_0 + FOM_\infty$ is the y-intercept representing the maximum value for an infinitely small device. For the fit in Figure 4-8 ($R^2 = 0.983$) $FOM_0 = 22.5 \pm 3.7$, $d_0 = 58.7$ μm ± 11.8 μm, and $FOM_\infty = 3.1 \pm 0.6$, putting the maximum scaled unitless figure of merit at 25.6 ± 4.2 for the given device set. This result is important, indicating that as devices are scaled down as required for massively interconnected systems, the device performance as measured by the figure of merit improves.

The above results are for devices with a 35 μm electrode gap and varying center dot diameter. By holding the gap constant the experiment is sensitive to the periphery-to-area ratio of the devices. Taking into account the extremely low resistivity of $LiNbO_2$, $\rho \approx 4 \times 10^{-4}$ Ω-cm, the bulk resistance component may be considered approximately constant, indicating the trend in Figure 4-8 is representative of the interfacial resistance

contribution. Also considering the inactive nature of the Ti contact as shown in previous generation volatile devices, demonstrated in Figure 4-11, and described in *Dey* et. al.[172], the trend in Figure 4-8 is most likely representative of a resistance change at the $LiNbO_2$/Ag interface.

4.1.4 Discussion

In general, a larger negative bias pulse compared to the corresponding positive bias pulse is required to observe an approximately equal resistance change. There are at least two possible explanations for this phenomenon, and they are not mutually exclusive. First, one must consider the device geometry. For concentric ring-dots the electric field is not equal at both electrodes. There will always be a local field of greater magnitude at the dot contact due to the confining geometry, as can be seen through solutions to the Poisson equation in radial symmetry discussed in Figure 4-9 and Section 4.1.5. To consider the role of device scalability on the figure of merit as shown in Figure 4-8 one must also consider the role of confining geometry for current crowding. With the concentric ring-dot structure used in this work, electric field confinement increases for decreasing dot diameter while holding the electrode gap constant. The solution to the Poisson equation in radial symmetry is shown in Figure 4-9 as computed by COMSOL Multiphysics modelling suite for geometries matching the devices shown in Figure 4-7. For this model a relative permittivity $\epsilon_r = 1$ is selected for $LiNbO_2$ due to the reported and observed semi-metallic conductivity. Setting boundary conditions of +3 V at the ring contact and

ground at the dot contact results in the solutions shown, demonstrating the increasing non-uniformity of the field distribution for decreasing dot diameter while holding the gap constant. An identical magnitude profile is observed by reversing the boundary conditions. The implications of this geometry are as follows: (1) for both positive and negative bias the active device area closest to the outer ring contact will experience a smaller local electric field than the center dot contact, and (2) decreasing dot diameter will further concentrate the electric field leading to lower operating voltages for smaller devices. It should be noted, however, that to take advantage of the concentric ring-dot geometry on an integrated circuit requires via contacts for all devices, and so it is possible that a different confining geometry will be more useful in future device generations.

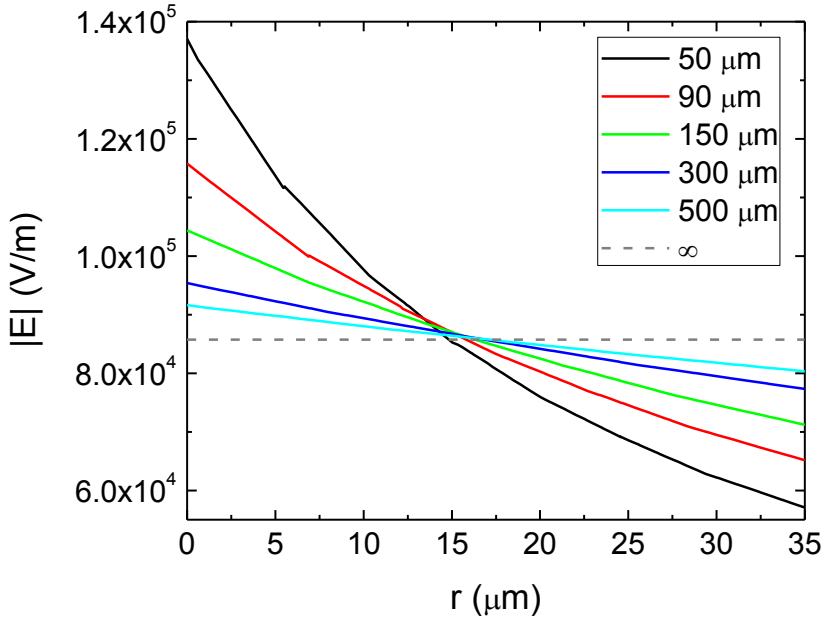

Figure 4-9. Modeled electric field magnitude as a function of length radially outward from the center contact in a concentric ring-dot structure. 3V is applied at the ring contact and the inner dot contact is grounded. r = 0 μm is the edge of the inner dot contact, and r = 35 μm is the edge of the ring contact. For a constant electrode gap of 35 μm, the electric field is increasingly non-uniform for decreasing dot diameters. For this model ϵ_r = 1 for $LiNbO_2$ due to its semi-metallic resistivity, even though it is considered a semiconductor.

It has been shown that the maximum effect on volatile $LiNbO_2$ memristors is achieved around 10x geometric confinement[174], however some inputs to this model were based on known $LiCoO_2$ parameters and the actual optimal confinement may be higher. No such confinement limit exists when considering purely electric-field driven events as modeled here; the optimal concentration is due to ion diffusion which counteracts drift.

The second consideration is the asymmetric contact metal scheme, where both the electrochemical potential and lithium alloying must be considered. For electrochemical reactions, one must consider the relevant half-cell reactions below.

$$Li^{+} + e^{-} \leftrightharpoons Li \qquad -3.04\ V \qquad (6)$$

$$Al^{3+} + 3e^{-} \leftrightharpoons Al \qquad -1.66\ V \qquad (7)$$

$$Ti^{2+} + 2e^{-} \leftrightharpoons Ti \qquad -1.63\ V \qquad (8)$$

$$Ti^{3+} + 3e^{-} \leftrightharpoons Ti \qquad -1.37\ V \qquad (9)$$

The possible electrochemical cell reactions are listed below in the direction giving the most positive cell potential (most favorable) with the cell potential listed.

$$Al^{3+} + 3Li \rightarrow 3Li^{+} + Al \qquad 1.38\ V \qquad (10)$$

$$Ti^{2+} + 2Li \rightarrow 2Li^{+} + Ti \qquad 1.41\ V \qquad (11)$$

$$Ti^{3+} + 3Li \rightarrow 3Li^{+} + Ti \qquad 1.67\ V \qquad (12)$$

These cell potentials indicate that a slightly higher potential is required to drive the electrochemical reaction of lithium and titanium should such an alloy exist. This small potential energy difference is insignificant compared to the above geometric effects which more likely explain the requirement of a higher negative bias to drive an equal resistance change in the device. It is therefore relevant to examine not only the electrochemical cell potentials but also phase diagrams of potentially formed alloys between the relevant materials. These phase diagrams are shown in Figure 4-10 and Figure 4-11[175].

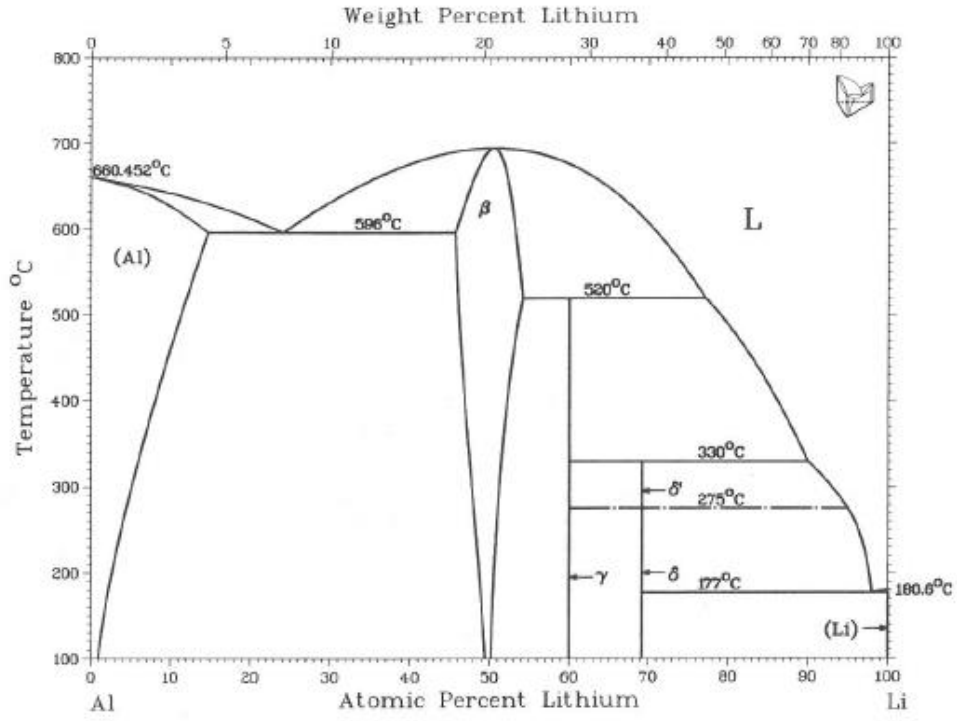

Figure 4-10. Al-Li binary phase diagram. Many phases exist along an isotherm, with a solid solubility of lithium in aluminum of ~ 1% at 100 °C[175].

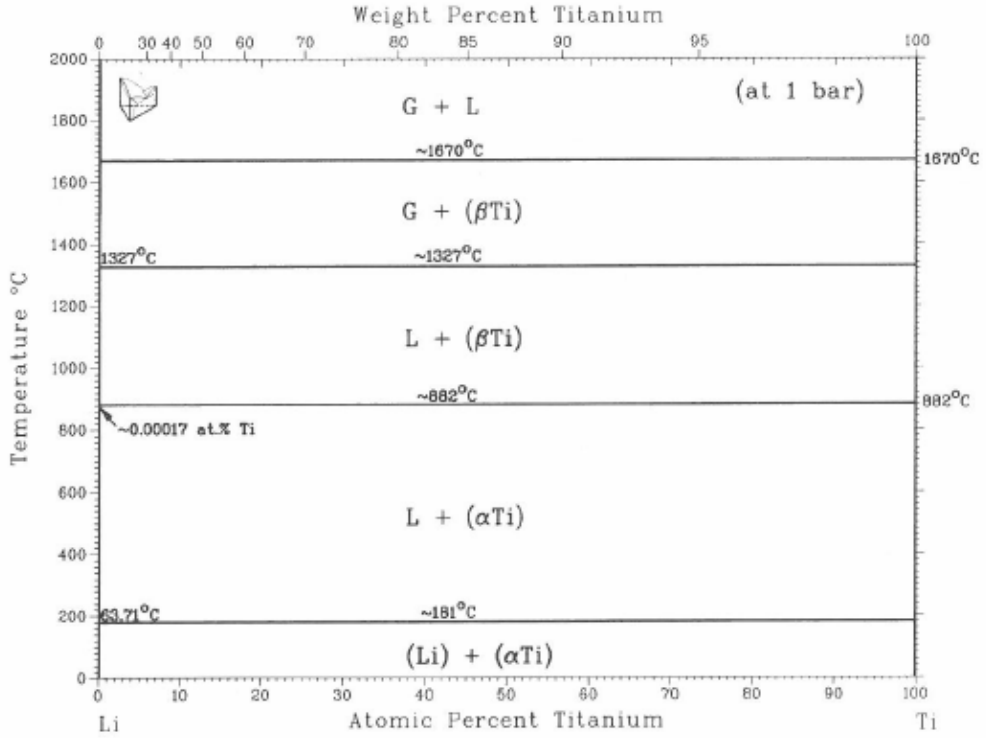

Figure 4-11. Li-Ti binary phase diagram. Titanium does not form any alloys with lithium along an isobar. The only device relevant phase change occurs at 181 °C[175].

Notably, aluminum shows many alloy phases along an isotherm, while titanium does not show any alloying. In contrast with the purely electrochemical understanding shown above, the phase diagram confirms the non-alloying nature of lithium with titanium as reported in *Dey et. al*[172]. These mechanisms, electrochemical reactions and binary alloying, point to comparisons with Li-ion battery technology. $LiNbO_2$ is very similar to the common battery cathode material $LiCoO_2$. Battery cathodes and anodes often are degraded on the first cycle by irreversible reactions, where lithium forms an alloy instead of intercalating or reversibly reacting, decreasing the overall capacity and cell potential[166].

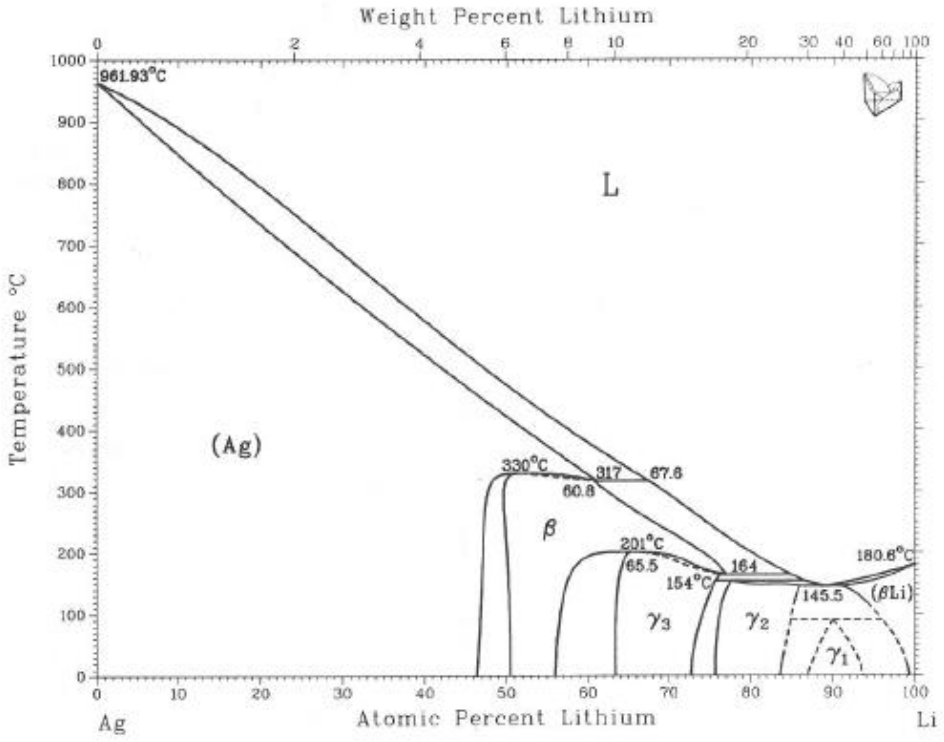

Figure 4-12. Ag-Li binary phase diagram. The solid solubility of Li in Ag is approximately 46.5 atomic % at room temperature[175].

It is therefore likely that the device degradation in the first generation Al devices is due to irreversible reactions at the $LiNbO_2$/Al interface, where a lithium-aluminum alloy increases the contact resistance. Increased cycleability, when compared to first generation Al-contact devices, was observed in the second generation devices with Ag/Ti/Au contacts. The binary phase diagram for Ag-Li is shown in Figure 4-12. In contrast to aluminum, silver can support a significant concentration of lithium without forming an alloy. The solid solubility of Li in Ag is ~45.6 atomic percent at room temperature,

indicating that it may be possible to cycle Ag based $LiNbO_2$ devices without forming potentially detrimental alloys.

In order to investigate the alloying of Li into the contacts, secondary ion mass spectrometry (SIMS) was performed on the first generation Al based devices. SIMS is a destructive mass spectrometry technique which analyzes secondary ions ejected by controlled sputtering. In this work the technique used is time-of-flight resolved SIMS, which in ideal conditions provides highly accurate spatial resolution as fine as 300 nm with a depth resolution of approximately 2 nm. The sensitivity to trace elements is in the range of parts-per-million, equivalent to a concentration of ~10^{15} cm^{-3} – 10^{16} cm^{-3}. Measurements were performed in burst mode with a liquid metal Bi source to increase

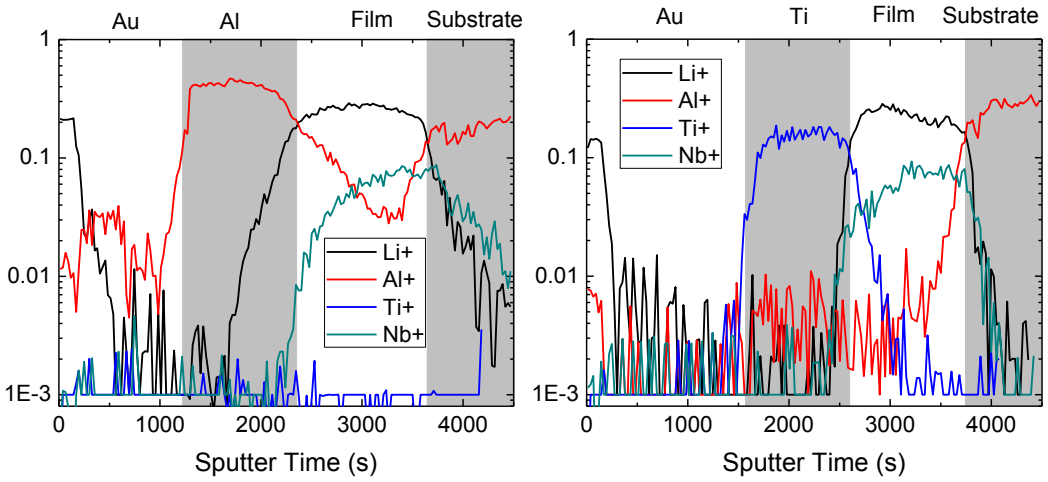

Figure 4-13. SIMS depth profiles of the center dot contact (left) and outer ring contact (right) for a device cycled to failure. In the dot, the Li signal precedes the Nb signal moving from the Al layer to the film, but in the ring contact the Li and Nb signals appear at the same depth. Al diffusion into the $LiNbO_2$ film is also observed.

the lateral resolution while sputtering with O_2 to increase the yield of positive ions. Depth profile analysis was performed on both ring and dot contacts, looking at both native devices and devices cycled to failure Figure 4-6. Depth profiling occurs in an interlaced manner where an O_2 sputter beam (2 kV acceleration energy) rasters across the etch pit removing a layer of material, after which the yield of secondary ions removed by the Bi liquid metal ion gun (LMIG) is analyzed corresponding to the newly exposed surface.

SIMS is an incredibly powerful technique, but care must be taken in data analysis due to the qualitative nature of the raw data. First, the mass spectra must be calibrated. Calibration is performed in this work by aligning the data to known species of H^+, $^6Li^+$, Li^+, surface carbon as CH_3^+, Al^+, and Nb^+. When analyzing a SIMS depth profile there are also multiple considerations concerning sputter yield. Each element has a different sputter yield meaning that multiple layers will not sputter at the same rate. When considering a material of more than one element there will be preferential sputtering due to sputter yield differences. For instance in $LiNbO_2$ niobium will not sputter as quickly as oxygen, increasing the surface roughness, leading to broadened sampling depths and degraded depth resolution. Another sputter yield complication involves the so-called "matrix effect" where the bonding structure of a compound material affects the sputter yield of the atoms involved. In TOF-SIMS the vertical position of analyzed atoms is determined by sputtering. The effect of these non-idealities is to ascribe a planar character to a non-planar structure. Corrections must be applied to account for differences

in structure height and non-uniform sputtering, both due to sputter yield complications and non-uniform sputtering from instrument non-idealities.

To account for these complications, the ring contact and dot contact were sputtered simultaneously and analyzed individually. In this way the analysis avoids structures of differing heights and compositions. Because the upper layers of the contact are single element composition, the depth resolution is expected to remain close to ideal (< 10 nm) until either the $LiNbO_2$ layer or an alloyed contact layer is reached. As such, the onset of signals in the contact layers is abrupt while the onset of the substrate is widened due to the effects listed above.

Figure 4-13 shows SIMS depth profiles of both dot and ring contact for the device characterized in Figure 4-2, where Al is the interface metal for the center dot contact and Ti is the interface metal for the ring contact. Examining the Li profile for both cases at the metal-film interface it is apparent that the two contacts do not have the same distribution of lithium. For the Al center dot contact, the Li signal extends further into the Al metal than the Nb signal, while for the Ti outer ring contact the Li and Nb signals appear at approximately the same depth. This is indicative of Li intercalating into or alloying with the Al contact. Due to the single composition of the upper Au layer it is reasonable to expect the Li and Nb signals to appear at the same depth point in the case of no alloying. The profile of the dot contact also shows significant Al in the $LiNbO_2$ layer.

This could either be due to diffusion and alloying or pits in the $LiNbO_2$ film which were filled with Al during evaporation, and is convoluted by the effects of sputter yield.

The layers of this device are also presented graphically in Figure 4-14 as 30 μm thick cross sectional slices rendered from TOF-SIMS data. Due to limitations in the SIMS software, the $LiNbO_2$ layer is visualized as Li. Au is not shown due to the poor ion yield of Au in positive analysis mode, but can be interpreted as the dark area above the Al or Ti metal layers. The topmost Li layer represents surface contamination before the onset of sputtering. Finally, due to geometric error sources in the SIMS, the edges of the SIMS cross-sectional scatter plots are ignored and qualitative analysis focuses on data away from the edges.

Both the ring and dot contacts were reconstructed separately to visualize the layers of the device. This analysis shows that for the outer ring electrode with Au/Ti contacts the layers are clearly defined with abrupt interfaces confirming the Li-blocking nature of the Ti contact. In contrast, the layers in the central dot electrode with Au/Al contacts do not show well defined layers or interfaces, confirming its lithium alloying nature. The Li signal extends well beyond the Nb signal thickness into the Al contact layer. This interface mixing layer is indicated with a white arrow. The Al contact from a similar device that had not been electrically tested is shown for comparison in Figure 4-14 (bottom). The interface between the Al (blue) and Nb (green) is more uniform than the electrically switched device and the Li (red) signal is observed in conjunction with Nb.

Because the native device (not electrically stressed) shows a lower degree of lithium-aluminum inter-penetration than the electrically stressed device (cycled-to-failure), this measurement indicates that the lithium inter-diffusion/alloying is in part electrically driven.

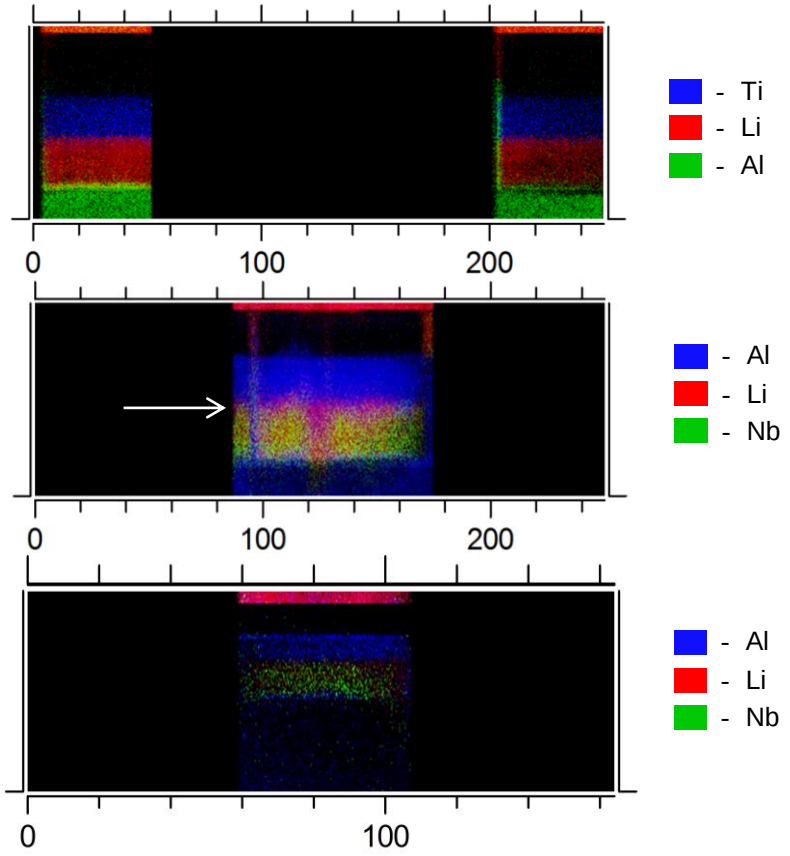

Figure 4-14. 30 µm wide cross-sectional slices of the Al based device showing the non-alloying Ti/Au (top) and alloying Al/Au (middle) contacts as measured by TOF-SIMS. There is a clearly defined transition between Ti and $LiNbO_2$ for the Ti contact with some Al visible in the $LiNbO_2$. For the Al contact there is a region of Li/Al intermixing, shown by the white arrow, between the Al and $LiNbO_2$ layers. Surface contamination of Li is also shown. In contrast, an as-deposited device (bottom) shows a more pristine interface indicating the alloying is at least partially electrically driven.

SIMS was also performed on linear non-volatile memristors which use Ag as the alloying contact. These devices, fabricated for ease of wire bonding and on-chip connections, consist of a $LiNbO_2$ mesa in a current crowding triangular shape with both alloying and non-alloying contacts. The contacts are large, 400 μm square, and only a portion of the contacts overlap the active device area to increase adhesion of the metal layer by directly contacting the sapphire substrate exposed during the mesa etch. The alloying contact consists of 50 nm Ag / 20 nm Ti / 350 nm Au, and the non-alloying contact is identical to the previous case consisting of 50 nm Ti / 350 nm Au. Details on the mask can be found in Appendix C.3 . The structure and electrical response of the linear non-volatile device with alloying Ag contacts is shown in Figure 4-15.

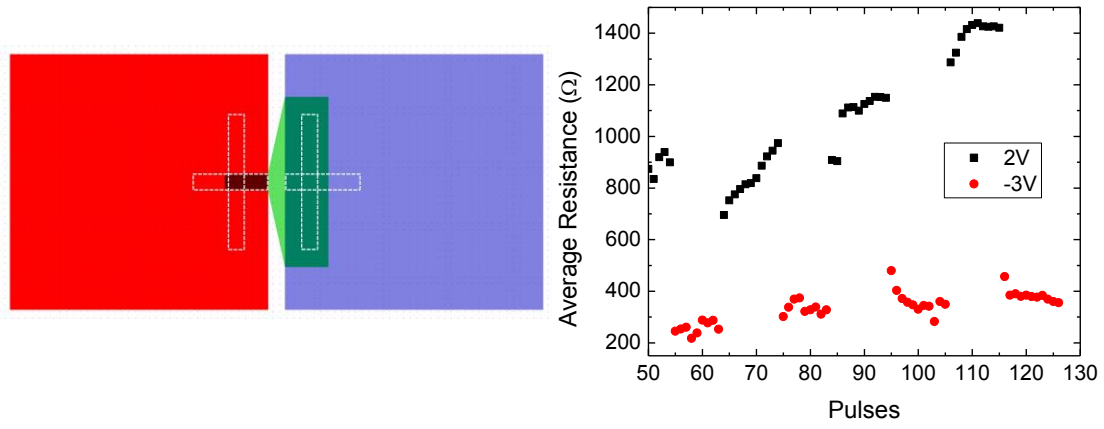

Figure 4-15. Device structure (left) and non-volatile pulse response (right) of a linear non-volatile memristor with a Ag/Ti/Au alloying contact. The electrical pulse response is more repeatable than the Al contact case, and the observed resistance change is ΔR/R ≈ 300%. The linear device consists of a $LiNbO_2$ mesa (green) using a current crowding geometry with both non-alloying Ti/Au (blue) and alloying (red) contacts. White dotted boxes represent the cross-sectional analysis areas shown in Figure 4-16.

Cross-sectional analysis was also performed on the linear non-volatile memristors to visualize atomic position and alloying. The cross-sectional renderings of TOF-SIMS data are shown in Figure 4-16. The slices shown are 6 μm thick to isolate the thin $LiNbO_2$ line element shown under the alloying contact in Figure 4-15. The alloying contact overlaying the narrow $LiNbO_2$ finger is shown on the bottom (X-Z) and left (Y-Z), and the non-alloying contact overlaying the wider section of the $LiNbO_2$ mesa is shown on the top (X-Z) and right (Y-Z). The secondary ion yield of Ag^+ is poor and so the signal is weak, however it is clear that for the alloying contact the Li layer extends all the way to the Ti blocking layer above the Ag layer. Identically to the previous ring-dot case, the non-alloying contact consists of sharp interfaces without inter-diffusion. The Y-Z scatterplot shows a non-ideality at approximately 100 μm which is likely a pit in the underlying $LiNbO_2$ created during wet etching.

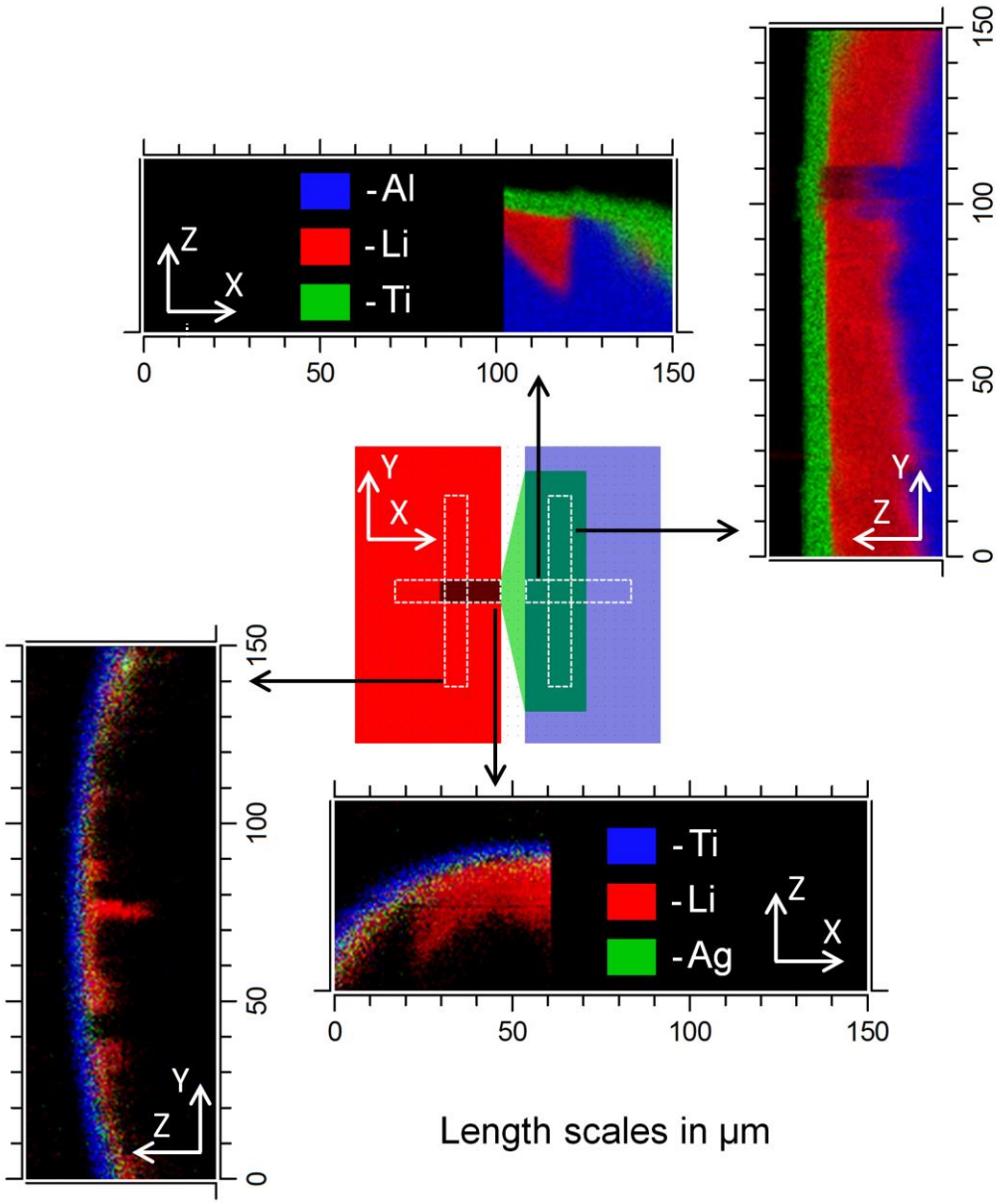

Figure 4-16. 6 µm wide X-Z and Y-Z slices obtained by TOF-SIMS of non-alloying Ti/Au (top and right) and alloying Ag/Ti/Au (bottom and left) contacts for a $LiNbO_2$ memristor. The device structure is shown in the center, indicating the location of each cross-sectional scatterplot with white dotted boxes. Top: green – Ti, red – Li, blue – Al. The Li in the $LiNbO_2$ layer is well bound. Bottom: green – Ag, red – Li, blue – Ti. Li extends fully into the Ag layer, and some Ag is observed in the Ti layer.

4.1.5 CTLM Model

Measuring highly conductive devices with resistivity values similar to titanium presents experimental challenges both in measurement and analysis. In order to separate the effects of bulk and contact resistance, a model was developed based on the circular transfer length measurement (CTLM) method. The transfer length, L_T, is defined as the average distance under the contact for which 1/e (63.2%) of the current is transferred from the semiconductor into the metal. CTLM is commonly used to analyze contacts by determining the transfer length from total resistance data as a function of gap spacing d as determined by:

$$R_T = \frac{R_{SH}}{2\pi r_0}(d + 2L_T)C \tag{13}$$

where R_T is the measured resistance, r_0 is the inner contact radius, and C is a geometric correction factor[176]. This equation is derived assuming the following:

1) $L \gg 3L_T$, the inner contact diameter is much greater than three times the transfer length[177],
2) The semiconductor sheet resistance is equivalent under the contacts and in the field, i.e. there is no alloying with the contact [176,178], and
3) The contact metals are identical.

When assumption 1 is not met Equation 13 is not a sufficient representation and the expression becomes[178]

$$R_T = \frac{R_{SH}}{2\pi}\left[\frac{\mathrm{L_T}}{r_0}\frac{I_0\left(\frac{r_0}{L_T}\right)}{I_1\left(\frac{r_0}{L_T}\right)} + \frac{L_T}{r}\frac{K_0\left(\frac{r_0}{L_T}\right)}{K_1\left(\frac{r_0}{L_T}\right)} + \ln\left(1+\frac{d}{r_0}\right)\right] \quad (14)$$

where r is the inner radius of the outer ring contact r_0 + d. When assumption 2 is not met the function becomes more complicated, and when assumption 3 is not met both contacts must be treated separately. In the current work it is likely all 3 assumptions are not met and so a separate formulation is necessary to accurately assess the data.

Starting from a transmission line model, the radial contact element transmission line equation is:

$$\frac{d^2V}{dx^2} + \frac{1}{x}\frac{dV}{dx} - \alpha^2 V = 0 \quad (15)$$

where $\alpha = \sqrt{\frac{R_S}{\rho_C}} = L_T^{-1}$, $\mathrm{R_S}$ denotes a generic sheet resistance, and ρ_C is the specific contact resistivity [179]. This is a modified form of the Bessel differential equation, satisfied by:

$$(x) = aI_0\left(\frac{x}{L_T}\right) + bK_0\left(\frac{x}{L_T}\right) \quad (16)$$

where I_n and K_n are the modified Bessel functions of the first and second kind, respectively. Following from the derivation for a single contact metallization scheme by Reeves[179], expressions can be derived for the inner contact R_1, semiconductor region R_{semi}, and outer contact R_2 of the device:

$$R_1 = \frac{R_{SC,1}L_{T,1}}{2\pi r_0}\frac{I_0\left(\frac{r_0}{L_{T,1}}\right)}{I_1\left(\frac{r_0}{L_{T,1}}\right)} \tag{17}$$

$$R_{semi} = \frac{R_{SH}}{2\pi}\ln\left(\frac{r}{r_0}\right) \tag{18}$$

$$R_2 = \frac{R_{SC,2}L_{T,2}}{2\pi r}\frac{A(r',r)}{B(r,r')} \tag{19}$$

$$R_T = R_1 + R_{semi} + R_2 \tag{20}$$

where $R_{SC,1}$ is the sheet resistance under the inner contact, $L_{T,1}$ is the inverse transfer length of the inner contact, $R_{SC,2}$ is the sheet resistance under the outer contact, $L_{T,2}$ is the transfer length of the outer contact, and r' is the outer radius of the outer ring contact, r plus the width of the outer contact which is a constant 50 μm in this experiment. A and B are complex Bessel function arguments given by Equations 21 and 22[179].

$$A(r',r) = I_1\left(\frac{r}{L_{T,2}}\right)K_0\left(\frac{r'}{L_{T,2}}\right) + I_0\left(\frac{r'}{L_{T,2}}\right)K_1\left(\frac{r}{L_{T,2}}\right) \tag{21}$$

$$B(r,r') = I_1\left(\frac{r}{L_{T,2}}\right)K_1\left(\frac{r'}{L_{T,2}}\right) - I_1\left(\frac{r'}{L_{T,2}}\right)K_1\left(\frac{r}{L_{T,2}}\right) \tag{22}$$

Resistance data for $LiNbO_2$ with Ti/Au inner and outer contacts is well fit by assuming large transfer lengths and no alloying of the contact with the semiconductor using Equation 14. A Monte Carlo simulation gives a sheet resistance of 55.5 Ω/□ ± 5.9 Ω/□ and a transfer length of 29.0 μm ± 5.6 um with R^2 = 0.996. The Al based device in this

work is assumed to have contact alloying at the center contact and must be fit by Equations 17-20. For large transfer lengths or sheet resistances under the contact Equation 20 shows a weak linear dependence of R_T on d but with unacceptably large L_T and R_{sc} errors resulting from the linear extrapolation of a near zero slope function. Conversely, for large transfer lengths or sheet resistances under the contact Equation 20 shows a non-linear dependence of R_T on r_0. The resulting non-linear fit where r_0 is the independent variable gives acceptably small errors for L_T and R_{SC}. The data is therefore fit against r_0 to mitigate these errors. Figure 4-17 shows Equations 17 - 19 plotted versus r_0 along with small signal ($V \leq 500$ mV) experimental data with a fixed d = 35 μm. As described above a non-linear trend is observed and a significant percentage of the resistance is dominated by the inner dot contact resistance (R_1 - red). This trend is also seen in the experimental data. Given the field resistivity and the metal contact resistivity are comparable this result is not surprising. The analysis demonstrates that for large contact resistances and/or large transfer lengths at the center contact, R_1 will dominate the total resistance R_T.

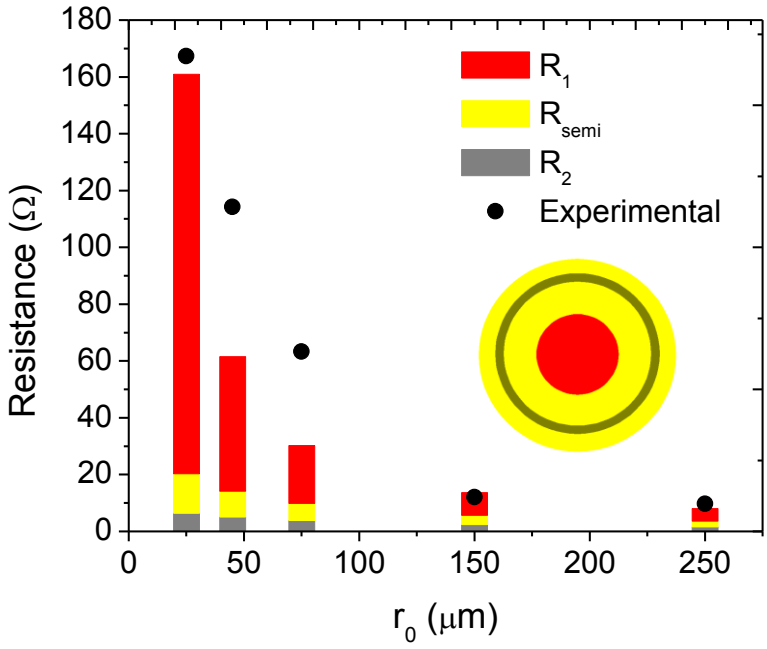

Figure 4-17. Modeled resistance components (Equations 17-19) from the outer ring contact interface (grey dots), semiconductor field (yellow dots), and inner dot contact interface (red dots) as a function of inner dot radius r_0. Gap spacing is held constant at 35 μm. Experimental data is shown in black. The inner contact interface dominates the resistance profile in contrast to traditional devices where gap spacing controls the resistance profile.

Separation of the contact resistance and transfer length from each resistive component in Equation 20 was also attempted. Fitting of this data to extract sheet resistance and transfer length is complicated by the number of parameters. The specific contact resistivity of a volatile Ti/Au contact on $LiNbO_2$ is known, on the order of 4.7×10^{-4} Ω-cm^2, from the single contact metal experiment allowing limits to be placed on R_{SH}, $L_{T,2}$, and $R_{SC,2}$. This leaves $L_{T,1}$ and $R_{SC,2}$ as fitting parameters. These parameters were fit to Equation 17 by Monte Carlo simulation and to a 4th order expansion of the equation by graphing and analysis software. For d = 35 μm the data is best fit by $R_{SC,1}$ = 163 Ω / □ ±

48 Ω / □ and L_T = 76 μm ± 23 μm with a coefficient of determination R^2 = 0.98 giving a specific contact resistivity for the Al/Au contact of 9.4×10^{-3} Ω-cm^2, 20 times larger than that of the Ti/Au contact. While the fit is good with a coefficient of determination near unity, the transfer length is greater than the inner contact radius of the smallest device representing current crowding at the interface. It is likely that non-zero metal resistances and an electrochemically formed interface layer are necessary additions to accurately model the devices[180,181]. Despite these non-idealities the above model may still be used to understand these devices noting that the transfer length is large and the sheet resistance is much larger than that of the $LiNbO_2$ in the field.

Changes to transfer length and sheet resistance were also investigated as a function of pulse history. It was originally assumed the device would become more conductive if Li was extracted from the bulk semiconductor into the contact by positive pulses; the resistance drop occurring due to additional lithium vacancy hole donors. As reported previously in this chapter, positive pulses increased the resistance of the device. Devices were pulsed to resistance saturation in the following order: 1 V, 2 V, 3 V, -1 V, -2 V, and -3 V. Following the application of positive pulses the total resistance increased. When the fit was attempted the coefficient of determination for the fit deteriorated to 0.28, indicating the model no longer describes the device. Upon the application of negative pulses the coefficient of determination returned to 0.95 indicating that the changes cannot be quantified but are at least partially reversible.

The development of a non-volatile memristor that can implement LTP is a major step toward functional neuromorphic circuitry. The unexplained opposite resistance programming behavior, however, indicates additional exploration is necessary. The effects of interfacial reactions, possible metal resistivity changes and other yet unknown effects resulting in resistance increases must be tested to complete the picture.

This model, understood alongside electrochemical potentials, binary phase alloys, and the SIMS data corroborates a resistance change dominated by lithium alloying into the aluminum contact itself, modifying the interface/contact resistance. It also suggests that resistance modification of the $LiNbO_2$ layer does not play a significant role in these non-volatile memristors. This understanding will enable further engineering and research to develop reliable and repeatable non-volatile devices for neuromorphic computing.

4.2 $LiNbO_2$ Batteries

Historically, $LiNbO_2$ batteries were first tested using a powdered polycrystalline cathode, prepared by the heated reaction of powders, with a lithium metal anode and liquid electrolyte ($LiClO_4$ dissolved in propylene carbonate). These batteries charged to an initial V_{OC} = 2.95 V, subsequently charging to V_{OC} = 2.5 V upon further charge cycles, and capacity was not reported[75]. Recently $LiNbO_2$ batteries have been reported with a high reversible capacity of ~ 190 mAh/g at a rate of 0.25C[47]. The lithium niobite was formed by electrochemical methods from molten salts, similar to the methods shown by *Moshopoulou et. al.*[81] and *Greenlee et. al* [46]. The battery cathodes in the above referenced

work were fabricated by ball-milling and mixing with acetylene black and a binder and then submerged in a $LiPF_6$ solute liquid electrolyte and measured against metallic lithium.

$LiNbO_2$ cathode batteries have been previously demonstrated on sputtered (101) oriented lithium niobite using a solid electrolyte for the first time. These batteries, which use a sputtered LiPON electrolyte and a nickel anode, did not show the theoretical maximum capacity expected for $LiNbO_2$ batteries (200 mAh/g), nor did they match the open circuit voltage of batteries based on powdered cathode material (V_{OC} = 2.4 V – 2.8 V)[56]. MBE based batteries with higher quality cathode material could solve this open-circuit voltage problem using the same electrolyte and metal anode structure. One possible complication is how the basal plane orientation of MBE grown $LiNbO_2$ will affect device performance due to the planar 2-dimensional nature of the Li layers. To understand these effects, a LiPON battery was fabricated on MBE grown $LiNbO_2$.

4.2.1 Fabrication and Structure

The device fabrication and structure is based on work using sputtered $LiNbO_2$ as a battery cathode[56]. After MBE growth of the 90 nm thick cathode, a 1 μm thick LiPON electrolyte was deposited through a 5 mm × 5 mm shadow mask by reactive sputtering from a Li_3PO_4 target with N_2 and Ar as the sputtering gases. The cathode contact was defined by shadowing a portion of the $LiNbO_2$ during LiPON deposition. Following the electrolyte deposition the device was immediately placed in an e-beam evaporator, using the same

shadow mask that defined the LiPON deposition area, to minimize reaction of the LiPON with water vapor in the air. The nickel anode and cathode contacts are then evaporated, completing the device which is shown in cross section in Figure 4-18. Nickel and aluminium were considered as candidate anode metals. In previous studies of nickel and aluminium anodes on LiPON/$LiNbO_2$ (both sputtered) the aluminium anode devices could not cycle repeatedly, whereas the nickel anode devices could be repeatedly cycled. Nickel was therefore used both as an anode and as a current spreading contact to the $LiNbO_2$ cathode due to its lithium blocking properties[172]. Nickel battery anodes do not uptake lithium ions during charging. The lithium ions electroplate on the nickel interface[182] in contrast with aluminium which is a lithium absorbing metal forming various alloys[172,183].

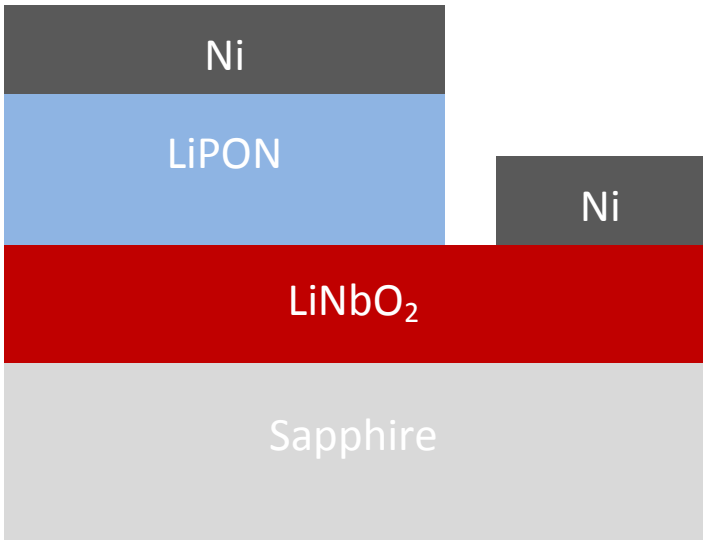

Figure 4-18. Cross sectional diagram of a $LiNbO_2$/LiPON/Ni battery based on MBE grown $LiNbO_2$ with a lateral cathode contact.

4.2.2 Characterization

The $LiNbO_2$/LiPON/Ni battery was characterized by electrical cycling through forced current charging and discharging. The charge and discharge current is forced by a Keithley 220 Programmable Current Source and measured by a Keithley 84401A digital multimeter. A separate Keithley 84401A digital multimeter records the voltage across the device. The battery was charged at a constant current density of 4 $\mu A/cm^2$ (0.4C) until it reached 3V, to prevent overvoltage failure. After reaching 3 V, the polarity of the current source was changed to discharge the battery completely to 0.2 V. Discharging also occurred at 4 $\mu A/cm^2$. This process was repeated for 100 cycles to establish a steady state battery capacity. Capacity, for the batteries presented in this section, is defined as:

$$\text{Capacity} = C(V_{charge}) - C(V_{discharge}) \tag{23}$$

where C(x) is the specific energy capacity, measured in mAh/g, as a function of charge state, measured by the open circuit voltage V_{OC}. Capacity is therefore, as defined in Equation 23, the difference in capacity between the charged and discharged states. For this work we define V_{charge} = 2.9 V and $V_{discharge}$ = 0.65 V.

4.2.3 Results

The battery charged to 3 V over a specific energy capacity of ~45 mAh/g and a clear charging plateau was visible. While the specific energy capacity is only about 25 % of the

theoretical capacity of a $LiNbO_2$ cathode (200 mAh/g), it is an order of magnitude higher than the capacity shown in sputtered $LiNbO_2$ batteries with nickel anodes[56].

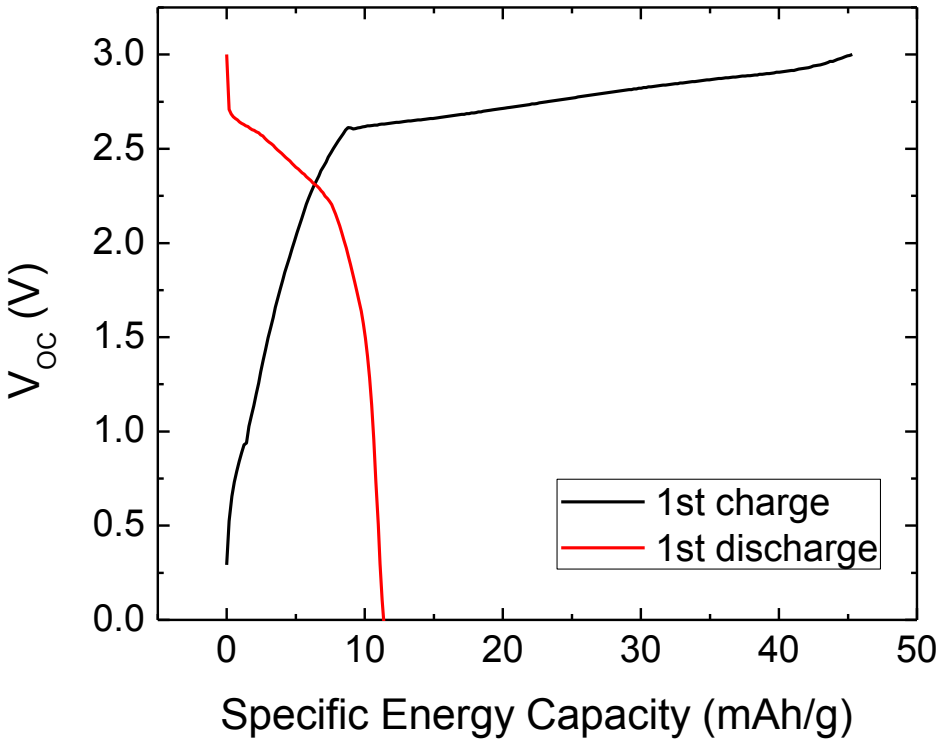

Figure 4-19. The first charge and discharge cycle of a $LiNbO_2$/LiPON/Ni battery using an MBE grown cathode. A 35 mAh/g charge plateau is clearly visible from 2.6 to 3 V, with a less pronounced 10 mAh/g discharge plateau from 2.71 to 2.2 V.

Upon reaching V_{OC} = 3 V current polarity is switched for discharging. A discharge plateau is observed, although it is less defined than the charging plateau, from V_{OC} = 2.0 V to V_{OC} = 2.7 V, similar to the electrochemical potential measured for bulk $LiNbO_2$

versus a lithium electrode of V_{OC} = 2.4 V – 2.8 V [75,184] and more ideal than measured for batteries using sputtered $LiNbO_2$ cathodes of V_{OC} = 1.5 V – 2.5 V.[56]

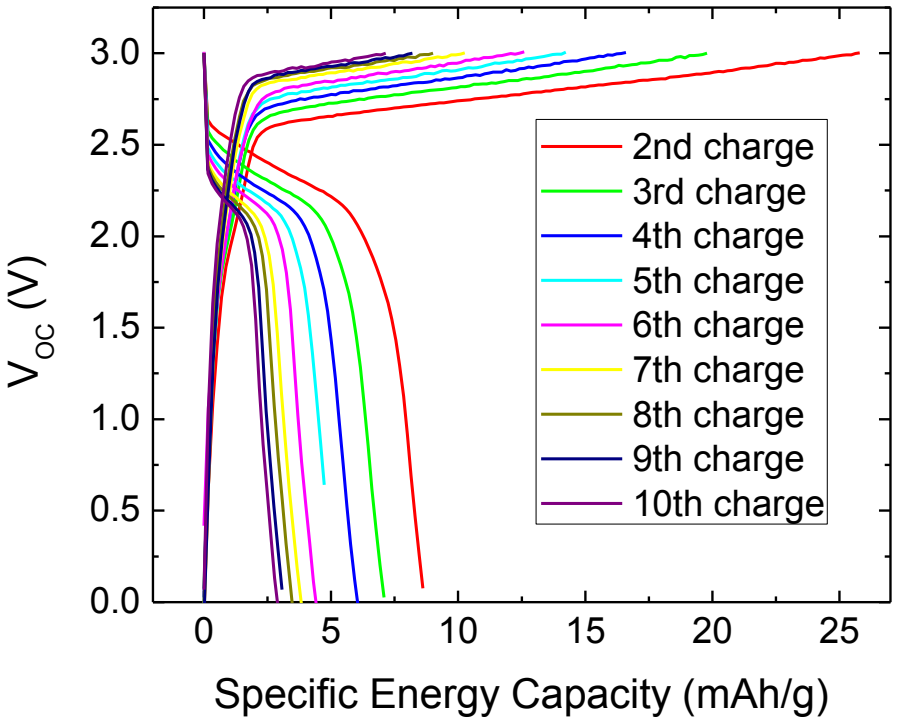

Figure 4-20. The 2nd through 10th charge and discharge cycles showing a decrease in capacity for each cycle.

Consecutive charge and discharge cycles show a rapid decrease in capacity as shown in Figure 4-20 for the 2nd through 10th cycle. This degradation is common in thin film batteries and is likely due to irreversible reactions at the nickel anode as is common in other Nickel anode batteries[182]. The device was cycled a total of 100 times to determine the steady state capacity which is shown in Figure 4-21. The saturated capacity value is

0.2 mAh/g, approximately 2 % of the original capacity. Similar batteries based on sputtered $LiNbO_2$ only degraded to 35 % of the original capacity over the same cycle period, indicating that this decrease in capacity can be localized to the cathode. It is possible that the loss in capacity is due to the crystalline orientation of the $LiNbO_2$ with respect to the electrolyte. The crystal structure of $LiNbO_2$ contains lithium in 2-dimensional planes, and the mobility of in-plane ion motion is higher than the mobility of out-of-plane ion motion[77].

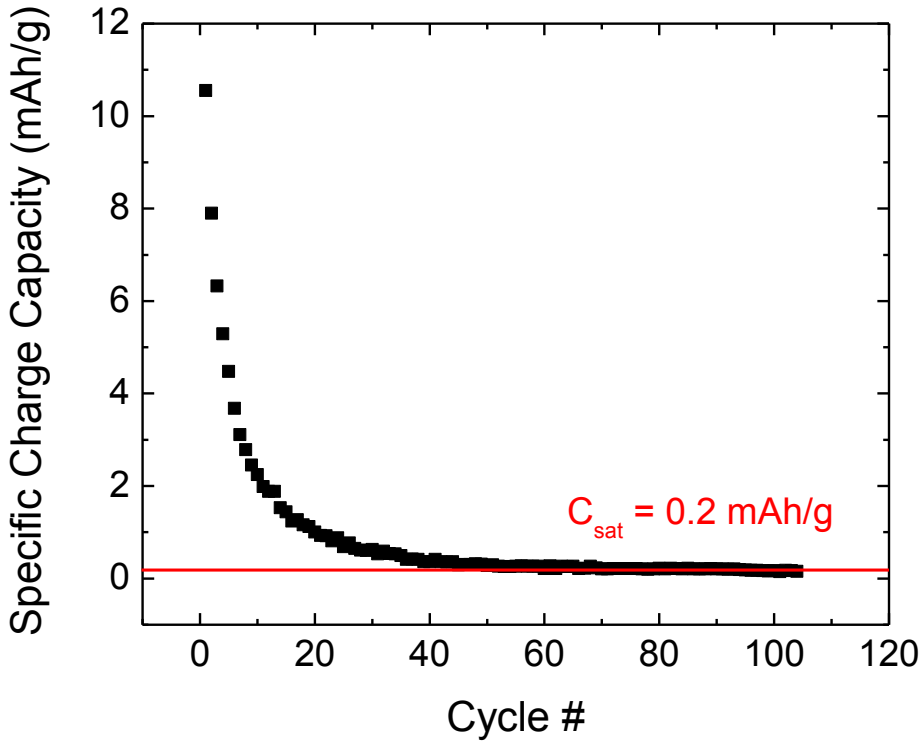

Figure 4-21. Specific charge capacity, as defined in Equation 23, for the first 100 discharge cycles. The capacity very quickly decays to a saturated value of ~0.2 mAh/g.

MBE grown $LiNbO_2$ is basal plane oriented (00l), and the lithium planes are parallel to the surface of the film. This means that for a vertical device, like the one measured in this work, lithium ions have to move in an energetically unfavorable direction to leave the $LiNbO_2$ cathode. It is also possible that the capacity is volumetrically limited, due to either the small volume cathode used or by a limited active volume within the cathode caused by the above mentioned parallel lithium planes. For this 90 nm thick $LiNbO_2$ cathode there are only ~ 6×10^{16} Li atoms total (2 atoms per unit cell, unit cell volume = 76.18 $Å^3$). Based on the theoretical capacity, the charging rate used here is 0.4C. The saturated capacity value of 0.2 mAh/g corresponds to a charge transfer of 5.8×10^{13} Li ions, or 0.01% of the total Li content. This either suggests that a small fraction of the Li is being removed from the cathode or that the electrolyte has degraded significantly. While complete delithiation of the cathode is not expected, the decreased capacity and charging time implies that only a small volume of the cathode is active, possibly just a few layers adjacent to the electrolyte.

Despite the low capacity observed these batteries, based on MBE grown $LiNbO_2$ cathodes, show promise for future research. The significant increase in initial capacity and operating voltage when compared to sputtered batteries of the same material illustrates the possibility for improvement. This is an engineering challenge which can be solved through processing and structure improvements. For neuromorphic computing applications it is desirable to have a leaky battery, and the current state of lithium niobite battery technology is likely sufficient for more complex neuromorphic circuits using

batteries like the one demonstrated here. Still, improvements in lithium niobite material quality and optimization of the battery structure could lead to exciting developments in traditional battery technology due to the low resistivity cathode and the potential for rapid charge and discharge.

4.3 $LiNbO_2$ – $LiNbO_3$ Heterostructures

The end benefit of a multifunctional material system such as the Li-Nb-O system is the variety of devices which can be obtained through the engineering of heterolayers. $LiNbO_3$ is a powerful component in many of these devices because it allows the incorporation of ferroelectric effects. One such device is a ferroelectric transistor, a transistor with a ferroelectric gate which requires no power to retain its current state[57]. A $LiNbO_2$/$LiNbO_3$ ferroelectric transistor could serve such a purpose with a high conductivity low-loss channel ($LiNbO_2$ $\sigma \approx 2500$ S/cm)[69]. A second use for such a structure is signal regeneration, i.e. gain, in a $LiNbO_2$ based neuromorphic system which, due to chemical compatibility concerns with silicon, could require a non-Si transistor for amplification. For these reasons, it is important to explore the feasibility and properties of a lithium niobite/lithium niobate heterojunction.

4.3.1 Experimental Details

The phase diagram in Figure 3-14 shows that the $LiNbO_2$ and $LiNbO_3$ growth windows are adjacent. It is therefore possible to switch the growth condition by modifying either

the flux ratio or the temperature. This provides a few possible schemes for growing the heterostructure.

(1) Set a constant flux and modify the grown phase by substrate temperature alone.

(2) Set a constant temperature and modify the grown phase by flux ratio alone.

(3) Modify both parameters to select phase.

Due to flux stability issues method 1 is useful; there will be no flux ramp period for single source cell growth but this method isn't compatible with superstructures or thin layers. Flux for these structures must be switched quickly because it cannot be accomplished with a second lithium cell and substrate temperature cannot be instantaneously switched. Method 2 is more appropriate for a 2 cell approach, however the temperature must be well calibrated as the window along an isotherm where both phases are possible is narrow. Method 3 allows access to the widest sections of each growth window, but requires switching both parameters. This is pictorially represented in Figure 4-22.

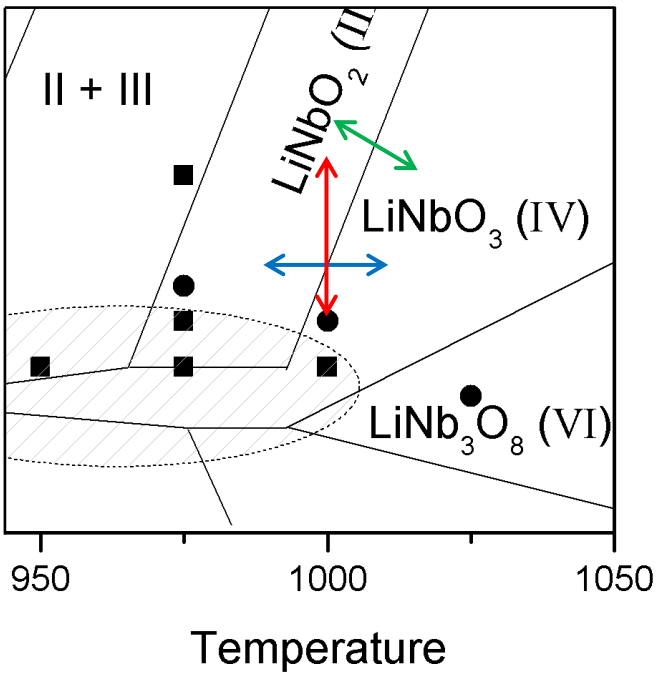

Figure 4-22. Enlarged view of the lithium niobium oxide phase space showing three schemes for phase selection in the $LiNbO_2$/$LiNbO_3$ heterostructure. Method 1 (red) - change flux ratio along an isotherm. Method 2 (blue) - constant flux ratio and change temperature. Method 3 (green) - change both variables to use the widest section of the growth window.

4.3.2 Results

Method 2 and method 3, as described above, were both used in attempts at $LiNbO_2$/$LiNbO_3$ heterostructure growths. Unfortunately, none of these growths were successful in producing a heterostructure which could be positively characterized. All films grown can only be identified as (006) $LiNbO_3$ by XRD, and C-V measurements do not show a buried conductive layer. The most likely cause of this undesired result is that the flux setpoints have drifted over the course of these growths which take much longer

than standard single layer growths. It has been previously observed that the Li flux can drift significantly over the course of a day, likely due to the constant-power control mode coupled with drifting temperatures in the building process chilled water. This constant-power control mode is required due to the lack of temperature feedback from the cell. Table 4-2 lists the attempted conditions for heterostructure growth, all targeting $LiNbO_2$ as the initial nucleation layer. A thin $LiNbO_2$ layer was targeted for half of the growths. This is a required feature to deplete the highly conductive $LiNbO_2$ channel layer in the desired $LiNbO_2/LiNbO_3$ transistor structure. A growth with thicker layers on the order of previously characterized films was also attempted. For all conditions, the substrate was vacuum annealed at 1050 ℃ for 10 minutes, followed by a 5-minute oxygen anneal at growth temperature and oxygen flux. Fluxes were allowed to stabilize for 30 minutes, under constant oxygen flux, between layers to avoid any grading of the junction. Other experiments were planned, but the growth campaign was terminated early due to equipment issues.

Table 4-2. Growth conditions for failed $LiNbO_2/LiNbO_3$ heterostructures.

Sample ID	Li flux target (BEP torr)	Li cell current (A)	$NbCl_5$ flux (BEP torr)	$NbCl_5$ bulk temperature (°C)	O_2 flow (SCCM)	Time (min)	Substrate Temperature (°C)
			$LiNbO_2$ Layer				
1345	2E-7	7.25	4E-7	45.8	4	7	1000
1346	5E-7	7.8	5E-7	46.5	4	15	950
1349	2E-7	7.15	4E-7	46.9	4	60	1000
1351	7E-7	8.15	7E-7	48.4	4	60	975
			$LiNbO_3$ Layer				
1345	1E-7	7	5E-7	45.8	5	35	1000
1346	2E-7	7.2	6E-7	46.5	5	60	1000
1349	1E-7	6.9	5E-7	47.2	5	60	1000
1351	2E-7	7.35	7E-7	48.4	5	60	1000

Future experiments aimed at a $LiNbO_2/LiNbO_3$ heterostructure will benefit greatly from increased flux control, particularly for the lithium cell. It is possible that the underlying $LiNbO_2$ layer was grown correctly, but was converted to $LiNbO_3$ during the 30 minute flux stabilization period which acts as an oxygen anneal. It is also possible that the thin $LiNbO_2$ layer cannot be characterized by the methods used and electron microscopy is required to confirm the presence of such a layer. It would also be beneficial to grow $LiNbO_3$ by the methods outlined in this dissertation on a conductive substrate in order to characterize its ferroelectric properties.

CHAPTER 5. CHEMICAL MODIFICATION OF LITHIUM CONTENT IN LITHIUM NIOBITE

Lithium niobite is a lithium intercalated suboxide, with lithium loosely bound in 2-dimensional planes between trigonal-prismatic oxygen-niobium complexes. As such, lithium may be intercalated (inserted) and deintercalated (removed) from the material which is more appropriately described as $Li_{1-x}NbO_2$ where $x \epsilon (0 \leq x \leq \sim 0.5)$. Lithium content can be modified by both chemical and electrochemical means, the same way that lithium ions are transported in Li-ion batteries.

Lithium content is related to the resistivity of $Li_{1-x}NbO_2$ through lithium vacancies which act as acceptors. Lithium niobite is, as grown, degenerately p-type doped by lithium vacancies on the order of 4×10^{21} holes/cm^3, or approximately 0.2 holes per molecule[185]. This makes lithium niobite one of the most conductive p-type oxides measured with a conductivity of approximately 2500 S/cm, on the same order as metallic titanium[69]. The resistivity trend with lithium content may be approximated by the following relationship between resistivity and carrier concentration.

$$\rho = \frac{1}{q(\mu_n n + \mu_p p)} \tag{24}$$

Considering that $p \gg n$, the donor concentration $N_A \approx p$, and the mole fraction of lithium vacancies $x \propto N_A$, the resistivity trend is $\rho \propto x^{-1}$ or $\rho \propto [Li]^{\alpha}$ where $\alpha > 1$. It is therefore

possible to exponentially increase or decrease the resistance of $Li_{1-x}NbO_2$ by a linear increase or decrease in lithium content. This trend is shown in Figure 5-1.

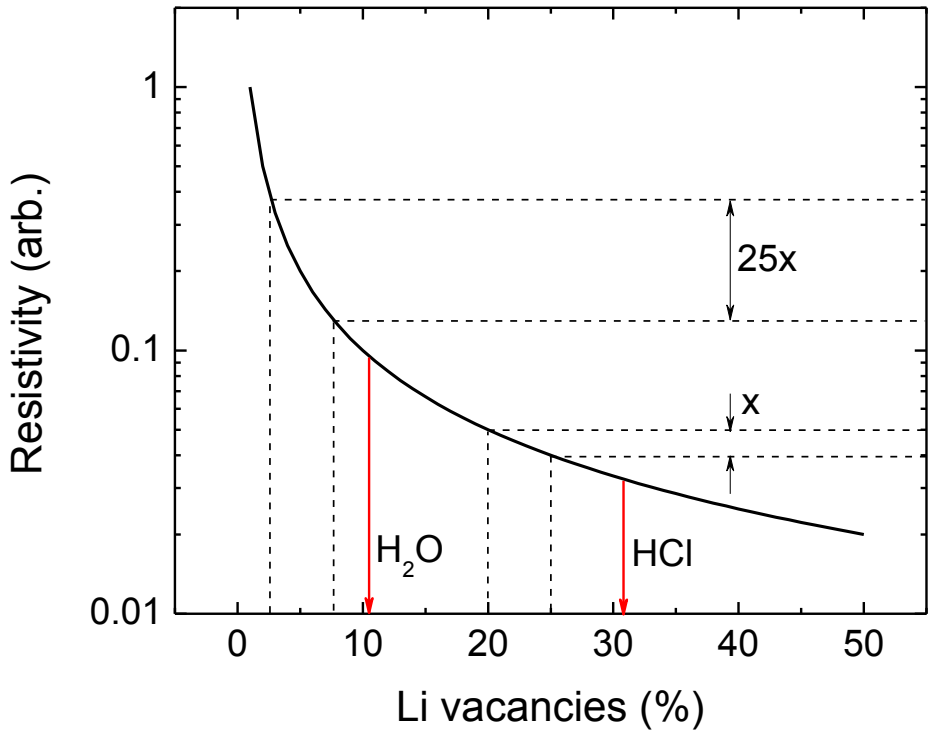

Figure 5-1. The relationship between lithium vacancies and resistivity in $Li_{1-x}NbO_2$ where x ∝ # Li vacancies. As the Li concentration approaches stoichiometry, the resistivity exponentially increases. A 5% change in Li vacancies produces a larger resistance change closer to stoichiometry, represented by dashed lines in the figure. Approximate delithiation values are shown for H_2O and HCl by red arrows.

The dashed lines in Figure 5-1 illustrate the main point, that an identical Li concentration change causes a larger resistance change when the concentration is closer to stoichiometry. In the figure a 5 % Li vacancy change is noted by dotted lines, from 2.5 -

7.5 % and from 20 % – 25 %. The range closer to lithium stoichiometry, 2.5 % – 7.5%, shows a 25x greater resistance change than the 20 % - 25% case. This indicates that device figure of merit (ΔR/R) and performance will increase for material closer to stoichiometry.

5.1 Chemical modification of lithium content

In order to study the effect of Li stoichiometry on various properties of lithium niobite it is often beneficial to modify the initial Li concentration in the material to be studied. Chemical delithiation has been performed by a variety of acids both in this work and in literature, some of which are shown in Table 5-1. Lithium niobite may also be chemically lithiated by submersion in a liquid with a sufficiently high concentration of free or loosely bound Li. The chemical typically used is n-butyllithium (n-BuLi), dissolved in cyclohexane or various other alkanes[186]. n-BuLi has been used by previous groups to

Table 5-1. Chemicals used to delithiate $Li_{1-x}NbO_2$ and approximate Li removal capacity, as given by *Kumada et. al.*[75] and *Moshopoulou et. al.*[81]

Chemical	~x in $Li_{1-x}NbO_2$
Bromine	~0.49
HBr	0.12
HCl*	~0.31
HNO_3	0.16
H_3PO_4	0.06
H_2SO_4	0.27
H_2O*	~0.11

* indicates chemicals used in this work

lithiate $Li_{1-x}NbO_2$ to $x \approx 0.04$[75]. Care must be taken when processing with n-BuLi due to its highly reactive behavior. Pure n-BuLi reacts with water vapor in the air to form LiOH and CO_2 to form lithium pentanoate ($C_4H_9CO_2Li$) and due to the exothermic nature of these reactions is pyrophoric. n-BuLi must therefore always be handled in solution and in an inert environment. Care must also be taken, when disposing of n-BuLi as a solvent, to heavily dilute with hexane as weakly diluted n-BuLi will react with other solvents to rapidly precipitate LiH as a white powder. After removal from the glove box, the heavily diluted n-BuLi is left in a fume-hood in ambient to form LiOH, and finally disposed of as a solvent.

5.2 Experiment and Discussion

To study the effects of chemical lithiation on MBE grown $LiNbO_2$, an as-grown sample was metallized with patterns for measuring the resistivity of the metal, semiconductor, and transfer length by the transmission line method (TLM). Changes to the crystalline structure were analyzed by XRD, and the optical properties of the material were tested by PL and optical switching response. The $LiNbO_2$ sample was submersed in n-BuLi for a total of 30 hours, pausing to measure various properties at 1, 3, 10, and 30 hours.

5.2.1 Structural characterization

Structural modifications to the $LiNbO_2$ crystal structure were analyzed by XRD symmetric scans which are sensitive to changes to the c-axis, which is normal to the basal

(00l) plane and film surface. Figure 5-2 shows the first and last diffraction scan of the $LiNbO_2$ (002) reflection with an inset enlarging the peak area. Clearly the peak has shifted to larger diffraction angle representing a compression of the lattice. This trend is consistent with previous literature, where the insertion of lithium acts to screen repulsive coulomb forces between neighboring oxygen layers[75].

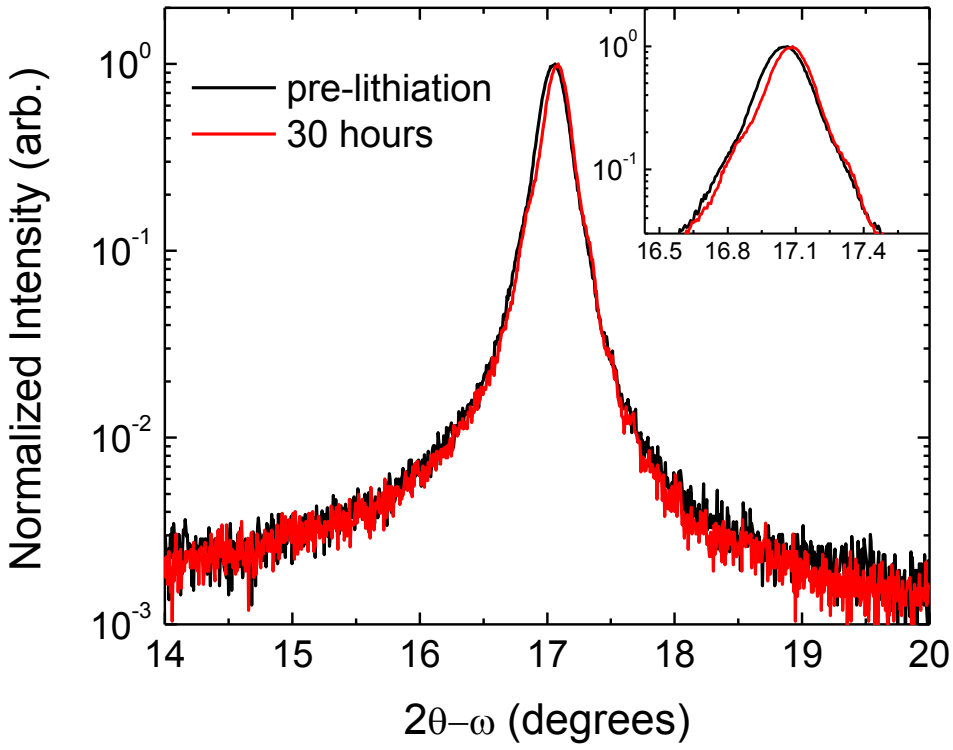

Figure 5-2. Normalized x-ray diffraction scans of the $LiNbO_2$ (002) reflection as grown (black) and after 30 hours submersion in n-BuLi (red). The shift in peak value is 0.0274 degrees 2θ, a 0.016 Å compression of the lattice normal to the surface.

The diffraction angle and c-spacing for each lithiation step are given in Figure 5-3 following a logarithmic trend as is expected for a diffusion-limited process. It is

noteworthy that the largest measured c-spacing is ~0.8 % smaller than reported in literature, 10.44 - 10.46 Å[71,75,76,81]. The XRD rocking curve FWHM values corresponding to these diffraction peaks are shown in the inset of Figure 5-3, with a decreasing trend for increasing lithiation time noting an obvious outlier at the 1 hour data point. This trend indicates that the crystalline uniformity with respect to tilt in the c-axis improves as lithium is inserted.

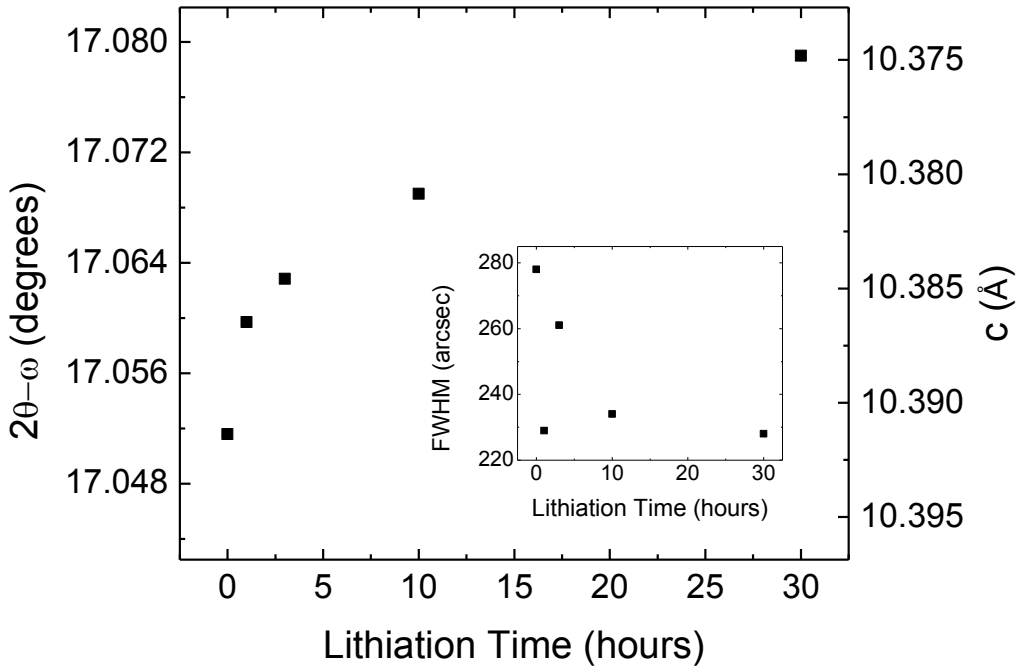

Figure 5-3. Diffraction angle and corresponding c-spacing for MBE grown $LiNbO_2$ as a function of time submersed in n-BuLi. The lattice contracts as lithium is intercalated due to screening of O-O layer repulsion. Inset: Rocking curve full width at half-maximum (FWHM) of the given diffraction peaks showing narrower values for increased lithiation time.

5.2.2 Electrical characterization

The $LiNbO_2$ sheet resistance was measured by linear TLM and the contact metal resistivity by four-point probe to analyze the effect of n-BuLi on both parameters, the results of which are shown in Figure 5-4. Both the $LiNbO_2$ sheet resistance and metal resistivity increase as a function of time in n-BuLi after an initial decrease at the 1 hour time point. It is possible that the pre-lithiation data point is subject to a non-ideal contact resistance from processing which is mediated during the first lithiation step, as no surface preparation steps were performed prior to metal deposition other than a solvent clean and DI water rinse. It was also observed that the metal contacts began degrading by cracking

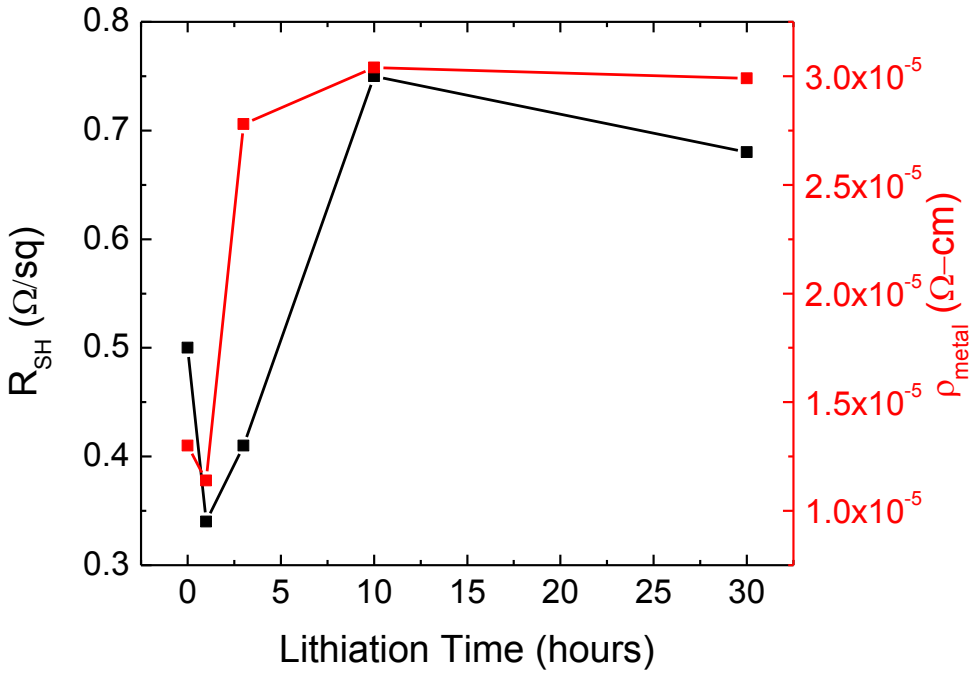

Figure 5-4. $LiNbO_2$ sheet resistance (black) and Ti/Au resistivity (red) as a function of time in n-BuLi.

and peeling after submersion, which makes interpretation of the metal resistivity data difficult. The trend of increased $LiNbO_2$ resistivity with increasing Li content is nonetheless confirmed, although further studies are necessary to correlate resistivity with lithium vacancy fraction x in $Li_{1-x}NbO_2$.

5.2.3 Optical characterization

Photoluminescence was performed at each lithiation step to determine the role of lithium stoichiometry on radiative versus non-radiative recombination, however photoluminescence response was not observed at any step. Lithium niobite has also shown opto-ionic coupling[48,56], where photons are absorbed by $LiNbO_2$ and the recombination energy (multiple eV) is sufficient to move lithium which has a hopping activation energy of about 100 meV[77,187]. The opto-ionic response, measured as a resistance change when switching on or off a broad spectrum ELH solar lamp, was investigated as a function of lithiation time.

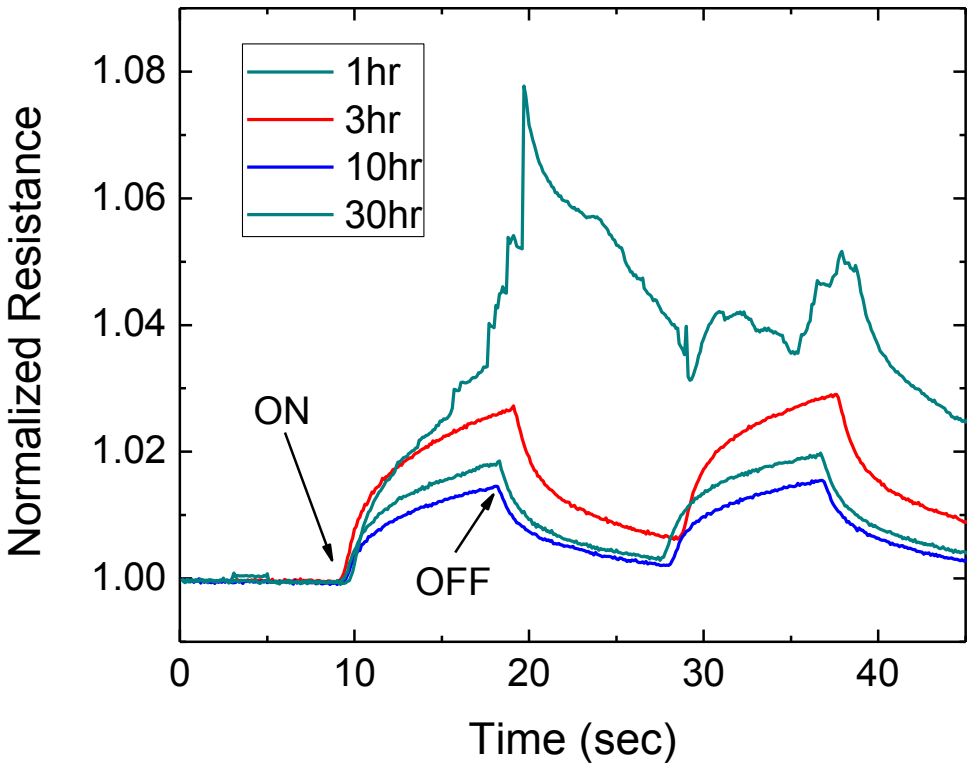

Figure 5-5. Optically induced resistance change in a 400 µm wide $LiNbO_2$ memristor after chemical treatment in n-BuLi for 1, 3, 10, and 30 hours. Increased lithiation does not show a trend with the magnitude of resistance change, but induces increased stability and repeatability of the measurement. Pre-lithiation of this device showed no trend with optical stimulation.

While there was no clear response in the magnitude of the optically induced resistance change, the measurements show an increase in stability and repeatability with increasing lithiation. The test was performed on 5 devices with electrode gaps from 25 µm to 400 µm, turning on and off the solar lamp while monitoring the resistance at 500 mV bias. Figure 5-5 is representative of the trend with lithiation, shown for the 400 µm wide device. While noise was often (but not always) measured before lithiation, by 10 hours

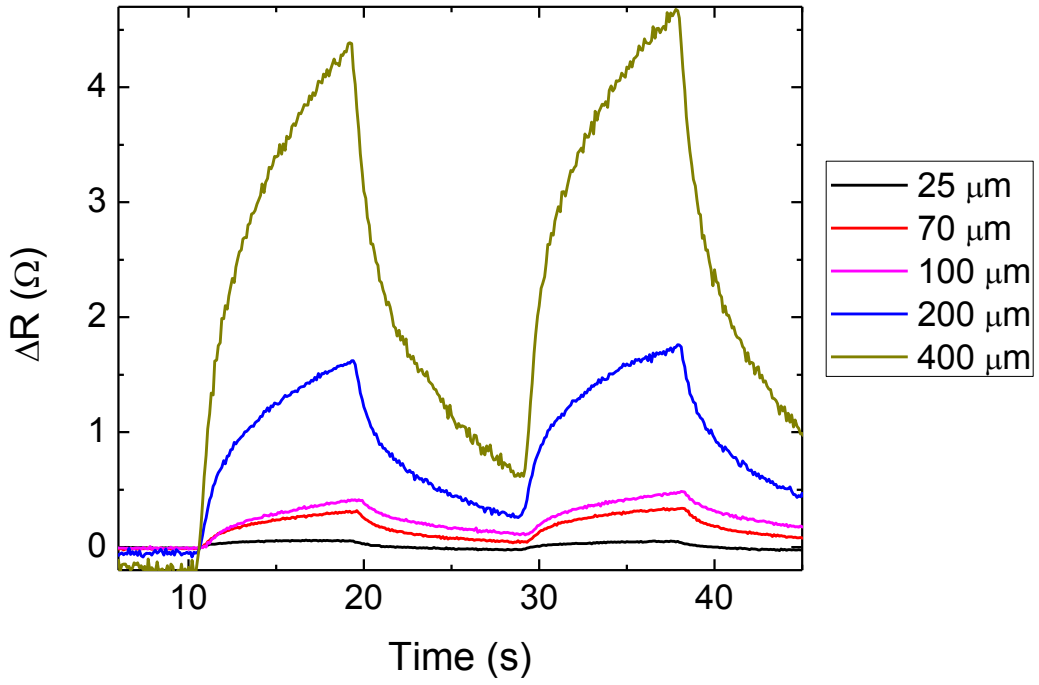

Figure 5-6. Optically induced resistance change for all devices after 10 hours in n-BuLi.

submersion in n-BuLi all devices showed a repeatable and stable response, shown below in Figure 5-6.

With the devices operating in a stable manner, comparisons may now be drawn not only as a function of lithiation time but as a function of device size. The saturating rise and decaying fall was best fit by a second order exponential of the form

$$\Delta R = A_1 e^{\frac{t}{\tau_1}} + A_2 e^{\frac{t}{\tau_2}} + R_0 \quad (25)$$

where τ_1 and τ_2 are the characteristic time constants with coefficients A_1 and A_2. For all devices $\tau_{1,rise} \approx \tau_{1,fall}$ and $\tau_{2,rise} \approx \tau_{2,fall}$ showing no trend with length, where τ_1 = 6.6 s ± 2.9 s and $\tau_2 \approx$ 0.80 s ± 0.36 s.

The overall resistance change did show an approximately linear trend with device length as shown in Figure 5-7. The linear fit shown (R^2 = 0.977) shows a slope of 12 mΩ/μm ± 0.91 mΩ/μm, although the trend cannot be isolated from an areal trend due to the constant device width (330 μm at 60 nm thick). This further study should be performed, to separate length and area trends, to determine whether the resistance change is

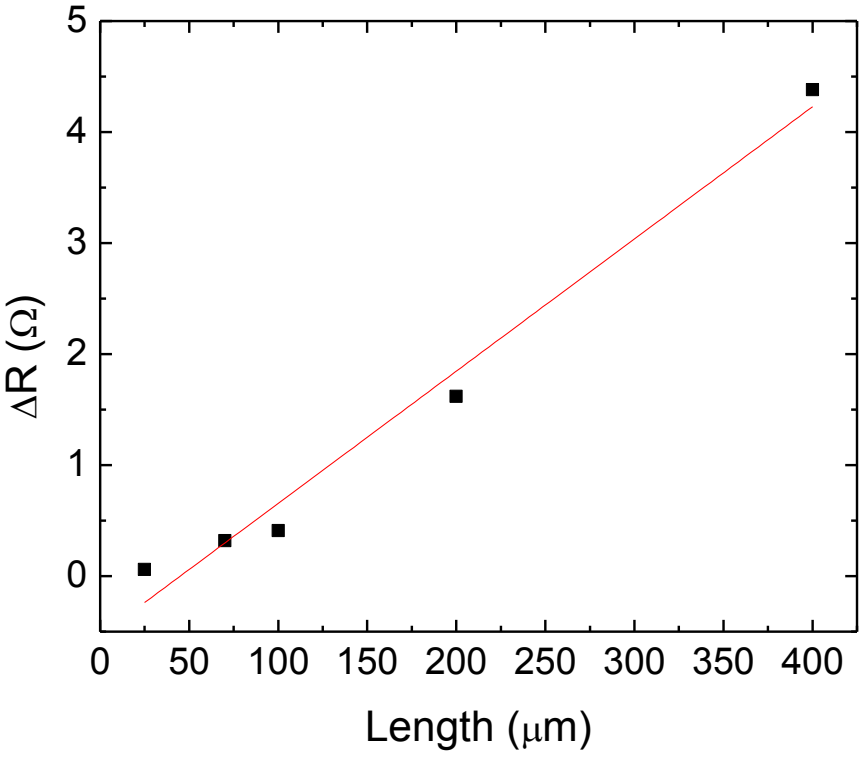

Figure 5-7. After 10 hours in n-BuLi, the opto-ionic resistance change shows an approximately linear trend with device length. For the given fit R^2 = 0.977.

determined by diffusion length, illuminated active area, or both. It is possible that there are multiple competing effects that would cause the resistance change to saturate, and further studies are required to determine the exact underlying physical phenomenon. Due to the unknown physical mechanism, a linear trend was chosen to quantify the resistance change observed. This trend should not be used to forecast device response until the physical mechanisms have been experimentally proven.

5.3 Impact

The ability to modify material properties *in-situ* is attractive, and any two coupled parameters could be used to create a sensor, emitter, or other functional device. The chemical modification of lithium content in MBE grown $Li_{1-x}NbO_2$ clearly causes shifts in both electrical and optical properties providing another mechanism for coupling physical parameters into a functional device. The relationship between lithium content and the properties studied herein is, however, not well defined. Further studies are required to link the quantified lithium mole fraction to properties including, but not limited to, electrical resistivity/doping concentration, electron mobility, ion mobility, photoluminescence, photoconductivity, thermoelectricity, opto-ionic coupling, lattice parameters, and defect concentrations. The role of material quality in these effects is also unknown. Experiments have been performed on powdered material[75], preferentially oriented sputtered material[84], bulk grown crystals[46,81], and epitaxial thin films[69,70,188], and

the relationship between material, lithium content, and functional properties should be studied to determine appropriate device synthesis methods.

CHAPTER 6. CONCLUDING REMARKS

6.1 Conclusions

The lithium-niobium-oxygen material family contains many multifunctional materials of significant interest to current research in materials science, optics, tunable materials, photocatalytic water splitting, and neuromorphic computing, among other topics. The research of the growth, characterization, fabrication, and application of these materials is therefore a worthwhile endeavor.

This dissertation has explored $LiNbO_2$ and $LiNbO_3$ in detail, examining MBE based growth conditions for high quality material and characterizing both materials and devices. NbO_2, Nb_2O_5, Li_3NbO_4, and $LiNb_3O_8$ have also been explored in less detail. The growth space for high temperature molecular beam epitaxy has been studied emphasizing the role of substrate temperature on the growing film. This research has produced a phase diagram in the Li:$NbCl_5$ ratio vs. substrate temperature phase space which shows the empirically determined complex relationships between possible phases. This study has also shown the power of high temperature MBE for the growth of high quality single-phase materials, enabling new research opportunities in complex oxide heterojunctions and devices.

Non-volatile $LiNbO_2$ based memristors for neuromorphic computing were also extensively studied in this dissertation. Previous work hypothesized that non-volatile

behavior could be obtained from the natively volatile $LiNbO_2$ by using alloying electrodes. This behavior is conclusively shown, although the originally suggested mechanism was incorrect. The resistance change mechanism was studied and determined by SIMS to be Li alloying with a metal contact to form a higher resistance interface. Al based devices suffered from irreversible reactions and poor cycleability. Ag was then explored as a superior alternative due to the high theoretical solid solubility of Li in Ag when compared to Li in Al. These Ag based devices show improved cycleability with a figure of merit that scales with electric field, a promising result for the future of these devices when considering scalability issues.

MBE grown $LiNbO_2$ based batteries were also successfully fabricated and tested, showing an order of magnitude increase in initial specific charge capacity when compared to similar batteries based on sputtered $LiNbO_2$. This capacity quickly decays to 2% of the original value after 100 cycles, however this result is likely due to the thin 90 nm cathode used, and a thicker MBE grown cathode may produce a battery of much higher saturated capacity.

MBE was also explored as a method for producing high quality epitaxial $LiNbO_3$ by using a 1000 ℃ substrate during growth. The material produced by this method shows the highest symmetric XRD rocking curve of any thin film material reported at 8.6” with no rotational defects (twin planes) observable by XRD pole figure. While the nucleation results in non-coalesced columnar grains when grown on lattice mismatched sapphire,

films of even higher quality are obtained by growing on isostructural $LiTaO_3$ indicating that substrate and buffer layer engineering can lead to optical device quality $LiNbO_3$ thin films and ferroelectric devices.

Other topics explored in this work include the effects of chemical lithiation and delithiation on MBE grown $Li_{1-x}NbO_2$, Nb_2O_{5-x} hysteretic rectifying diodes for neuromorphic computing, radiation tolerance studies of both $LiNbO_2$ and Nb_2O_5, $LiClO_4$ as a solid state oxygen source for MBE, the growth characteristics of Li_3NbO_4, $LiNb_3O_8$, NbO_2, and Nb_2O_5, and an exploration of possibility of $Li(Nb,Co)O_2$ alloys and $LiNbO_2/LiNbO_3$ heterojunctions.

6.2 Outlook

Like many emerging materials, the research presented in this dissertation has served to produce at least as many questions as it has answered. Materials research is only the first in many steps towards useful devices, and the roles of materials in the lithium-niobium-oxygen family must be exhaustively studied in heterostructures and devices to determine their eventual usefulness in next generation sensing and computing. Likewise the device characterization presented here merely scratches the surface of what is possible.

The field of neuromorphic computing was pioneered by Carver mead in the late 80's and early 90's, but non-silicon functional device research began in earnest after the first HP press conference on "the missing memristor" in 2008. After 10 years of research it can be

conclusively stated that memristors are a viable synaptic device, but only when considering the importance of short- and long-term dynamics on learning rules and synaptic function. For the first few years of memristor based synaptic research the focus was on achieving multiple weighted states and emulating STDP from an amplitude-only standpoint. The community has only recently begun to explore the role of more complicated learning rules and how they work in concert to provide efficient and accurate learning, memory storage, and memory recall. Neuromorphic materials research must be able to implement these complex learning functions to have any hope of creating a biomimetic system. The question that remains revolves not around the functional replication of a biomimetic system, but rather its necessity. The end goal of a biomimetic system is not to have a biomimetic system, but rather to have an energy efficient platform for abstract data analysis. It is therefore important to explore all algorithms for hardware-up parallel computing and not just biomimetic methods.

To these ends, research of $LiNbO_2$ is only in the beginning stages. From a materials standpoint the effects of lithium stoichiometry in $Li_{1-x}NbO_2$ is poorly studied. There is no current understanding of the role of MBE growth conditions on lithium content. Likewise, the effect of epitaxial strain on $LiNbO_2$ is completely unstudied and may lead to useful modifications of the already interesting multifunction properties. The role of defects in $LiNbO_2$ and the effect of crystal quality on material parameters will be important to study for the future of this material in functional systems.

$LiNbO_2$ has yet to be incorporated into a successful heterostructure based device. It is easy to describe functional devices from $LiNbO_2$ based heterostructures when considering the multifunctional properties found in the material. Tunable resistance, tunable band structure, and opto-ionic coupling could enable a new generation of tunable devices and sensors. To take advantage of these properties, the nucleation and interface dynamics must be studied between $LiNbO_2$, other lithium-tolerant substrates such as SiC, and other materials in the Li-Nb-O family.

From a characterization prospective, relatively little is known about the properties of lithium niobite. Simple parameters such as the thermal conductivity and coefficient of thermal expansion are not yet measured. To the authors knowledge only 32 refereed journal papers exist on the subject of $LiNbO_2$, most of which concern basic structural properties, battery applications, and superconductivity, leaving a significant amount of research to be performed.

From a device perspective, very little research has been done outside of the results on volatile and non-volatile memristors presented in this dissertation. To prove scalability, nanometer-sized devices must be fabricated and electrically tested. From a power perspective, $LiNbO_2$ is an interesting divergence from common research practices. The majority of memristor research focuses on high resistance devices which take advantage of extremely low currents for low I^2R power consumption. $LiNbO_2$ is, in contrast, one of the most conductive p-type oxides ever measured. To be a viable option for next-

generation low power computing, $LiNbO_2$ must be able to operate at extremely low voltages for low V^2/R power consumption. For purely electric field based devices this is a reasonable assumption. The activation energy for Li-ion motion in lithium niobite is low, and operating voltages should scale down with device size to maintain an appropriate electric field. This dissertation has shown that concentric ring-dot devices should improve at smaller scales due to the increased periphery-to-area ratio and the effect geometry has on the local electric field. At this point it has not been determined whether electrochemical barriers or electric fields are the driving force for non-volatile memristors. If electrochemical potentials are the primary energy barrier for non-volatile behavior in $LiNbO_2$ memristors then operating voltages will not scale with device size. This research must be performed to determine the viability of non-volatile $LiNbO_2$ memristors for scalable computing. In addition to the alloying contact metals explored in this dissertation, there are many other possibilities to be explored. Other metals may offer superior cycleability and/or figures of merit depending on the solid solubility and reversibility of the reactions. Additional opportunities can be borrowed from battery technology. Anode materials for lithium ion batteries include (1) carbon bearing materials, primarily graphite, (2) alloying anodes including Al, Ni, Sn, and Si, (3) conversion materials which are primarily metal-oxides, and (4) intercalating materials such as $Li_4Ti_5O_{12}$. Each of these anode options possess benefits and tradeoffs in battery applications, but for the non-volatile memristors described in this dissertation considerations such as discharge rate and high-voltage capability are not necessary.

Graphite is the most exhaustively studied anode material and is used in many commercially available Li-ion batteries today. It benefits from excellent stability and high reversibility through an intercalation reaction, and should be tested as a non-volatile electrode for lithium niobite memristors. Silicon can reversibly alloy with lithium but undergoes significant volumetric expansion upon alloying, > 300 %. Due to this volumetric constraint anodes are often Si nanoparticles, Si nanowires, or porous Si to prevent device failure upon expansion. $Li_4Ti_5O_{12}$ nanoparticles show rapid and reversible intercalation of lithium ions at near-zero strain, and are also excellent candidate materials for the improvement of the non-volatile memristors presented in this dissertation. For more information on common battery anode materials see *Marom et. al.*[164] and the references contained within.

The widespread research of thin-film $LiNbO_3$ was widely abandoned in the early- to mid-2000's due to insufficient crystal quality for optical and ferroelectric devices. If the growth methods explored in this work can be extended to produce fully coalesced high-quality material it would open significant paths forward for influential research and commercially viable devices. The most obvious research objectives are twofold. (1) Ferroelectrically active material which can be poled single-domain is useful for low power ferroelectric transistors, poled optics, ferroelectric oscillators, and sub-threshold swing negative capacitance devices. (2) Material which can be grown to sufficient thickness for optical waveguides which could then be applied to integrated optics and tunable cavities. To achieve these goals, the nucleation dynamics of $LiNbO_2$ on various

substrates and buffer layers must be explored. Of particular interest are using SiC as a substrate and using either $LiNbO_2$ or Li_3NbO_4 as a nucleation buffer layer.

Like many exploratory works, this dissertation has uncovered more questions than it has answered. The viability of lithium niobite memristors in biomimetic neuromorphic computing architectures has yet to be determined, however the ability of a single material to demonstrate the full range of biologically realistic synaptic decay times is promising. The additional possibility of heterostructures combining memristive, ferroelectric, piezoelectric, photocatalytic, photoelectric, and opto-ionic properties (among many others) leads to theoretical applications in low power transistors, sensors, tunable waveguides, water splitting, and batteries among other equally exciting options. The phase diagram understanding presented in this dissertation is a major step towards the fabrication of such heterostructures and devices, although there is still significant research to be done. There are many questions surrounding the feasibility of the many functional materials and devices presented here, the only certainty is that there are many more fascinating discoveries to be made.

APPENDIX A. X-RAY DIFFRACTION (XRD) METHODS

A.1 XRD of Lithium Niobium Oxides

For all films grown, X-Ray Diffraction (XRD) is the primary method of crystalline phase identification due to the superior amount of information which can be obtained, ease of use, and the exhaustive existing database of characterized materials. While most phases are easily identified in XRD based on a cursory knowledge of the material under test, (lithium) niobium oxides provide a challenge due to the existence of many suboxide and oxide phases of similar crystal structure. $LiNbO_2$ (002), Nb_{BCC} (110), and $LiNbO_3$ (006) are all easily identified, while the other possible phases are not. Table A-1 lists the various possible phases and their XRD peak locations based on Cu-K_α radiation (λ = 1.54056 Å).

There are five possible phases in the narrow range 36.772 – 37.069 degrees 2θ-ω, and 3 of those materials fall within 0.4 degrees of each other, making phase identification extremely difficult. It is possible to differentiate them all, however, using multiple XRD scans as well as knowledge of the material in question. FCC oriented niobium films can generally be ruled out of oxide film growth due to the tendency of niobium to react with oxygen, reducing the number of possibly degenerate oxide phases to four. Niobates with valence +5 are typically transparent ceramics, and in certain situations can be visually distinguished from suboxide states. $LiNb_3O_4$ and Li_3NbO_8 both have valence Nb^{+5} and

are often identified by transparency, while NbO and NbO_2 will not be transparent. The $LiNb_3O_8$ reflection within the 2θ-ω range in question is the (600) reflection and has a corresponding (400) and (800) allowed reflection which can help to distinguish it from Li_3NbO_4 assuming the intensity of the peaks are large enough. If visual transparency confirmation is not possible, the phases may be distinguished by asymmetric off-axis scans using XRD. While NbO and $LiNb_3O_4$ are both cubic and separated in 2θ-ω by only 0.036 degrees, the NbO reflection is (111) while the $LiNb_3O_4$ reflection is (222), resulting in a doubling of the Li_3NbO_4 peaks in reciprocal space. NbO_2, having a different crystal structure and oriented to the a-plane, is easy to identify by this method.

While the previous method describes a procedure for discerning each individual phase from another, it is not always easy to put in to practice. The values listed in Error! Reference source not found. are ideal bulk values, while many films grown are under considerable epitaxial strain causing these values to shift. Niobium oxides often exist in oxygen poor phases which can also shift the d-spacing of the material, and in phases where lithium is not chemically bound it can act as a defect, shifting the lattice spacing. Due to these difficulties the materials to be analyzed are not always exhaustively identified but sometimes referred to as an "unwanted suboxide". Any phase that is definitively identified is labeled by its chemical name.

Table A-1. X-Ray Diffraction reflections, structure, and chemical valence for various niobium and niobium oxide films. λ=1.54056 Å for Cu-K_α radiation.

Material	Structure	Nb Valence	Conduction	2θ-ω	h k l
$LiNbO_2$	Hexagonal	+3	S	16.941	0 0 2
α-$LiAlO_2$	Rhombohedral		I	18.680	0 0 3
γ- $LiAlO_2$	Tetragonal		I	22.275	1 0 1
$LiNb_3O_8$	Orthorhombic	+5	I	24.42	4 0 0
$LiNbO_2$	Hexagonal	+3	S	34.267	0 0 4
Nb_2O_5	Monoclinic	+5	I	35.998	0 0 7
Nb	FCC	+0	M	36.772	1 1 1
NbO	Cubic	+2	M	36.953	1 1 1
Li_3NbO_4	Cubic	+5	I	36.989	2 2 2
$LiNb_3O_8$	Orthorhombic	+5	I	36.993	6 0 0
NbO_2	Tetragonal	+4	S	37.069	4 0 0
Nb_2O_5	Monoclinic	+5	I	37.602	$\bar{6}$ 1 0
$LiNb_3O_8$	Orthorhombic	+5	I	38.104	6 0 $\bar{2}$
Nb	BCC	+0	M	38.475	1 1 0
$LiNbO_3$	Rhombohedral	+5	I	38.949	0 0 6

Conduction: M – metallic, S – semiconducting, I - insulating

A.2 **Wafer Mapping**

As noted in the previous sections, multi-phase films are common in the lithium niobium oxide material system, and due to non-uniformities on the substrate films can grow laterally separated. An example is shown in Figure A-1. Due to this propensity for multi-

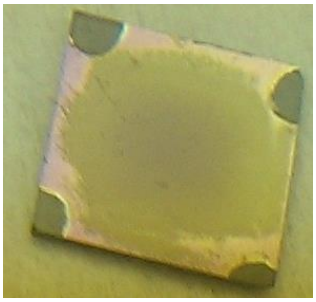

Figure A-1. Laterally separated phase growth caused by a radial thermal gradient. A purple transparent phase is observed in the center surrounded by a reflective red/pink phase.

phase films, XRD based wafer mapping can be a useful technique for characterizing multiple phases on a single growth.

The most basic wafer map setup uses a 1/16° or 1/32° slit on the incident optics of the hybrid monochromator with the smallest available beam mask (1 or 2 mm) restricting the beam vertically. After aligning to the substrate, the true x-y center can be found through scanning the x and y motors. At this point a grid of repetitive scans can map the wafer, limited only by beam divergence and slit/mask size. For a 2 mm mask the maximum grid size is 25 scans (5x5) taken every 2 mm.

For characterizing lithium-niobium-oxides a single scan from 34 – 42° 2θ can capture every major possible constituent including the substrate (Al_2O_3 or SiC), and the scans can be analyzed by a number of parameters including peak area, normalized peak height, peak width, and peak position. This is similar to the characterization procedures performed on films grown by combinatorial methods. As an example, the phase

constituents of the film in Figure A-1 may be positively identified by plotting peak intensity vs. position for all constituents observed in a broad area diffraction scan.

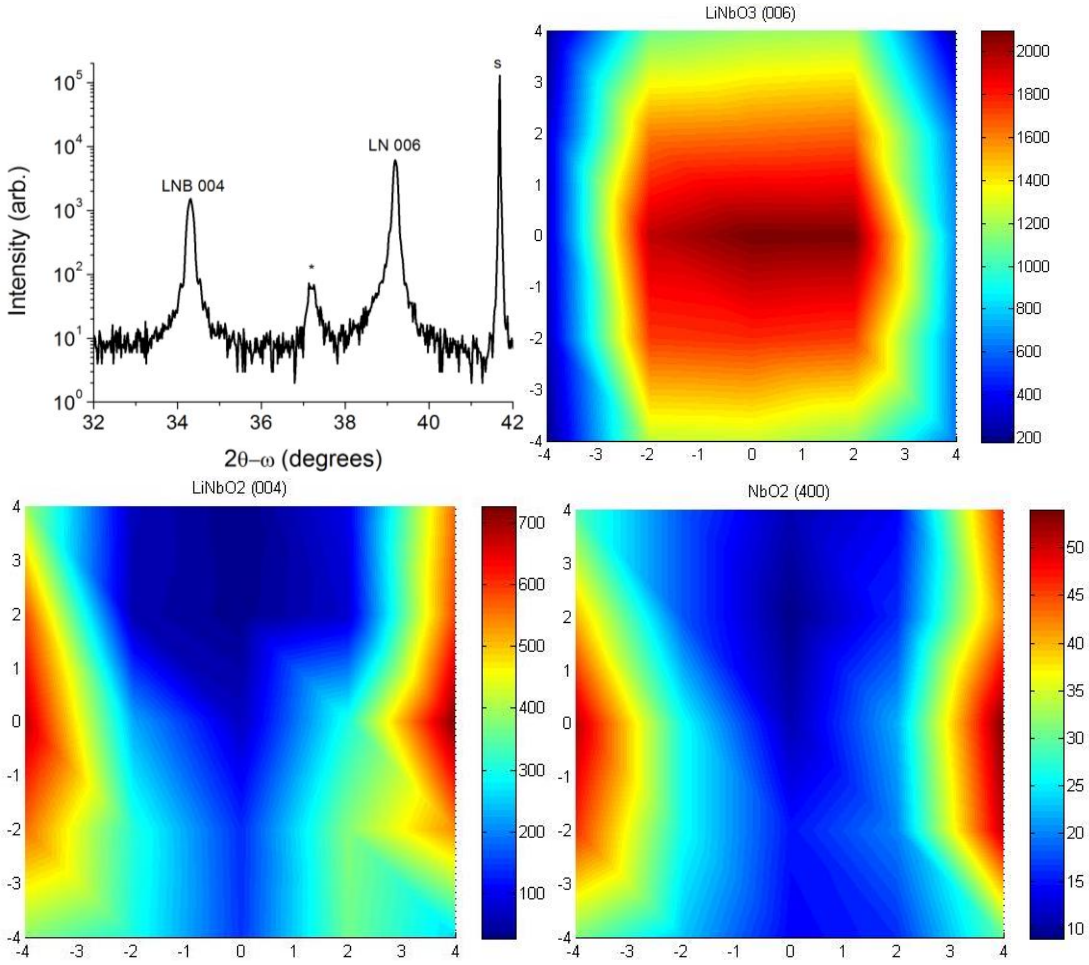

Figure A-2. X-ray diffractogram and corresponding wafer maps for the film shown in Figure A-1. The x- and y-axis for the wafer maps represent position in mm, while the scale bar represents peak intensity. Clearly the fully oxidized $LiNbO_3$ is the central transparent film while the red outer film is $LiNbO_2$. NbO_2 is barely above the noise floor (~20 counts) and is likely nucleated around $LiNbO_2$.

The results of a wafer map analysis on the film in Figure A-1 are shown in Figure A-2. The diffraction scan in the top left was repeated at 25 points on the wafer in a 5x5 grid using a 2mm mask and the resulting data was parsed for peak intensity values for $LiNbO_2$ (004), $LiNbO_3$ (006), and NbO_2 (440) as a function of position. The results clearly indicate that the center transparent phase of Figure A-1 is $LiNbO_3$ while the surrounding red/pink reflective phase is $LiNbO_2$. The presence of low intensity NbO_2 around $LiNbO_2$ is not surprising as they often co-nucleate, and the visual appearance of the film (color and transparency) corroborates this phase analysis. In this way a wafer map may be used to identify multiple laterally separated phases from a single sample, useful in aiding visual identification or, in the future, for the analysis of combinatorial growths. It is important to note that due to beam divergence the only way to truly measure the diffractogram of a single area is to apply a mask at the sample.

A.3 **X-ray Reflectometry (XRR)**

X-ray Reflectometry (XRR) is a reflectance mode x-ray technique used to determine thin film sample thickness, film density, surface roughness, and interface roughness. With ideal optics, all four of these film parameters may be obtained with a single scan.

XRR relies on specular reflection and interference patterns. Incident X-rays are brought in contact with an aligned thin film sample at very low angles to the surface (parallel to the film surface). The angle 2θ-ω is slowly increased from 0°, and at an

incident angle (critical angle) θ_c proportional to the film density, X-ray's begin to penetrate the film. Due to the low incidence angle bragg diffraction does not occur, although the X-rays penetrate the entire film. Upon encountering a change in the index of refraction, reflection can occur. This occurs at a boundary layer, such as a thin film – substrate interface. Upon exiting the sample surface, constructive or destructive interference can occur with partially reflected photons at the surface, causing an interference pattern based on the path length through the film and the wavelength of incident radiation. By sweeping the angle 2θ-ω, the path length may be varied and the interference frequency observed in the form of fringes, called Kiessing fringes. This frequency is related to the film thickness, and forms the basis of the XRR technique.

A.3.1 Information Obtainable by XRR

A.3.1.1 Thickness

Thickness data may be obtained by XRR according to the frequency of oscillation of the Kiessing fringes in the XRR profile. Film thickness and oscillation period are inversely related, so that a thicker film will correspond to a shorter period of oscillation (or a higher frequency). Oscillations occur, as described above, due to constructive and destructive interference of the wave reflected from the film – substrate interface and the partial reflection from the material surface. When the path length through the film is varied by changing the angle 2θ-ω, Kiessing fringes are observed. A typical XRR scan is shown in Figure A-3, illustrating the difference in Au on a Si substrate at 2 different thicknesses.

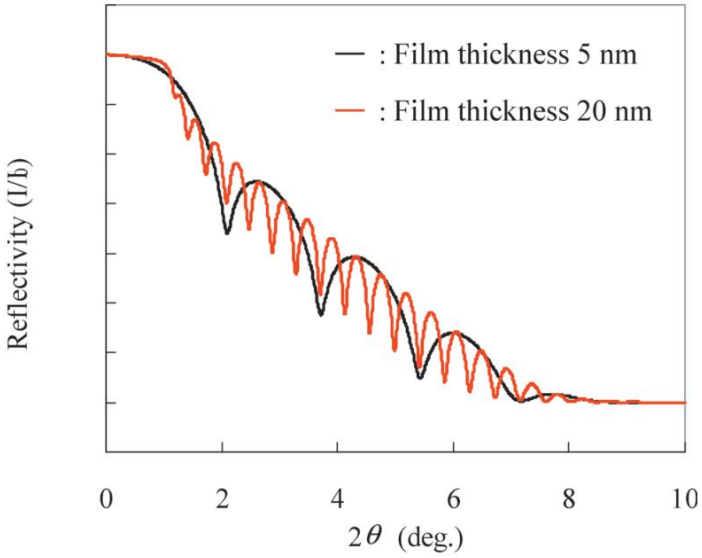

Figure A-3. XRR scan showing the effect of layer thickness on Kiessing fringes for a single epilayer on a thick substrate[189].

Films with multiple layers may also be analyzed with XRR. The interference patterns appear as an enveloped oscillation. Films of more than 2 layers or with layers of similar thickness will require modeling to successfully analyze. An example of a 3 layer film is shown in Figure A-4.

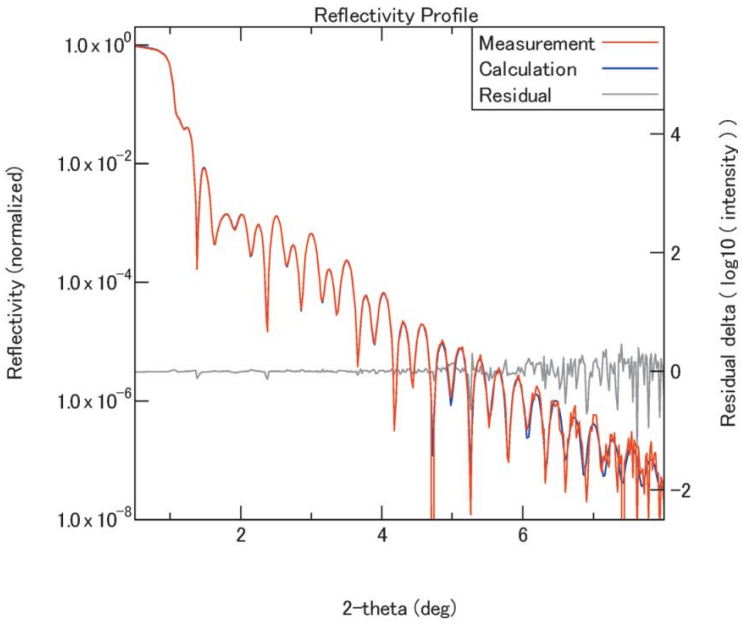

Figure A-4. Reflectivity profile of a 3 layer film. Fringes convolve into envelopes and beats which contain the thickness information from all layers[189].

A.3.1.2 Film Density

The critical angle, θ_c, is directly proportional to the film density. The condition for complete reflection is dependent on the index of refraction of the material, which is density dependent. The equations are complicated, but can be found in the reference material. The trends are, however, that a greater density will appear as a larger critical angle. The amplitude of the oscillations is also dependent upon the ratio of film density to substrate density, with larger amplitude indicating a greater disparity between the two densities. Figure A-5 shows XRR scans of three different materials, all of the same thickness (20 nm), all on a Si substrate.

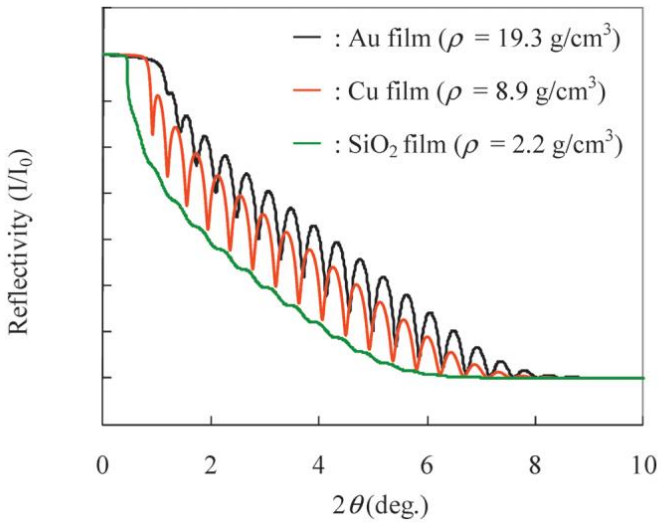

Figure A-5. The effect of film density on the reflectivity profile, evidenced as a change of the critical angle. Higher density films exhibit larger critical angles[189].

A.3.1.3 Surface and Interface Roughness

Surface roughness will affect the coherence of the light scattered off the surface of the film, and will therefore smear the total intensity of the reflection profile. A larger surface roughness causes the **total** signal to decrease more rapidly. An example of how surface roughness can affect an XRR scan is shown in Figure A-6.

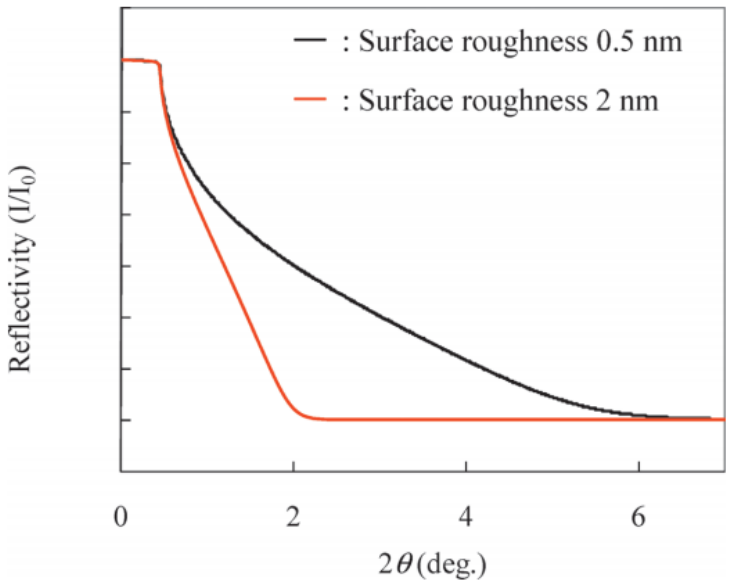

Figure A-6. The effect of surface roughness on a reflectivity scan. A larger surface roughness value causes the reflectivity profile to decay in total intensity[189].

Interface roughness will affect the attenuation rate of the Kiessing fringes. Interface roughness will cause the path length of each photon to vary slightly, smearing out the overall condition for constructive and destructive interference, so that fewer fringes occur. Figure A-7 shows an example of how interface roughness can affect an XRR scan.

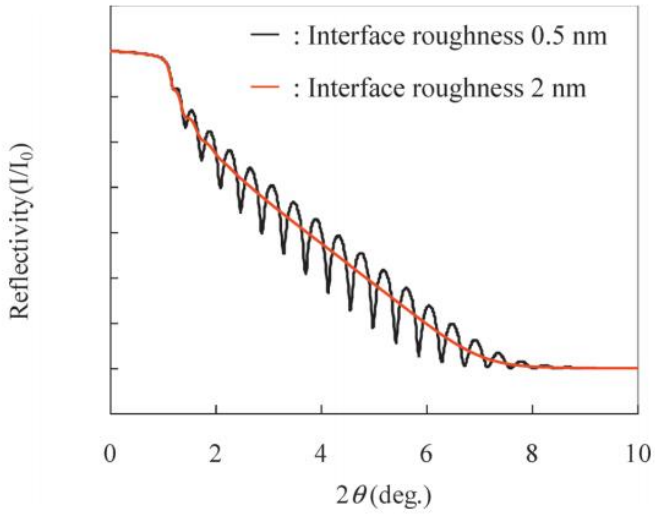

Figure A-7. The effect of interfacial roughness on a reflectivity scan. Increased interface roughness increases the oscillation attenuation through a non-uniform vertical coherence length[189].

A.3.1.4 Total Effect

The scan in Figure A-8 illustrates all pieces of data that can be extracted from a single XRR scan.

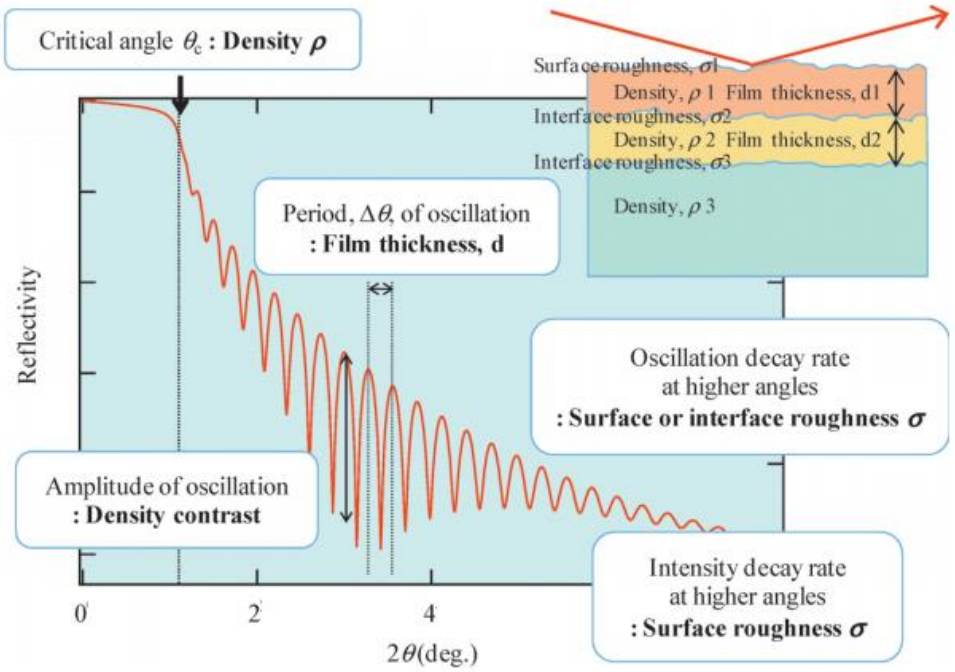

Figure A-8. Summary of data obtainable through a single XRR scan[189].

A.3.2 Methods

A.3.2.1 Recommended Optics

Table A-2. Recommended optics for reflectivity scans, based on film thickness[189].

Monochrometer	Relative intensity (Reference estimation)	Resolution (Angular divergence)	Wavelength monochromaticity	Applicable film thickness (nm)
Multilayer mirror	200	$\leq 0.04°$	$K\alpha_1 + K\alpha_2 (+ k\beta)$	0.5 - 100
Ge(220) 2-bounce	10	$\leq 0.02°$	$K\alpha_1$	50 - 200
Ge(220) 4-bounce	1	$\leq 0.003°$	Part of $K\alpha_1$	> 200

A.3.2.2 Alignment

The alignment procedure for XRR is extremely important. Deviation from alignment will result in poor measurements, or possibly no visible interference pattern.

1) Align emitter to detector. Scan 2Θ around 0° to find the center of the X-ray beam.
2) Coarse Z-align. Bring the stage forward in Z until the detector counts are approximately half of the original maximum value. Accuracy of ~10 % necessary.
3) Omega Alignment. Run the optimize program around the most intense substrate peak. Once the program has finished, set $\omega = \Theta$ in sample offsets, and zero the ψ sample offset.

4) Fine Z-align. Set Z height to a more exact location for half maximum counts at the detector. Accuracy better than 5 % is necessary.
5) Find the critical angle. Scan 2Θ-ω from 0° to a value above the expected critical angle Θ_c, usually $0.2° < \Theta_c < 0.7°$. A quick scan is sufficient. Using the move mode, set 2Θ to a value slightly less than the critical angle. Clear the offset.
6) Specular reflection condition. Scan ω 0.6° around the current value. A quick scan is sufficient. Align to the maximum. If no peak is observed either $2\Theta > \Theta_c$ or the film surface is too rough for coherent specular reflection. Set $\omega = \Theta$ in sample offsets.
7) Psi scan. Scan 2-3° in ψ, and align to the maximum. Set the offset to zero.
8) Repeat step 6 and 7 until no further alignment is needed.
9) Check Z height and adjust if necessary until the counts are as close to half maximum as possible.

A.3.2.3 XRR Measurement

Once properly aligned, the XRR data may be obtained by a 2Θ-ω scan. In ideal conditions fringes may be observed up to 10° 2Θ, but in practice you will not see reflections beyond 2-3° 2Θ unless you use the proper optics and have an extremely smooth film. Fringes at higher angles will become more resolved with longer scan parameters; however a quick scan can resolve thickness information if the sample is relatively smooth.

A.3.2.4 Software Analysis

Analysis of XRR data is performed in the WINGIXA software suite, installed on the computer in room VL 116. Before performing analysis, the scan must be exported in the .xnn format via X'pert Organizer.

Open WINGIXA. To load the data, select Graphics → Read Data to Fit → Reflectivity.

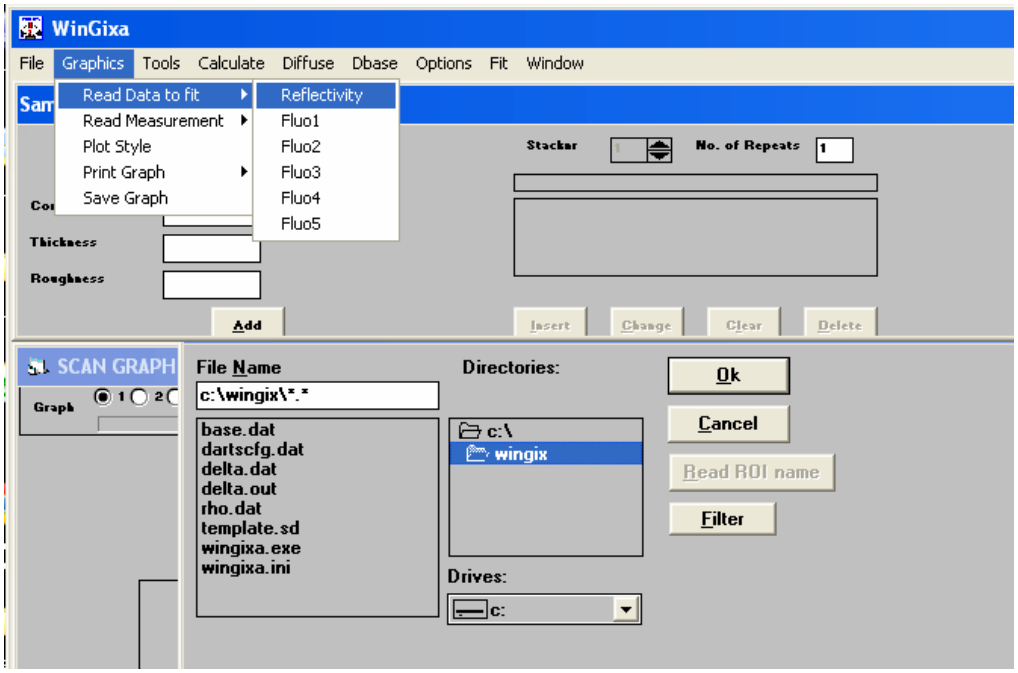

Method 1 – Periods

This method is less accurate, but can provide approximate results for scans that do not have clearly defined fringes and must be "eyeballed".

To analyze thickness, select Tools → Periods → Reflectivity

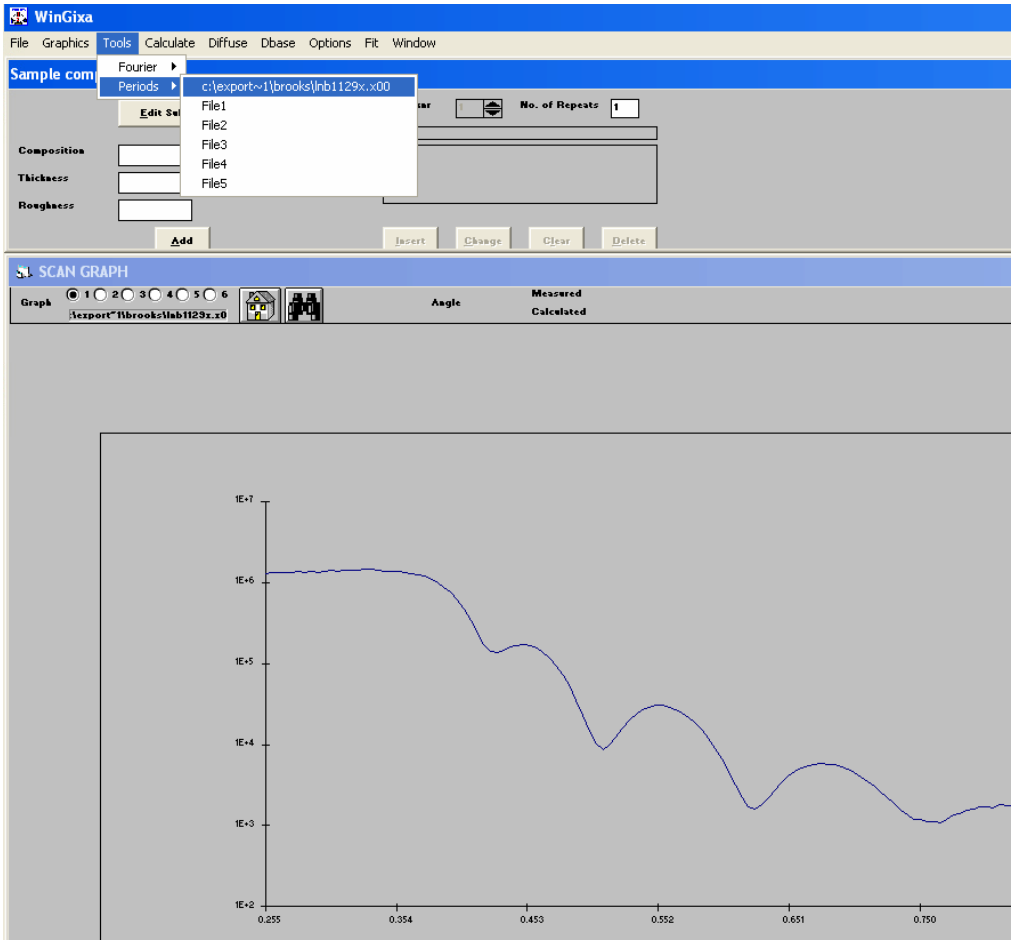

Click the Select Critical Angle button in the top menu, then select the location of the critical angle on your data.

Click the Select First Angle button in the top menu, then select the first angle by clicking the maxima of the first thickness fringe.

Repeat the process for the second angle.

Click calculate. Thickness is displayed in angstroms.

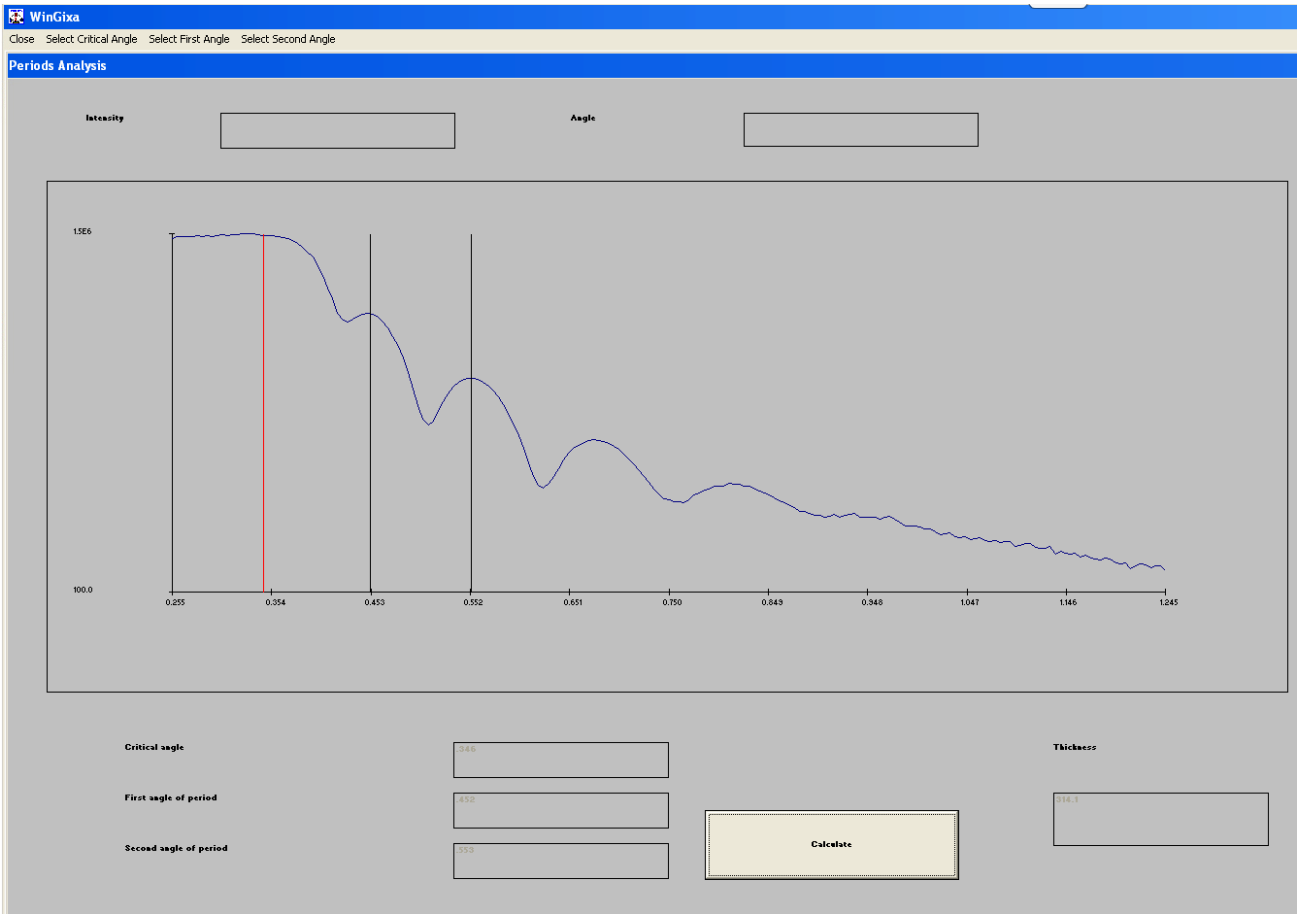

To approximate more accurately, you may only select the first angle, but select the second fringe. Then multiply the calculated thickness by 2.

Method 2 – Fourier Transform

This method is more accurate, but requires well defined fringes. Accuracy is given within 5 Angstroms. At the time of writing this document the error of uncertainty is unknown.

To analyze thickness, select Tools → Fourier → Reflectivity

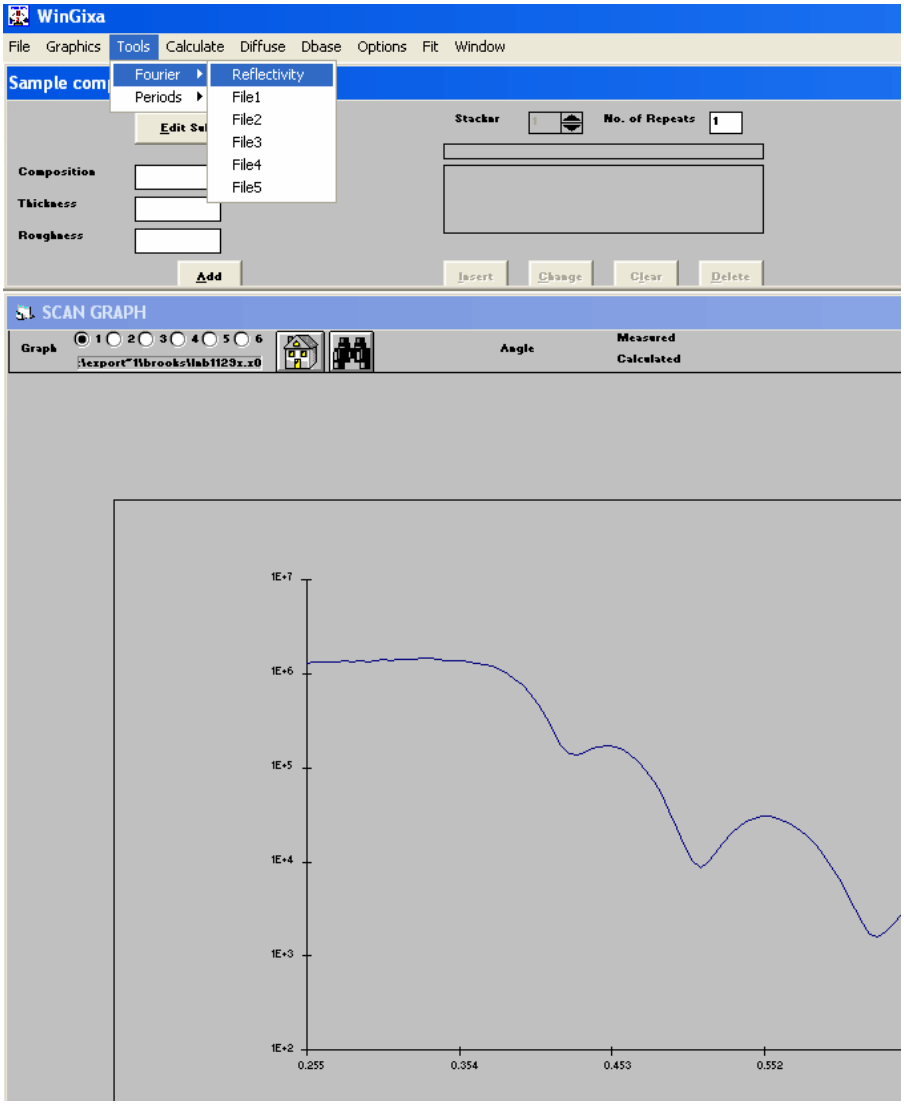

The scan is displayed in the Fourier analysis window.

Click the Binoculars to zoom in on the oscillating portion of the scan. Click once, at an angle larger than the critical angle but smaller than that of the first oscillation, to select the lower bound. Click again to select the upper bound, at an angle larger than the final resolvable oscillation. The selected portion of the scan will be displayed.

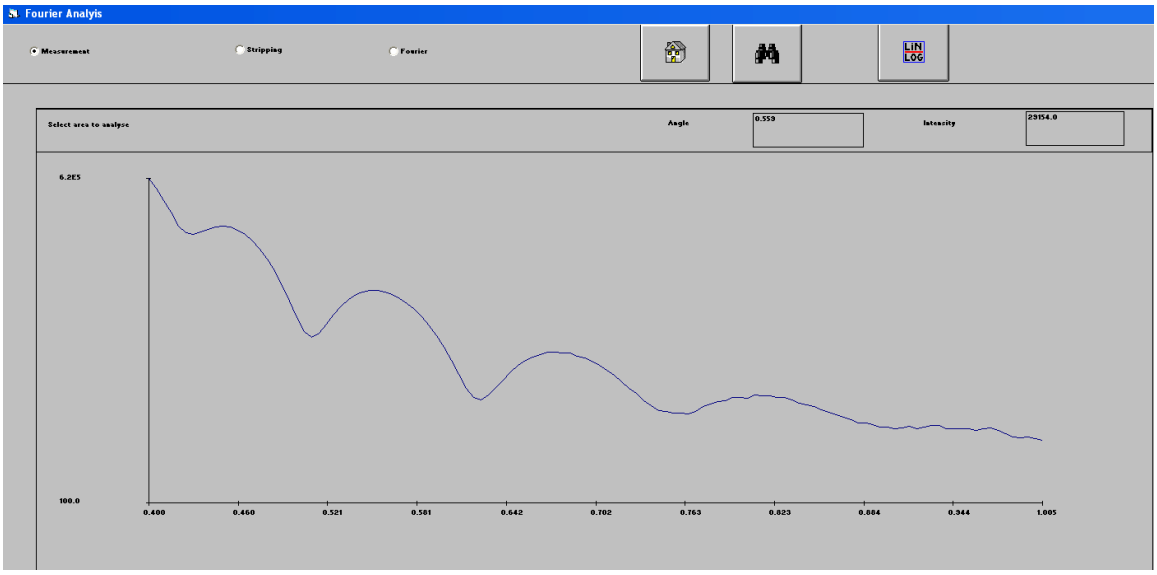

Press F2 to filter the background out of the scan. The filtered data should oscillate around zero for increasing angle.

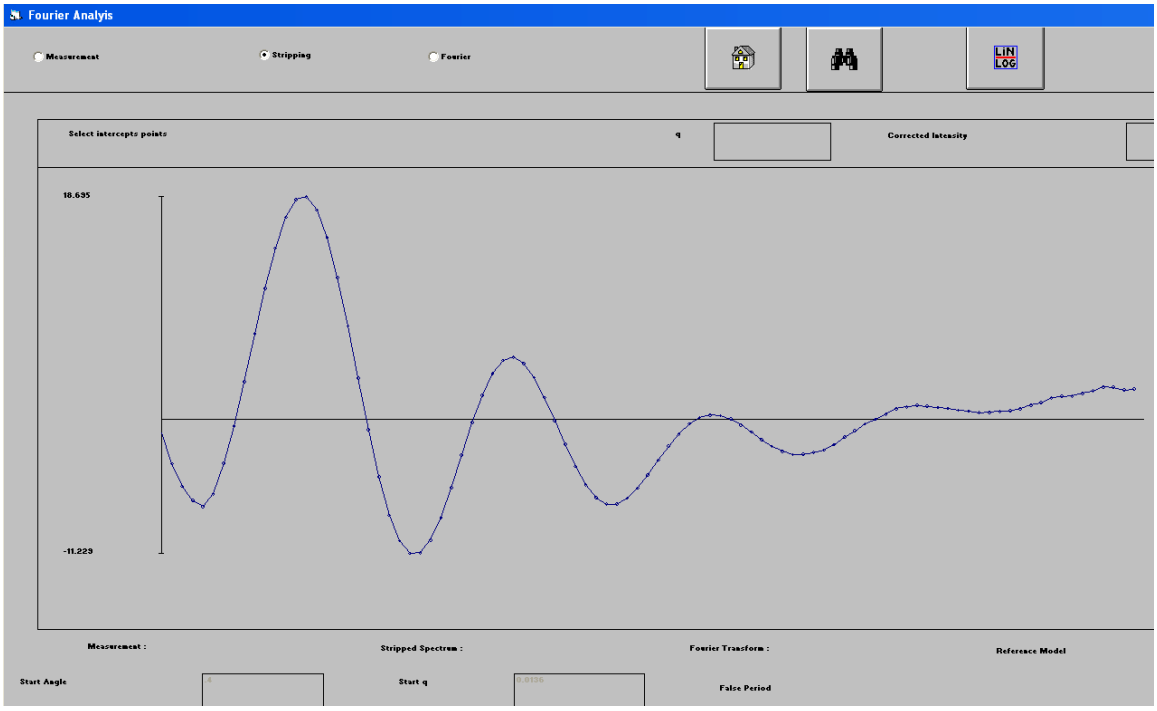

Press F3 to take the Fourier transform of the data, giving intensity as a function of film thickness. The peak following the background decay corresponds to the film thickness. A more defined peak correlates with a lower uncertainty error in the measurement.

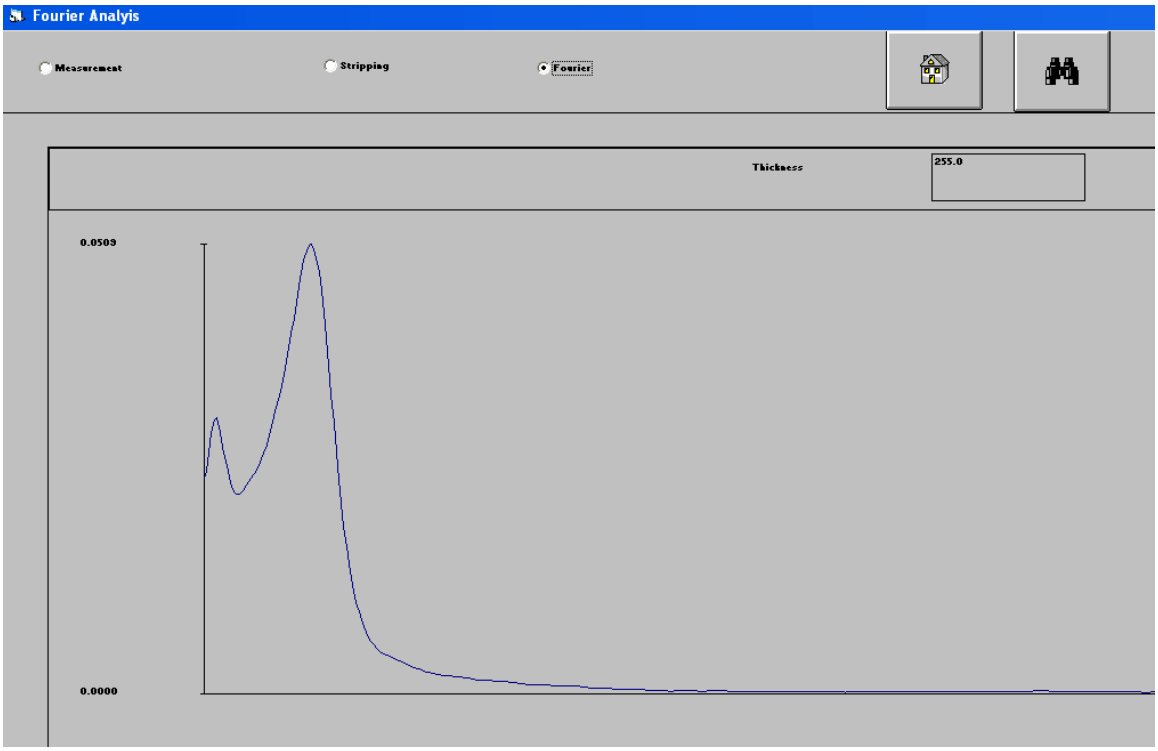

Modeling and Data fitting

The WINGIXA program is able to model reflectivity based upon surface and interface roughness, film thickness, density, and optics. The entire model must be defined, as a substrate and film with thickness, density, and roughness. At the time of writing the exact methods for modeling and fitting are unknown. Walter Henderson is able to walk you through the process if you need it, and this document may be updated to reflect these methods.

Yasaka (2010)[189] is an excellent guide to the XRR technique. Equations and methods are given, as well as a full alignment procedure.

APPENDIX B. LITHIUM NIOBITE PROCESSING

B.1 **Photolithography**

To date, nearly all photolithographically defined $LiNbO_2$ devices have been processed using AZ 5214 image reversal photoresist and a Karl Zuss MJB-3 mask aligner. The optimized photolithography recipe is shown below:

Positive process

1) Solvent Clean
2) Dehydration bake – 5 minutes in top right oven
3) Spin – AZ 5214 500 rpm for 5 seconds then 3500 rpm for 30 seconds
4) Soft bake – 100 seconds in top right oven
5) Exposure – 100 mJ/cm^2
6) Develop – AZ 300 MIF – typically 40 seconds, test first
7) Rinse – DI water
8) Dry – N_2

Negative process

1) Solvent Clean
2) Dehydration bake – 5 minutes in top right oven
3) Spin – AZ 5214 500 rpm for 5 seconds then 3500 rpm for 30 seconds

4) Soft bake – 100 seconds in top right oven
5) Exposure – 50 mJ/cm^2
6) Image Reversal Bake – 50 seconds bottom left oven
7) Flood Exposure – 500 mJ/cm^2 with no mask and HP turned on
8) Develop – AZ 300 MIF – typically 25 - 35 seconds, test first
9) Rinse – DI water
10) Dry – N_2

Positive Process – S1813 and LOR5B

A recipe was also developed for dual layer photoresist enabling metal liftoff through a negative slope sidewall profile. In this process the bottom layer of resist develops more rapidly than the top layer. This recipe was formulated for use with a hot plate.

1) Solvent Clean
2) Dehydration Bake – 10 minutes at 110 ℃
3) Spin - LOR 5B: 5000rpm for 30 seconds
4) Soft Bake - 5min at 155 ℃
5) Spin - S1813: 5000rpm for 30 seconds
6) Soft Bake - 1min at 110 ℃
7) Exposure - 175 mJ/cm^2
8) Develop - MF319 for 24 seconds
9) Rinse - DI water

10) Dry – N_2

11) Dehydration bake: 10min @110C

B.2 **Wet Etching**

It is sometimes desirable to isolate a $LiNbO_2$ device to provide a finite source of lithium to a single device; therefore a wet etching process has been developed for $LiNbO_2$ for quick mesa isolation. First, a positive mask is prepared using the positive S1813/LOR5B recipe above, noting that some undercutting could occur due to the LOR5B layer. Ideally a double layer of positive AZ5214 would be used as a mask; however this process has not yet been tested. The etching chemistry is given in Table B-1. It should be noted that due to the speed of the 1:1 $HF:HNO_3$ etch, the calculated etch rate may have a large associated error.

Table B-1. Chemistries used for $LiNbO_2$ wet etching and associated etch rates.

Etch composition	Approximate Etch Rate (nm/min)
1:1 $HF:HNO_3$	720
1:1:5 $HF:HNO_3:H_2O$	400

B.3 **Dry Etching**

Dry etching $LiNbO_2$ is a possible solution for increasing the etch anisotropy. Fluorine is needed to chemically etch niobium[190], but lithium bearing compounds are often hard to

etch due to the high vapor pressure and bond strength of LiF and Li_2O formed during this process, as shown in Figure B-1.

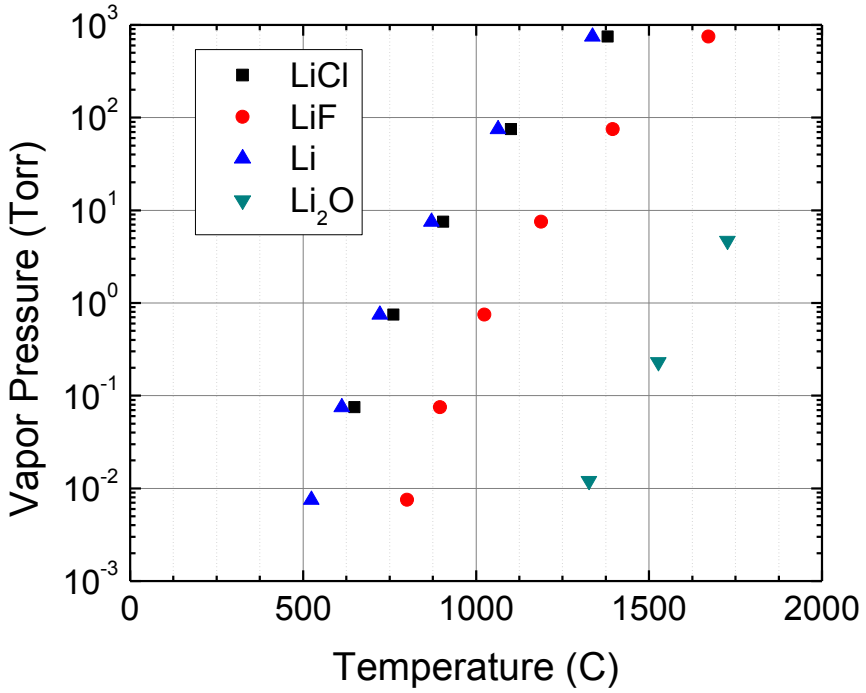

Figure B-1. Vapor pressure of common lithium compounds formed during the dry etching process. LiF and Li_2O are essentially non-volatile at typical etching temperatures assuming a 1 mTorr threshold for thermal desorbtion. Data from references [198,199].

As a result it is difficult to etch more efficiently than an argon ion mill, which operates at approximately 10 – 60 nm/min[191]. Etch rates of up to 190 nm/min have however been achieved in $LiNbO_3$ by using a mixed Ar/SF_6 inductively-coupled plasma (ICP) at

1000W with 90W RIE power with a selectivity of >10 over the NiCr mask[192]. This result means it may be possible to increase the ICP etch rate and selectivity of $LiNbO_2$ through the same chemistry, although photoresist is the desired mask due to ease of processing and removal. It is also unknown how the NiCr etch mask removal process will affect the $LiNbO_2$ (any oxidizing acid will remove Li from $LiNbO_2$). Regardless, dry etching was attempted as a proof of concept experiment. The etch gases used were 25 SCCM Ar:25 SCCM CHF_3:10 SCCM SF_6:5 SCCM O_2 at 70 mTorr 300 W RIE power. This recipe etched the $LiNbO_2$ film, but did not show sufficient selectivity over Cr-Au, Cr, or photoresist masks. It was found, however, that a quick dry etch following the wet etch procedure in the previous section was successful in removal of $LiNbO_2$ and any interface oxides. In light of these findings it is likely that the appropriate etching procedure consists of a thick photoresist mask (hard baked), a wet etch which is prematurely stopped to prevent undercutting of thin features, and a dry etch to remove the final oxide and improve anisotropy. It is also theorized that the dry etching process will be improved by the removal of CHF_3 and O_2 from the etch recipe and operating at high ICP power rather than pure RIE as was shown in previous $LiNbO_3$ experiments[192].

APPENDIX C. MASK DESIGN

Multiple photomasks have been designed in order to explore the behavior of $LiNbO_2$ in various geometries and metallization conditions. The masks were all designed using Clewin mask design software using legacy alignment marks and van-der-pauw resistivity patterns from previous design files. Masks are fabricated on 4 inch square plates with chrome metallization and positive photoresist with a clearfield down polarity scheme. Masks were created using a MICROTECH LaserWriter in Marcus Nanotechnology Building operated by the Institute for Electronics and Nanotechnology (IEN) which gives a minimum feature size of 1 μm.

C.1 Memtransistor and Version 1 Ring-Dot Mask

The first fabricated mask is for the fabrication of two separate devices, a transistor structure with either ground-signal-ground (GSG) double-gate or concentric electrodes and an array of concentric ring and dot devices for studying a varying periphery-to-area ratio. The ring dot structure is shown below in Figure C-1. The mask contains layers for mesa isolation, shown in yellow, and separate ring and dot contacts, shown in grey and red respectively. A separate pattern allows both ring and dot contact to be defined in a single exposure. The devices are intended to provide a wide range of periphery-to-area ratios in order to study bulk vs. interfacial effects. Patterns exist for separate ring and dot patterns to enable asymmetric metallization schemes as may be required for non-volatile

devices, as well as a single joined pattern for symmetric metallization schemes. Also included are visual alignment marks, computer aided alignment marks, and a four-point van-der-pauw resistivity pattern. On this mask the minimum electrode dimension for probing is 50 µm.

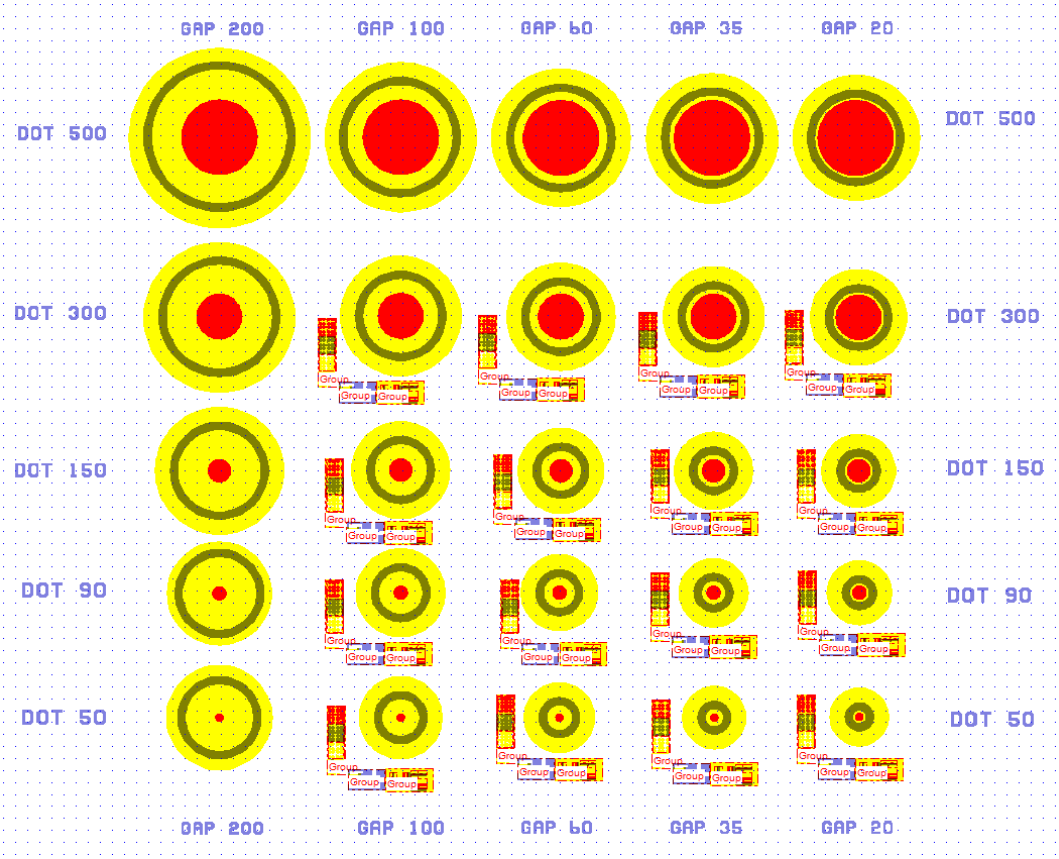

Figure C-1. Concentric ring-dot devices of varying periphery-to-area ratio. The dot diameters are constant by row and listed on the left and right in blue and the distance between ring and dot electrodes is constant by column and listed on the top and bottom in blue. All dimensions are in µm. The isolation mesa is shown in yellow.

The version 1 ring-dot mask contains gaps ϵ (200, 100, 60, 35, 20) μm and dot diameters ϵ (500, 300, 150, 90, 50) μm with a 50 μm wide outer ring and a 50 μm space to the edge of the mesa.

The memtransistor section of the mask, shown in Figure C-2, consists of double-gate GSG and concentric transistors. Blue (grey when overlaid on yellow) represents the source/drain, yellow the mesa isolation, and red the gate. The gate-drain distance is constant by row and the source-drain distance is constant by column. For the double-gate structure the gate-drain distance is ϵ (1.5, 3, 6, 10, 20) μm and the source-drain distance is ϵ (10, 15, 20, 30, 50) for a minimum gate size of 7 μm and a maximum of 47 μm. For the concentric transistor structure the gate width is held at 50 μm (minimum size for a probed structure) while the gate to source distance, equal to the gate to drain distance, is ϵ (10, 20, 30) μm. The transistor pattern shares the same alignment marks and van-der-pauw structures as the ring-dot pattern.

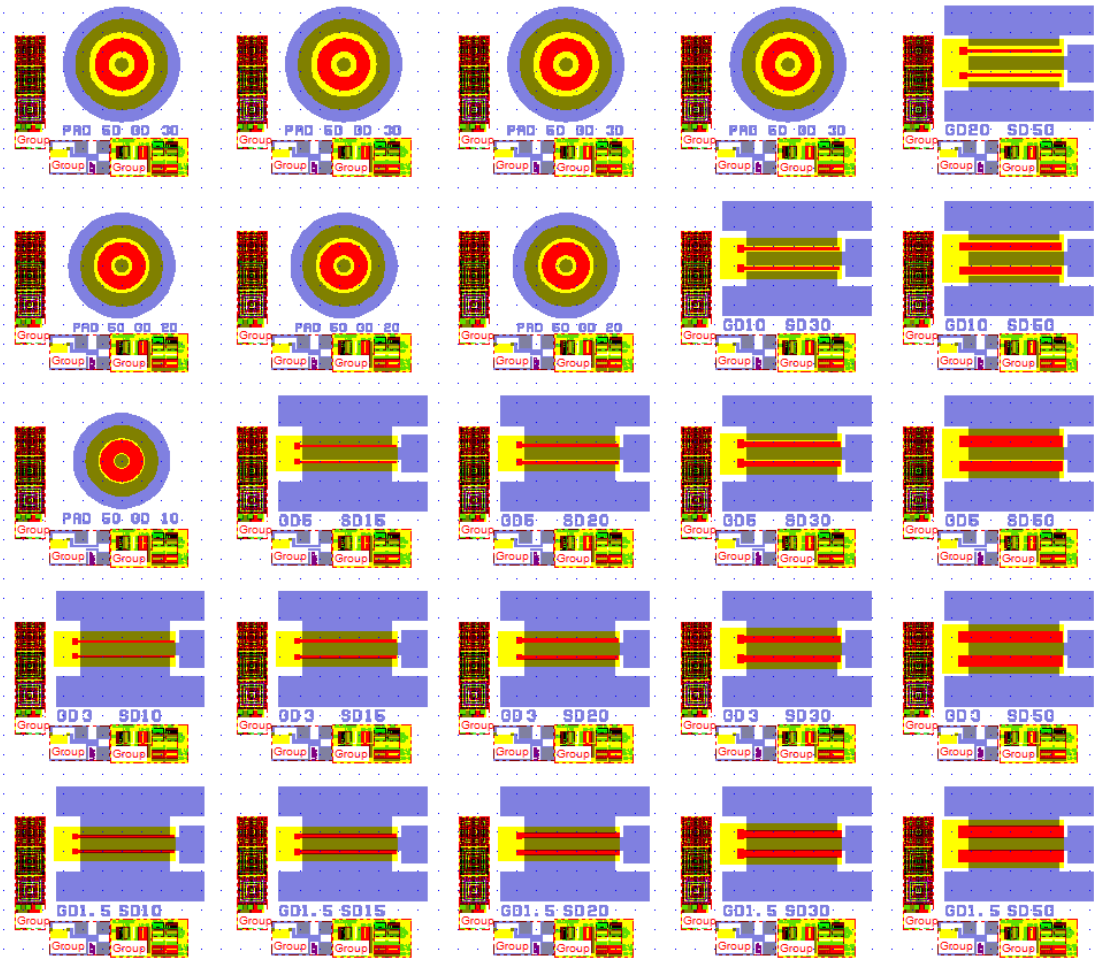

Figure C-2. Memtransistor patterns in both concentric and GSG double-gate configurations. Rows contain devices with constant gate-drain spacing, while columns consist of constant source-drain spacing. Source/drain – blue. Gate – Red. Mesa – yellow.

C.2 **Ring-Dot Mask - Version 2**

After producing devices with the version 1 ring-dot mask it became apparent that multiple devices for comparison would be more important than a range of periphery-to-

area ratios. Results from the version 1 mask indicated that smaller electrode gaps yielded a larger figure of merit ΔR/R. It was also shown that traditional CTLM does not give useful results due to the extremely low resistance of $LiNbO_2$, instead an alternate method was developed to investigate resistance versus inner dot diameter (or interfacial area), therefore the version 2 mask, shown in Figure C-3, holds electrode gap constant while varying dot diameter.

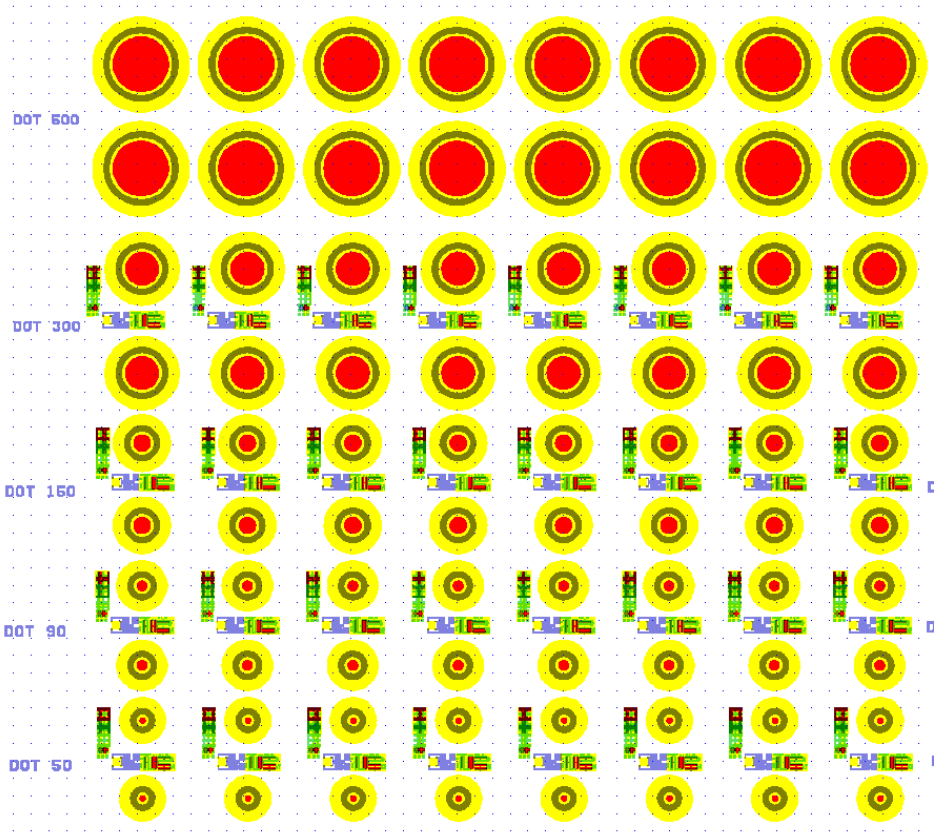

Figure C-3. Version 2 ring-dot mask electrode configuration. Devices are constant by row, varying dot diameter by column. All electrode gaps are 35 µm here, with another pattern for a 100 µm gap.

In addition to separating the ring and dot patterns, a pattern was added to metallize 2 columns of dots at a time so that up to four dot metallization schemes can be tested on the same sample. This was done to correct for sample-to-sample variation in non-volatile metallization studies.

C.3 **Linear Non-Volatile Mask**

It is often beneficial to wire bond a sample prior to testing, depending on the measurement. For instance, any *in situ* scanning probe microscopy needs to have the device bonded so that contact probes do not get in the way of the scanning probe head. In the case of Ag and Al on $LiNbO_2$, the poor adhesion does not allow direct wire bonding without de-laminating the contact. The most common solution to this problem is to wire bond to conductive paste which is then used to contact the device, however this is not possible for concentric ring-dot structures. In order to facilitate wire bonding for such measurements, a linear non-volatile memristor mask was designed and fabricated. This mask is shown in Figure C-4.

The linear non-volatile mask uses large pads, ideal for wire bonding, which cover the active mesa area as well as the substrate post-etch. The active mesa areas are shaped to implement geometric current-concentration as shown by *Greenlee et. al.*[63], and for testing purposes the mask includes 0x, 2x, and 10x concentration with the larger dimension ϵ (100, 50, 10, 2) μm for the 0x and 2x case and ϵ (200, 100, 50, 10) μm for the 10x case. The 10x pattern is shown in Figure C-5. The electrode spacing is constant by column at a

width ϵ (100, 50, 20, 10) μm. The mask provides mesa options for using all current concentrations on one mask (shown in Figure C-4), or using only 0x, 2x, or 10x. All mesa patterns also include large blocks on the right hand side of the mask for various characterizations which might be impeded by metallization. This is ideal for analyzing any post-processing treatment on both electrical characteristics and material properties.

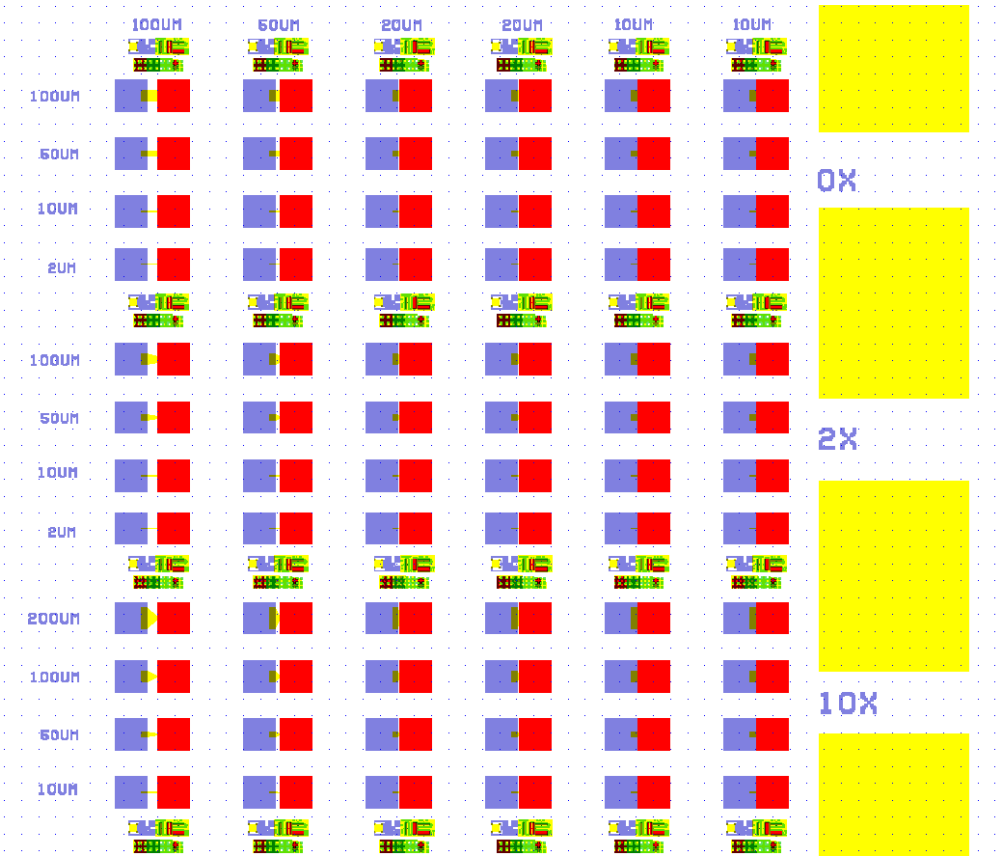

Figure C-4. Linear non-volatile memristor mask. Blue and red represent the non-alloying and alloying contacts, respectively. The mesas are depicted in yellow.

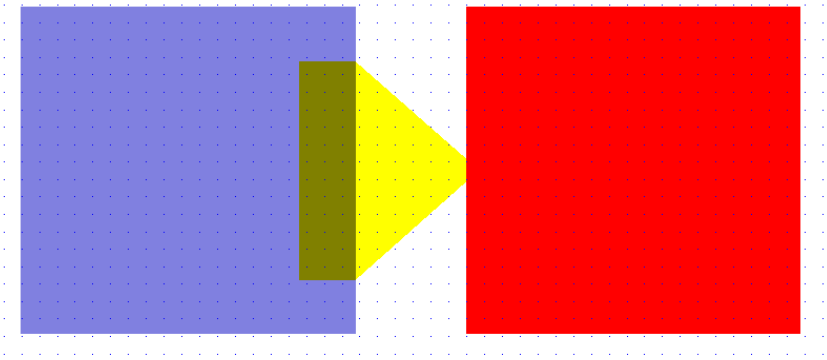

Figure C-5. Current concentrating geometry on the linear non-volatile memristor mask. Blue – non-alloying contact. Red – alloying contact. Yellow – mesa isolation.

REFERENCES

[1] V. V Zhirnov, R.K. Cavin, J.A. Hutchby, S. Member, and G.I. Bourianoff, **91**, (2003).

[2]International Technology Roadmap for Semiconductors <www.itrs.net>(2013).

[3] C. Mead, Proc. IEEE **78**, 1629 (1990).

[4] M.A. Lynch, Physiol. Rev. **358**, 643 (2003).

[5] C. Zamarreño-Ramos, L.A. Camuñas-Mesa, J.A. Perez-Carrasco, T. Masquelier, T. Serrano-Gotarredona, and B. Linares-Barranco, Front. Neurosci. **5**, 1 (2011).

[6] W.T. Franks, D.H. Zhou, B.J. Wylie, B.G. Money, D.T. Graesser, H.L. Frericks, G. Sahota, and C.M. Rienstra, Neuroscience **1**, 1 (2015).

[7] N. Han, M.U. Park, and K.-H. Yoo, ACS Appl. Mater. Interfaces **8**, 9224 (2016).

[8] S. Kim, J. Park, J. Woo, C. Cho, W. Lee, J. Shin, G. Choi, S. Park, D. Lee, B.H. Lee, and H. Hwang, Microelectron. Eng. **107**, 33 (2013).

[9] D.B. Strukov, G.S. Snider, D.R. Stewart, and R.S. Williams, Nature **453**, 80 (2008).

[10] S. Lee, I. Hwang, S. Oh, S. Hong, Y. Kim, Y. Nam, K. Lee, C. Yoon, W. Kim, and B.H. Park, Sci. Rep. **4**, 6871 (2014).

[11] S. La Barbera, D. Vuillaume, and F. Alibart, ACS Nano **9**, 941 (2015).

[12] S.H. Jo, T. Chang, I. Ebong, B.B. Bhadviya, P. Mazumder, and W. Lu, Nano Lett. **10**, 1297 (2010).

[13] M. Hansen, M. Ziegler, L. Kolberg, R. Soni, S. Dirkmann, T. Mussenbrock, and H. Kohlstedt, Sci. Rep. **5**, 13753 (2015).

[14] S. Kim, C. Du, P. Sheridan, W. Ma, S. Choi, and W.D. Lu, Nano Lett. 2203 (2015).

[15] S. Ambrogio, N. Ciocchini, M. Laudato, V. Milo, A. Pirovano, P. Fantini, and D. Ielmini, Front. Neurosci. **10**, 1 (2016).

[16] B.L. Jackson, B. Rajendran, G.S. Corrado, M. Breitwisch, G.W. Burr, R. Cheek, K. Gopalakrishnan, S. Raoux, C.T. Rettner, A. Padilla, A.G. Schrott, R.S. Shenoy, B.N. Kurdi, C.H. Lam, and D.S. Modha, J. Emerg. Technol. Comput. Syst. **9**, 12:1 (2013).

[17] C.D. Wright, Y. Liu, K.I. Kohary, M.M. Aziz, and R.J. Hicken, Adv. Mater. **23**, 3408 (2011).

[18] M. Suri, O. Bichler, D. Querlioz, O. Cueto, L. Perniola, V. Sousa, D. Vuillaume, C. Gamrat, and B. DeSalvo, 2011 Int. Electron Devices Meet. 79 (2011).

[19] S. Saïghi, C.G. Mayr, T. Serrano-Gotarredona, H. Schmidt, G. Lecerf, J. Tomas, J. Grollier, S. Boyn, A.F. Vincent, D. Querlioz, S. La Barbera, F. Alibart, D. Vuillaume, O. Bichler, C. Gamrat, and B. Linares-Barranco, Front. Neurosci. **9**, 1 (2015).

[20] D.O. Hebb, *The Organization of Behavior: A Neuropsychological Theory* (John Wiley & Sons, New York, 1949).

[21] S. Lowel and W. Singer, Science (80-.). **255**, 209 (1992).

[22] G.Q. Bi and M.M. Poo, J. Neurosci. **18**, 10464 (1998).

[23] S. Mandal, A. El-Amin, K. Alexander, B. Rajendran, and R. Jha, Sci. Rep. **4**, 5333 (2014).

[24] R.S. Zucker and W.G. Regehr, Annu. Rev. Physiol. **64**, 355 (2002).

[25] J. Trommershäuser, R. Schneggenburger, A. Zippelius, and E. Neher, Biophys. J. **84**, 1563 (2003).

[26] L.F. Abbott and W.G. Regehr, Nature **431**, 796 (2004).

[27] Z. Wang, S. Joshi, S.E. Savel'ev, H. Jiang, R. Midya, P. Lin, M. Hu, N. Ge, J.P. Strachan, Z. Li, Q. Wu, M. Barnell, G.-L. Li, H.L. Xin, R.S. Williams, Q. Xia, and J.J. Yang, Nat. Mater. **16**, (2016).

[28] C. Du, W. Ma, T. Chang, P. Sheridan, and W.D. Lu, Adv. Funct. Mater. **25**, 4290 (2015).

[29] L.F. Abbott and S.B. Nelson, Nat. Neurosci. **3**, 1178 (2000).

[30] G. Bi and M. Poo, Annu. Rev. Neurosci. **24**, 139 (2001).

[31] T.V.P. Bliss and T. Lømo, J. Physiol. **232**, 331 (1973).

[32] A. Artola, S. Bröcher, and W. Singer, Nature **347**, 69 (1990).

[33] H.Z. Shouval, M.F. Bear, and L.N. Cooper, Proc. Natl. Acad. Sci. **99**, 10831 (2002).

[34] F. Zenke, E.J. Agnes, and W. Gerstner, Nat. Commun. **6**, 6922 (2015).

[35] J.E. Lisman, Proc. Natl. Acad. Sci. U. S. A. **82**, 3055 (1985).

[36] U. Frey and R.G. Morris, Nature **385**, 533 (1997).

[37] A.B. Posadas, A. O'Hara, S. Rangan, R.A. Bartynski, and A.A. Demkov, Appl. Phys. Lett. **104**, 9 (2014).

[38] D. Redfield and W.J. Burke, J. Appl. Phys. **45**, 4566 (1974).

[39] A. Dhar and A. Mansingh, J. Appl. Phys. **68**, 5804 (1990).

[40] P.P. Sahoo and P. a. Maggard, Inorg. Chem. **52**, 4443 (2013).

[41] Z. Weibin, W. Weidong, W. Xueming, C. Xinlu, Y. Dawei, S. Changle, P. Liping, W. Yuying, and B. Li, Surf. Interface Anal. **45**, 1206 (2013).

[42] C. Nico, T. Monteiro, and M.P.F. Graça, Prog. Mater. Sci. **80**, 1 (2016).

[43] E. Wimmer, R. Podloucky, P. Herzig, a. Neckel, and K. Schwarz, Solid State Commun. **42**, iv (1982).

[44] R. Weis and T. Gaylord, Appl. Phys. A Mater. Sci. Process. **37**, 191 (1985).

[45] L.W. Martin, Y.-H. Chu, and R. Ramesh, Mater. Sci. Eng. R **68**, 89 (2010).

[46] J.D. Greenlee, J.C. Shank, M.B. Tellekamp, B.P. Gunning, C.A.M. Fabien, and W.A. Doolittle, Cryst. Growth Des. **14**, 2218 (2014).

[47] W. Li, C. Hu, M. Zhou, K. Wang, H. Li, S. Cheng, and K. Jiang, Electrochim. Acta **189**, 231 (2016).

[48] J.C. Shank, M.B. Tellekamp, and W.A. Doolittle, J. Appl. Phys. **117**, 35704 (2015).

[49] M.D. Pickett, G. Medeiros-Ribeiro, and R.S. Williams, Nat. Mater. **12**, 114 (2013).

[50] S. Li, X. Liu, S.K. Nandi, D.K. Venkatachalam, and R.G. Elliman, Appl. Phys. Lett. **106**, 212902 (2015).

[51] D. Zhou, H. Wang, L.-X. Pang, X. Yao, and X.-G. Wu, J. Am. Ceram. Soc. **91**, 4115 (2008).

[52] M.A. Aegerter, Sol. Energy Mater. Sol. Cells **68**, 401 (2001).

[53] E. a. Mikajlo, K.L. Nixon, V. a. Coleman, and M.J. Ford, J. Phys. Condens. Matter **14**, 3587 (2002).

[54] N. Yabuuchi, M. Takeuchi, M. Nakayama, H. Shiiba, M. Ogawa, K. Nakayama, T. Ohta, D. Endo, T. Ozaki, T. Inamasu, K. Sato, and S. Komaba, Proc. Natl. Acad. Sci. **112**, 7650 (2015).

[55] Y.J. Hsiao, T.H. Fang, S.J. Lin, J.M. Shieh, and L.W. Ji, J. Lumin. **130**, 1863 (2010).

[56] J.C. Shank, Memristive Devices for Neuromorphic Computing Applications, SMARTech, 2016.

[57] W.A. Doolittle, A.G. Carver, and W. Henderson, J. Vac. Sci. Technol. B Microelectron. Nanom. Struct. **23**, 1272 (2005).

[58] W. Doolittle, G. Namkoong, A. Carver, and A. Brown, Solid. State. Electron. **47**, 2143 (2003).

[59] A. Reisman and F. Holtzberg, J. Am. Chem. Soc. **80**, 6503 (1958).

[60] J.J. Yang, D.B. Strukov, and D.R. Stewart, Nat. Nanotechnol. **8**, 13 (2013).

[61] H.S.P. Wong, H.Y. Lee, S. Yu, Y.S. Chen, Y. Wu, P.S. Chen, B. Lee, F.T. Chen, and M.J. Tsai, Proc. IEEE **100**, 1951 (2012).

[62] F. Miao, W. Yi, I. Goldfarb, J.J. Yang, M.X. Zhang, M.D. Pickett, J.P. Strachan, G. Medeiros-Ribeiro, and R.S. Williams, ACS Nano **6**, 2312 (2012).

[63] J.D. Greenlee, J.C. Shank, M.B. Tellekamp, and W. Alan Doolittle, J. Appl. Phys. **114**, 34504 (2013).

[64] R.A. Betts and C.W. Pitt, Electron. Lett. **21**, 960 (1985).

[65] Z. Sitar, F. Gitmans, W. Liu, and P. Gunter, Mater. Res. Soc. Symp. Proc. **401**, 255 (1996).

[66] M. Petrucci, C.W. Pitt, S.R. Reynolds, H.J. Milledge, M.J. Mendelssohn, C. Dineen, and W.G. Freeman, J. Appl. Phys. **63**, 900 (1988).

[67] Y. Wang, R.B. Comes, S. Kittiwatanakul, S.A. Wolf, J. Lu, R.B. Comes, and S.A. Wolf, J. Vac. Sci. Technol. A Vacuum, Surfaces, Film. **33**, 21516 (2015).

[68] W. Doolittle, A. Carver, W. Henderson, and W. Calley, ECS Trans. **2**, 103 (2006).

[69] W.E. Henderson, W. Laws Calley, A.G. Carver, H. Chen, and W. Alan Doolittle, J. Cryst. Growth **324**, 134 (2011).

[70] J.D. Greenlee, W.L. Calley, W. Henderson, and W.A. Doolittle, Phys. Status Solidi **9**, 155 (2012).

[71] G. Meyer and R. Hoppe, J. Less Common Met. **46**, 55 (1976).

[72] A. Miura, K. Tadanaga, E. Magome, C. Moriyoshi, Y. Kuroiwa, T. Takahiro, and N. Kumada, J. Solid State Chem. **229**, 272 (2015).

[73] J. Van Elp, J.L. Wieland, H. Eskes, P. Kuiper, G. a. Sawatzky, F.M.F. De Groot, and T.S. Turner, Phys. Rev. B **44**, 6090 (1991).

[74] M. Ménétrier, I. Saadoune, S. Levasseur, and C. Delmas, J. Mater. Chem. **9**, 1135 (1999).

[75] N. Kumada, S. Muramatu, and F. Muto, J. Solid State Chem. **39**, 33 (1988).

[76] M. Geselbracht, T. Richardson, and A. Stacy, Nature **345**, 324 (1990).

[77] M. Geselbracht and A. Stacy, J. Phys. Chem. 7102 (1993).

[78] D. Novikov, V. Gubanov, V. Zubkov, and A. Freeman, Phys. Rev. B **49**, 15830 15835 (1994).

[79] E. Ylvisaker and W. Pickett, Phys. Rev. B **74**, 75104 (2006).

[80] J.C. Shank, M.B. Tellekamp, and W.A. Doolittle, J. Appl. Phys. **117**, (2015).

[81] E. Moshopoulou, P. Bordet, and J. Capponi, Phys. Rev. B **59**, 9590 (1999).

[82] J.D. Greenlee, C.F. Petersburg, W. Laws Calley, C. Jaye, D. a. Fischer, F.M. Alamgir, and W. Alan Doolittle, Appl. Phys. Lett. **100**, 182106 (2012).

[83] J. Greenlee, W. Calley, M. Moseley, and W. Doolittle, IEEE Trans. Electron Devices **60**, 427 (2013).

[84] J.C. Shank, M.B. Tellekamp, and W.A. Doolittle, Thin Solid Films **609**, 6 (2016).

[85] G. Poberaj, H. Hu, W. Sohler, and P. Günter, Laser Photonics Rev. **6**, 488 (2012).

[86] T. Kanata, Y. Kobayashi, and K. Kubota, J. Appl. Phys. **62**, 2989 (1987).

[87] N. Fujimura, T. Ito, and M. Kakinoki, J. Cryst. Growth **115**, 821 (1991).

[88] M. Shimizu, Y. Furushima, T. Nishida, and T. Shiosaki, Jpn. J. Appl. Phys. **32**, 4111 (1993).

[89] P.R. Meek, L. Holland, and P.D. Townsend, Thin Solid Films **141**, 251 (1986).

[90] J.J. Kingston, D.K. Fork, F. Leplingard, and F.A. Ponce, Mater. Res. Soc. Symp. Proc. **341**, 289 (1994).

[91] S. Ono, O. Bose, W. Unger, Y. Takeichi, and S. Hirano, J. Am. Ceram. Soc. **81**, 1749 (1998).

[92] Y. Shibata, K. Kaya, K. Akashi, M. Kanai, T. Kawai, and S. Kawai, J. Appl. Phys. **77**, 1498 (1995).

[93] S.-H. Lee, T.K. Song, T.W. Noh, and J.-H. Lee, Appl. Phys. Lett. **67**, 43 (1995).

[94] F. Veignant, M. Gandais, P. Aubert, and G. Garry, J. Cryst. Growth **196**, 141 (1999).

[95] K. Matsubara, S. Niki, M. Watanabe, P. Fons, K. Iwata, and a. Yamada, Appl. Phys. A Mater. Sci. Process. **69**, S679 (1999).

[96] H. Tamada, A. Yamada, and M. Saitoh, J. Appl. Phys. **70**, 2536 (1991).

[97] S. Miyazawa, S. Fushimi, and S. Kondo, Appl. Phys. Lett. **26**, 8 (1975).

[98] S.Y. Lee and R.S. Feigelson, J. Cryst. Growth **186**, 594 (1998).

[99] R.S. Feigelson, J. Cryst. Growth **166**, 1 (1996).

[100] A.A. Wernberg, H.J. Gysling, A.J. Filo, and T.N. Blanton, Appl. Phys. Lett. **62**, 946 (1993).

[101] A. Dabirian, S. Harada, Y. Kuzminykh, S.C. Sandu, E. Wagner, G. Benvenuti, P. Brodard, S. Rushworth, P. Muralt, and P. Hoffmann, J. Electrochem. Soc. **158**, D72 (2011).

[102] X. Lansiaux, E. Dogheche, D. Remiens, M. Guilloux-viry, A. Perrin, and P. Ruterana, J. Appl. Phys. **90**, 5274 (2001).

[103] L. Chua, IEEE Trans. Circuit Theory **18**, 507 (1971).

[104] E. Gale, Phys. Status Solidi **1**, 1 (2014).

[105] L. Chua and S. Kang, Proc. IEEE **64**, (1976).

[106] L. Chua, Appl. Phys. A **102**, 765 (2011).

[107] T.W. Hickmott, J. Appl. Phys. **33**, 2669 (1962).

[108] J.H. Hur, M.J. Lee, C.B. Lee, Y.B. Kim, and C.J. Kim, Phys. Rev. B - Condens.

Matter Mater. Phys. **82**, 1 (2010).

[109] A. Leshem, E. Gonen, and I. Riess, Nanotechnology **22**, 254024 (2011).

[110] T. Driscoll, H. Kim, and B. Chae, Appl. Phys. Lett. **95**, (2009).

[111] M.D. Pickett and R.S. Williams, Nanotechnology **23**, 215202 (2012).

[112] Y. V. Pershin and M. Di Ventra, Phys. Rev. B - Condens. Matter Mater. Phys. **78**, 5 (2008).

[113] A. Chanthbouala, V. Garcia, R.O. Cherifi, K. Bouzehouane, S. Fusil, X. Moya, S. Xavier, H. Yamada, C. Deranlot, N.D. Mathur, M. Bibes, A. Barthelemy, and J. Grollier, Nat. Mater. **11**, 860 (2012).

[114] J.P. Strachan, D.B. Strukov, J. Borghetti, J.J. Yang, G. Medeiros-Ribeiro, and R.S. Williams, Nanotechnology **22**, 254015 (2011).

[115] A. Wedig, M. Luebben, M. Moors, D.Y. Cho, K. Skaja, T. Hasegawa, K.K. Adepalli, B. Yildiz, R. Waser, and I. Valov, Nat. Nanotechnol. **11**, 67 (2015).

[116] Z. Wei, Y. Kanzawa, K. Arita, Y. Katoh, K. Kawai, S. Muraoka, S. Mitani, S. Fujii, K. Katayama, M. Iijima, T. Mikawa, T. Ninomiya, R. Miyanaga, Y. Kawashima, K. Tsuji, A. Himeno, T. Okada, R. Azuma, K. Shimakawa, H. Sugaya, T. Takagi, R. Yasuhara, K. Horiba, H. Kumigashira, and M. Oshima, 2008 IEEE Int. Electron Devices Meet. 1 (2008).

[117] H.Y. Lee, P.S. Chen, T.Y. Wu, Y.S. Chen, C.C. Wang, P.J. Tzeng, C.H. Lin, F. Chen, C.H. Lien, and M.J. Tsai, Tech. Dig. - Int. Electron Devices Meet. IEDM 3 (2008).

[118] T. Ohno, T. Hasegawa, T. Tsuruoka, K. Terabe, J.K. Gimzewski, and M. Aono, Nat. Mater. **10**, 591 (2011).

[119] R. Yang, K. Terabe, Y. Yao, T. Tsuruoka, T. Hasegawa, J.K. Gimzewski, and M. Aono, Nanotechnology **24**, 384003 (2013).

[120] Y.E. Syu, T.C. Chang, J.H. Lou, T.M. Tsai, K.C. Chang, M.J. Tsai, Y.L. Wang, M. Liu, and S.M. Sze, Appl. Phys. Lett. **102**, (2013).

[121] G.A. Gibson, S. Musunuru, J. Zhang, K. Vandenberghe, J. Lee, C.C. Hsieh, W. Jackson, Y. Jeon, D. Henze, Z. Li, and R. Stanley Williams, Appl. Phys. Lett. **108**, (2016).

[122] S. Slesazeck, H. Mähne, H. Wylezich, A. Wachowiak, J. Radhakrishnan, A. Ascoli, R. Tetzlaff, and T. Mikolajick, RSC Adv. **5**, 102318 (2015).

[123] S. Kumar, J.P. Strachan, and R.S. Williams, Nature **548**, 318 (2017).

[124] S. Kumar, Z. Wang, N. Davila, N. Kumari, K.J. Norris, X. Huang, J.P. Strachan, D. Vine, A.L.D. Kilcoyne, Y. Nishi, and R.S. Williams, Nat. Commun. **8**, 658 (2017).

[125] H.D. Crane, Proc. IRE **50**, 2048 (1962).

[126] A. Hodgkin and A. Huxley, Proc. R. Soc. London. Ser. B, Biol. Sci. **140**, 177 (1952).

[127] S. Lai, IEEE Int. Electron Devices Meet. 255 (2003).

[128] S. Raoux and M. Wuttig, *Phase Change Materials: Science and Applications*, 1st ed. (Springer US, 2009).

[129] J.H. Oh, J.H. Park, Y.S. Lim, H.S. Lim, Y.T. Oh, J.S. Kim, J.M. Shin, J.H. Park, Y.J. Song, K.C. Ryoo, D.W. Lim, S.S. Park, J.I. Kim, J.H. Kim, J. Yu, F. Yeung, C.W. Jeong, J.H. Kong, D.H. Kang, G.H. Koh, G.T. Jeong, H.S. Jeong, and K. Kim, Tech. Dig. - Int. Electron Devices Meet. IEDM 8 (2006).

[130] T. Tuma, A. Pantazi, M. Le Gallo, A. Sebastian, and E. Eleftheriou, Nat. Nanotechnol. **11**, 693 (2016).

[131] A. Sebastian, M. Le Gallo, and D. Krebs, Nat. Commun. **5**, 1 (2014).

[132] D. Kuzum, R.G.D. Jeyasingh, B. Lee, and H.P. Wong, Nano Lett. 2179 (2012).

[133] T. Tuma, M. Le Gallo, A. Sebastian, and E. Eleftheriou, IEEE Electron Device Lett. **37**, 1238 (2016).

[134] F. Gitmans, Z. Sitar, and P. Gunter, Vacuum **46**, 939 (1995).

[135] D.G. Schlom, A.F. Marshall, J.T. Sizemore, Z.J. Chen, J.N. Eckstein, I. Bozovic, K.E. Von Dessonneck, J.S. Harris, and J.C. Bravman, J. Cryst. Growth **102**, 361 (1990).

[136] J.A. Peters, M. Klanchar, T.G. Hughes, and J.C. Mankin, US Pat. 5,376,352 (1994).

[137] M. Markowitz, D. Boryta, and H.J. Stewart, Ind. Eng. Chem. Prod. Res. Dev. **3**, 321 (1964).

[138] M. Markowitz and D. Boryta, J. Phys. Chem. **11**, 383 (1961).

[139] K.H. Stern, *High Temperature Properties and Thermal Decomposition of Inorganic Salts with Oxyanions* (CRC Press, 2000).

[140] M. Markowitz and D. Boryta, J. Phys. Chem. 358 (1962).

[141] P.G. Staib, J. Vac. Sci. Technol. B Microelectron. Nanom. Struct. **29**, 03C125 (2011).

[142] W. Laws Calley, J.D. Greenlee, W.E. Henderson, J. Lowder, M.W. Moseley, W. Alan Doolittle, and P.G. Staib, J. Vac. Sci. Technol. B Microelectron. Nanom. Struct. **31**, 03C126 (2013).

[143] J.. Sanz and S. Hofmann, J. Less Common Met. **92**, 317 (1983).

[144] K. Kitamura, Y. Furukawa, S. Takekawa, and S. Kimura, US 6,464,777 B2 (2002).

[145] D.K. Finnemore, T.F. Stromberg, and C. a. Swenson, Phys. Rev. **149**, 231 (1966).

[146] J. Halbritter, Appl. Phys. A **43**, 1 (1987).

[147] a. R. Wildes, J. Mayer, and K. Theis-Bröhl, Thin Solid Films **401**, 7 (2001).

[148] G.V. Chandrashekhar, J. Moyo, and J.M. Honig, J. Solid State Chem. **2**, 528 (1970).

[149] W.W. Schulz and R.M. Wentzcovitch, Phys. Rev. B **48**, 16986 (1993).

[150] V. Eyert, Europhys. Lett. **58**, 851 (2002).

[151] J. Laverock, A.R.H. Preston, D. Newby, K.E. Smith, S. Sallis, L.F.J. Piper, S. Kittiwatanakul, J.W. Lu, S.A. Wolf, M. Leandersson, and T. Balasubramanian, Phys. Rev. B - Condens. Matter Mater. Phys. **86**, 1 (2012).

[152] A. O'Hara, T.N. Nunley, A.B. Posadas, S. Zollner, and A.A. Demkov, J. Appl. Phys. **116**, (2014).

[153] F.J. Wong, N. Hong, and S. Ramanathan, Phys. Rev. B - Condens. Matter Mater. Phys. **90**, 1 (2014).

[154] A. O'Hara and A.A. Demkov, Phys. Rev. B **91**, 94305 (2015).

[155] F.J. Wong and S. Ramanathan, J. Mater. Res. **28**, 2555 (2013).

[156] B. King, H. Patel, D. Gulino, and B. Tatarchuk, Thin Solid Films **192**, (1990).

[157] H. Roth, G. Meyer, Z. Hu, and G. Kaindl, Zeitschrift Für Anorg. Und Allg. Chemie **619**, 1369 (1993).

[158] S.O. Yoon, J.H. Yoon, K.S. Kim, S.H. Shim, and Y.K. Pyeon, J. Eur. Ceram. Soc. **26**, 2031 (2006).

[159] K.K. Lee, G. Namkoong, W.A. Doolittle, M. Losurdo, G. Bruno, and D.H. Jundt, J. Vac. Sci. Technol. B **24**, 2093 (2006).

[160] B. Zielińska, E. Borowiak-Palen, and R.J. Kalenzuk, J. Phys. Chem. Solids **69**, 236 (2008).

[161] K.K. Lee, G. Namkoong, S.M. Madison, S.E. Ralph, W.A. Doolittle, M. Losurdo, G. Bruno, and H.K. Cho, Mater. Sci. Eng. B Solid-State Mater. Adv. Technol. **140**, 203 (2007).

[162] S.R. Lee, A.M. West, A.A. Allerman, K.E. Waldrip, D.M. Follstaedt, P.P. Provencio, D.D. Koleske, and C.R. Abernathy, Appl. Phys. Lett. **86**, 1 (2005).

[163] K. Lee, Implementation of AlGaN/GaN Based High Electron Mobility Transistor on Ferroelectric Materials for Multifunctional Optoelectronic-Acoustic-Electronic Applications, Georgia Institute of Technology, 2009.

[164] R. Marom, S.F. Amalraj, N. Leifer, D. Jacob, and D. Aurbach, J. Mater. Chem. **21**, 9938 (2011).

[165] R. Baddour-Hadjean and J.-P. Pereira-Ramos, Chem. Rev. **110**, 1278 (2010).

[166] C. Liu, Z.G. Neale, and G. Cao, Mater. Today **19**, 109 (2016).

[167] D. Mikhailova, O.M. Karakulina, D. Batuk, J. Hadermann, A.M. Abakumov, M. Herklotz, A.A. Tsirlin, S. Oswald, L. Giebeler, M. Schmidt, J. Eckert, M. Knapp, and H. Ehrenberg, Inorg. Chem. **55**, 7079 (2016).

[168] H. Tukamoto and A. West, J. Electrochem. Soc. **144**, 3164 (1997).

[169] Q. Lin, Q. Li, K.E. Gray, and J.F. Mitchell, Cryst. Growth Des. **12**, 1232 (2012).

[170] T. Motohashi, T. Ono, Y. Sugimoto, Y. Masubuchi, S. Kikkawa, R. Kanno, M. Karppinen, and H. Yamauchi, Phys. Rev. B **2**, 29 (2009).

[171] L. Dahéron, R. Dedryvère, H. Martinez, M. Ménétrier, C. Denage, C. Delmas, and D. Gonbeau, Chem. Mater. **20**, 583 (2008).

[172] a. N. Dey, J. Electrochem. Soc. **118**, 1547 (1971).

[173] J.M.J. Murre and J. Dros, PLoS One **10**, 1 (2015).

[174] J.D. Greenlee, J.C. Shank, M. Brooks Tellekamp, and W. Alan Doolittle, J. Appl. Phys. **114**, 34504 (2013).

[175] T.B. Massalski, H. Baker, L.H. Bennet, and J.L. Murray, *Binary Alloy Phase Diagrams* (ASM International, 1986).

[176] J.H. Klootwijk and C.E. Timmering, Proc. 2004 Int. Conf. Microelectron. Test Struct. (IEEE Cat. No.04CH37516) **17**, 8 (2004).

[177] A.J. Willis and A.P. Botha, Thin Solid Films **146**, 15 (1987).

[178] Dieter K. Schroder, Semicond. Mater. Device Charact. (2005).

[179] G.K. Reeves, Solid. State. Electron. **23**, 487 (1980).

[180] G.K. Reeves and H.B. Harrison, IEEE Trans. Electron Devices **42**, 1536 (1995).

[181] G.S. Marlow and M.B. Das, Solid State Electron. **25**, 91 (1982).

[182] W.C. West, J.F. Whitacre, V. White, and B. V Ratnakumar, J. Micromechanics Microengineering **12**, 58 (2001).

[183] J. Song, X. Yang, S.-S. Zeng, M.-Z. Cai, L.-T. Zhang, Q.-F. Dong, Ming-SenZheng, S.-T. Wu, Q.-H. Wu, M.-S. Zheng, S.-T. Wu, and Q.-H. Wu, J. Micromechanics Microengineering **19**, 45004 (2009).

[184] S.-H. Chang, H.-H. Park, A. Maazaz, and C. Delmas, Comptes Rendes l'Academie Des Sci. Ser. II **308**, 475 (1989).

[185] D.G. Kellerman, V.S. Gorshkov, A.P. Tyutyunnik, V.G. Zubkov, V.A. Perelyaev, T.V. D'yachkova, N.I. Kadyrova, A.S. Fedyukov, S.A. Turzhevsky, V.A. Gubanov, G.P. Shveikin, A.E. Kar'kin, and V.I. Voronin, Supercond. Physics, Chem. Technol. **5**, 2035 (1992).

[186] M.B. Dines, Mater. Res. Bull. **10**, 287 (1975).

[187] A. McDowell, D. Snyderman, M. Conradi, B. Silbernagel, and A. Stacy, Phys. Rev. B. Condens. Matter **50**, 15764 (1994).

[188] M.B. Tellekamp, J.D. Greenlee, J.C. Shank, and W.A. Doolittle, J. Cryst. Growth **425**,

225 (2015).

[189] M. Yasaka, Rigaku J. **26**, 1 (2010).

[190] T.T. Foxe, B.D. Hunt, C. Rogers, A.W. Kleinsasser, and R.A. Buhrman, J. Vac. Sci. Technol. **19**, 1394 (1981).

[191] K. Williams, K. Gupta, and M. Wasilik, J. Microelectromechanical Syst. **12**, 761 (2003).

[192] Z. Ren, P.J. Heard, J.M. Marshall, P. a. Thomas, and S. Yu, J. Appl. Phys. **103**, 34109 (2008).

[193] W. Laws Calley, J.D. Greenlee, W.E. Henderson, J. Lowder, M.W. Moseley, W. Alan Doolittle, and P.G. Staib, J. Vac. Sci. Technol. B Microelectron. Nanom. Struct. **31**, 03C126 (2013).

[194] Y.S. Kim and R.T. Smith, J. Appl. Phys. **40**, 4637 (1969).

[195] E.R. Dobrovinskaya, L.A. Lytvynov, and V. Pishchik, *Sapphire: Material, Manufacturing, Applications* (Springer US, 2009).

[196] Z. Li and R.C. Bradt, J. Appl. Phys. **69**, 863 (1986).

[197] F. Campbell, ASM Int. **#05224G**, 672 (2008).

[198] A. Kent, <http://www.physics.nyu.edu/kentlab/How_to/ChemicalInfo/VaporPressure/morepressure.pdf>.

[199] R.H. Lamoreaux and D.L. Hildenbrand, J. Phys. Chem. Ref. Data **13**, 151 (1984).